Three dimensional spheroids and gold nanoparticles in combined cancer therapy

by

Kyle William Bromma
B.Sc., University of Victoria, 2018

A Dissertation Submitted in Partial Fulfillment of the
Requirements for the Degree of

DOCTOR OF PHILOSOPHY

in the Department of Physics and Astronomy

© Kyle William Bromma, 2023
University of Victoria

All rights reserved. This Dissertation may not be reproduced in whole or in part, by photocopy or other means, without the permission of the author.

We acknowledge and respect the Lək̓ʷəŋən peoples on whose traditional territory the university stands and the Songhees, Esquimalt and W̱SÁNEĆ peoples whose historical relationships with the land continue to this day.

Three dimensional spheroids and gold nanoparticles in combined cancer therapy

by

Kyle William Bromma
B.Sc., University of Victoria, 2018

Supervisory Committee

Dr. Devika Chithrani, Co-Supervisor
(Department of Physics and Astronomy)

Dr. Wayne Beckham, Co-Supervisor
(Department of Physics and Astronomy)

Dr. Bob Chow, Outside Member
(Department of Biology)

ABSTRACT

One of the major issues in cancer radiotherapy (RT) is normal tissue toxicity. Introduction of radiosensitizers like gold nanoparticles (GNPs) into cancer cells to enhance the local RT dose is a promising technique that is being explored. However, a large portion of experimentation involving GNPs has been done in simple two-dimensional (2D) monolayer models that cannot properly encapsulate the complex heterogeneous interactions that occur *in vivo*. By introducing an *in vitro* three-dimensional (3D) model that better mimics the tumour microenvironment (TME), we can more rapidly facilitate a quicker translation of various treatment technologies like GNPs to the clinic. Further, clinical trials show that the chemotherapy drug docetaxel (DTX) given in conjunction with RT can improve survival in high-risk cancers. Addition of GNPs to this current DTX/RT protocol is expected to further improve therapeutic benefits. Elucidation of a combined therapy of GNPs, DTX, and RT to optimize treatment can better improve patient outcome and reduce normal tissue toxicity by specifically targeting tumours and is completely novel research.

The work in this dissertation explores the application of GNPs to various elements that are present in a TME. Many cell types are present in TME and contribute in different ways to the proliferation of cancer. One of these cell lines, cancer associated fibroblasts (CAFs), which can promote tumour growth and metastasis, was compared to cancer epithelial cells and normal fibroblasts (FBs). Hence, we used FBs and CAFs to evaluate the differences in GNP uptake and resulting radiation induced damage. It was found that the CAFs had a much larger uptake of GNPs relative to the other cells, with on average 265% more GNPs relative to cervical cancer cells while FBs had only 7.55% the uptake of the tumour cells and 2.87% the uptake of CAFs. This translated to increases in 53BP1-related DNA damage foci in CAFs (13.5%) and tumour cells (9.8%) along with FBs (8.8%), compared to control with RT treatment. This difference in DNA damage due to selective targeting of cancer associated cells over normal cells may allow GNPs to be an effective tool in future cancer RT to battle normal tissue toxicity while improving local RT dose to the tumour.

To expedite a quicker clinical translation, 3D tumor spheroid models were optimized and compared to 2D monolayer. The uptake of various sizes of GNPs was tested on monolayer and spheroids to evaluate the differences between a 2D and 3D model in similar conditions. Moreover, combined treatment of GNPs with DTX was introduced and how they effect the uptake of the GNPs was elucidated.

In the 2D monolayer model, the addition of DTX induced a small increase of uptake of GNPs of between 13% and 24%, while in the 3D spheroid model, DTX increased uptake by between 47% and 186%. It was observed that the more complex spheroid, which introduces an extracellular matrix, had larger uptake and penetration of smaller GNPs (15 nm) relative to larger GNPs (50 nm). Moreover, while the addition of DTX had a beneficial effect on the uptake of GNPs into cells, it also synchronized the cells into a radiosensitive cell cycle phase. This translated to a larger effect when radiation was introduced, in a combined treatment modality with GNP, DTX, and RT. In spheroids, the addition of GNPs to the treatment regime decreased the surviving tumour cells by 16-32% compared to samples not treated with GNPs. Further, the addition of DTX seems to synergistically increase damage in some cancer cell lines. This work highlights the necessity to optimize GNP treatment conditions in a more realistic tumor-like environment. A 3D spheroid model can capture important details which are absent from a simple 2D monolayer model.

Contents

Supervisory Committee ii

Abstract iii

Table of Contents v

List of Tables ix

List of Figures x

Acknowledgements xiii

Abbreviations xiv

1 Introduction 1

1.1 The worldwide burden of cancer . . . 1

1.2 Current cancer treatment modalities . . . 1

1.2.1 Radiotherapy . . . 2

1.2.2 Chemotherapy . . . 3

1.3 Improving cancer treatment with nanomedicine . . . 5

1.3.1 Normal tissue toxicity . . . 5

1.3.2 Nanoparticle applications in cancer treatment . . . 6

1.4 Gold nanoparticles in cancer therapeutics . . . 7

1.4.1 Gold nanoparticle characteristics . . . 7

1.4.2 Gold nanoparticles in chemotherapy and radiotherapy . . . 9

1.5 Towards personalized medicine . . . 11

1.5.1 Two dimensional vs three dimensional models . . . 11

1.6 Scope of dissertation . . . 14

2 Gold nanoparticles and radiobiology 16

2.1 Biology of the tumour . . . 16
2.1.1 Selective proliferative advantage . . . 16
2.1.2 Altered stress response . . . 18
2.1.3 Angiogenesis . . . 20
2.1.4 Invasion and metastasis . . . 21
2.1.5 Metabolic rewiring . . . 22
2.1.6 Immune modulation . . . 23
2.1.7 Abetting tumor microenvironment . . . 23
2.2 Radiobiology . . . 24
2.2.1 The DNA damage response . . . 24
2.2.2 Cell cycle and radiosensitivity . . . 25
2.2.3 DNA damage repair . . . 26
2.2.4 Five Rs of radiotherapy . . . 28
2.3 Radiation and the interaction with matter . . . 29
2.3.1 The Atom and Photon Absorption . . . 30
2.3.2 Photoelectric Effect . . . 31
2.3.3 Rayleigh Scattering . . . 32
2.3.4 Compton Scattering . . . 32
2.3.5 Pair Production . . . 34
2.4 Gold nanoparticles as a radiosensitizer . . . 35
2.4.1 Intracellular fate of gold nanoparticles . . . 35
2.4.2 Gold nanoparticles and radiotherapy . . . 38
2.5 Summary . . . 39

3 Optimizing gold nanoparticle treatment in two-dimensional cancer cell models 40
3.1 Preamble . . . 40
3.2 Introduction . . . 41
3.3 Results . . . 43
3.3.1 Characterization of gold nanoparticle complexes . . . 43
3.3.2 Cellular uptake of GNP complexes . . . 46
3.3.3 Effect of radiation on cell proliferation . . . 50
3.3.4 Probing the radiation damage using DNA double stand breaks (DSB) assay . . . 54
3.4 Discussion . . . 54

3.5 Conclusions . . . 61
3.6 Materials and methods . . . 61
3.6.1 Cells and materials . . . 61
3.6.2 Synthesis, surface modification, and characterization of Gold Nanoparticles . . . 62
3.6.3 Cellular uptake and retention of GNP complex . . . 66
3.6.4 Preparation of cells for darkfield and confocal imaging . . . 67
3.6.5 Radiation treatment . . . 68
3.6.6 Doubling time assay . . . 68
3.6.7 Immunofluorescence assay . . . 70
3.6.8 Statistical Analysis . . . 70

4 Docetaxel to improve gold nanoparticle-based radiotherapy in multiple cell models 72
4.1 Preamble . . . 72
4.2 Introduction . . . 73
4.3 Results and Discussion . . . 76
4.3.1 Characterization of GNPs . . . 76
4.3.2 Characterization of spheroids and docetaxel . . . 80
4.3.3 Uptake of gold nanoparticles with docetaxel . . . 83
4.4 Conclusion . . . 92
4.5 Materials and methods . . . 93
4.5.1 Synthesis, Surface Modification, and Characterization of Gold Nanoparticles . . . 93
4.5.2 Cell Culture and Growth of Spheroids . . . 94
4.5.3 Proliferation Assay of Docetaxel in Monolayer and Spheroids . . . 94
4.5.4 Cellular Uptake of Gold Nanoparticle Complex . . . 95
4.5.5 Preparation of Cells for Imaging Using Darkfield and Hyper Spectral Imaging . . . 96
4.5.6 Cell Cycle Analysis of Docetaxel Using Flow Cytometry . . . 96
4.5.7 Statistical Analysis . . . 97

5 Combined cancer therapy and gold nanoparticles 98
5.1 Preamble . . . 98
5.2 Introduction . . . 99

5.3 Results and Discussion . . . 102
5.3.1 Characterization of gold nanoparticles and spheroids . . . 102
5.3.2 Docetaxel in spheroids and monolayer . . . 105
5.3.3 Radiation response in monolayer . . . 110
5.3.4 Radiation response in spheroids . . . 116
5.4 Conclusions . . . 123
5.5 Materials and methods . . . 123
5.5.1 Cells and culture conditions . . . 123
5.5.2 Synthesis, surface modification, and characterization of gold nanoparticles . . . 124
5.5.3 Cell culture and growth of spheroids . . . 125
5.5.4 Proliferation assay of docetaxel in monolayer and spheroids . . . 125
5.5.5 Cellular uptake of gold nanoparticle complexes . . . 126
5.5.6 Preparation of cells for imaging using darkfield and hyper spectral imaging . . . 127
5.5.7 Preparation for live cell confocal imaging . . . 127
5.5.8 Cell cycle analysis of Docetaxel using flow cytometry . . . 127
5.5.9 Radiation of monolayer and spheroids . . . 128
5.5.10 Radiation proliferation assays . . . 128
5.5.11 Immunofluorescence assay . . . 130
5.5.12 Growth analysis of spheroids . . . 130
5.5.13 Hypoxic analysis of spheroids . . . 131
5.5.14 Statistical analysis . . . 131

6 Conclusion **132**
6.1 Conclusions . . . 132
6.2 Preliminary Future Work . . . 134
6.2.1 Materials and Methods . . . 134
6.2.2 Results and Discussion . . . 138
6.2.3 Conclusion . . . 144
6.3 Future Directions . . . 144

Bibliography **147**

List of Tables

Table 3.1 **Linear Accelerator set-up parameters** 70

List of Figures

Figure 1.1 Introduction to nanotechnology. 6
Figure 1.2 Monolayer vs Spheroid. 12
Figure 1.3 Spheroid model. 13

Figure 2.1 Hallmarks of Cancer. 17
Figure 2.2 The Cell Cycle. 18
Figure 2.3 The DNA damage response. 25
Figure 2.4 Cell survival curve. 27
Figure 2.5 The therapeutic index. 28
Figure 2.6 Mass attenuation coefficients. 31
Figure 2.7 Photoelectric Effect. 32
Figure 2.8 Compton Scattering. 33
Figure 2.9 Uptake of nanoparticles into a cell. 35
Figure 2.10 Ratio of gold mass attenuation coefficient with water mass attenuation coefficient. 37
Figure 2.11 Gold nanoparticles as a radiosensitizer. 39

Figure 3.1 Normal and cancer associated fibroblasts in cancer therapeutics. 42
Figure 3.2 Characterization of gold nanoparticles. 43
Figure 3.3 Supplementary characterization of gold nanoparticles 44
Figure 3.4 Uptake and retention of gold nanoparticles. 46
Figure 3.5 Surface Area Normalized Uptake and retention of Gold Nanoparticles. 47
Figure 3.6 Microtubule transport of nanoparticles. 48
Figure 3.7 Z-stack using confocal imaging of three cell lines. 49
Figure 3.8 Monolayer Radiation Proliferation Assay 51
Figure 3.9 Proliferation of cells after radiation. 52
Figure 3.10 Immunofluorescence assay using 53BP1 foci. 53
Figure 3.11 Images of immunofluorescent double strand break assay. 55

Figure 3.12Immunofluorescent assay with γH2AX and confirmation of encapsulated GNPs 56
Figure 3.13Experimental clonogenic assay result for HeLa. 58
Figure 3.14Ultraviolet-visible spectrometer schematic 64
Figure 3.15Experimental linear accelerator setup 69

Figure 4.1 Two-Dimensional Tissue Culture Model vs. Three-Dimensional Tissue Culture Model. 75
Figure 4.2 Characterization of gold nanoparticles. 77
Figure 4.3 Supplemental gold nanoparticle characterization. 78
Figure 4.4 Characterization of spheroids. 79
Figure 4.5 Synchronization of tissue culture models with docetaxel. 82
Figure 4.6 Gold nanoparticle uptake in two-dimensional cell model. 84
Figure 4.7 Darkfield images of gold nanoparticle uptake in HeLa. 85
Figure 4.8 Gold nanoparticle update in three-dimensional cell model. . . . 87
Figure 4.9 Darkfield images of gold nanoparticles uptake in HeLa spheroid model. 89
Figure 4.10Depth of penetration of gold nanoparticles in spheroids. 90
Figure 4.11Total gold content uptake in monolayer and spheroids. 91

Figure 5.1 Improved cell kill with combined cancer therapy. 100
Figure 5.2 Characterization of gold nanoparticles. 103
Figure 5.3 Characterizing spheroid size. 104
Figure 5.4 Docetaxel characterization in HeLa. 105
Figure 5.5 Docetaxel characterization in LNCaP. 107
Figure 5.6 Darkfield images of control monolayer and spheroids. 108
Figure 5.7 Gold nanoparticle uptake in monolayer and spheroid. 109
Figure 5.8 Radiation response in monolayer. 112
Figure 5.9 Confocal images of 53BP1 foci in monolayer of HeLa. 114
Figure 5.10Confocal images of 53BP1 foci in monolayer of LNCaP. 115
Figure 5.11Hypoxia analysis in spheroids. 117
Figure 5.12Radiation response in spheroids. 118
Figure 5.13Growth of HeLa spheroids following radiation. 120
Figure 5.14Growth of LNCaP spheroids following radiation. 122
Figure 5.15Plate set up for radiation. 129

Figure 6.1 Gold nanoparticle uptake in two-dimensional and three-dimensional models. 139
Figure 6.2 Treatment of PC-3 subcutaneous tumour with docetaxel. 141
Figure 6.3 Gold nanoparticle uptake in *in vivo* mouse xenograft model. . . 143

Acknowledgements

First of all, I would like to thank my supervisor Dr. Devika Chithrani. I am extremely grateful to you for giving me the opportunity to prove myself in undergrad and trusting me through out my graduate studies. Your passion and drive to always be the best is inspiring, and I am proud to be part of your lab.

I would also like to extend my gratitude to my co-supervisor, Dr. Wayne Beckham. You were always a positive role model and every time we spoke was a delight. You reinforce a very positive culture in the field of Medical Physics which I hope to carry on. Thank you as well to Dr. Bob Chow, the final member of my committee. You challenged me during our meetings to explain key concepts and explore the field of biology, leading me to a deeper understanding.

I would also like to thank Dr. Magdalena Bazalova-Carter, who helped mentor me on various topics and really instilled a lot of confidence in my ability. Even though I was not your student, you still sat down with me and gave me advice on research and career goals, which I am extremely grateful for.

To the many peers that went through the lab during my time, of which there are too many to name, it was a pleasure working with you and I appreciated working with each one of you. I would very much like to also thank Devon Richtsmeier, Alex Hart, and Dr. Matt Gwilliam, for helping me survive the earlier years of our graduate studies and being great friends ever since.

Thank you to the many Medical Physicists at BC Cancer who helped teach and guide me throughout my graduate studies. A special thank you to Dr. Derek Wells, who taught me over the years and mentored me in my professional career goals.

I want to thank my parents, my grandparents, and my brother. Without your support, I doubt I could have made it this far. I would also like to thank my wonderful partner, Anika, for your patience.

Thank you all.

Abbreviations

2D Two Dimensional

3D Three Dimensional

53BP1 p53-Binding Protein 1

ATCC American Type Culture Collection

ATM Ataxia Telangiectasia Mutate

ATP Adenosine Triphosphate

BCL2 B-cell Lymphoma-2

BSA Bovine Serum Albumin

CAF Cancer Associated Fibroblast

CDK Cyclin-Dependent Kinase

CDKI Cyclin-Dependent Kinase Inhibitor

CT Computed Tomography

CTL Control

CTLA4 Cytotoxic Lymphocyte Antigen 4

DLS Dynamic Light Scattering

DMEM Dulbecco's Modified Eagle Medium

DMSO Dimethyl Sulfoxide

DNA Deoxyribonucleic Acid

DSB Double Strand Break

DTX Docetaxel

EBRT External Beam Radiotherapy

ECM Extracellular Matrix

EMT Epithelial-Mesenchymal Transition

EPR Enhanced Permeability and Retention

FB Normal Fibroblast

FBS Fetal Bovine Serum

G1 Gap 1

G2 Gap 2

GFP Green Fluorescent Protein

GNP Gold Nanoparticle

H2AX H2A histone family member X

HR Homologous Repair

HSI Hyper Spectral Imaging

ICP-MS Inductively Coupled Plasma Mass Spectrometry

IGRT Image Guided Radiotherapy

IMRT Intensity Modulated Radiotherapy

LSPR Local Surface Plasmon Resonance

M Mitosis Phase

MET Mesenchymal-Epithelial Transition

MLC Multileaf Collimator

MMP Matrix Metalloproteinase

MOMP Mitochondrial Outer Membrane Permeabilization

MT Microtubules

NHEJ Non-Homologous End Joining

NP Nanoparticle

OAR Organs At Risk

OCT Optical Cutting Temperature

PBS Phosphate Buffered Saline

PD1 Programmed Death 1

PDL1 Programmed Death Ligand 1

PEG Polyethylene Glycol

PET Positron Emission Topography

PFA Paraformeldahyde

PI Propidium Iodide

RGD Arginine-Glycine-Aspartic Acid

RME Receptor Mediated Endocytosis

ROS Reactive Oxygen Specie

RT Radiotherapy

S Synthesis Phase

SBRT Stereotactic Body Radiotherapy

SF Survival Fraction

SSB Single Strand Break

STEM Scanning Transmission Electron Microscopy

TEM Transmission Electron Microscopy

TI Therapeutic Index

TME Tumor Microenvironment

UV-VIS Ultra Violet-Visible Spectrometry

VEGF Vascular Endothelial Growth Factor

VMAT Volumetric Modulated Arc Therapy

kVp Peak Kilovoltage

rhTNF Human Tumor Necrosis Factor Alpha

Chapter 1

Introduction

1.1 The worldwide burden of cancer

Cancer is a family of genetic diseases arising from dysregulation of the expression of multiple genes and is characterized by a loss of the ability to control growth, among other hallmarks. However, cancer is a unique genetic malfunction, as it has its origins in multiple somatic mutations, relative to other genetic diseases which are based in germ-line mutations [1]. According to the Global Cancer Statistics 2020, there were 19.3 million new cancer cases worldwide, which is expected to rise to 28.4 million new cases by 2040 [2]. Cancer is a complex disease that has a large inter- and intra-disease heterogeneity, indicating a vast difference in cellular morphology, gene expression, proliferation, and metastatic potential even in populations that have the same cancer type. This heterogeneity in cancer populations introduces a difficult challenge in implementing an effective treatment strategy for individual patient. However, treatment options exist, the main ones including surgery, chemotherapy, and radiotherapy (RT), with the treatment plan of each cancer patient varying depending on the type of cancer and the advancement of cancer.

1.2 Current cancer treatment modalities

RT is one of the most widely used treatment approaches, being used in approximately 50% of all cancer patients. In RT, a high dose of ionizing radiation is delivered to the tumor site, which interacts with and excites the atoms inside the cancer cells, causing damage to important structures, ultimately killing the cell [3]. Currently, the clinic mainly employs gamma or X-ray photons, ion-based electrons, or protons as radiation sources in the treatment [4, 5]. Chemotherapy is also used to eradicate

micro-metastases and to improve local control of the primary tumor [6]. In chemotherapy, anticancer drugs are administered either orally or intravenously to disrupt the rapid overgrowth of malignant cells [7, 8]. Both RT and chemotherapy are widely used and cost-effective options for treating cancer that continue to have increasing demand.

1.2.1 Radiotherapy

Modern day RT functions by sending high energy X-rays in the range of 100 keV – 25 MeV through tissue, where it will interact with and cause damage to the cancerous tissue. There can be various sources of X-rays, such as from radioactive sources (i.e. ^{60}Co) or from medical linear accelerators (linac). The end goal of RT is to deliver a uniform dose to the tumour, while restricting the dose to organs at risk (OAR) and normal tissue around the tumour site. Monte Carlo simulations based on a RT utilisation tree, produced from indications of RT effectiveness in literature, suggest 48-52% of patients could benefit from external beam RT (EBRT), in line with clinically estimated treatment numbers [9, 10, 11].

Following the discovery in 1895 of the X-Ray by Röntgen and in 1896 of natural radioactivity by Becquerel, the era of radiotherapy had begun [12, 13]. However, due to limitations in technology, kilovoltage (kV) energies, and lack of understanding of radiation and biology, curative treatments was limited to superficial tumours such as skin or vocal cords [14]. By the 1950s, the use of megavoltage (MV) photons was adopted, with the production of a cobalt-60 source in EBRT, which emits a 1.2 MeV photon beam and can be synthetically produced [15]. This allowed, for the first time, for deep-seated tumours to be treated compared to the kV units that were used prior. This was closely followed by the introduction of clinical linacs, allowing for X-ray beams with between 6 MV and larger energy spectrums.

With the introduction of the computed tomography (CT) scan by Hounsfield [16], and improved computing power, radiotherapy transitioned to more three dimensional (3D), computer assisted planning. This allowed for the introduction of intensity modulated radiotherapy (IMRT), in the late 1990s [17]. The use of a multileaf collimator (MLC) allows IMRT to combine several complex fluence patterns to form a highly conformal dose to the tumour, while keeping doses to OAR within safe tolerances, thus permitting a tumour dose escalation [18]. IMRT is especially useful for cancers such as head and neck cancer [19], prostate cancer [20], gastrointestinal cancers [21],

and many others where it is required to limit the deposited dose to the healthy tissue. Improvements to treatment time, while maintaining a highly conformal dose, in modern RT have been introduced with volumetric modulated arc therapy (VMAT), which combines field shaping present in IMRT with continuous adjustments in dose rate, gantry arcing, and couch motion [22].

While IMRT and VMAT have pushed fluence shaping to its physical limit, there are some challenges still present in current day treatment. There are many biological factors in play when treating cancer, and no two patients are the same. Therapy today involving ionizing radiation can be delivered using photons, electrons, protons, neutrons, or light ions, all with different biological effects[23, 24] . However, photon-based RT is the most common. Protocols like stereotactic body radiotherapy (SBRT) aim to take advantage of these radiobiological factors through a combination of dose conformality, improved target accuracy through image guidance, and a hypofractionated dose [25]. SBRT has proven to be beneficial in the treatment of many different cancers, including prostate cancer [26], pancreatic cancer [27], non-small cell lung cancer [28], and spinal disease [29].

While SBRT has exploited some of the biological factors present in the tumor to improve treatment outcome, there is far more that can be explored. While much of the research in medical physics has centred on improving dose conformality, imaging, and accuracy of dosimetry, there is an opportunity to drastically improve treatment response by targeting biological aspects such as the tumour microenvironment and the varying radiosensitivities that different cell lines have [30]. Further, while current RT regimes that have been employed have proven beneficial, they can be improved upon by introducing concomitant treatments of varying regimes, such as chemotherapy [31], immunotherapy [32], and nanotherapy [33]. Integration of these new technologies can further bolster the effectiveness of radiotherapy, improving tumour control and reducing patient side effects.

1.2.2 Chemotherapy

While anti-cancer drugs can be curative in select cancers, chemotherapy is a modality of treatment that is predominately used in adjuvant treatment with radiotherapy and/or surgery to reduce micrometastases and further dissemination of the cancer [34, 35]. Chemotherapy involves the administration of cytotoxic compounds and can have many different goals, depending on the type of cancer and the goal of the

treatment [8]. Various drugs have been found to be effective towards limiting cancer, including docetaxel, bleomycin, and cisplatin. The standard treatment sequence refers to a chemotherapy regimen before a traditional external beam radiation therapy treatment [36]. Considering the variety of drugs available for cancer treatment, the possible choice of sequencing of combined chemotherapy and radiation therapy is countless, and the treatment plan differs between each patient. Chemotherapy used prior to irradiation is expected to cause maximal tumor regression for locally advanced tumors. The major limitation of combining chemotherapy and radiation therapy is normal tissue toxicity, since either modality can cause major side effects [37]. There are various issues currently associated with improving the effectiveness of chemotherapy, including the biodistribution of pharmaceuticals, the lack of drug-specific affinity towards the tumor, limited plasma half-life, poor solubility and stability in physiological fluids, and nonspecific toxicity [38]. Many different drugs can be used for different purposes and have different modes of actions to target various cancer types. The main chemotherapeutic used throughout this work is the taxane Docetaxel.

Docetaxel

Docetaxel (DTX) is a chemotherapy agent that can be limited due to high normal tissue toxicity. DTX is a cytotoxic member of the taxanes, antimicrotubular agents that are effective in the treatment of multiple different types of cancers including head and neck, breast, prostate, and non-small-cell lung cancer [39, 40, 41, 42]. DTX's mechanism of action is primarily through the ability to enhance microtubule assembly and stabilize free microtubules within the cytoplasm, thus preventing their depolymerization during normal cell division [43]. This has many consequences for the fate of the cell, including inhibition of progression through the cell cycle and inevitably death *via* mitotic catastrophe, depending on the dose [44].

While DTX is useful as a chemotherapy agent, it can also be used as a radiosensitizer [45, 46]. DTX is highly effective at synchronizing cells in the G2/M phase of the cell cycle, due to its mechanism of action causing mitotic arrest. Cells are highly sensitive to radiation in the G2/M phase, as it is the most radiosensitive phase of the cell cycle [47]. When combined with radiation, DTX can be a very potent radiosensitizer, and synergizes well in a chemo-radiotherapy treatment regime.

1.3 Improving cancer treatment with nanomedicine

While current treatment options like RT and chemotherapy have been proven to be effective for many patients, there is still a need in the clinic to improve the outcomes for many different cancer types as well as reduce the damage to normal tissue. For example, chemotherapy is a non-targeted treatment option that can cause a host of issues in patients due to the negative effects to normal, healthy tissue, while radiotherapy must deposit a large dose of radiation through healthy tissue before reaching the tumour. Finding options to better avert these side effects while promoting cell kill in the tumour is essential.

1.3.1 Normal tissue toxicity

In RT, there can be a host of side effects manifesting as early as the weeks following treatment, or as late as months or years after. The side effects largely depend on the tumour site, with the major organs surrounding the cancer having the most impact on the potential severity. In general, after radiotherapy, many patients report fatigue, with up to 30% experiencing this effect months to years after treatment [48].

Head and neck cancer is a common variety of cancer to have radiotherapy as a frontline treatment. This cancer also has many radiosensitive organs in the region, such as the many mucosal membranes, salivary glands, thyroid glands, and the brain. Oral and oropharyngeal mucositis are common, negatively impacting the patient's ability to swallow, eat, and speak. Thyroid dysfunction can lead to fluctuations in hormone levels, leading to ailments such as hypothyroidism, and alterations in taste is relatively common [49, 50]. Many other side effects can occur, including dysphagia [51], RT-induced fibrosis affecting swallowing [52], xerostomia resulting in hyposalivation [53], trismus resulting in restriction of jaw movement [54], and mandibular osteoradionecrosis [55].

Prostate cancer is another cancer type that is often treated with RT - either EBRT or brachytherapy - as the primary treatment. RT is also used in patients who go through surgery with locally advanced prostate disease with positive resection margins [56]. In prostate cancer, there are many different organs at risk such as the bladder, the rectum, and the urethra. Some potential adverse side effects as a result of RT include urinary urgency and frequency, dysuria, diarrhea, erectile dysfunction, urinary incontinence, and proctitis [57]. Similarly, cervical cancer is treated concurrently with RT and chemotherapy for very large tumours, or in metastatic presentations

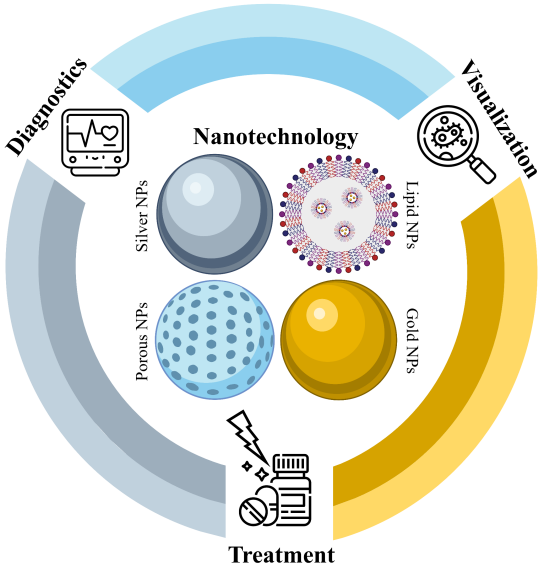


Figure 1.1: **Introduction to nanotechnology.** Nanomedicine in the form of nanoparticles can be used for many different applications, including diagnostics, imaging, and treatment.

[58]. Cervical cancer also is surrounded by many organs at risk, like the bladder, rectum, small intestine, and spinal cord. Side effects comparable to RT treatment of prostate can occur after treatment of the cervix, affecting systems such as the gastrointestinal system and the genitourinary system along with the gynecological system [59]. Improvements in treatment in these cancer types to minimize normal tissue toxicity and improve cancer cell kill would optimize patient outcome and quality of life.

1.3.2 Nanoparticle applications in cancer treatment

The introduction of nanotechnology, as seen in Figure 1.1, as a method of improving current treatment regimes has the potential to radically improve patient outcomes. Nanotechnology - specifically nanoparticles (NPs) - are characterized by their size range of 1-100 nm, with specific physical properties that allow for manipulation for a desired application, such as cancer nanomedicine. NPs can be engineered as platforms for effective and targeted delivery of chemotherapeutics by overcoming many biological barriers. Some NP-based therapeutic systems have already been introduced into the pharmaceutical market. For example, Doxil, a polyethylene glycol

(PEG)-liposome containing chemotherapeutic Doxorubicin, is approved for AIDS-related Kaposi's sarcoma, ovarian cancer, and multiple myeloma [60, 61]. Liposomal nano-drugs and polymer drug conjugates account for most of the FDA (Food and Drug Administration)-approved systems so far [62]. The use of NPs has been shown to be a proven treatment option when it comes to effective targeting and delivery of chemotherapeutic agents.

In radiotherapy, NP-driven radiosensitization strategies that use inorganic high Z materials have been pursued to improve the local radiation dose and minimize the damage to surrounding healthy tissue [63]. The interaction of high Z materials with therapeutic X-ray photons results in an increase in the production of cell damaging species, such as free radicals and low energy electrons [64, 65]. Inorganic NP systems such as gold nanoparticles (GNPs), silver NPs, gadolinium-based NPs, lanthanide-based NPs, and titanium oxide nanotubes have been reported as radiosensitizers [66, 67, 68, 69, 70, 71, 72]. Gadolinium-based NPs offer an innovative approach because of their capacity to act as a radiosensitizer as well as a powerful contrast agent in magnetic resonance imaging [71]. The high Z nature of silver-based NPs along with their antimicrobial properties make them a good candidate in radiotherapy [72]. However, GNPs are the most widely used NP system in radiotherapy due to their ease of production, high Z nature, advantageous surface chemistry, and biocompatibility [70, 73, 74, 75].

1.4 Gold nanoparticles in cancer therapeutics

With recent advances in nanotechnology, there are multiple options to explore when it comes to the use of metal NPs. Of the many systems that exist, GNPs are one of the most popular and widely explored. Due to their physiochemical properties, GNPs have applications in many different aspect of cancer treatment, including imaging, drug delivery, diagnostics, and radiation therapeutics [76]. The vast utility of GNPs allows it to act as a model nanotechnology to experiment with and elucidate treatment options.

1.4.1 Gold nanoparticle characteristics

Noble metal nanoparticles, such as GNPs, have many physiochemical characteristics, like the local surface plasmon resonance (LSPR), which allow control of the size and shape of the nanoparticles [77]. The LSPR occurs due to the stimulation of light

on the conduction electrons localized on the surface of noble metal NPs. When the collective oscillation of these electrons is resonant with the incident photons, a band of absorption - the LSPR - will occur. The surface plasmon band can be influenced not only by size, but also by shape, solvent, surface ligands, core charge, temperature, and the proximity of other NPs nearby, due to aggregation affecting the effective size of the nanoparticle [78]. Much of these physicochemical properties can be adjusted and tuned for specific treatment requirements. Due to this highly customizable behaviour, GNPs are an effective tool to use in biomedical applications, such as photothermal therapy, photodynamic therapy, radiotherapy, chemotherapy, and more.

There are different gold-based nanotherapeutic systems available, such as spherical GNPs, gold nanorods, gold nanoshells, gold nanoclusters, and GNP-incorporated liposomal nanoparticles, with many new anisotropic geometries being developed regularly. Spherical GNPs are the most commonly used gold-based nanotherapeutic, as their production is relatively simple and alteration of size and surface chemistry, such as conjugation with PEG, is easily achieved [79, 80]. Spherical GNPs have useful attributes such as their large surface-to-volume ratio, biocompatibility, and low toxicity [81]. It is simple to measure the size of spherical GNPs by observing the absorption band that arises due to the LSPR effect [82]. These many properties can be taken advantage of to form an ideal nanoplatform.

There are many beneficial chemical properties of GNPs that give them an advantage over alternative platforms. There are numerous methods of conjugation to the surface of GNPs, such as via non-covalent modes like hydrophobic interactions and ionic interactions [83]. However, this has the downside of not being a very strong attraction, and molecules on the surface can be replaced by others in a biological sample. It is far easier to couple GNPs to other moieties via the covalent bond between gold and sulphur, usually done through thiols, which leads to a stable conjugation [84]. There is also a slightly weaker covalent bond that allows GNPs to interact with amines, which can be nearly as stable as thiol-capped moieties [85]. These covalent bonds make GNPs a solid base for many different applications, such as targeted delivery combined with radiosensitization.

While the cytotoxicity and biocompatibility of a nanomaterial is governed by multiple factors, including the physiochemical properties, there are a wide range of GNPs that have proven to be safe and biocompatible [86]. Depending on the size and shape, there can be different effects. With smaller nanoparticles, there tends to be a larger cytotoxic effect. Due to a higher surface area relative to volume, smaller

NPs have more interaction with biomolecules in the cell that could disrupt normal function, with 15 nm being a safe diameter in spherical GNPs [87]. However, this highly depends on surface functionalization, and PEGylation has shown to eliminate many adverse interactions [88]. Likewise, shape is an important factor to consider. It has been found that gold nanorods were highly toxic while gold nanospheres are the safest shape to utilize [87]. The many physiochemical properties that are easily tunable allow GNPs to be an ideal platform for cancer nanotherapeutics.

1.4.2 Gold nanoparticles in chemotherapy and radiotherapy

Gold nanoparticles and chemotherapy

GNP-based platforms are being researched and have been tested extensively in the field of cancer nanomedicine, both in chemotherapy and radiotherapy. Anticancer drugs pose many issues during the treatment of tumours *in vivo*, despite treating the cancer effectively [89]. Improving the bioavailability of the drug within the tumour region may lead to reduced side effects and larger therapeutic effects. This is defined as an increase in the therapeutic index. GNPs, due to their high surface area-to-volume ratio, as well as a large number of surface bio conjugation possibilities, are an ideal platform for delivering pharmaceutics for chemotherapy. For example, a novel nanomedicine that conjugated human tumor necrosis factor alpha (rhTNF) and thiolated PEG onto the surface of colloidal GNPs (named CYT-6091) has been tested in phase 1 clinical trial in cancer patients [90]. The results from the CYT-6091 trial showed that doses up to 600 μg/g of rhTNF were administered without encountering dose-limiting toxicity and was less toxic than a treatment with just rhTNF, as evidenced by a lack of hypertension in patients. Furthermore, the GNPs had gathered in the tumor and mostly avoided healthy tissue. Other phase 1 clinical trials involved the use of PEGylated gold nanoshells around a silica nanoparticle, called AuroLase, in head and neck, lung, and prostate cancer, with laser irradiation [91, 92, 93]. Results have, however, not translated to an effective treatment outcome. Another early phase 1 clinical trial involves the use of NU-0129, a platform consisting of nucleic acids attached to the surface of spherical GNPs [94]. The goal of this study is to use the conjugated nucleic acids to bypass the blood-brain barrier and target the BCL2L12 gene present in recurrent glioblastoma. If successful, this platform could suppress this gene, which would lead to reduced proliferation and contain the spread of the tumor. However, translation of GNPs to the clinic is still in progress,

and further optimization of protocols will have to be elucidated before most of the drug-based research can move out of the preclinical stage.

Gold nanoparticles and radiotherapy

Radiation dose enhancement due to GNPs was first demonstrated using 1.9 nm GNPs in a mouse model, in one of the pioneering studies in GNP-mediated radiation dose enhancement by Hainfeld et al [73]. A radiation dose of 30 Gy with 250 kVp X-rays to subcutaneous tumors in mice resulted in a significant decrease in tumor volume. However, the concentration of gold in this study was relatively large, at 2.7 g Au/kg body weight, which is not clinically feasible. Furthermore, the use of kV energies, while allowing for prominent photoelectric interactions in gold, is hindered due to the reduced penetration for deep-set tumors. Thus, optimization of the internalization of the GNPs into the tumor cells, both *in-vitro* and *in-vivo*, is required for ideal efficacy. Whenever gold was internalized *in vitro*, radiosensitization was achievable at MV energy ranges, at concentrations as low as 1 ng gold/g tissue[70, 95, 96, 97]. When moving to an *in vivo* environment, radiosensitization was seen at a delivered dose as low as 10 μg/g of body weight [98]. The addition of targeting and improvements in the optimization of uptake has allowed significant progress in facilitating the progress of gold nanomaterials to the clinic.

Gold nanoparticles and combined therapy

For patients with locally advanced disease, a combination of treatments, such as surgery with chemotherapy and/or RT is being used. A combination of chemotherapy and RT (referred to as chemoradiation) is a logical and reasonable approach that has greatly improved the cure rates of solid tumor [37, 36]. This combined treatment modality provides local control of the primary tumor mass through radiation while tumor metastasis is suppressed through anticancer drugs. Considering the variety of drugs available for cancer treatment, the possible choices of combined chemotherapy and radiation therapy is countless, and the treatment plan differs between each patient. The standard treatment sequence refers to chemotherapy regimen before a traditional external beam radiation therapy treatment [36]. The major limitation of combining chemotherapy and radiation therapy is normal tissue toxicity since either modality can cause major normal tissue toxicity individually. GNPs offer a useful option as a drug delivery system (DDS) in combined treatment therapy. The combi-

nation of the GNPs with RT and chemotherapy is part of the natural progression of the exploration of GNPs as a complete treatment modality.

1.5 Towards personalized medicine

A large issue that is plaguing nanotechnology in general is that a very low (≈0.7%) portion of the administered dose is being delivered to the tumor [99]. While Wilhelm et al. describe the issue as improving understanding of the processes present in the body that inhibit the uptake of NPs, and then optimizing those processes, a more personalized approach could be introduced. Beyond using genomic information to improve each individual's cancer treatments, the use of an *in vitro* model that can better mimic the *in vivo* environment present in a patient may allow for the actual testing of treatment prior to administration. This can be achieved through the use of 3D organoid models [100].

1.5.1 Two dimensional vs three dimensional models

A large portion of preclinical work involving GNPs have utilized a two-dimensional (2D) monolayer cell model, which cannot accurately represent the complex heterogeneous environment present in the tumor microenvironment. The introduction of a 3D model that can more accurately characterize an *in vivo* environment is essential to more successful clinical translation and to better optimize GNPs in a reliable manner.

The utilization of a 3D spheroid cell model can allow for modelling of an essential aspect of the tumor microenvironment which was previously inaccessible to 2D monolayer models: the extracellular matrix (ECM), as can be seen in Figure 1.2. The ECM acts as a scaffold for cell growth and is comprised of a network of macromolecules secreted by local cells, mainly polysaccharide glycosaminoglycans, adhesive proteins such as fibronectin, and structural proteins such as collagen [101]. The ECM is also involved in the regulation of cellular function in the tissue, such as cell-to-cell communication, proliferation, and cell adhesion [102]. NPs have also been shown to interact with the ECM via hydrodynamic interactions, physical interactions such as collision of the NPs with the matrix fibers, as well as electrostatic interactions when dealing with charged particles, all of which act as limiting forces to the diffusion of the NPs. Functionalization of NPs with suitable peptides to facilitate transport through the ECM can enhance therapeutic effects [103, 104]. Thus, improvements in treatment in an environment that appropriately models these more complex interactions is critical.

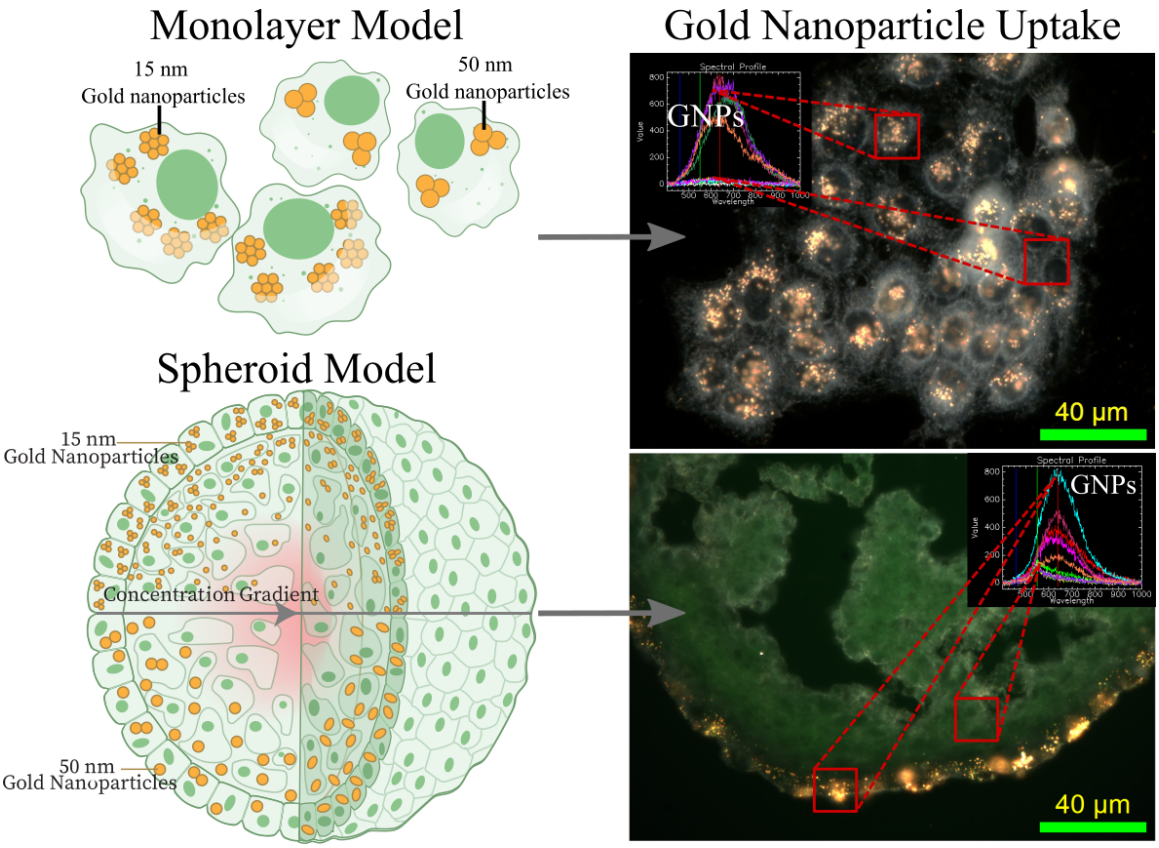


Figure 1.2: **Monolayer vs Spheroid.** A monolayer of cells is a single layer of cells that will have access to all the nutrients and molecules in the media, such as GNPs. Thus, all cells will be treated equally and have the same access to uptake GNPs. With a spheroid, there is an introduction of a concentration gradient that can reduce the uptake of nutrients towards the core of the spheroid. Cells in image are CAL-27, a head and neck cancer cell line.

An important aspect that must be taken into account is the size of the GNPs, which is a characteristic that controls the *in vivo* blood circulation, tumor accumulation and penetration, and cellular uptake. Due to the inter-matrix spacing present in the ECM, the size of the NPs used is important as the 20–40 nm spacing between collagen fibrils sets the upper limit for effective penetration [105]. The use of spheroids with GNPs has been explored previously in a limited fashion. An exploration of gold nanorods, nanospheres, and oligonucleotide-functionalized nanospheres was undertaken by Rane et al. who showed the difference in uptake profiles present in a 3D model compared to the 2D monolayer [106]. Further studies on how functionalization and size of the GNPs have been explored recently, all agreeing that smaller GNPs will more effectively penetrate deeper into the cells [107, 108]. More complex *in vivo* sys-

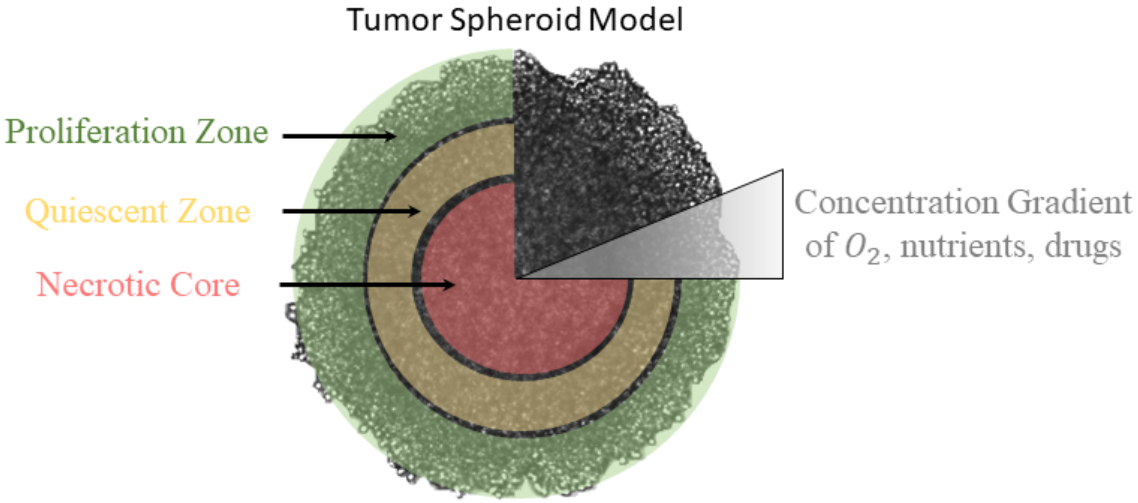


Figure 1.3: **Spheroid model.** A three dimensional spheroid model can be grown in the lab to better approximate the *in vivo* environment. Spheroids will form the characteristic necrotic core present in *in vivo* tumours when the diameter grows to a large enough size (>500 μm).

tems can also be reproduced in a spheroid model, such as a blood-brain barrier made up of multiple cell types in a multicellular spheroid. This was explored by Sokolova et al. that showed that ultrasmall GNPs can cross this barrier, illustrating the useful nature of the 3D spheroid [109]. Ultrasmall GNPs have previously been explored in a 3D tumor spheroid model, demonstrating that smaller 2 nm and 6 nm GNPs can penetrate deeper into the tissue when compared to that of 15 nm GNPs [110]. The smaller GNPs also accumulated in the nucleus, due to the nuclear pore being 9 nm in diameter, which could add therapeutics that target the DNA [111]. However, smaller nanoparticles (<10 nm) will have a rapid elimination via renal pathways compared to larger nanoparticles [112]. Thus, a balance between optimized uptake and circulation time due to choice of GNP size is essential.

Spheroids (Figure 1.3) have very similar growth to what is observed in solid *in vivo* tumours, where it is organized in three distinct layers: a outer proliferating shell, an inner layer with quiescent cells, and a necrotic core. With increased complexity in the 3D tumor spheroid, we can see the introduction of a concentration gradient that will alter the ability of deeper-set cells, which often are hypoxic and thus more treatment-resistant, to uptake GNPs [113]. This is also useful when evaluating treatment options involving radiation, as oxygen levels are important for increased efficacy. Furthermore,

spheroids have similar growth kinetics, metabolic rates, and resistance to treatment as *in vivo* solid tumours [114]. Spheroids are also capable of being produced in a co-culture, allowing the introduction of other cell types such as fibroblasts and immune cells, which are integral to the tumour microenvironment [115]. Optimization in a more complex environment is essential to bridge the gap between the lab and the clinic, to facilitate a quicker translation of the radiosensitizer and drug delivery system platform that GNPs provide.

1.6 Scope of dissertation

The purpose of this dissertation is to explore the optimization of a combined treatment modality of chemotherapy and radiotherapy with GNPs in the more complex 3D spheroid model. This model will be compared to what is observed in a 2D monolayer to ascertain the differences and where efforts should be put forward for moving towards an *in vivo* tumour microenvironment (TME).

This dissertation will first focus on optimization of GNPs in monolayer, including cell types that are part of the tumour microenvironment such as fibroblasts. As the goal of this research is to further the application of GNPs to clinical treatment modalities, the applicability of GNPs to various elements of the TME is important. Following this, we introduce the chemotherapy drug DTX and optimize in both monolayer and spheroids. DTX is both a radiosensitizer and affects the uptake of GNPs, and thus can act synergistically when combined with GNPs and radiotherapy. This has many other benefits as well when moving to an *in vivo* environment such as increased retention of the GNPs. Following assessment of the benefit that DTX provides in GNP uptake dynamics, we will then investigate a combined chemoradiotherapy platform with clinically relevant energies.

Chapter 1 contains a broad overview of cancer treatment and the motivations for an improved treatment option. This also introduces the concept of nanomedicine and the use of GNPs, as well as an improved *in vitro* testing environment to facilitate a more rapid translation to the clinic.

Chapter 2 presents a more in-depth background on the tumour microenvironment, radiation physics, radiobiology, and the use of GNPs in this complex treatment environment.

Chapter 3 will explore the effects of GNP accumulation in monolayer in various cell types that are present in the TME. This will include cancer cells, normal fibroblasts,

and cancer associated fibroblasts. The effect RT has on these cells after addition of GNPs is also elucidated.

Chapter 4 demonstrates the effect DTX has on the uptake of GNPs, and how it affects the different cell environments, in monolayer and spheroids. The use of DTX is optimized to improve the uptake dynamics on various GNP sizes.

Chapter 5 combines the use of DTX with radiotherapy in the presence of GNPs. The previously optimized DTX and GNP treatment will be utilized with clinically relevant radiation doses to elucidate the benefit of chemoradiotherapy in monolayer and spheroids.

Chapter 6 will summarize these results, how these will translate to clinical significance, and potential future work with preliminary data in an *in vivo* mouse model.

Chapter 2

Gold nanoparticles and radiobiology

2.1 Biology of the tumour

The development of cancer requires specific changes in the normal regulatory functions, such as cell proliferation and homeostasis. Understanding the so-called 'hallmarks' of cancer as seen in Figure 2.1 is essential for discovering effective treatment modalities. It is suggested that there are seven different capabilities acquired by tumors that allow them to overcome the defence inherent in normal cells: selective proliferative advantage, altered stress response, angiogenesis, invasion and metastasis, metabolic rewiring, immune modulation, and an abetting tumor microenvironment [116]. Some of these characteristics may prove to be more important than others when it comes to the experiments described in this works.

2.1.1 Selective proliferative advantage

Healthy, normal cells tend to proliferate only in the presence of specific growth factors and will cease to grow if in the presence of growth-inhibiting factors. However, through accumulation of genetic mutations, cancer cells can not only ignore growth-inhibiting factors through alteration of growth ligands, but can also produce growth factors in an autocrine fashion to promote tumor proliferation [117]. The division of normal cells is tightly controlled by the highly regulated cell cycle as seen in Figure 2.2, where genetic information is duplicated during synthesis phase (S) and the cell divides into two daughter cells during mitosis phase (M). The M phase is made up of five separate stages: prophase, prometaphase, metaphase, anaphase, and telophase, ending with cytokinesis. During prophase, chromosomes begin to undergo a condensation process, the nucleolus breaks down, and the mitotic spindle begins to form on opposite poles of the cell from duplicated centromeres and microtubules. This is followed by the

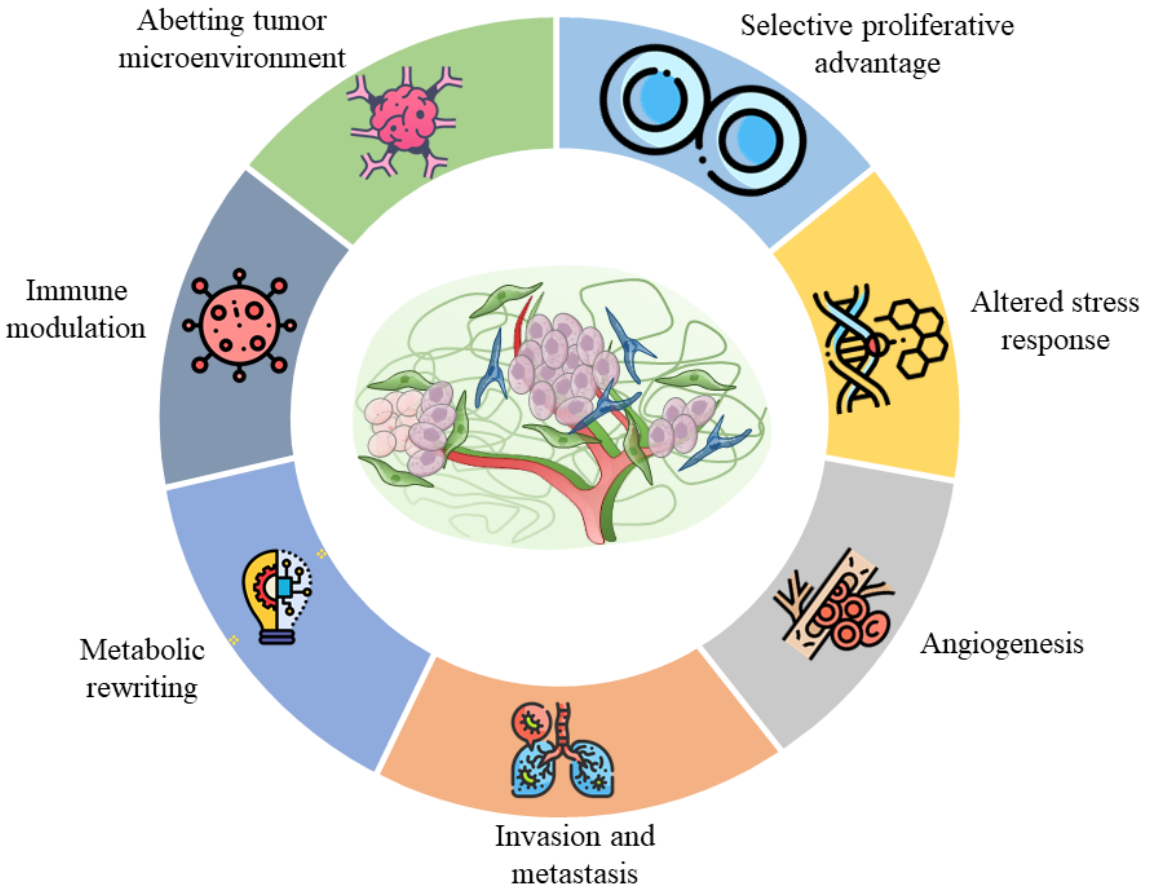


Figure 2.1: **Hallmarks of Cancer.** The seven main hallmarks of cancer that define the characteristics of the deadly disease.

prometaphase, which begins with the fragmentation of the nuclear envelope, releasing the chromosomes and allowing the microtubules on the mitotic spindle to attach to the chromosomes via their kinetochore. Once all the chromosomes are captured and aligned at the center of the cell, metaphase begins, which simply acts as a checkpoint to ensure proper spindle alignment. The cell then progresses into anaphase, characterized by a separation of sister chromatids by the kinetochore-attached microtubules, followed by elongation of the cell. Finally, telophase commences with the reformation of the nuclear membranes and nucleoli and the chromosomes begin to de-condense, forming two nuclei. Cytokinesis, which may start in either anaphase or telophase, and ends after telophase, involves the final splitting of the cytoplasm into two daughter cells with identical genetic compositions if all checkpoints throughout worked. In between S phase and M phase are two gap phases, G1 and G2 [118, 119]. In G1 phase,

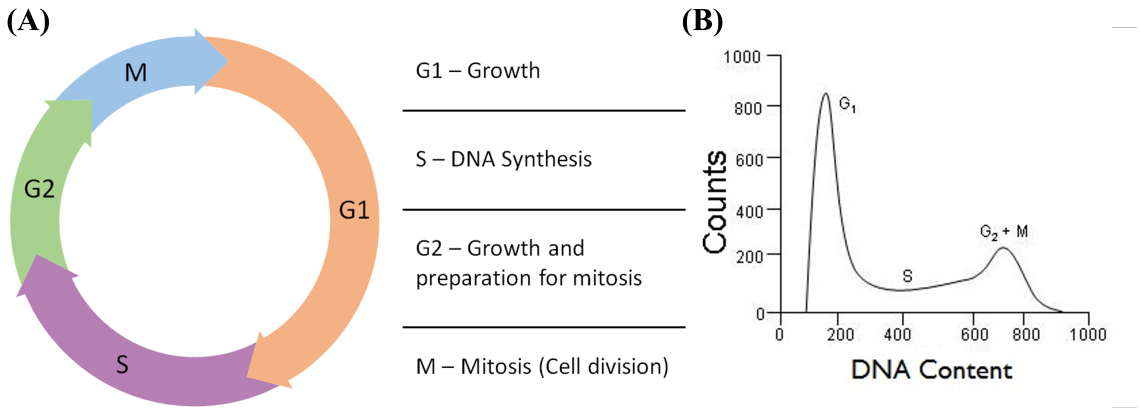


Figure 2.2: **The Cell Cycle.** (A) The highly regulated cell cycle describes the various stages that cells go through during their lifespan. (B) A normal cell cycle population as measured in a control sample of the cervical cancer cell line HeLa, using a flow cytometer and fluorescently labelled DNA.

there is a decision window where cells either decide to initiate deoxyribonucleic acid (DNA) replication and enter the cell cycle or exit the cell cycle in a non-proliferative state called quiescence. Similarly, these occurs in G2 as well before entering mitosis.

The cell cycle is largely controlled by proteins called cyclins and cyclin-dependent kinases (CDKs), as a regulatory mechanism to ensure cells that have mistakes can be repaired or destroyed before they can cause damage due to genetic errors [119]. However, in cancer cells, dysregulation of the cell cycle occurs, allowing unscheduled proliferation and additional genomic instability that could allow for the accumulation of genes that are highly beneficial for increased growth and survival. The continuous cell division and accumulation of gene defects compromise cell cycle exit and prevent cell death via apoptosis [120].

2.1.2 Altered stress response

Generally, cells when faced with stresses such as DNA damage, hypoxia, or anticancer treatment will have responses that allow the cell to adapt, or if not possible, to self-eliminate for the benefit of the healthy tissue. Cancer cells can grow to subvert the intended outcome of many of these responses to improve survival. For example, the apoptotic pathways that regulate cell proliferation and cell death are altered, allowing them to evade programmed death [121]. Apoptosis is a highly regulated cellular process that allows for the elimination of unnecessary or unhealthy cells from the body. The process of apoptosis starts from cellular events, such as DNA damage,

that activate a family of cysteine aspartyl-specific proteases called caspases. There are initiator caspases (caspase-2, -8, -9, and -10) that are activated by apoptotic stimuli, which then activate executioner caspases (caspase-3 ,-6, and -7). The executioner caspases result in the proteolytic cleaving of specific cellular substrates, such as the cytoskeletal and nuclear proteins, leading to cell death [122]. The activation of the initiator caspases can be undertaken intrinsically or extrinsically. Extrinsically, extracellular ligands such as tumor necrosis factors can interact with cell surface receptors, activating caspase-8 and -10. Intrinsically, mitochondrial outer membrane permeabilization (MOMP) is triggered, allowing pro-apoptotic proteins such as cytochrome c to enter the cytosol. These proteins then activate caspase-9, which then activate executioner caspases.

The intrinsic pathway in particular is regulated by the B-cell lymphoma-2 (BCL-2) protein family, which includes pro-apoptotic BH3-only proteins, pro-apoptotic effector proteins, and anti-apoptotic BCL-2 proteins, and is in a balanced equilibrium to ensure homeostasis in normal cells [123]. Cancer cells that block apoptosis often are up-regulating the production of the anti-apoptotic BCL-2 proteins which prevent MOMP from occurring. Similarly, the transcription factor p53, which has tumour suppression functionality and regulates cellular response due to stresses such as DNA damage, can activate production of pro-apoptotic BCL-2 proteins [124]. Many cancer types have inhibited p53 expression and thus can no longer effectively go through DNA-damage-induced apoptosis [123].

Paradoxically, cancer cells can also have increased pro-apoptotic behaviour following treatment, which actually shifts the subpopulations of the tumour towards more aggressive subclones, yielding higher levels of tumorigenesis [125]. This is a result of the heterogeneity of subclones of cancer cells within a tumor. Spontaneous cell death, such as that following RT treatment, can lead to a smaller tumor in the short term, but enhance tumorigenesis in the long term due to some tumor subclones being pro-apoptotic and some not. These pro-apoptotic subclones will die following treatment, allowing for more aggressive subclones to take over and flourish. The abilities for tumours to survive treatments due to their altered stress response is a key marker of cancer.

2.1.3 Angiogenesis

Endothelial cells, such as those lining bloods vessels, generally are quiescent but can be induced to start angiogenesis by factors such as vascular endothelial growth factor (VEGF) and fibroblast growth factor 2 (FGF-2). During normal events such as wound healing, angiogenesis ceases when the need for new blood vessels has been met, while it is highly unregulated in tumors. Angiogenesis is generally activated during embryogenesis for expansion and remodeling of pre-existing vasculature, such as during wound healing or during chronic inflammation [126]. However, while this is a controlled process in normal tissue, in tumours pro-angiogenic factors override anti-angiogenic factors and thus have continuous angiogenesis [127]. This is known at the angiogenic switch, and various signals can trigger an imbalance, such as hypoxia, mechanical stress, inflammatory response, and genetic mutations. In cancer, these factors are produced and secreted by tumor cells and surrounding stroma as well, and are associated with tumor progression, increased vessel density, invasiveness, metastasis and tumor recurrence [128].

To have effective circulation, there has to be ordered division of the vascular tree into arteries, arterioles, capillaries, venules, and veins, but the constant pro-angiogenic signals given off by tumors causes the newly formed vasculature to be immature. This leads to a lack of division into arterioles, capillaries, and venules, as well as a largely heterogeneous vessel size leading to chaotic blood flow [129]. This poorly organized blood flow also leads to areas of hypoxia and endothelial junctions are often disrupted. This allows the tumour vessels to be 'leaky' [130]. Due to this disruption, the tumour vasculature has an enhanced permeability and retention (EPR) effect. The increased retention comes from a lack of lymphatic vessels in a tumour, leading to a lack of drainage, which also increases interstitial pressure.

The EPR effect is very useful when designing therapies that take advantage of tumor targeting [131]. The disruption in the endothelial junctions leads larger pores of about 100 nm to 3 μm in diameter. This gives the ability for smaller molecules, such as NPs, to more effectively enter the tumor compared to normal tissue, while the lack of lymph drainage ensures the NPs are retained for a longer period. The EPR effect may be very useful when utilizing nano-based therapeutics, which will have improved uptake as a result, improving treatment efficacy. However, due to the chaotic nature of tumor vasculature, the full benefit of the EPR effect has yet to be elucidated [132]. The abnormal vasculature and high tumor cell density prevents the

deep penetration of nano-sized drugs into the tumour, such as in places where hypoxia exists, and the drug would be most beneficial. Thus, further targeting or improving of the EPR effect is desirable.

2.1.4 Invasion and metastasis

Tumor metastases is the primary cause of death in most patients [133]. Metastases is a complex process, comprised of invasion of cancer cells through the ECM and tumor vasculature into circulation, where the cancer must survive and then be extravasated at the parenchyma of various organs. The cancers cells must then not only survive the distant microenvironment but also manipulate it to form micrometastases that can eventually grow into full blown metastases [134]. Overcoming these hurdles is linked to the epithelial-mesenchymal transition (EMT), which is a reversible biochemical process that allows epithelial cells to transition into mesenchymal derivatives [135].

Generally, EMT occurs during embryogenesis, implantation of an embryo, organ development, tissue regeneration, or organ fibrosis [136]. When this occurs in neoplastic cells, metastatic dissemination occurs. Epithelial cells can be described as having polygonal shapes and are tightly connected to one another, reducing motility, whereas mesenchymal cells have spindle-like morphology and are loosely attached to the ECM, with high motility. Mesenchymal cells also display an increased resistance to apoptosis and improved production of ECM components. However, upon migration completion, cancer cells must also undergo the opposite transition, a mesenchymal-epithelial transition (MET), during secondary tumor formation.

The degradation of the ECM through matrix metalloproteinases (MMPs), which have important functions in remodelling and embryogenesis, are linked to tumor invasion and metastasis, and are upregulated in almost every type of cancer [137, 138]. The ECM is made up of many different macromolecules, such as collagens, proteoglycans, glycoproteins [139]. Further, the ECM has two forms: the interstitial matrix which forms a porous 3D network around cells to ensure structural integrity, and the basement membrane which is a more stable sheet-like structure that separates tissues into organized compartments [140]. The overexpression of MMPs allows for a tumor to replace a normal ECM with its own tumor-derived version and allows for degradation of the basement membrane for increased motility, leading to tumor invasion.

2.1.5 Metabolic rewiring

Cancer cells have developed different pathways for improved uptake of nutrients such as glucose and glutamine. Cancer cells can over-utilize glucose both in the absence and in the presence of oxygen, a trait that has been highly utilized in the field of positron emission topography (PET) [141, 142]. This effect was originally attributed to defective oxidative phosphorylation in mitochondria, leading to adenosine triphosphate (ATP) production through glycolysis, called the "Warburg effect" [143].

More recent evidence suggests that mitochondria in tumor cells work normally, and that glycolysis is increasingly utilized in proliferating cells like cancer due to its use as a multipurpose production line of metabolic intermediates. Respiration is done to promote flux through the tricarboxylic acid cycle, or Krebs cycle, which provides the necessary metabolites for growth. It has been suggested that the reason for the increased respiration that is observed is due to the cancer cell's need to synthesize nucleotides and haem, essential macromolecules that are not readily available in the TME [144]. These metabolites include succinyl-CoA for haem production and oxaloacetate, which is produced via glutamine-dependent reductive carboxylation, for nucleotide synthesis [145]. The increased production of these metabolites helps tumor initiation and progression. However, the reason for the increase of cellular respiration that occurs in cancer cells is still highly debated and is an active field of research.

Cancer cells also rewire the way they balance the equilibrium of reactive oxygen species (ROS). The major ROS that are generated in cancer cells include superoxides (O_2^-), hydrogen peroxide (H_2O_2), hydroxyl radicals (^-OH), and lipid hydroperoxides (LOOH) [146]. Many cancer cells have a high rate of superoxide production from the mitochondria, which is rapidly converted to hydrogen peroxide. The hydrogen peroxide can then oxidize cysteine residues in some proteins to alter their function, a signal that promotes proliferation, survival, and metastatic potential [147, 148]. To increase the production of these reactive species, cancer cells inhibit production of *some* antioxidant proteins which are used to keep the cell in homeostasis. Superoxides, hydroxyl radicals, and lipid hydroperoxides in high levels can be toxic to the cells, and thus cancer cells actually boost antioxidant production that target these species via the expression of the TP53-induced glycolysis regulatory phosphatase gene during tumorigenesis [149]. Thus, it is theorized that cancer cells promote production of hydrogen peroxide for pro-tumorigenic signals, but produce antioxidants that target the other damaging ROS molecules so as to not induce high cellular toxicity [146].

2.1.6 Immune modulation

The immune system has been shown to have the ability to identify and destroy developing tumours, known as 'immune surveillance' [150]. This is mediated by $CD8^+$ cytotoxic T cells and $CD4^+$ helper T (Th)1 cells, typically, but excess inflammation can reduce the effectiveness of the immune response [151]. Further, 'tumour immunoediting' has been proposed recently as an explanation for how tumours can grow despite the presence of the immune system [152]. Essentially, the immune system can not only destroy tumours, but also shape them. This has a Darwinian nature to it, where the immune system will eliminate the cancer cells that present tumor antigens, but due to the huge amount of genetic instability, reduced immunogenicity can occur. This can occur via different mechanisms, such as loss of target antigen expression. Some immune resistant cancer cell variants thus can survive the initial onslaught by the immune system, which then mutate further until becoming completely insensitive to detection, resulting in the formation of a malignancy.

There are several T cell immune checkpoint molecules that help modulate the immune response and regulate immune cell activation. Two highly researched molecules are the cytotoxic lymphocyte antigen 4 (CTLA4) and programmed cell death 1 (PD1) [153]. CTLA4 is known to inhibit the T cell response by directly interfering with CD28 activity, which is one of the signals that T cells use to activate. The addition of CTLA4 to $CD4^+CD25^+$ regulatory T cells (T_{reg}) was able to counteract the inhibitory effects that conventional T cells would experience [154]. Analogously, PD1 acts in a similar manner with the programmed death-ligand 1 (PDL1). PD1 works by inhibiting intracellular signalling in effector T cells and T_{reg} cells [155]. When PD1 engages with PDL1, it can induce a state of T cell dysfunction called T cell exhaustion. Tumors will take advantage of this and up-regulate the production of PDL1 to induce increased amounts of T cell exhaustion, allowing cancer cells to survive immune surveillance [156].

2.1.7 Abetting tumor microenvironment

The role of the TME has been recently been recognized as a major contributor to tumour propagation [157]. The TME is a complex amalgamation of the ECM, stromal cells such as fibroblasts, immune cells, vasculature, and the basement membrane [158]. Of particular importance to the growth and progression of cancer are fibroblasts [159]. Fibroblasts, specifically activated fibroblasts or myofibroblasts, are associated

with the wound healing response [160]. However, these activated fibroblasts can be recruited by the cancer cells, becoming cancer associated fibroblasts (CAFs) [161]. While normal fibroblasts (FBs) have anti-tumouriogenesis properties, CAFs promote the proliferation of tumours through release of cytokines and chemokines like VEGF and through ECM remodelling involving MMPs [162, 163]. CAFs have also been shown to be related to metastasis and chemoresistance [164, 165]. The function of CAFs supports the idea that tumours are 'wounds that do not heal' and targeting of CAFs may prove beneficial towards better therapeutic outcomes [166]. Moreover, CAFs have shown to not only improve the radioresistance of the tumour cells but to be highly radioresistant themselves [167].

2.2 Radiobiology

2.2.1 The DNA damage response

Ionizing radiation from high energy X-rays can damage the cells directly via fragmentation of the DNA, such as single strand breaks (SSBs) or double strand breaks (DSBs), or indirectly via production of free radicals and low energy electrons [168]. A majority of the energy from RT is initially deposited into the water present in tissue, leading to formation of reactive oxygen species, such as the hydroxyl $[OH^-]$ group, within 10^{-14} to 10^{-4} seconds, causing DSBs [169]. An important goal of RT is to target the tumour and generate DSBs, the most deadly DNA damage, as it is highly biologically important to the function and survival of the cancer cells [170].

Following DNA damage, the cell can respond with a large range of sensors and effectors as seen in Figure 2.3. The sensors include a group of proteins that constantly survey for the presence of DNA damage, which then relay this to effector pathways that determine the exact DNA repair mechanism [171]. There are many different checkpoints throughout the cell cycle to check for DNA damage to ensure mitosis is not initiated. During these checkpoints, the H2AX protein is autophosphorylated in the presence of DNA damage, becoming γH2AX foci [172]. There are few related kinases that can phosphorylate H2AX at the sites of DSB, allowing the formation of foci. Following radiation, this is primarily done by the ataxia telangiectasia mutated (ATM) protein, following recruitment to the DSB by a complex made up of three proteins, MRE11, RAD50, and NBS1 (MRN).

Another important regulator of the DNA DSB repair mechanism is p53-binding protein 1 (53BP1) [173]. This protein has many functions, one of which is to help

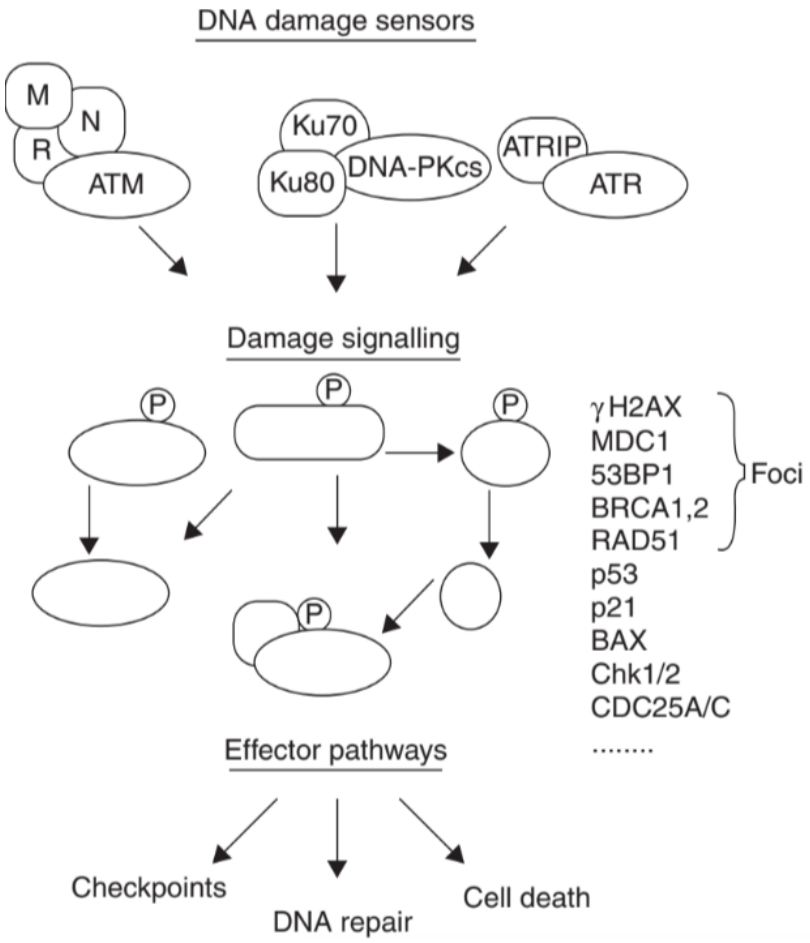


Figure 2.3: **The DNA damage response.** The DNA damage response is mediated by a multiple cascades of sensors and effectors. Adopted from [3].

make a choice of DSB repair pathway, such as non-homologous end joining, which is facilitated positively by 53BP1. Similarly to γH2AX, 53BP1 recruitment can also be tracked by the subnuclear foci that occur at locations of damaged chromatin. While the recruitment of 53BP1 is independent of γH2AX, the association of 53BP1 with DSBs relies on a cascade that is activated downstream of γH2AX, and thus both foci tend to be localized to each other [174].

2.2.2 Cell cycle and radiosensitivity

The cell cycle is largely controlled by a multitude of cell cycle checkpoints, to prevent the accumulation of genetic errors during cell division [119]. All movement through the cell cycle is controlled via CDKs which are activated by specific cyclin partners. Inhibition of the cyclin-CDK complex can cause entry into a checkpoint, which is

largely done by activation of other proteins called CDK inhibitors (CDKIs). The DNA damage response will activate four distinct checkpoints due to radiation, depending on different points in the cell cycle.

The DNA damage checkpoints can be separated into those controlled by p53 and those under control of the checkpoint kinases Chk1 and Chk2 [175]. In G1, when ATM finds a DNA DSB, it can activate p53 which then upregulates the CDKI p21. p21 inhibits the G1 cyclin-CDK complex and thus will delay entry of the cell from G1 into S phase. In S phase, if there is DNA damage, then ATM will phosphorylate Chk1 and Chk2, which then phosphorylate the CDK2 kinase to prevent S-phase progression. DNA damage in the early G2 phase acts similarly to that in S phase, except Chk2 will phosphorylate the mitotic cyclinB-CDK1 complex and stop progression to mitosis. There are also checkpoints that occur during mitosis, via Chk1 and Chk2 [176].

The cell cycle checkpoints in the early portion of the cell cycle limit the radiosensitivity of the cell. The G2/M phase has been observed as being the most radiosensitive phase of the cell cycle [47]. This is due to a couple reasons, namely that chromatin is more radiosensitive in M phase due to the difficulty in repairing it following radiation. Further, there are far fewer cell cycle checkpoints to have to bypass in M phase that check for damage, and thus there may not be enough time to repair the DNA before the cell progresses through mitosis. Thus, the daughter cells will have DNA damage, causing eventual cell kill. Targeting of the cell in G2/M phase for cancer cells is therefore quite desirable.

2.2.3 DNA damage repair

The cell has many different mechanisms for DNA damage repair, depending on the damage from the incoming radiation [177]. Most importantly are the repair mechanisms for DSBs, namely homologous recombination and nonhomologous end-joining, as one DSB is enough to induce death of a cell [178]. Homologous recombination works by using an undamaged sister chromatid sequence as a template for repair, whereas nonhomologous end-joining directly ligates the break ends, which can allow imprecise repair and loss of nucleotides. Nonhomologous end joining, as a result, can lead to more mutations, and possibly cancer in the future [3].

There are various assays that can be used to measure the damage to cells due to radiation, most of which are based on the measure of proliferative capabilities post-treatment [169]. Radiation can induce death in multiple ways, such as apoptosis,

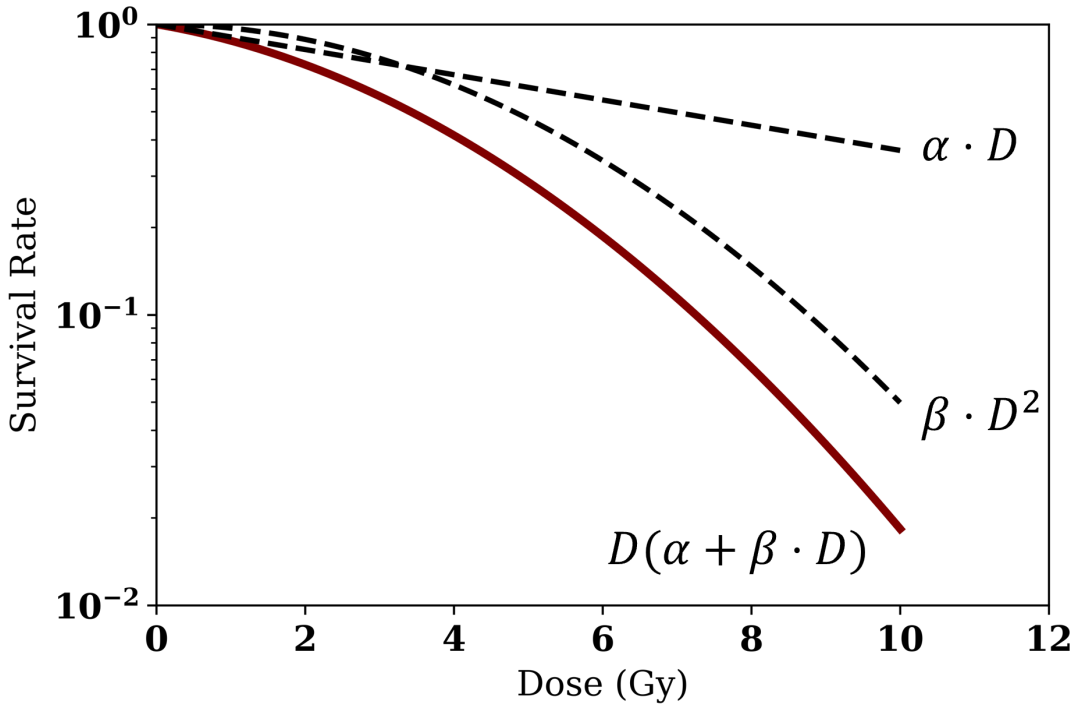


Figure 2.4: **Cell survival curve.** With a series of doses, a survival curve can be plotted and modelled using the linear-quadratic model. The linear quadratic model has a linear portion and a quadratic portion, which, when combined, form the final resulting curve. This curve, for example, is simulated using a β of 0.03, and an α of 0.1, leading to an α/β of 3.33.

necrosis, mitotic catastrophe, or through senescence. A clonogenic assay is the gold standard for measuring long-term proliferative abilities, which will measure all of these different modes of death [179]. With a range of irradiation doses, a cell survival curve can be plotted and is usually fitted using the linear-quadratic model [180]. The linear-quadratic model is defined as

$$S = \exp(-\alpha D - \beta D^2) \tag{2.1}$$

where S is survival, D is dose, and α, β are parameters of radiosensitivity, which can be seen in Figure 2.4. The ratio of α/β defines how radiosensitive a cell is, with high ratios seeing a more linear survival curve and thus low radiosensitivity, and lower ratios seeing a more quadratic curve with high radiosensitivity [181]. The term α can be thought of as death from lethal damage by a single particle while β represents multiple hit cell death from multiple radiation tracks.

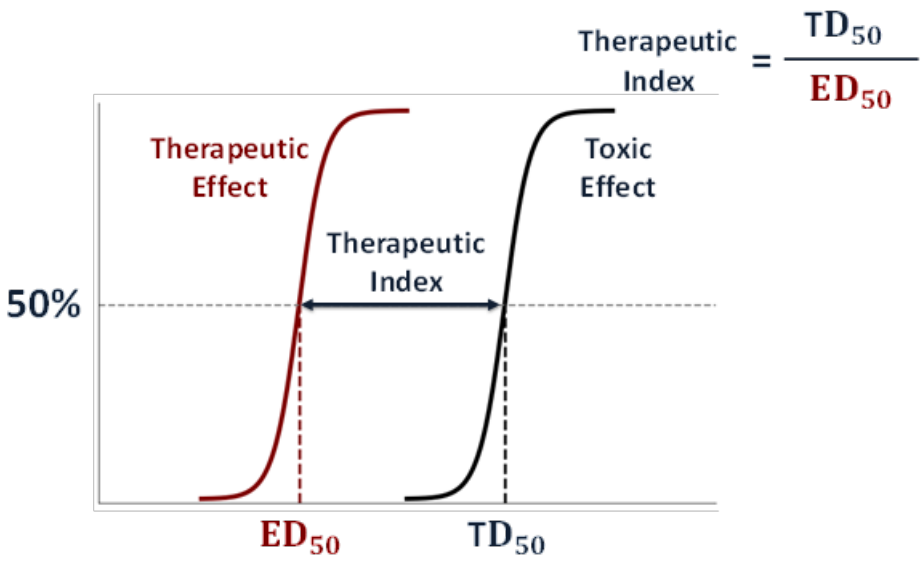


Figure 2.5: **The therapeutic index.** The ratio of the toxic effect to the therapeutic effect defines the therapeutic ratio. Optimization of this ratio will lead to better outcomes in treatment.

An important metric to consider when treating tumours with any therapy is the therapeutic index (TI) [182]. The TI is the ratio of the normal tissue response to the tumor control, as seen in Figure 2.5. RT can cause a loss of function in normal tissue, as it is a non-specific treatment, though improvements have been made in targeting using methods such as IMRT [183]. One of the major issues that faces current RT modalities is the normal tissue toxicity in radiosensitive tissue localized closely to tumours. Sparing of healthy tissue while delivering a toxic dose to the tumour is an ongoing issue present in all treatment options. Increasing the TI can allow for a more optimized treatment, as more of the tumor can be killed off before side-effects become the limiting factor.

2.2.4 Five Rs of radiotherapy

To improve the treatment of tumours and reduce normal tissue toxicity, treatment has been broken up into multiple fractions of a total dose [184]. For many tumours, a normal fraction is 2 Gy to a total dose of 50-70 Gy. Treatments that have less than 2 Gy per fraction are hyperfractionated while those with larger than 2 Gy are hypofractionated. To describe how tumours would respond during the course of fractionated RT, the 5Rs of radiotherapy were introduced [185]. These are:

1. Radiosensitivity - Some cell lines are more sensitive to radiation than other cell lines, which can be described by the α/β ratio. Knowledge of this can help determine the outcome of a treatment. Further, the radiosensitivity of a cell line can help determine whether a treatment schedule should be hypofractionated, hyperfractionated, or follow a normal fraction setup.

2. Repair - Many malignant cells have suppressed the pathways that are often used to quickly repair damage. Thus, by doing a fractionated treatment regime, normal cells can properly repair and limit toxicity while cancer cells will still be damaged.

3. Reoxygenation - As RT can create ROS that can indirectly cause permanent damage, oxygen is an essential component to improve treatment outcome. Tumours chaotic vasculature can cause hypoxia, which can lead to radioresistance [186]. By treating with a fractionated regime, the parts of the tumour that are well oxygenated can be killed off, akin to peeling an onion, allowing for deeper parts of the tumour to be reoxygenated for the next fraction.

4. Repopulation - Tissue will respond to radiation and the resulting decreased number of cells by increasing the repopulation rate. Some tissue types will be early responders and begin repopulating at 4 weeks after treatment. By increasing total treatment time beyond this period via fractionation, a reduction in early tissue toxicity can be achieved. However, some tumours also have this effect. Accelerated treatment plans may have to be implemented instead to reduce any negative tumour repopulation phenomena.

5. Redistribution - Cells are dividing according to the cell cycle, and some are in the radiosensitive G2/M phase. Following treatment, many of these cells will be killed off, leaving cells in the non-radiosensitive phases. Fractionation gives cells time to redistribute through the cell cycle following treatment and transition into the radiosensitive G2/M phase for the next fraction.

2.3 Radiation and the interaction with matter

It is important to understand the atomic structure and the electromagnetic interactions that occur both in the keV range and MeV range, as these are critical to the understanding of GNPs being a radiosensitizer.

2.3.1 The Atom and Photon Absorption

The atom is the building block of all matter and is key to understanding how we can use radiation as a cancer treatment option. The nucleus of the atom is made up of positively charged protons and neutral neutrons, which are surrounded by a cloud of negatively charged electrons. The number of protons in an atom corresponds to the atomic number (Z), denoting a specific element. For example, hydrogen has a Z of 1 while gold has a Z of 79. Atoms that have the same amount of protons as electrons will have no charge, while those with an imbalance will result in an ion. Atoms with the same number of protons but different number of neutrons are referred to as isotopes. Further, compounds can be described using an effective atomic number (Z_{eff}), which takes into account all the elements involved and is described by [187]:

$$Z_{eff} = \sqrt[2.94]{\sum_i f_i Z_i^{2.94}} \tag{2.2}$$

where Z_i is the atomic number of the element i, f_i is the fraction of the total electrons of element i in the compound. The effective atomic number of water (H_2O) is 7.42, which is what is commonly used to describe the Z_{eff} of tissue.

When a beam of photons, such as the x-rays used in RT, pass through an absorbing medium such as body tissue, there will be energy transfer that happens following photon absorption. This occurs largely *via* three important mechanisms: the photoelectric effect, Compton incoherent scattering, and pair production [188]. There is also an elastic Rayleigh scattering which has no net energy transfer. If we assume that a medium of length x has N_0 photons incident on it, then the number of photons that will be transmitted is:

$$N = N_0 \exp(-\mu x) \tag{2.3}$$

where μ is the linear attenuation coefficient. The linear attenuation coefficient is the fraction of photons that interact per unit thickness of an attenuator and is material and energy dependent. Often, μ is tabulated as a function of energy divided by material density ρ, where $\frac{\mu}{\rho}$ is known as the mass attenuation coefficient.

The linear attenuation coefficient is the combination of all the various cross sections of the previously mentioned principal photon, as seen in Figure 2.6. The partial mass coefficients are made up of τ/ρ, σ_{coh}/ρ, σ_{inc}/ρ, κ/ρ for photoelectric effect, Rayleigh scattering, Compton scattering, and pair production respectively. The cross

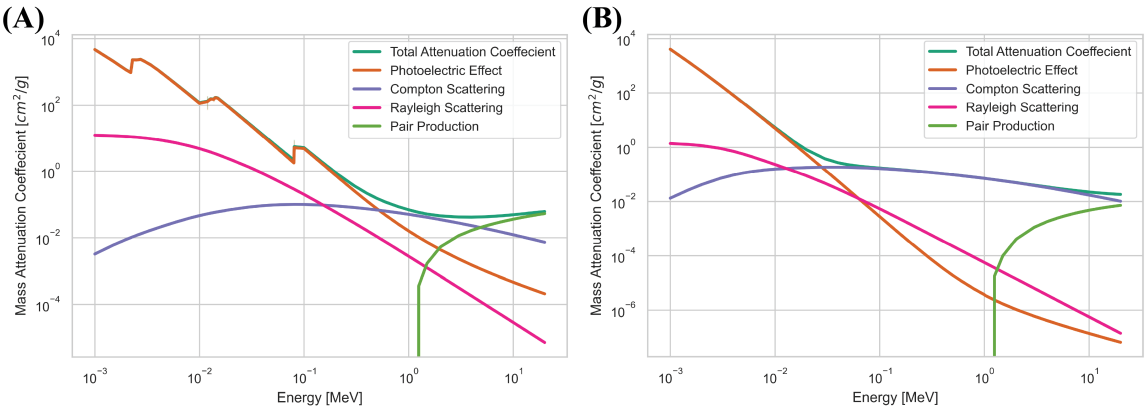


Figure 2.6: **Mass attenuation coefficients.** Total mass attenuation coefficients for (A) gold and (B) water. Includes contributions from coherent and incoherent scattering, the photoelectric effect, and pair production. Data from NIST "XCOM" tables [189].

sections can be likened to the probability of the occurrence of a particular photon interaction, with the sum of them adding up to the total probability of any interaction.

2.3.2 Photoelectric Effect

When a photon with energy $h\nu$ is incident on an atom, it can eject one of the bound electrons from its atomic orbital, as seen in Figure 2.7. The emitted electron is called a 'photoelectron' and has an energy $h\nu - E_s$, where E_s is the binding energy of the specific shell the electron is emitted from. The discontinuities that are visible in Figure 2.6A are caused by the photoelectric effect, due to the binding energy. A photon needs to have energy $h\nu$ larger than the binding energy of each orbital shell to eject a photoelectron. The first spike for gold occurs in the K-shell at 80.7 keV, and the other discontinuities occur due to the binding energies of the other shells. After a photoelectron is released, there is now a vacancy in the shell which is then filled from a higher orbital. Energy will be released from the atom to fill in the vacancy in the form of characteristic fluorescent x-rays or Auger electrons.

The photoelectric mass attenuation coefficient (τ/ρ) varies with both energy and atomic number. In general, it is proportional to $Z^3/h\nu^3$ for high Z materials and closer to $Z^{3.8}/h\nu^3$ for low Z materials. Thus, the photoelectric effect is only really important at lower keV energy ranges and is far more prevalent in high atomic number materials like gold compared to soft tissue.

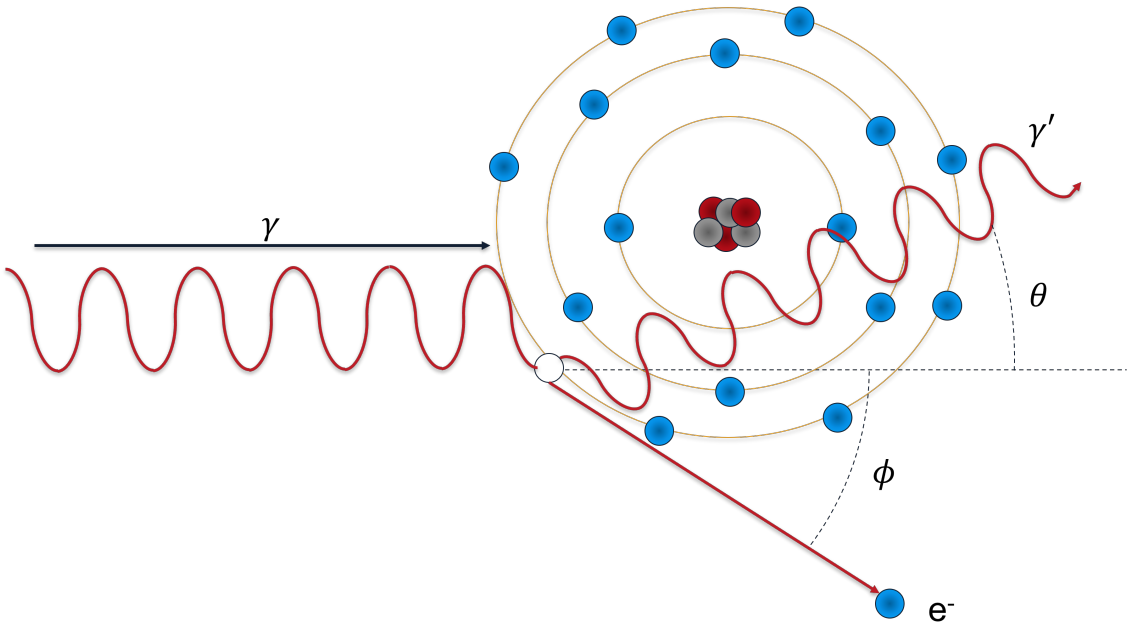


Figure 2.7: **Photoelectric Effect.** Diagram of the photoelectric effect, where a photon (γ) ejects a photoelectron (e^-) from its innermost atomic orbital.

2.3.3 Rayleigh Scattering

Otherwise known as coherent scattering, Rayleigh scattering occurs when a photon interacts with a bound electron in an atomic orbital. The oscillating electric field in the incident electromagnetic wave cause the electrons in the atom to momentarily vibrate, which releases radiation of the same wavelength λ. This interaction is not highly important to RT, as the photon scatter angle is small and there is no net energy transfer from the photon to the electron. The occurrence of Rayleigh scattering decreases rapidly with increase in photon energy and is negligibly small for energies greater than 100 keV in low atomic number material. It does occur more commonly in high Z materials, but only at low energies.

2.3.4 Compton Scattering

Otherwise known as incoherent scattering, the Compton effect occurs when a photon of energy hν interacts with an electron in an atomic orbital and transfers some of its energy to it, causing it to be ejected. The photon and electron will be scattered with angles θ and ϕ respectively, relative to the incoming photon, such that the energy and momentum is conserved, as seen in Figure 2.8. The scattered photon will have

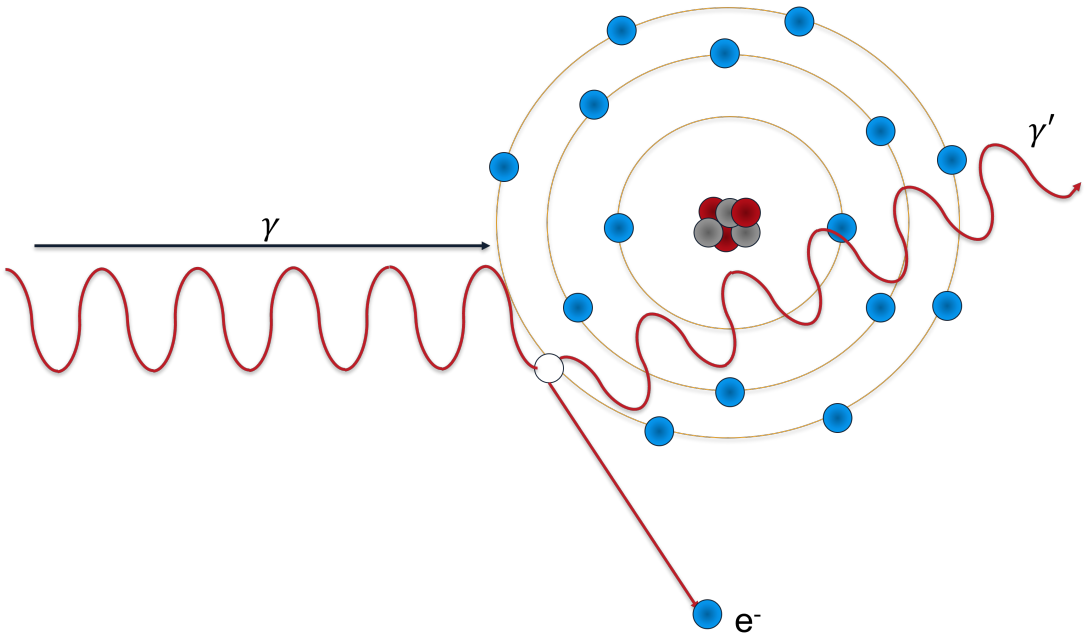


Figure 2.8: **Compton Scattering.** Diagram of a Compton Scattering event, where an incident photon (γ) ejects an electron (e^-) and the incident photon is scattered with a new energy (γ'). The photon and electron are scattered with angles θ and ϕ respectively, relative to the incident photon trajectory.

lower energy $h\nu'$ which is dependent on its scattering angle:

$$h\nu' = h\nu \frac{1}{1 + \alpha(1 - \cos\theta)} \tag{2.4}$$
$$\text{where } \alpha = \frac{h\nu}{m_0 c^2} = \frac{h\nu}{0.511\text{MeV}}$$

The energy of the ejected electron E_k is found by conservation of energy ($E_k = h\nu - h\nu'$) and its scattering angle can be described by

$$\cot\phi = (1 + \alpha)\tan\frac{\theta}{2} \tag{2.5}$$

The probability for a photon to undergo Compton scattering is dependent largely on incident photon energy. This has been shown by Klein and Nishina and is derived from quantum mechanics in equation 2.6 [190].

$$\frac{\mathrm{d}\sigma}{\mathrm{d}\Omega} = \frac{r_0^2}{2}(1+\cos^2\theta)F_{KN}$$
$$\text{where } F_{KN} = \left\{\frac{1}{1+\alpha(1-\cos\theta)}\right\}^2\left\{1+\frac{\alpha^2(1-\cos\theta)^2}{[1+\alpha(1-\cos\theta)](1+\cos^2\theta)}\right\} \tag{2.6}$$

with $r_0 = 2.818 \times 10^{-15}$ m^2 being the classical electron radius. For a free electron, the total probability that a photon will then interact can be found by multiplying by $\mathrm{d}\Omega = 2\pi \sin\theta \mathrm{d}\theta$ and integrating over all angles of θ, yielding

$$\sigma = \frac{3}{4}\sigma_0\left\{\left(\frac{1+\alpha}{\alpha^2}\right)\left(\frac{2(1+\alpha)}{1+2\alpha} - \frac{\ln(1+2\alpha)}{\alpha}\right) + \frac{\ln(1+2\alpha)}{2\alpha} - \frac{1+3\alpha}{(1+2\alpha)^2}\right\} \tag{2.7}$$

where $\sigma_0 = 66.525 \times 10^{-30}$ m^2 is the classical Thomson coefficient. The Klein-Nishina equation describes a wide distribution of scattering angles for low (<100 keV) photons and more forward scattering for high (>1 MeV) energy photons. The probability of Compton scattering occurring as energy increases will eventually reduce, as can be seen in Figure 2.6. It is important to understand Compton scattering as it is the dominant photon interaction that will occur in soft tissue at normal therapeutic energy ranges and is thus the cause of a large portion of the absorbed energy.

2.3.5 Pair Production

If the energy of an incident photon is greater than 1.022 MeV, then the photon can be absorbed through pair production. When a photon of such energy passes near the nucleus of the atom, it can be subjected to the strong field of the nucleus, causing the photon to disappear, and become an electron and a positron. If the photon has energy in excess of 1.022 MeV, then the energy is shared between the positron and electron ($h\nu - 1.022 = E_+ + E_-$) via kinetic energy, with a negligible amount also given to the nucleus as recoil energy.

The probability of pair production occurring is zero until the photon is high enough energy, and then increases dramatically with increasing energy. If the main attenuation process is pair production in a material, then a high energy beam is less penetrating, in contract with the photoelectric effect and Compton scattering. The pair coefficient κ is proportional to Z^2, and thus larger atomic number materials will have a larger occurrence of pair production at high energies. However, in normal

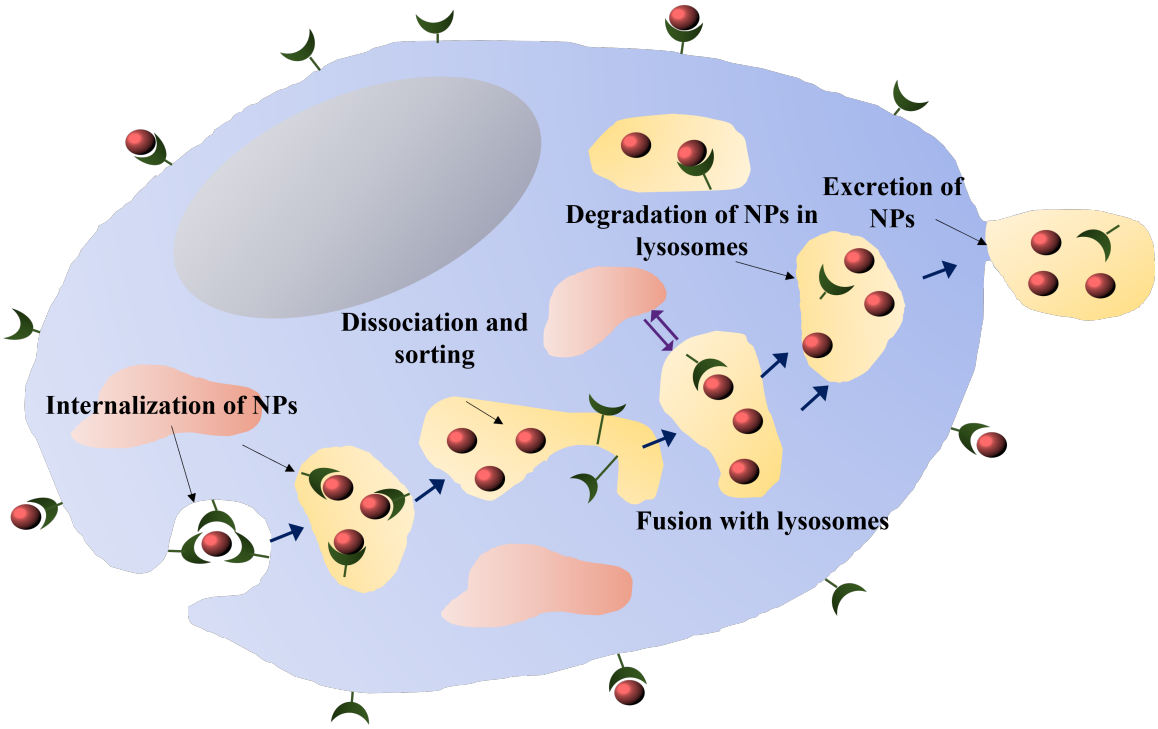


Figure 2.9: **Uptake of nanoparticles into a cell.** Once NPs are attached to the receptors on the surface of the cell, membrane invagination occurs followed by budding into the cell, forming a vesicle. The internalized GNPs are sorted inside the vesicle and eventually fuse with lysosomes. NPs are then excreted out of the cell.

therapeutic ranges, pair production is not a very dominant process, and only occurs in special treatment modalities.

2.4 Gold nanoparticles as a radiosensitizer

2.4.1 Intracellular fate of gold nanoparticles

There are different methods of entry into cells for NPs, including clathrin-mediated endocytosis, clathrin-caveolin independent endocytosis, and caveolae-mediated endocytosis [191]. Most NPs, including GNPs, enter the cell mostly via clathrin-mediated, otherwise known as receptor-mediated, endocytosis (RME)[192, 193]. The efficiency of the RME process depends on the interaction between molecules on the NP surface (ligands) and the cell membrane receptors. Cell surface receptors bind to molecules on the surface of NPs causing membrane wrapping of the NP with a corresponding increase in elastic energy. The receptor-ligand binding immobilizes receptors causing configurational entropy to be reduced. More receptors diffuse to the wrapping

site, driven by the local reduction in free energy, allowing the membrane to wrap completely around the particle [194]. RME is therefore an energy dependent process where the path of the NPs within the cell is explained in Figure 2.9. NPs first reach the cell membrane and connect with the cell membrane receptors, which are mobile on the surface. Internalization of NPs occurs via invagination of the membrane, which then get trapped in endosomal vesicles. These internalized NPs are sorted inside the vesicle and eventually fuse with lysosomes. NPs are then excreted out of the cell [195, 196].

The RME is also dependent on the size, shape, and surface properties of NPs [197]. Among the size range of 10-100 nm, bare GNPs of diameter 50 nm had the highest uptake in a monolayer of cells. The cellular uptake of rod-shaped NPs was lower than their spherical counter parts. This is a result of balance between energy needed for membrane wrapping of NPs and kinetics of receptor diffusion along the cell membrane [198, 199]. However, the common use of citrate-capped NPs which are not functionalized, where the RME process of the NPs was facilitated via non-specific binding of serum proteins on the NP surface once they were introduced to the tissue culture media, is not optimum for *in vivo* treatment [200]. It is important to optimize NPs properly for efficient *in vivo* delivery to the tumour.

There are many factors to consider when optimizing GNPs for use in an *in vivo* environment. GNPs exhibit very complex and varying pharmacokinetics, due the vast number of options in size, shape, and functionalization. Avoidance of opsonization and the reticuloendothelial system (e.g. liver and spleen) while also targeting the tumor are important goals in nanotechnology. If not functionalized properly, the opsonin protein in the blood plasma will attach to the NP surface, leading to the removal of the NP from the circulatory system by macrophages [201]. Further, the protein corona that can form from interactions of the GNPs with blood, as a result of size, shape, charge, and functionalization, can alter the behavior of the nanoplatform [202]. Therefore, surface modifications of GNPs are done to protect the particle from the environment and to target the particle to a specific cell or tissue type. This is critical because the GNPs need to be present long enough for the process of accumulation within a tumour through its leaky vasculature, via the EPR effect. The addition of PEG molecules to the surface of NPs increases blood circulation time [203]. The process of PEGylation allows for the ethylene glycol to form associations with water molecules, causing the formation of a protective hydrating layer, which in turn hinders protein adsorption and clearance by macrophages. GNPs functionalized

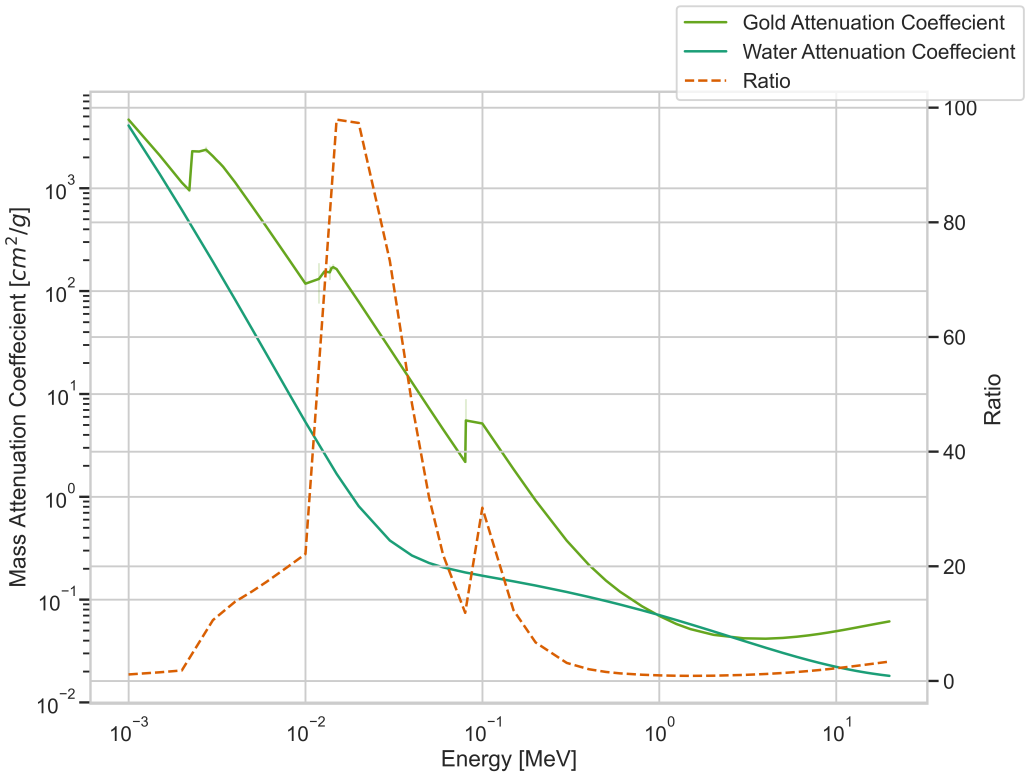


Figure 2.10: **Ratio of gold mass attenuation coefficient with water mass attenuation coefficient.** Ratio of total mass attenuation between gold and water (equivalent to soft tissue). Data from NIST "XCOM" tables [189].

with PEG molecules have also shown the capacity to evade the immune system and remain in the blood undetected by macrophages [201]. However, the drawback of PEGylating the NP surface is that RME is very much retarded. To overcome this lower uptake of NPs, researchers have added targeting moieties to overcome the reduced NP uptake. One approach was to add a peptide containing arginine-glycine-aspartic acid (RGD) sequence [203]. The RGD sequence can recognize the integrin $\alpha_v\beta_3$ that is highly expressed by several solid tumours, and has demonstrably higher uptake than GNPs functionalized with just PEG [204]. The use of RGD is also beneficial in targeting the extracellular matrix, as the RGD motif is expressed within various proteins such as fibronectin, vitronectin, fibrinogen, osteopontin, and bone sialoprotein [205]. Targeting cancers in this way will improve uptake of NPs and allow RT to be a more effective modality.

2.4.2 Gold nanoparticles and radiotherapy

In kV beams, GNPs have a drastic radiosensitizing effect, due to a large portion of photons being in the photoelectric regime for gold [73]. When considering clinically relevant energies of low MV (e.g. 6 MV) X-rays, the predominant interaction for all photons in most materials, including gold (Z=79) and soft tissue (Z≈7.5), is the Compton effect. Moreover, the Compton effect has little Z dependence, and thus minimal dose enhancement is predicted by some Monte Carlo simulations using GNPs [206, 207]. However, experimental studies have shown a larger dose enhancement [208, 209, 70]. This may be due to electrons and low energy photons forming in the build-up region prior to the target volume, due to previous high energy photon interactions along the path they travel. Further, a beam from a linear accelerator which is used to produce the X-rays in EBRT is not monoenergetic, and thus will have a spectrum of photons ranging from keV to MeV energies with a mean of 1/3 the max energy. Due to the polyenergetic spectrum of the 6 MV beam having a significant amount of keV photons, there will be photoelectric contributions, which is highly dominated by high Z materials like GNPs, relative to low Z materials like soft tissue at clinically relevant energies. Because the photoelectric effect preferentially excites electrons from inner shells at higher energies, this interaction will lead to an inner-shell vacancy which is typically filled through the Auger effect. This can lead to a large cascade of a dozen or more low energy Auger electrons being ejected. In bulk gold, these electrons tend to be too weak to escape, but due to the nano-nature of the GNPs, there is a large enough range for the electrons to escape into the soft tissue and cause damage, such as radiolysis and formation of ROS.

A large portion of the radiosensitizing effect observed in GNPs is believed to be due to the ratio of the mass attenuation coefficient at every energy level (Figure 2.10). While the absorption of x-rays is orders of magnitude larger in the photoelectric regime in GNPs at keV energy ranges, there is a slight increase at MeV ranges, where Compton dominates. However, there are other mechanisms in play, such as biological pathways. Even in the absence of radiation, GNPs have been shown to induce the production of ROS, leading to oxidative stress [210]. Following radiation, the increase of ROS production leads to an elevated radiosensitizing effect. This is further exacerbated by the increase in free radical production caused by the cascade of electrons that follow interactions with GNPs, as seen in Figure 2.11. This radiosensitizing effect can be further increased by synchronizing cells in the G2/M phase via

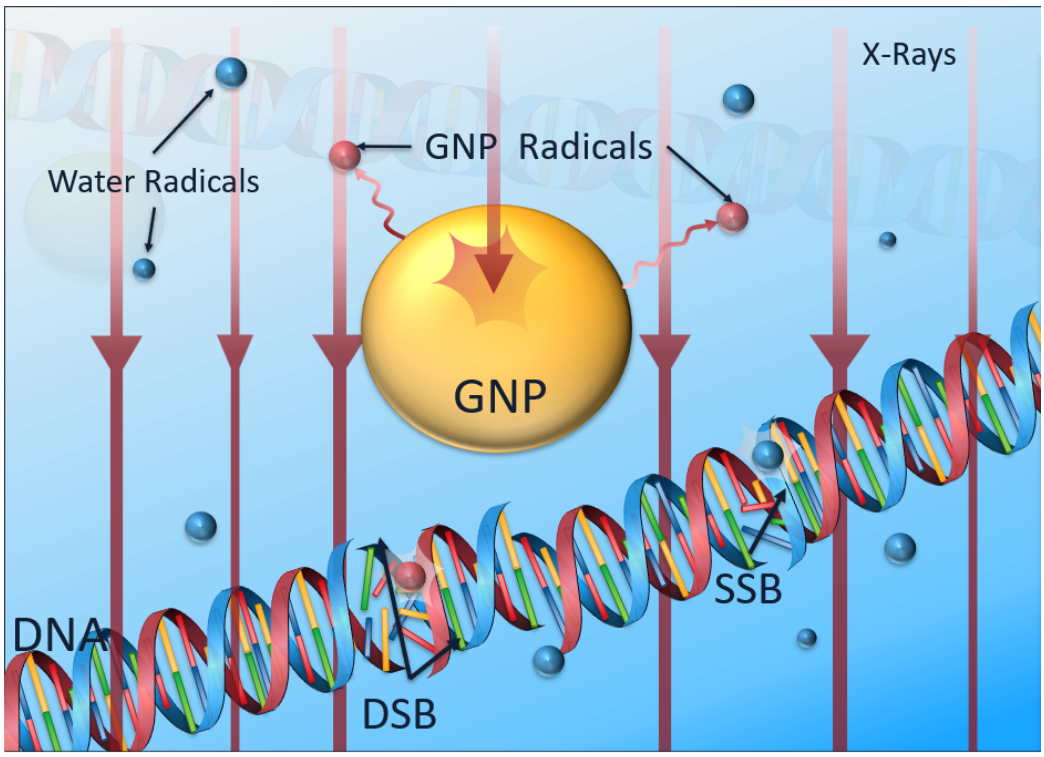


Figure 2.11: **Gold nanoparticles as a radiosensitizer.** When high energy radiation interacts with GNPs, due to their high Z nature, there will be a cascade of electrons and photons that will form free radicals and cause damage within the cell.

alternative chemicals, such as DTX, to compound the damage.

2.5 Summary

This chapter went over the fundamentals of tumours and the hallmarks that describe them. Knowledge of these hallmarks allows us to target specific functionalities that tumours express and gives us an understanding of where we can improve in the future. Further, the radiobiology that describes the tumours response to radiation and the DNA damage response gives us understanding of how to target specific mechanisms in the cell and improve treatment modalities by, for example, synchronizing cells in the radiosensitive G2/M phase. Finally, the actual physical interactions that occur with radiation in matter and how we can take advantage of the physics to utilize high Z materials such as GNPs to radiosensitize cells to high energy X-rays was summarized. The next chapter will go over many of the methods that will be used throughout the experiments undertaken in this work, and their theoretical background.

Chapter 3

Optimizing gold nanoparticle treatment in two-dimensional cancer cell models

3.1 Preamble

Content in this section is reproduced with permission from Nature: Scientific Reports, and it has been published with the following citation:

> Bromma, K., Cicon, L., Beckham, W., Chithrani, DB., Gold nanoparticle mediated radiation response among key cell components of the tumour microenvironment for the advancement of cancer nanotechnology. *Scientific Reports.* https://doi.org/10.1038/s41598-020-68994-0 (2020)

The candidate, KB, made substantial and direct contributions to the conception and design of the experimental plan. KB made substantial contribution to sample preparation, collection, and processing. KB made substantial contribution to the acquisition of the data.

Experimental Conception: KB, WB, DBC
Experimental Design: KB, DBC
Performed Experiments: KB, LC, DBC
Analyzed Data: KB
Made Figures: KB
Writing of Manuscript: KB

3.2 Introduction

Much of the GNP-mediated radiation dose enhancement research has so far focused on cancer cells. However, the role of the TME has been recently been recognized as a major contributor to tumour propagation [212]. The TME is a complex amalgamation of the ECM, stromal cells such as fibroblasts, immune cells, capillaries, and the basement membrane [213]. Of particular importance to the growth and progression of cancer are fibroblasts [214]. Fibroblasts, specifically activated fibroblasts or myofibroblasts, are associated with the wound healing response [157]. However, these activated fibroblasts can be recruited by the cancer cells, becoming CAFs [215]. While FBs have anti-tumorigenesis properties, CAFs have been shown to be related to increase proliferation, metastasis, and chemoresistance [164, 165]. Moreover, CAFs increase the radioresistance of the tumour [167]. Therefore, focusing only on cancer cells while ignoring the CAFs in TME when optimizing radiotherapy-based treatment using GNPs would ignore a large part of what allows tumours to grow and propagate. It is not yet known the cross section of GNP uptake and resulting radiation sensitizing effects across tumour cells, CAFs, and FBs. Hence, this study aims to investigate the GNP-mediated radiation sensitization in three of the main interrelated cell components of the TME as illustrated in the thematic Figure 3.1A.

In order to better understand GNP mediated radiation dose enhancement, we first determined the uptake of GNPs across cancer cells, CAFs, and FBs (Figure 3.1B, i). Followed by uptake studies, we proceeded to radiation treatment studies with a clinically relevant 6 MV photon beam as illustrated in Figure 3.1B, ii. Our final goal was to map the cell damage due to GNP-mediated radiation dose enhancement by probing DNA DSBs (see Figure 3.1B, iii). Prior to this work, comparison of GNP uptake and GNP-mediated radiotherapy across cancer cells, FBs, and CAFs with GNPs using clinically relevant 6 MV photon beams had not been investigated yet. The use of GNPs to enhance the local dose in the CAFs as well as the tumour could prove to have a significantly beneficial therapeutic outcome. Reducing the ability of CAFs to influence the progression of the tumour such as in Figure 3.1C could reduce future complications in patients and improve current treatment modalities. As discussed, normal FBs are recruited into CAFs to promote tumour progression. This study will also elucidate the extent of NP uptake and resulting radiosensitization effects in normal cells compared to other cancer associated cells within TME. Thus, this work will emphasize the importance of considering key cell components of the

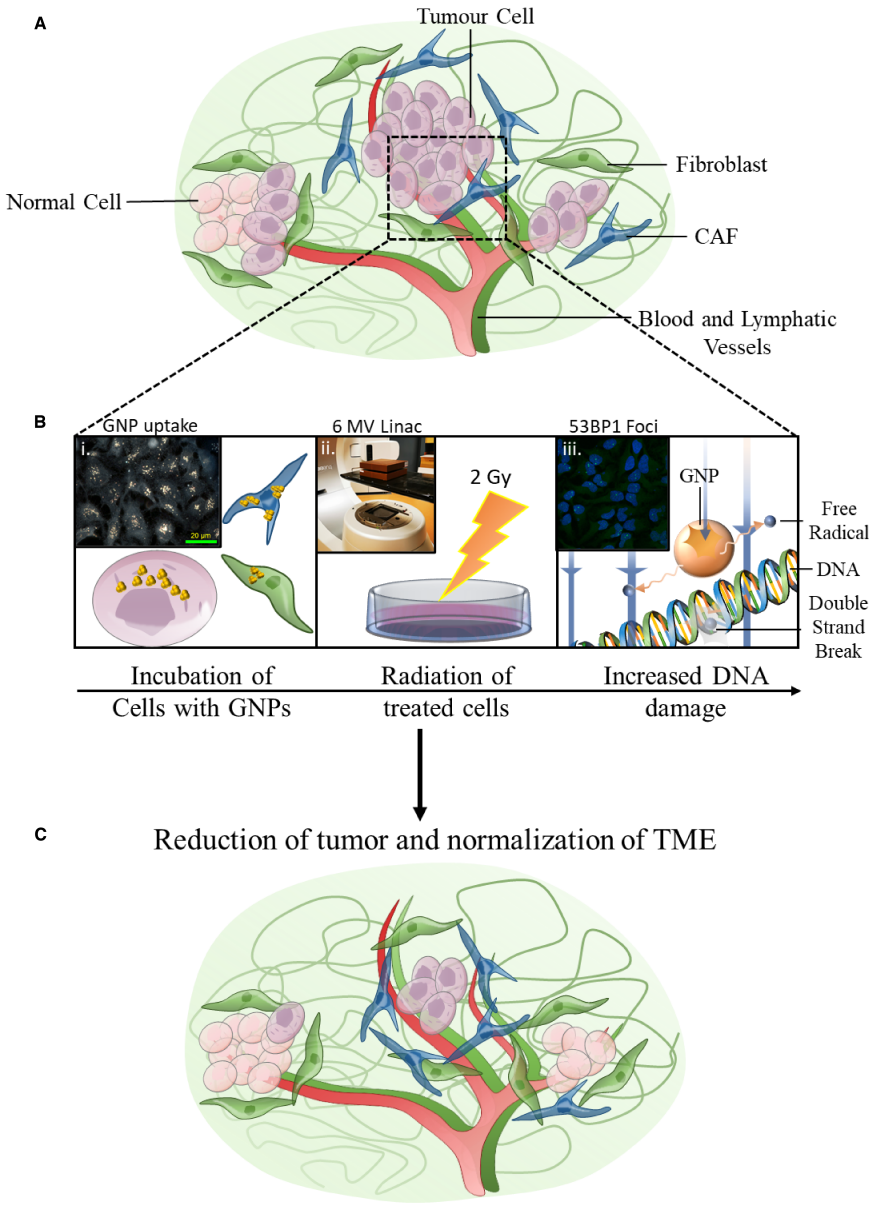


Figure 3.1: **Normal and cancer associated fibroblasts in cancer therapeutics.** (A) In normal tissue, FBs have anti-tumorigenic properties that suppress proliferation of cancer. However, when CAFs are introduced, a largely pro-tumorigenic influence is now exerted on the tumour microenvironment, leading to growth and eventual metastasis. (B) i) Cells uptake GNPs at differing rates, which is directly related to the efficacy of the treatment. ii) Cells are irradiated with a 2 Gy dose using a 6 MV linac. iii) GNPs have been shown to have a radiosensitization effect on cancer cells, through improved formation of free radicals (C) Upon treatment with the dual combination of GNPs and radiation, the TME is more normalized and there is a reduction in tumour growth as well as invasive and migratory behaviour. Reproduced with permission [211]. Copyright Nature, 2020.

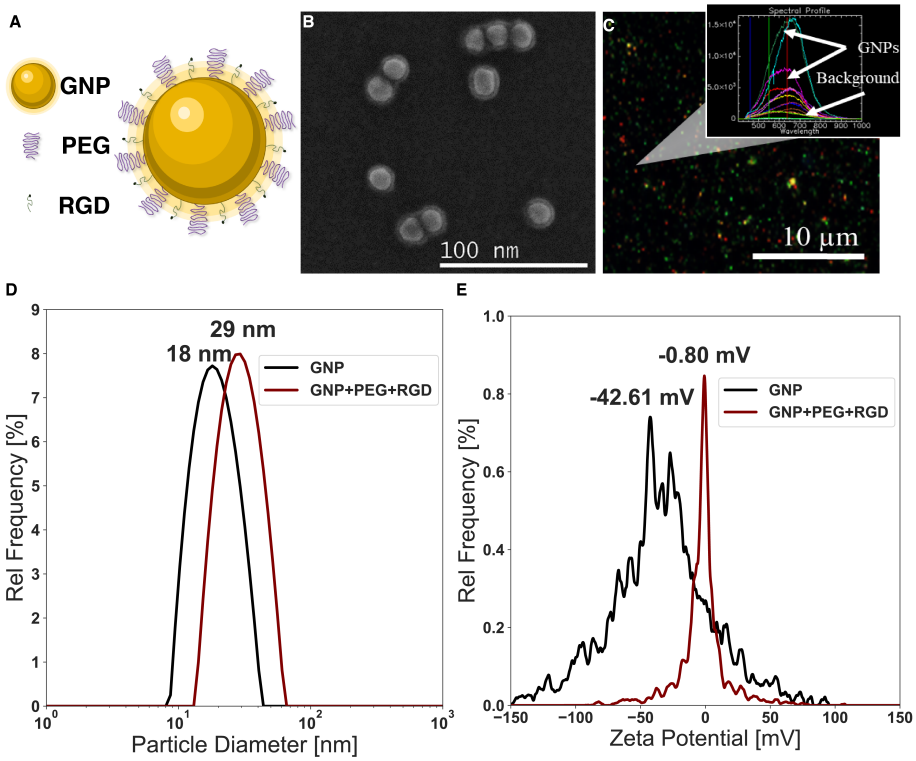


Figure 3.2: **Characterization of gold nanoparticles.** (A) Schematic diagram of the GNP and all the ligands used to form the $GNP_{PEG\text{-}RGD}$ complex. (B) Secondary electron TEM images of $GNP_{PEG\text{-}RGD}$ complexes (C) Darkfield image of GNPs overlayed with spectrum measured using hyper spectral imaging. The GNPs have a clear spectrum relative to background. (D) Hydrodynamic diameter from DLS and (E) ζ-potential of the GNPs before and after conjugation with PEG and RGD. Reproduced with permission [211]. Copyright Nature, 2020.

TME when integrating GNPs into current RT protocols for improved outcome in cancer patients in the near future.

3.3 Results

3.3.1 Characterization of gold nanoparticle complexes

The GNPs used for this study were conjugated with PEG and a peptide containing integrin binding domain RGD (Figure 3.2A). The functionalized GNP complex is referred to as $GNP_{PEG\text{-}RGD}$. The addition of the PEG molecules prior to RGD peptide is intended as a method to improve stability in the presence of serum, such as media. The use of PEG has been widely documented, and its concentration used in this study is in agreement with literature [216]. The GNP formulation was tested, for 24 hr,

A

Functionalization	Peak Absorption Wavelength (nm)	Hydrodynamic Diameter (nm)	Zeta Potential (mV)
GNP	520.05 ± 0.05	18.02 ± 0.36	-42.61 ± 1.98
GNP+PEG	520.95 ± 0.05	21.34 ± .43	-25.19 ± 1.62
GNP+PEG+RGD	523.07 ± 0.05	29.3 ± 0.59	-0.8 ± 0.39

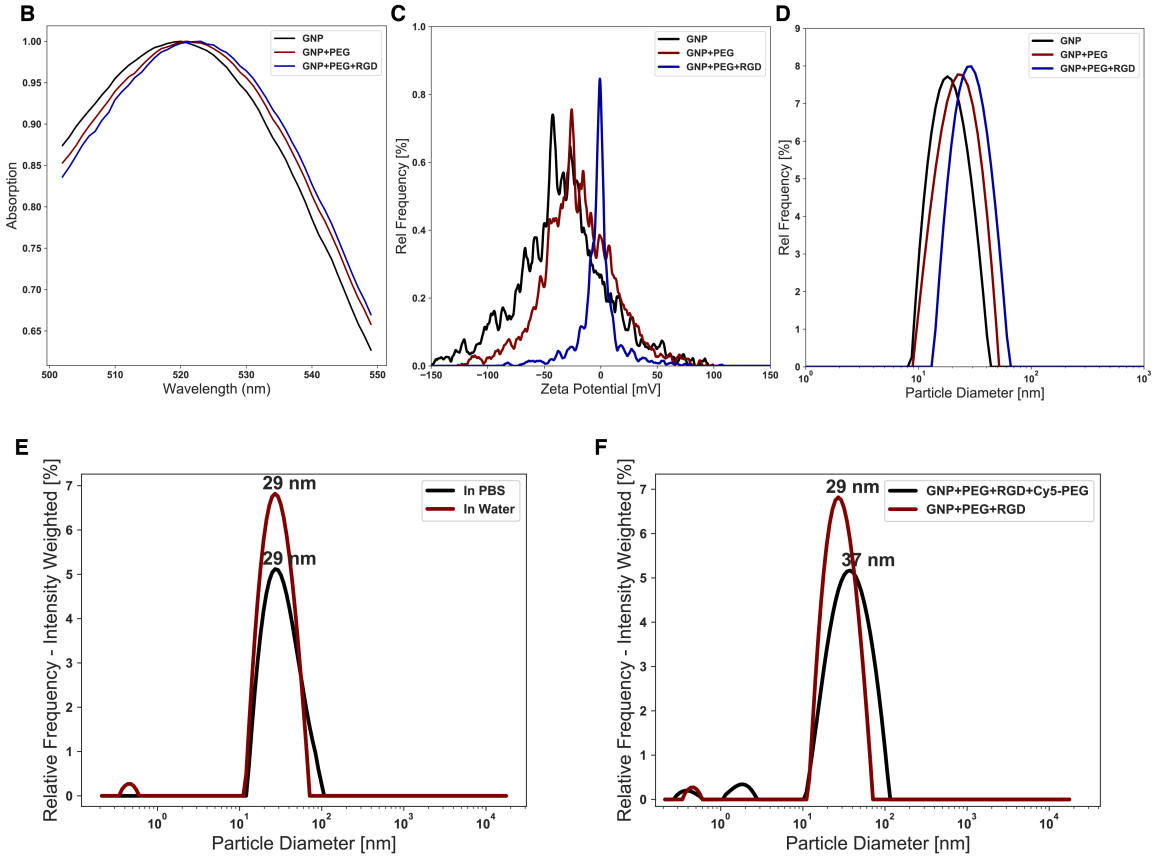


Figure 3.3: **Supplementary characterization of gold nanoparticles.** (A) Characterization data for GNPs, $GNP_{PEG\text{-}RGD}$ complexes, and GNP_{PEG} complexes from UV-Vis, DLS, and zeta potential. All sample measurements in (B) UV-Vis, (C) DLS, and (D) ζ-potential are plotted. (E) DLS measurements of $GNP_{PEG\text{-}RGD}$ in phosphate buffered saline (PBS) as compared to the base solvent of water. (F) DLS measurements of fluorescent $GNP_{PEG\text{-}RGD}$ tagged with PEG-thiol-Cy5 as compared to normal $GNP_{PEG\text{-}RGD}$. Reproduced with permission [211]. Copyright Nature, 2020.

in colorless tissue culture media, as this was the time period the GNPs were in cell culture medium. No significant changes, such as aggregation, to the formulation were observed. Conjugation of the GNPs with PEG and RGD have previously been shown to have improved uptake of PEGylated GNPs. TEM images of the $GNP_{PEG\text{-}RGD}$ complexes are displayed in Figure 3.2B. The average core of the NPs was measured

to be a diameter of 17.73 nm ± 0.17 nm, while the total diameter including surfactants was 20.90 nm ± 0.14 nm. Darkfield imaging and the spectrum of each pixel gathered from HSI can be seen in Figure 3.2C. The spectrum confirms the presence of GNPs and is used to further verify uptake into cells in further experiments. The size and shape of the GNPs and GNP complexes used in this study were measured using UV-VIS spectroscopy, DLS, and ζ potential measurements as summarized in Figure 3.3A. UV-Vis spectrometry was used to estimate the size and concentration of the GNPs relative to GNP_{PEG} and $GNP_{PEG\text{-}RGD}$ complexes (Figure 3.3B). UV–VIS has previously been found to be an accurate measurement of the concentration [217]. Further, the efficacy of UV–VIS for measurement of GNP concentration was independently verified through the use of ICP-MS, which found that a concentration of 0.2 nM from UV–VIS led to a measured concentration of 0.204 nM. The ratio of the absorbance at the surface plasmon resonance peak to the 450 nm absorbance gave an approximate size of 14 nm for both the bare and functionalized GNPs [217]. A slight red shift in the peaks occurred, but the general shape of the spectrum did not change appreciably, signifying stability of the nanoparticle complex.

Further, DLS and ζ-potential were measured before and after mixture with PEG and RGD peptide to verify conjugation (Figure 3.2E, F). DLS measurements were completed as well after conjugation with Cy5-thiol-PEG (Figure 3.3F), to confirm stability. DLS confirmed the hydrodynamic diameter of the bare GNPs to be 18.02 nm with a polydispersity index of 14.84%, while the $GNP_{PEG\text{-}RGD}$ complexes had a diameter of 29.3 nm and a polydispersity index of 11.08%. The Cy5-thiol-PEG $GNP_{PEG\text{-}RGD}$ complex had a hydrodynamic diameter of 37.01 nm with a polydispersity index of 15.68%. This increase in the hydrodynamic radius is consistent with conjugation of the moieties. Further, the difference in the size of the fluorescent GNPs is most likely due to the larger PEG moiety (3.4 kDa for Cy5 vs. 2 kDa for normal).

The ζ-potential of the bare GNPs and $GNP_{PEG\text{-}RGD}$ complexes was measured to be -42.61 mV ± 1.98 mV and -0.80 mV ± 0.39 mV respectively. This is due to the replacement of the negatively charged citrate molecules with neutral PEG molecules and the positively charged RGD peptides. The $GNP_{PEG\text{-}RGD}$ complex was also measured for stability in PBS at a concentration of 0.2 nM, as seen in Figure 3.3E. The GNPs were stable in PBS, with a similar hydrodynamic diameter of 29.42 nm and a polydispersity of 14.54%. Previous studies have shown that GNPs tagged with 1 PEG/nm^2 surface area demonstrated the best stability, which is the capping

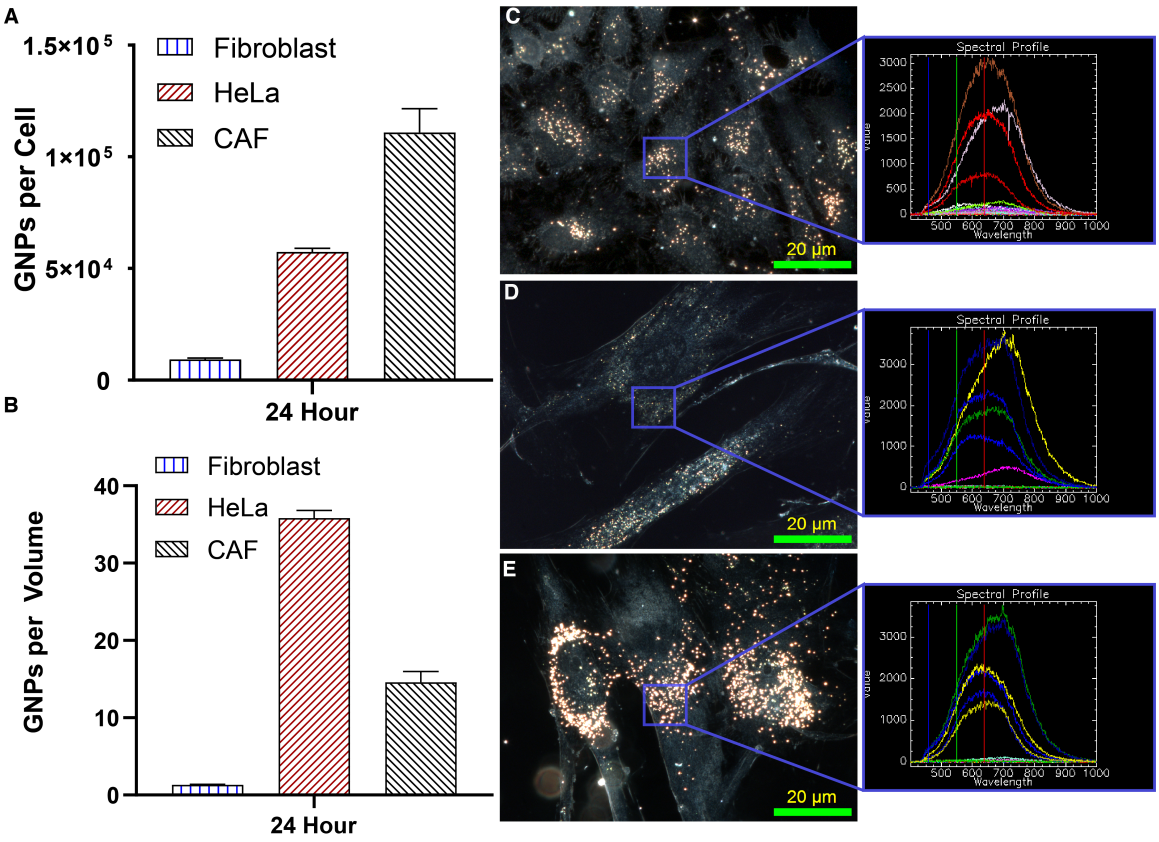


Figure 3.4: **Uptake and retention of gold nanoparticles.** (A, B) Quantification of uptake of 0.2 nM GNPs into all three cell lines as measured using ICP-MS. Error bars are standard deviations from triplicate measurements. (A) is GNP per cell, while (B) is normalized to the average volume of each cell line. (C–E) Darkfield images of the GNPs encapsulated in the three cell lines with HeLa on top, FBs in the middle, and CAFs on the bottom. Overlay: the spectrum from HSI is matched in each sample to that of GNPs previously measured. Images taken after 24 h of GNP exposure. Experiments were repeated three times and the data presented is the average. The error bars represent standard deviation. Scale bar is 20 μm. Reproduced with permission [211]. Copyright Nature, 2020.

density employed in this study.

3.3.2 Cellular uptake of GNP complexes

We chose HeLa as our model cancer cell line while CAFs and FBs were selected as our other two main types of cells in the TME (see Figure 3.1). HeLa was chosen as our model cancer cell line as it is highly characterized and simple to model. In order to map the GNP uptake cross section among these three cell lines, we incubated them

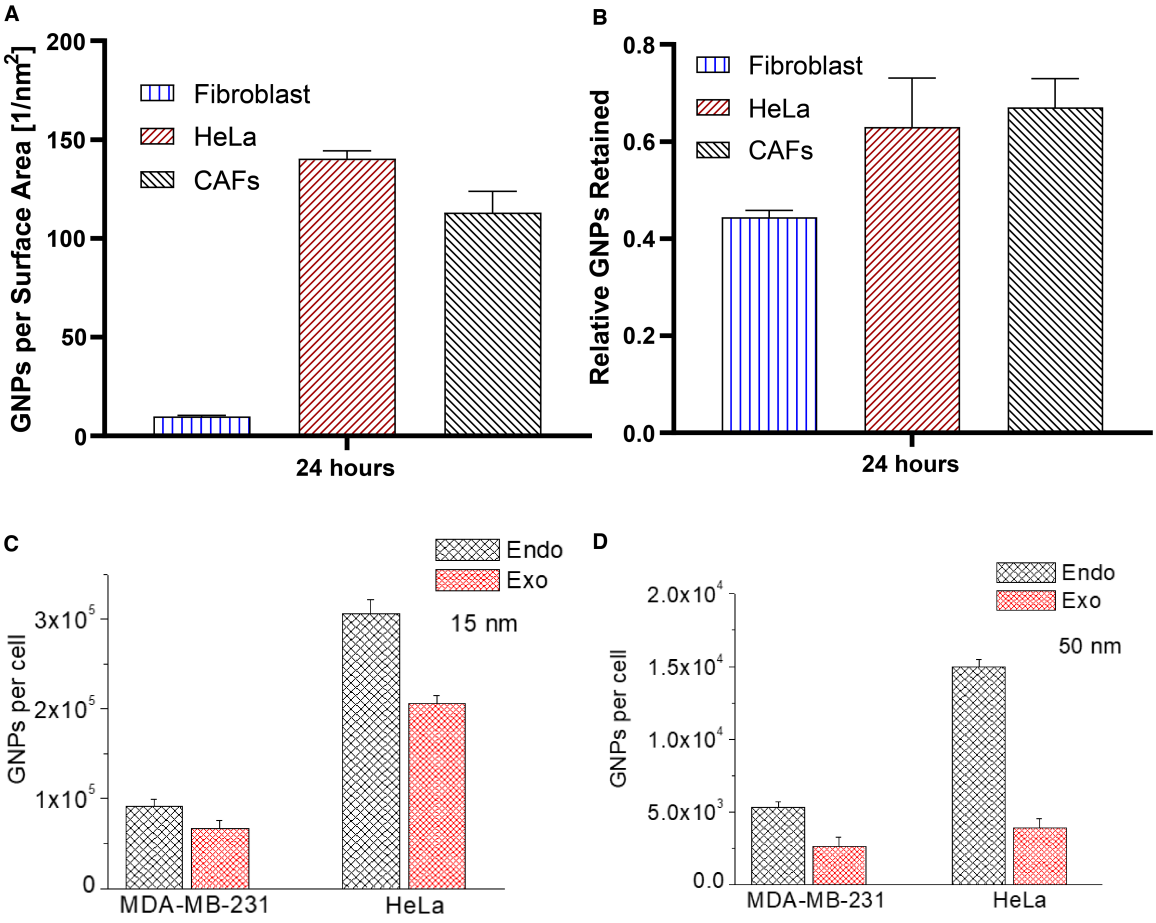


Figure 3.5: **Surface Area Normalized Uptake and retention of Gold Nanoparticles.** (A) Surface area normalized uptake of GNPs. (B) Relative retention of GNPs after 24 hours. Uptake of (C) smaller 15 nm GNPs and (D) larger 50 nm GNPs in two cancer cell lines, HeLa and MDA-MB-231, a breast cancer cell line, after 4 hours of uptake (endo) and after another 24 hours of release (exo). Reproduced with permission [211]. Copyright Nature, 2020.

with $GNP_{PEG\text{-}RGD}$ complex at a concentration of 0.2 nM for 24 hr. The uptake of the $GNP_{PEG\text{-}RGD}$ complex was quantified using ICP-MS (Figure 3.4A). The CAFs had the largest uptake of the GNPs per cell, with on average 265% as many GNPs relative to HeLa, which had the second largest GNPs/cell. FBs had, on average, only 7.55% the uptake of HeLa and 2.87% the uptake of CAFs. We also presented the GNP update data per unit volume of the cell (Figure 3.4B). The average volume per unit of CAFs, FBs, and Hela were 8181 $\mu m^3 \pm 82$ μm^3, 7700 $\mu m^3 \pm 77$ μm^3, and 2205 $\mu m^3 \pm 22$ μm^3, respectively. We found that CAFs have 50% of the average GNPs/volume found

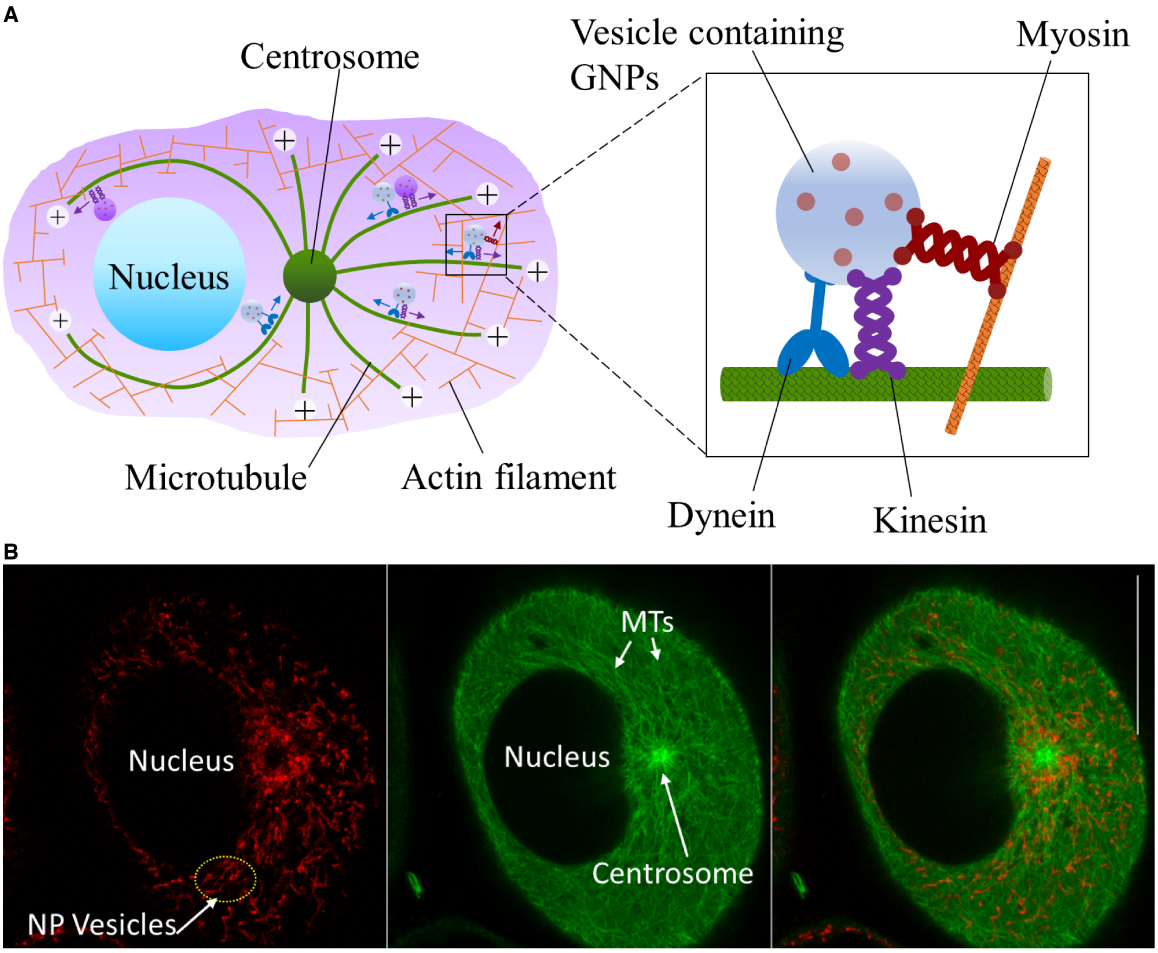


Figure 3.6: **Microtubule transport of nanoparticles.** (A) Transport of vesicles containing the GNPs along the cellular microtubule (MT) network. MTs are long tubulin polymers, often anchored at the centrosome, where transport of vesicles is controlled via motor proteins, dynein and kinesin (inset figure). (B) Live cell imaging of vesicles containing GNPs (marked in red; left), MTs (marked in green; center), and the two images merged(right). Scale bar is 20 μm. Reproduced with permission [218]. Copyright MDPI 2020.

in HeLa, while FBs have 5% of the GNPs found in HeLa (Figure 3.4B). Similar results are seen when adjusting for GNPs per surface area (Figure 3.5A). We have also looked at the ability of these cells to retain the internalized GNPs once the tissue culture media was replaced with fresh media (no GNPs). After 24 hr of incubation with the fresh media, it was found that retention of the $GNP_{PEG\text{-}RGD}$ complexes was higher in cancer cells and CAFs (≈65%) when compared to FBs (≈45%) (Figure 3.5B).

GNP uptake was imaged using darkfield microscopy in combination with HSI as

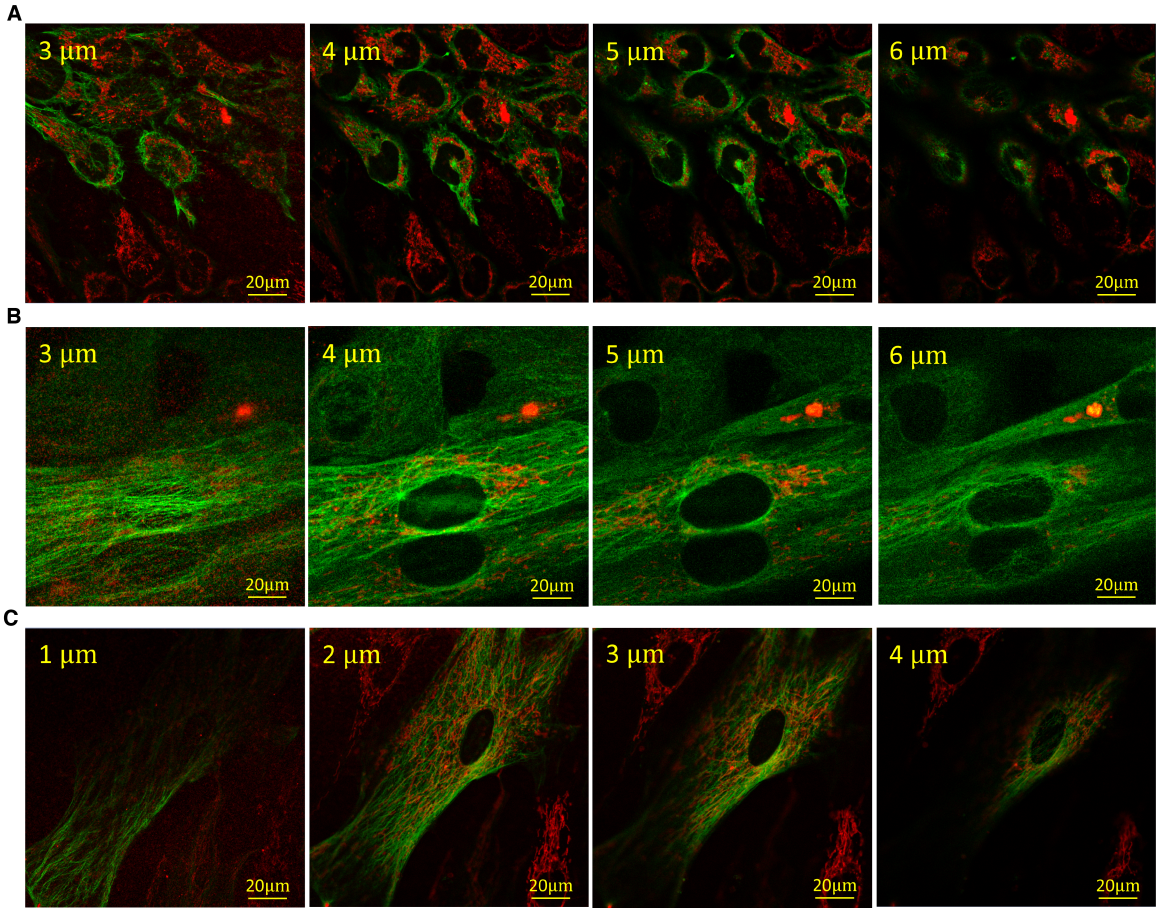


Figure 3.7: **Z-stack using confocal imaging of three cell lines.** (A–C) Confocal images of distribution of GNPs (marked in red) and microtubules (marked in green) in Hela, FBs, and CAFs throughout a z-stack of the cells 24 h after treatment. (A) HeLa cells proliferate quickly, thus many of the cells do not have the microtubule viral stain. GNPs tend to be bundled close to the nuclei. (B) FBs are much larger cells compared to HeLa and have relatively low GNP content. (C) CAFs are comparatively similar in size to FBs, but qualitatively have much larger uptake, gathered around the nuclei and throughout the cell. Scale bar=20 μm. Top left corner is depth in cell for each slice. Reproduced with permission [211]. Copyright Nature, 2020.

seen in Figure 3.4C–E. The combination of darkfield microscopy with HSI imaging allows for a more complete analysis of a sample with GNPs, including mapping of GNPs and verification of the materials presence [219]. Qualitatively, the cells appear to follow the same trend as quantitative data in Figure 3.4A. Furthermore, the GNPs appear to localize closer to the nuclei in the CAFs and HeLa while being more distributed throughout the cells in the FBs. It is known that the vesicles and organelles in the cells are transported along the microtubules (MTs) within the cells. Similarly,

vesicles containing GNPs within the cell have previously been shown to travel along the MTs following uptake [193]. The process by which this occurs is explained in Figure 3.6. Hence, we also looked at the MT network and distribution of vesicles containing GNPs across these three cell lines using confocal microscopy (see Figure 3.7). The MT structure of the cells was tagged with a viral transfection stain containing the GFP while the $GNP_{PEG\text{-}RGD}$ complexes were tagged with the red fluorescent Cy5. These images in Figure 3.7 showcase the increased uptake of GNPs in HeLa and CAFs relative to FBs, which agrees with quantitative data in Figure 3.4.

3.3.3 Effect of radiation on cell proliferation

The gold standard in measuring cell reproductive death following treatment with radiation is the clonogenic assay. The clonogenic assay works by treating cells and letting them grow for the equivalent of 6 doubling times to form colonies. While effective with cell lines such as HeLa that proliferate quickly and in colonies, the FBs and CAFs proliferate very slowly and do not form clear colonies. Thus, we used cell growth curves to calculate the cell survival fraction. The experimental proliferation or relative growth data for HeLa, FBs, and CAFs were plotted in Figure 3.8A-C, respectively. The experimental data was fitted using Eq. 3.1 to generate parameters for determining the survival fraction (see dotted and solid lines in Figure 3.8A–C) [220]. The experimental and fitted data presented in Figure 3.8A–C corresponds to cells treated with radiation while corresponding data for non-radiated cells are presented in Figure 3.9. The relative growth (y) is described by Eq. 3.1 where μ is the growth rate, A is the asymptote or maximum growth, and λ is the lag time.

$$y = \frac{A}{\left\{1 + \exp\left[\frac{4\mu}{A}(\lambda - t)\right]\right\}} \tag{3.1}$$

The values of fitted parameters such as μ and A from growth curves were used to calculate cell doubling time (T_D) as outlined in Eq. 3.2

$$T_D = \ln 2 \cdot \left(\frac{4\mu}{A}\right)^{-1} \tag{3.2}$$

Finally, the survival fraction (SF) was calculated using Eq. 3.3, where T_D is the doubling time and T_{delay} is the delay time.

$$SF = 2^{-\frac{T_{\text{delay}}}{T_D}} \tag{3.3}$$

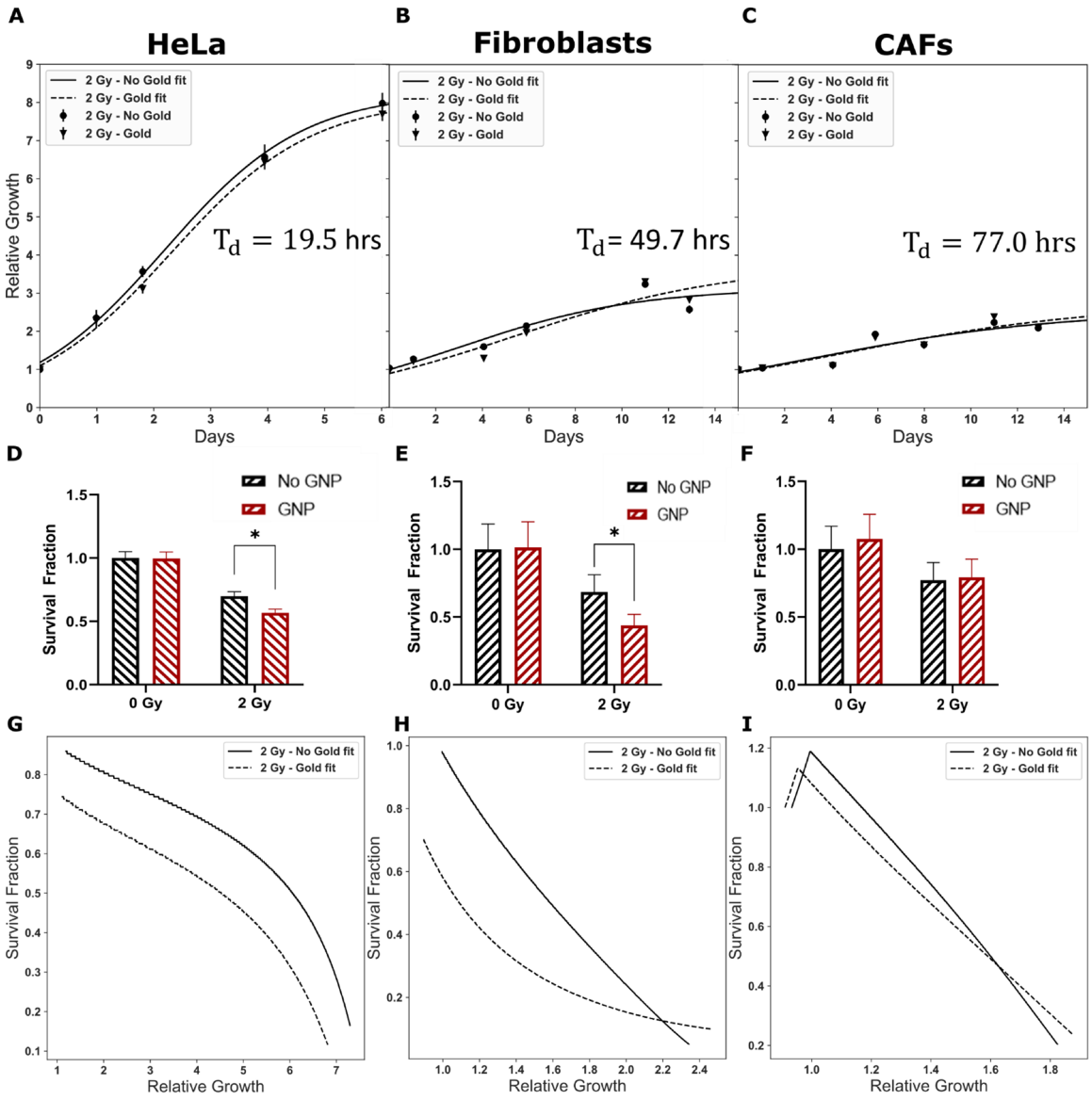
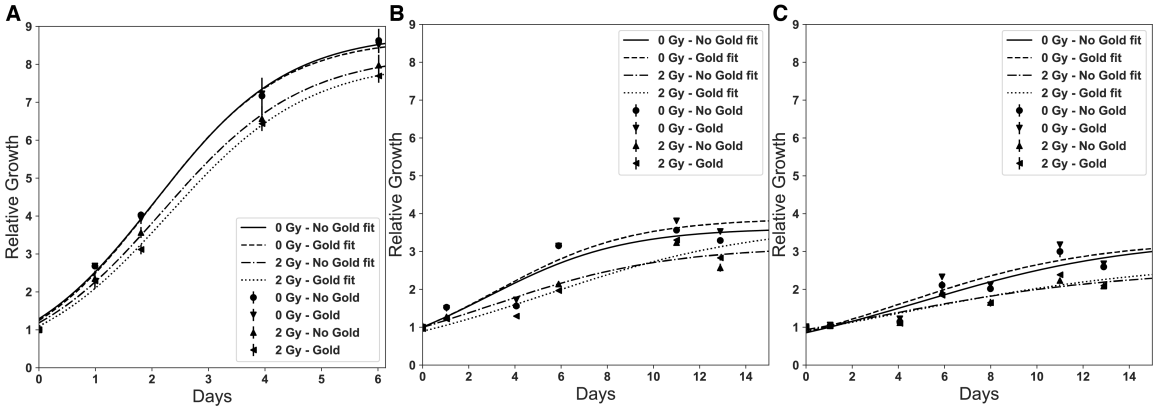


Figure 3.8: **Monolayer Radiation Proliferation Assay** (A–C) Reparametrized logistic curve fit (line) using non-linear least square to collected data (points). (D–F) Survival fraction estimated from delay in growth curve after one doubling time. * represents a significant difference. (G–I) The change in calculated survival fraction as a function of relative growth. A crossover indicates return to control growth. (A, D) HeLa doubling time is estimated from the control curve (T_D=19.5 hr), where the SF was calculated from a delay time estimated at a relative growth of 2.25. (B, E) FBs (T_D=49.7 hr) had a delay time estimated from a relative growth of 1.65, from which the SF was calculated. (D, F) CAFs (T_D=77.0 hr) SF was calculated from a delay time estimated from a relative growth of 1.36. Experiments were repeated three times and the data presented is the average. The error bars represent standard deviation. Reproduced with permission [211]. Copyright Nature, 2020.



D

Sample	HeLa			Fibroblast			CAFs		
	Param 'A'	Param 'λ'	Param 'μ'	Param 'A'	Param 'λ'	Param 'μ'	Param 'A'	Param 'λ'	Param 'μ'
0 Gy - No Gold	8.82 ± 0.40	-0.28 ± 0.21	1.88 ± 0.19	3.62 ± 0.57	-3.06 ± 2.59	0.31 ± 0.13	3.34 ± 1.13	-4.31 ± 2.59	0.18 ± 0.05
0 Gy - Gold	8.69 ± 0.33	-0.24 ± 0.18	1.91 ± 0.17	3.88 ± 0.50	-2.79 ± 1.98	0.33 ± 0.11	3.31 ± 0.93	-4.00 ± 2.80	0.20 ± 0.07
2 Gy - No Gold	8.27 ± 0.27	-0.26 ± 0.14	1.69 ± 0.11	3.13 ± 0.63	-4.73 ± 3.12	0.20 ± 0.08	2.54 ± 0.89	-7.90 ± 4.60	0.12 ± 0.05
2 Gy - Gold	8.10 ± 0.30	-0.18 ± 0.15	1.63 ± 0.11	3.74 ± 1.44	-3.90 ± 2.44	0.20 ± 0.062	2.76 ± 1.23	-7.49 ± 4.04	0.12 ± 0.04

E

	HeLa - T_d [hrs]	**Fibroblast - T_d [hrs]**	**CAF - T_d [hrs]**
0 Gy - No Gold	19.40	49.70	77.00
0 Gy - Gold	19.38	49.29	76.5
2 Gy - No Gold	20.38	63.64	90.25
2 Gy - Gold	20.63	71.2	96.3

Figure 3.9: **Proliferation of cells after radiation.** (A-C) Relative growth patterns for (A) HeLa, (B) NFs, and (C) CAFs. The data is fit with a biologically reparametrized logistic function, where the parameters can be found in (D). Calculated doubling times from the parameters can be found in (E). Reproduced with permission [211]. Copyright Nature, 2020.

T_{delay} is defined as the time taken to reach the same growth in the treated curves compared to control after one doubling time. The calculated survival fraction corresponding with the relative growth can be seen in Figure 3.8D–F. The values corresponding to each cell line's fit are listed in Figure 3.9.

Based on the survival fraction data in Figure 3.8D, we noticed a significant decrease in survival (p=0.0009) of 13.0% when radiated cells are treated with GNPs relative to control for HeLa cells. The cells treated with GNPs do not recover to similar levels as control, as seen in Figure 3.8G. At the same time, FBs (Figure 3.8E) sees a significant drop in the survival fraction (p=0.008) of 24.7% after one doubling time when treated with GNPs in the radiated samples, which eventually recovers to similar levels of the non-GNP radiated sample, after $> 2T_D$. CAFs (Figure 3.8F), on the other hand, have a significant reduction (p=0.002) in survival between radi-

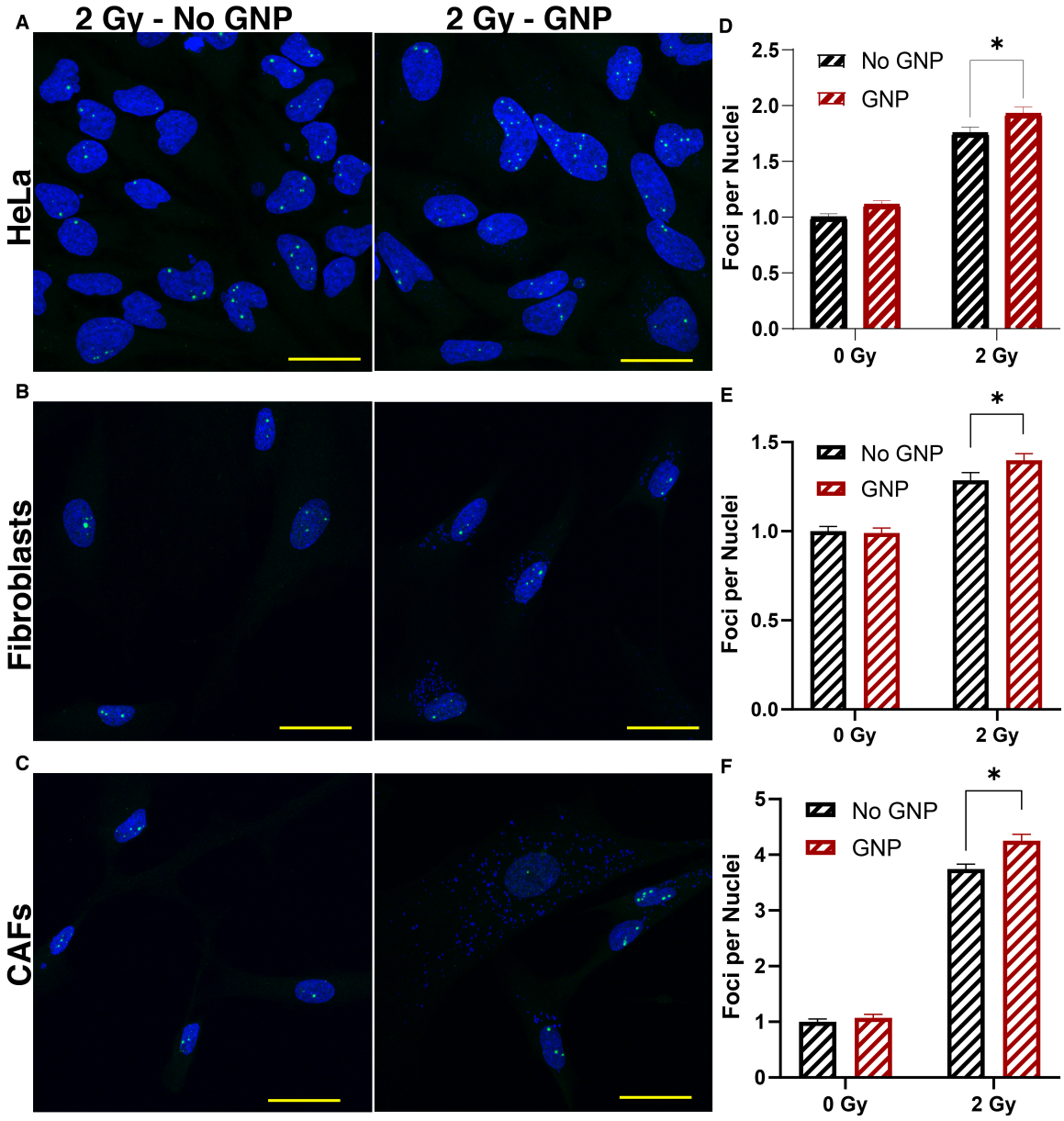


Figure 3.10: **Immunofluorescence assay using 53BP1 foci.** (A-C) Image panels of the three cell lines with 0 Gy and 2 Gy doses, with or without GNPs. The nuclei are marked in blue while 53BP1 are marked in green. The green dots present in the nuclei are the foci, while the excess staining seen outside the nuclei is a non-specific fluorescence signal. (D-F) Quantitative data of the number of foci per nuclei, gathered from a minimum 50 cells. * represents a significant difference. Experiments were repeated three times and the data presented is the average. The error bars represent standard error. Scale bar = 20 μm. Reproduced with permission [211]. Copyright Nature, 2020.

ated versus non-radiated samples, but has no significant difference between irradiated samples treated with and without GNPs. The change in calculated survival fraction in radiated CAFs does not change over time (Figure 3.8I).

3.3.4 Probing the radiation damage using DNA double stand breaks (DSB) assay

We performed an immunofluorescent assay to further validate the data generated from cell proliferation curves in addition to measuring the survival fraction discussed in the previous section. This was done by probing DNA damage using antibodies against two proteins, 53BP1 and γH2AX, which are present in the event of a DNA DSB. All three cell lines were treated as described in section 3.6 and imaged using confocal microscopy (Figure 3.10A–C). For HeLa (Figure 3.10D) and FBs (Figure 3.10E), we see a significant increase ($p=0.00004$; $p=0.01$) of 9.8% and 8.8%, respectively, in the number of 53BP1 foci formed after irradiating with GNPs *vs* without GNPs (control), in agreement with previous results. However, for irradiated CAFs, unlike previously measured, we see a significant ($p=0.004$) increase of 13.5% in the 53BP1 foci formation relative to control, signifying an increase in damage. For all cell lines, there was no significant change in control foci formation when treated with or without GNPs. Results with γH2AX can be seen in Figure 3.11, with the resulting foci per nuclei in Figure 3.126A–C. Furthermore, we verified the presence of the GNPs using pseudo-brightfield imaging from the confocal microscope, which revealed GNP clusters, as seen in Figure 3.12.

3.4 Discussion

One of the major limitations in current RT is that the dose cannot be further increased due to normal tissue toxicity. One of the ways to increase the local dose to the tumour is through the introduction of high Z materials such as GNPs. Hence, one of the goals of this study was to evaluate the GNP uptake and resulting damage due to radiation in normal cells such as FBs compared to cancer cells. It has been reported that FBs are present within TME and they can turn into CAFs to support tumour growth [215, 162, 163]. Hence, if we were to build a successful GNP-based approach to improve current RT, it is necessary to understand the GNP uptake and resulting radiation induced damage across these multiple cell types, not just in cancer cells, as laid out in schematic Figure 3.1. The ultimate goal of using GNPs in RT will be to

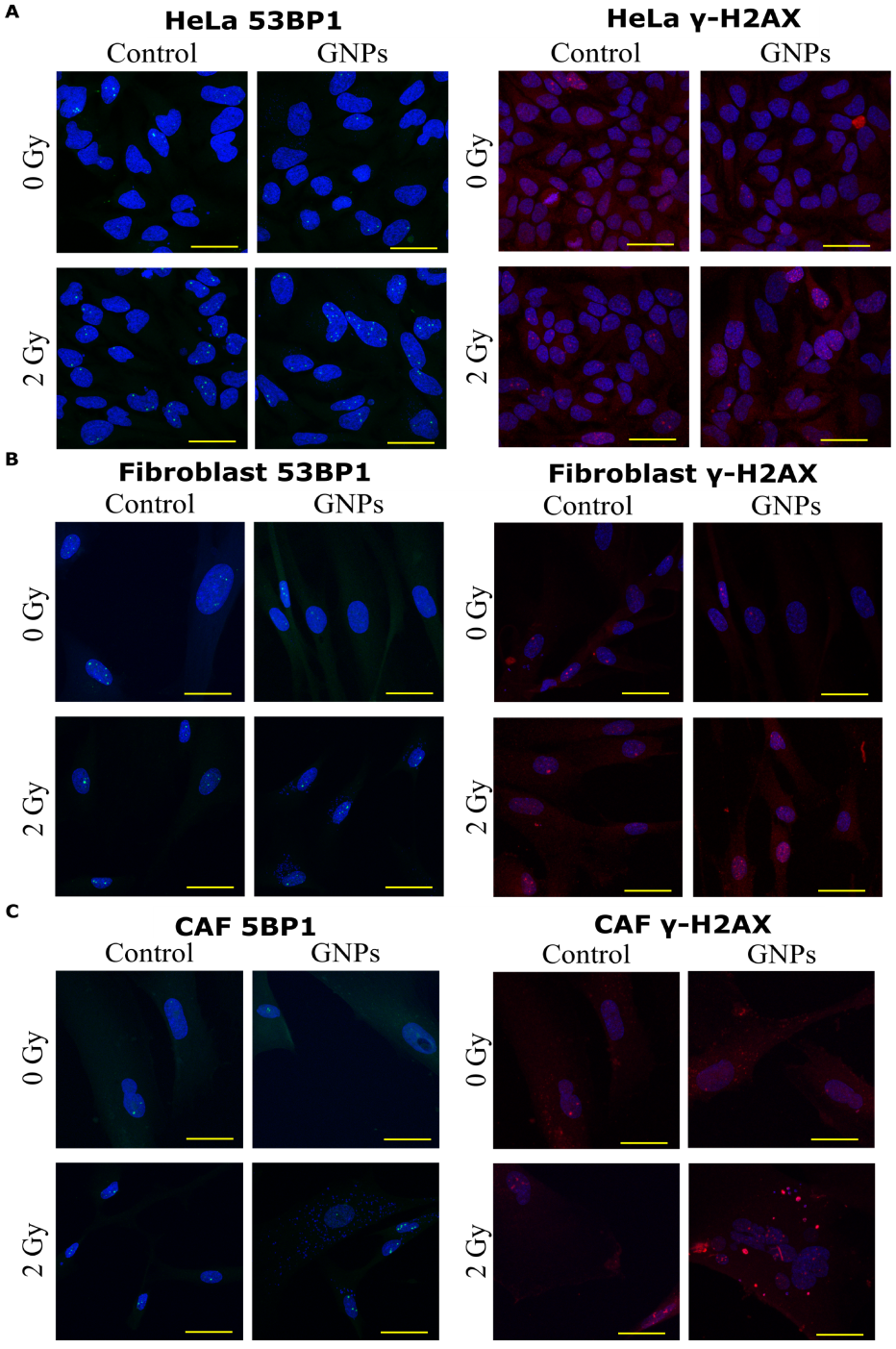


Figure 3.11: **Complete Immunofluorescent Double Strand Break assays.** Example images of control and irradiated (A) HeLa cells, (B) NFs, and (C) CAFs treated with and without GNPs, then stained for 53BP1 and γH2AX foci. The nuclei are marked in blue while 53BP1 foci are marked in green and γH2AX foci are marked in red. Scale bar = 20μm. Reproduced with permission [211]. Copyright Nature, 2020.

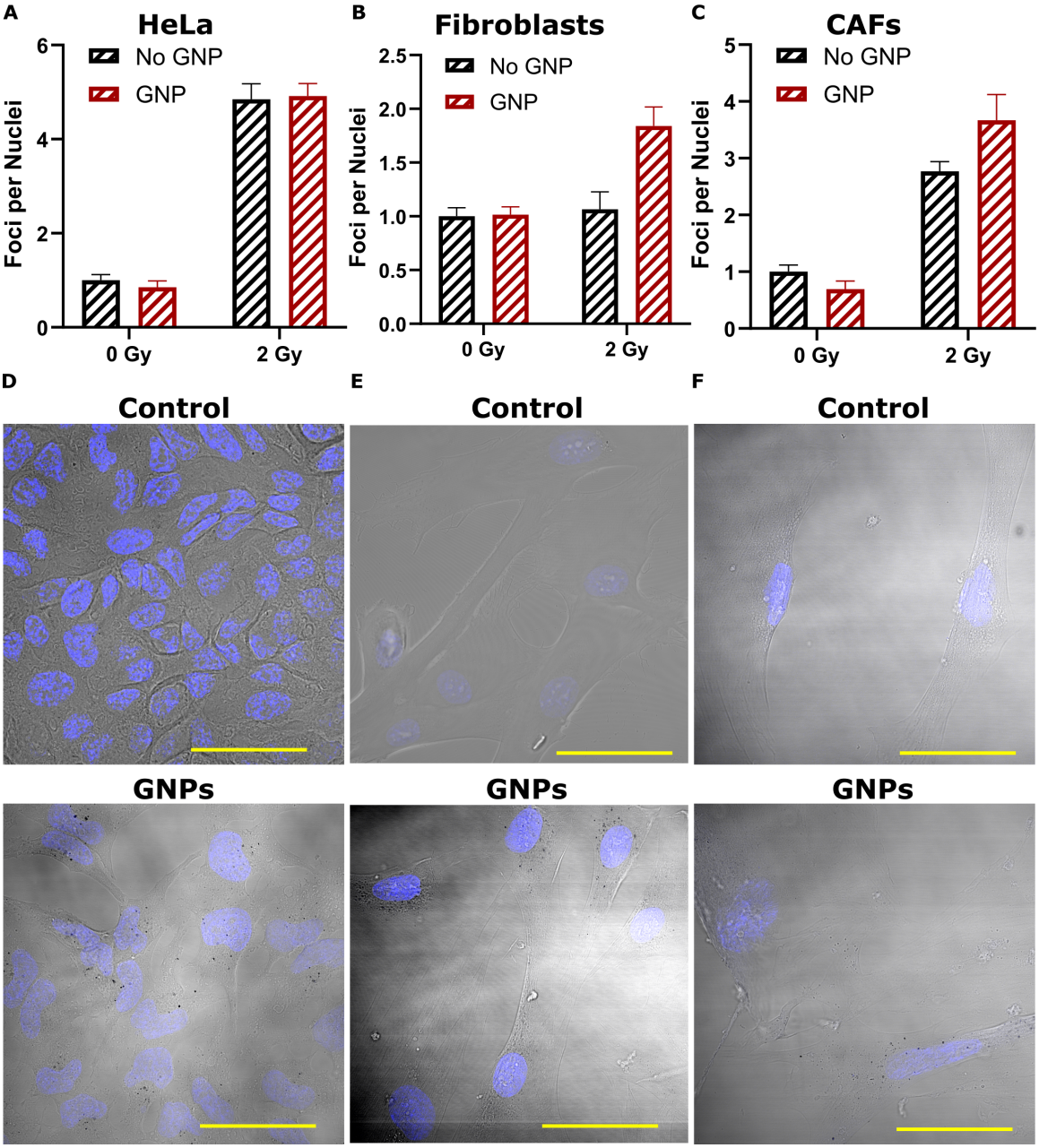


Figure 3.12: **Immunofluorescent assay and confirmation of encapsulated gold nanoparticles.** Quantification of γH2AX Foci from a minimum of 50 different imaged nuclei for (A) HeLa, (B) FBs, and (C) CAFs. (D-F) are pseudo brightfield images of cells with and without gold for (D) HeLa, (E) FBs, and (F) CAFs. In the bottom images, the black dots present are clusters of GNPs aggregated in the cells. Scale bar = 20 μm. Reproduced with permission [211]. Copyright Nature, 2020.

reduce the tumour cells while preserving FBs and minimizing the activity of CAFs.

Size and surface properties of GNPs play a significant role in their cellular uptake,

tissue penetration, and residence time. GNPs of size 50 nm have previously been shown to have the best uptake in a monolayer of cells [193]. However, when moving to a more complex environment such as a 3D *in vitro* structure like spheroids, the use of smaller GNPs of sizes ≈20 nm have been shown to have improved uptake and penetration when compared with larger NPs, especially those of size 100 nm or larger [221]. Furthermore, the use of GNPs with PEG and RGD of size 15 nm and 50 nm have been tested previously, and due to the addition of the moieties, GNPs of smaller size had a more optimum uptake as can be seen in Figure 3.5C–D. Thus, towards the goal of optimizing the use of GNPs in a more complex environment, we chose smaller GNPs of diameter 15 nm functionalized with both PEG and RGD peptide. The GNP complex ($GNP_{PEG\text{-}RGD}$) was characterized fully as shown in Figure 3.2 and 3.3. PEG is an important molecule to be conjugated to the NP surface as it has been shown to improve the stabilization and circulation of macromolecules, facilitating better tumour targeting [222]. However, previous studies have shown that the PEG reduces the uptake of GNPs, and thus a peptide containing integrin binding domain RGD was introduced to counteract this effect. The RGD peptide has been shown to improve endocytosis as well as effectively target tumours. HeLa has previously been shown to highly express $\alpha_v\beta_3$, an RGD-specific integrin, and may express at least 2 others, $\alpha_5\beta_1$ and $\alpha_v\beta_5$ [223]. Further, FB cell lines have been shown to have abundant surface expression of integrins, of a particularly high nature compared to other cells [224]. CAFs have largely been shown to express many different RGD-specific integrins on their surface, partially as a means of crosstalk between cancers cells. However, exact differences in integrin expression between cancer associated cells and FBs used in this study are not fully known yet.

Our *in vitro* studies were conducted at a GNP concentration of 0.2 nM or 0.05 μg/g, which can be achieved *in vivo*. It is also important to note that such concentrations in tumour tissue led to significant GNP-mediated radiosensitization *in vivo* [97, 98]. Our results show very promising outcomes in the use of GNPs in RT. For example, normal cells (FBs) had the least uptake of GNPs compared to cancer associated cells (HeLa and CAFs). According to Figure 3.4C–E, size and shape of these three cell lines were different from each other. We also estimated the volume of each cell type using a Z2 Coulter Counter and Figure 3.4B represents number of GNPs per unit volume. The cancer cell line, HeLa, appears to have a denser concentration of GNPs compared to CAFs. This could be due to the overall smaller size of HeLa compared to CAFs. Based on previous research, different cell lines have previously been

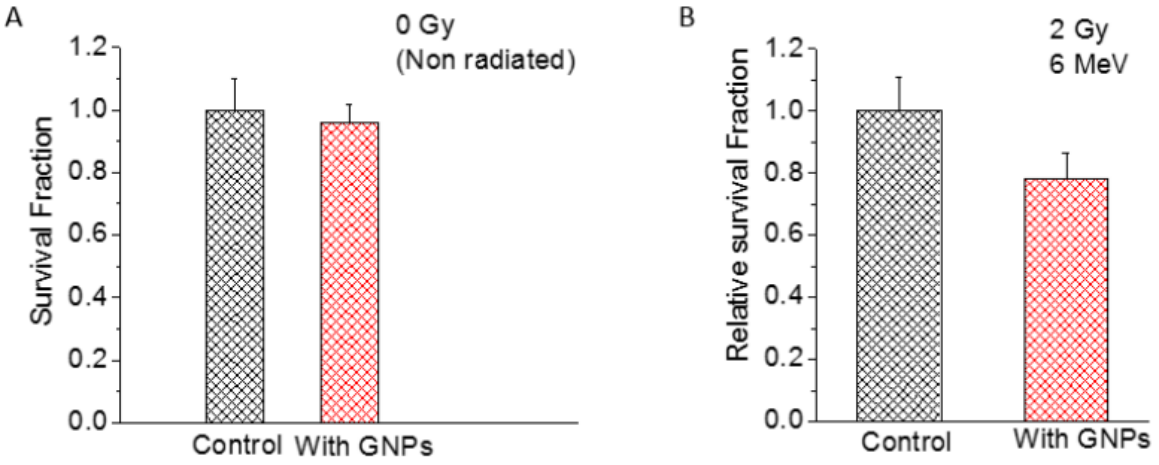


Figure 3.13: **Experimental clonogenic assay result for HeLa.** (A-B) Comparison of survival fractions for non-radiated and radiated cells, respectively. Reproduced with permission [211]. Copyright Nature, 2020.

shown to alter the efficacy of endocytosis of GNPs, explaining some of the measured difference [209].

Much of the GNP-mediated radiation dose enhancement research has been focused just on cancer cells. Hence, one of the major goals of this study was to assess GNP-mediated radiation damage in other cells within TME such as FBs and CAFs. The clonogenic assay is the gold standard in measuring the radiation induced cell damage. The survival fraction generated using clonogenic assay for HeLa is given in Figure 3.13. However, it was not possible to generate colonies for measuring survival fraction in the case of FBs and CAFs due to their longer doubling time at 0 Gy (T_D (FBs) = 49.7 hr and T_D (CAF) = 77.0 hr). Hence, we used cell proliferation data to generate parameters to calculate the survival fraction, as seen in Figure 3.8A–C. Control data for all cell lines and their respective fit parameters can be found in Figure 3.9. There was a significant decrease of 13.0% in survival (p=0.0009) corresponding to HeLa cells treated with both GNPs and radiation compared to cells just treated with radiation (control). Most importantly, this decrease in survival was maintained throughout the entire growth curve resulting in a lower survival after few doubling times (see Figure 3.8G). This could be very important in fractionated RT which is heavily used in the clinic. This is one of the reasons we chose a fractionated dose of 2 Gy for our experiments. We saw very promising data for FBs (Figure 3.8E,H) where there was a significant drop in the survival fraction (p=0.008) of 24.7% due to GNP-mediated RT vs control after one doubling time, which eventually recovered to similar levels of the

control irradiated sample, after $> 2T_D$. This could be important since their survival after the treatment could suppress the progression of the tumour. This highlights the ability of normal tissue to repair, given time, which is the basis for fractionated RT. Further, the idea of normal tissue recovering is also utilized in chemotherapy, via different dose schedules. In contrast, CAFs (Figure 3.8F,I) had a significant reduction (p=0.002) in survival between radiated vs non-radiated samples but has no significant difference between irradiated samples treated with and without GNPs. It has been shown that the proliferation of CAFs is inherently very low. Hence, the use of proliferation data may be not that relevant to measure radiation induced damage. Therefore, we used DNA DSBs assay to probe the radiation induced damage, especially in CAFs.

Mapping of DNA DSBs is widely used as another measure of evaluation of the radiation induced damage. We used antibodies against repair proteins such as 53BP1 and γH2AX to measure the extent of radiation induced damage 24 hr post-radiation. By measuring foci formation 24 hr after treatment with ionizing radiation, residual damage is captured, representing DNA damage that is unrepaired and likely to lead to loss of clonogenic potential [225]. Furthermore, the number of foci can depend on the type of damage as well as the damage repair mechanism. The 53BP1 foci signal non-homologous end joining (NHEJ) as a repair mechanism, while a lack of the 53BP1 but presence of a γH2AX foci could signal homologous repair (HR) in the S/G2 phase [226]. This could lead to a varying number of γH2AX foci compared 53BP1 foci. Further to this point, during S phase, there is a pan-nuclear γH2AX speckle that can form, leading to miscounting of these foci. Meanwhile, during the S-phase, 53BP1 can still act, via NHEJ, in a H2AX independent manor, suggesting that 53BP1 can function in DNA repair independently of H2AX [227]. High expression of γH2AX can also be suggestive of defective DNA repair pathway and/or genomic instability, whereas 53BP1 is a conserved checkpoint protein DNA DSB sensor. For these reasons, solely 53BP1 data is discussed here while γH2AX data has been added to Figure 3.11 and 3.12A–C. For all three cell lines studied, there was a statistically significant difference in number of foci per cells after 24 hr of radiation for cell treated with GNPs plus RT vs RT alone (Figure 3.10). For example, the increase in number of foci for HeLa (Figure 3.10D) and CAFs (Figure 3.10E) was 9.8% and 13.5%, respectively while it was 8.8% for FBs. The results of the DSB foci assay correlates well with the difference in uptake of GNPs in the different cell lines, with CAF having the largest increase in DSBs while having the most GNPs, followed similarly by HeLa

and FBs. The number of GNPs in a cell during radiation is directly correlated to the dose enhancement factor, defined here as the ratio of foci formed in GNP-treated irradiated cells to control irradiated cells. Furthermore, even when correcting for cell volume, where HeLa has a larger ratio of GNPs/volume, the total quantity is arguably more important. As Figure 3.4E showcases, the GNPs tend to cluster closer to the nuclei in the CAFs which may improve treatment efficacy: the more GNPs gathered near the nuclei, the larger the resulting dose enhancement upon radiation.

Despite the increase of DNA damage in the irradiated CAFs (Figure 3.10), there is no measurable difference or delay in the proliferation of the CAFs treated with GNPs plus RT vs RT alone over time (Figure 3.8). This may be a result of CAF cell lines responding to radiation differently that other cell lines. Hellevik *et al.* found that using stereotactic ablative radiotherapy on CAFs resulted in an increase in 53BP1 foci, but no increase in cell death, even with increasing doses. There was, however, an induced senescence response, as well as compromised migratory and invasive ability with larger doses, correlating with increased 53BP1 foci [184]. Resazurin, the proliferation assay used in this experiment, is directly correlated with cell number. Thus, our proliferation assay may be showing the GNP treated CAFs entering senescence at the same rate as irradiated control, while actual cell death did not occur in either sample. However, despite the lack of cell proliferation, there was a radiosensitization effect present due to the measured increase in DSBs. Increase in DNA DSBs could be due to the enhancement in the absorbed dose due to GNPs. Further experiments are required to investigate how the observed increase in DNA DSBs in CAFs affect cancer cell growth in the TME. Understanding of the tumour stroma on GNP-mediated radiosensitization is critical to fully exploit the benefits of this novel therapeutic approach in future cancer treatments. We used a simplified monoculture for this study, in order to better understand important individual components of the TME. In the future, testing of the tumour cells, CAFs, and FBs with GNP-mediated radiotherapy will be done in co-culture. Further, future studies will involve engineering of a 3D models, such as spheroids, with both cancer cells and CAFs.

Targeting of the cancer cells is still the main priority when using GNPs with RT; however, CAFs have been shown to be largely important to the growth and metastasis of the tumor. This study suggests that CAFs have a larger DNA damage response due to the inclusion of GNPs into radiation treatment and thus could prove to be a useful target in the future. An improved tumour response due to selective targeting of cancerous tissue such as CAFs over normal tissue will allow for GNPs to be an

effective tool in radiotherapeutics.

3.5 Conclusions

The use of GNPs has been largely explored as a radiation dose enhancer which can effectively increase the dose to the tumour while sparing normal tissue. GNPs have been shown to successfully increase the deposited dose at clinically relevant energies. However, the introduction of the TME with stromal cells such as CAFs adds complexities that cannot be ignored if the goal is to eradicate the malignancy *in vivo* before proceeding to clinical trials. Thus, towards removing this obstacle, the uptake of GNPs into CAFs *in vitro* was measured and compared to that of normal cells and cancer cells. There is an observed increase in the uptake of GNPs into CAFs relative to the other cell lines, which translated to an increased dose enhancement into CAFs vs HeLa and FBs as measured with a 53BP1 and γH2AX foci immunofluorescent assay after irradiation with a 2 Gy dose. Moving towards a 3D *in vitro* model such as spheroids could prove beneficial to elucidating the effect of radiation on CAFs further effects. Overall, this study unveils the feasibility of using GNPs as a tool to cross barriers within the TME to yield a better therapeutic outcome in future cancer RT. The next step in this work is the introduction of a more complex environment, such as a 3D spheroid.

3.6 Materials and methods

3.6.1 Cells and materials

HeLa, fibroblast (Hs. 895.Sk), and cancer associated fibroblasts (Hs 895.T) were purchased from the American Type Culture Collection (ATCC) and the catalogue numbers are CCL-2, CRL-7636, and CRL 7637, respectively. All cell lines were cultured in high glucose Dulbecco's Modified Eagle Medium (DMEM; Gibco) supplemented with 10% fetal bovine serum (FBS; Gibco), 1% penicillin/streptomycin (Gibco), and 4 mM of GlutaMax (Gibco), and trypsin–EDTA(Gibco) was used for cell dissociation. For confocal experiments, FluoroBrite DMEM (Gibco) was supplemented with 10% FBS and 1% penicillin/streptomycin after staining with CellLight Tubulin-Green Fluorescent Protein (GFP; BacMam 2.0, Thermo-Fisher), while the cells were grown on 3 cm coverslip-bottom dishes supplied by MatTek. Cells were fixed using paraformaldehyde (PFA; Sigma Aldrich). For synthesis of GNPs, chloroauric acid ($HAuCl_4 \cdot 3H_2O$; Sigma

Aldrich) and sodium citrate tribasic dihydrate ($HOC(COONa)(CH_2COONa)_2 \cdot 2H_2O$; Sigma Aldrich) were used. Both PEG-thiol and PEG-thiol-Cy5 were purchased from Nanocs. The peptide Cys-Lys-Lys-Lys-Lys-Lys-Lys-Gly-Gly-Arg-Gly-Asp-Met-Phe-Gly was purchased from AnaSpec. For proliferation assays, plates were covered with Breathe-Easy sealing membranes (Sigma-Aldrich) and treated with PrestoBlue (Invitrogen). For immunofluorescence assays, primary antibodies anti-phospho-Histone H2A.X (Ser139; Millipore Sigma) and phospho-53BP1 (Ser1778; Cell Signaling Technology) and secondary antibodies donkey anti-Mouse, Alex Fluor 647 (ThermoFisher) and donkey anti-Rabbit, Alexa Fluor 488 (ThermoFisher) were employed. Bovine serum albumin (BSA; Invitrogen), Triton-X (Sigma-Aldrich), and Tween-20 (Sigma-Aldrich) were also used in the immunofluorescence assay.

3.6.2 Synthesis, surface modification, and characterization of Gold Nanoparticles

To prepare spherical GNPs of approximately 15 nm in diameter, a citrate reduction method was used [228]. On a hotplate, 300 μL of 1% chloroauric acid was added to 30 mL of double distilled water and brought to 100 ^{o}C while spinning vigorously. Once boiling, 1 mL of 1% sodium citrate tribasic dihydrate was added to the mixture. Upon addition, the solution's color changes from clear to black to a ruby red, signifying formation of GNPs. The solution was then brought back to room temperature while spinning.

The GNPs were PEGylated using 2 kDa PEG-thiol at a ratio of 1 PEG molecule per nm^2 of surface area, assuming a perfect sphere. For each 15 nm PEGylated GNP (GNP_{PEG}), 707 PEG molecules were added to the GNP solution and mixed. For confocal imaging, $GNP_{PEG\text{-}Cy5}$ was synthesized with a mix of the 2 kDa PEG and a 3.2 kDa PEG-thiol-Cy5 in equal proportions, with a total of 707 PEG per GNP. Both complexes were than tagged with a peptide containing integrin binding domain RGD (Cys-Lys-Lys-Lys-Lys-Lys-Lys-Gly-Gly-Arg-Gly-Asp-Met-Phe-Gly) at 1 molecule per every 2 PEG molecules. A schematic of the $GNP_{PEG\text{-}RGD}$ complex can be seen in Figure 3.2A.

GNPs, GNP_{PEG}, and $GNP_{PEG\text{-}RGD}$ complexes were characterized via ultraviolet–visible (UV–VIS) spectrometry (Perkin Elmer λ 365 Spectrophotometer) for size and concentration estimates, as well as dynamic light scattering (DLS) and ζ-potential (Anton Paar LiteSizer 500) for measurement of the hydrodynamic radius and surface

charge. Stability of the $GNP_{PEG\text{-}RGD}$ was measured using DLS in phosphate buffered saline.

Dynamic Light Scattering

The hydrodynamic diameter is the measurement of the diameter of a hypothetical hard sphere that diffuses with the same speed as the particle being measured, in this case GNPs, and can be measured using DLS. DLS is a useful technique to measure a large population of NPs, as well as confirm conjugation of peptides to the surface. The addition of moieties to the surface of particles theoretically increases the hydrodynamic diameter.

DLS works by measuring the random Brownian motion of particles in a solution. As the movement is random, they particles are all uncorrelated. This motion can be modelled using the Stokes-Einstein equation (Equation 3.4), where D is the translational diffusion coefficient (speed of the particles), k_B is the Boltzmann constant, T is the temperature, η is the dynamic viscosity, and D_H is the hydrodynamic diameter.

$$D = \frac{k_B \cdot T}{3\pi\eta D_H} \tag{3.4}$$

As light from a laser scatters off the randomly moving particles, it can be detected at a certain angle over time by a fast photon counter. This signal will have random fluctuations according to the speed of the particles and how fast they diffuse. Smaller particles will show larger fluctuations than larger particles, which can be measured by measuring the intensity of the beam shifted be a delay time τ. By altering τ, a correlation function which relates to the speed of the particles can be formed and fit to a Cumulant algorithm to find the diffusion coefficient and thus the hydrodynamic diameter.

DLS in this work was done using an Anton Paar LiteSizer 500 with samples in 1 cm path length using a quartz small volume cuvette. The light source is a laser light of wavelength 658 nm. The average of three measurements was used for the hydrodynamic diameter.

ζ Potential

The ζ potential is a physical property that is exhibited by a particle in a suspension, such as a fluid. When the material of the particle comes in contract with the liquid, the functional groups on the surface will react, forming a surface charge. This surface

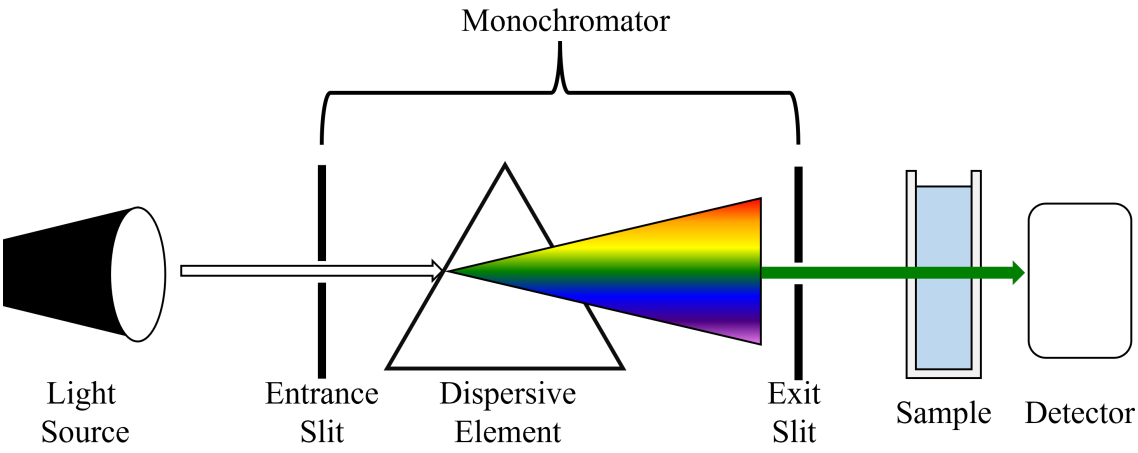


Figure 3.14: **Ultraviolet-visible spectrometer schematic.** A light source, either deuterium or tungsten, is shot through a grating that disperses the light which is focused onto an exit slit into the sample.

charge then attracts oppositely charged ions which arrange themselves in an electrochemical double layer. The ζ potential is defined as the sum of the initial surface charge that forms and the resulting accumulated layer. This is a useful measure as the ζ potential is a marker of stability in bare GNPs and can be used to confirm conjugation of moieties like PEG due to alteration in measurements.

This can be measured using electrophoretic light scattering, which measures the speed of the particles in an electric field. This was done using the Anton Paar LiteSizer 500 with an Anton Paar Omega cuvette. The average of three measurements was used for the ζ potential.

Ultraviolet-visible spectroscopy

A UV-Vis spectrometer was used to measure the absorbance of ultraviolet or visible light by a sample by performing a scan over a range in the electromagnetic spectrum; UV region is equal to 190-400 nm, and visible 400-800 nm. UV-VIS is able to measure the LSPR, which is described in Section 1.4.1, and seen in Figure 3.14. UV-Vis measurements were performed using Perkin Elmer λ 365 Spectrophotometer with wavelength range of 400 to 600 nm and a resolution of 0.05 nm. 1 mL of GNP sample was measured in a 1 cm path length quartz low-volume cuvette. The light source was provided by deuterium and tungsten and covers 200-800 nm in the visible and near ultraviolet radiation spectrum. Output is focused on a diffraction grating that splits

incoming light into colours of different wavelengths.

A cuvette of deionized water was used as a reference signal. For each wavelength the intensity of light passing through the sample is measured (I) as well as reference cell (I_0). If I is less than I_0, the sample has absorbed some light as seen in Equation 3.5. The detector can measure this by converting the incoming light into current, relative to the intensity.

$$A = \log_{10} \frac{I_0}{I} \tag{3.5}$$

Using the Beer-Lambert Law, the absorbance can be related to the concentration of a substance by Equation 3.6, where A is absorbance, l is optical path length, C is concentration of the solution, and ϵ is the molar extinction coefficient.

$$A = \epsilon C l \tag{3.6}$$

To calculate the molar extinction coefficient, Mie theory can be utilized. Mie theory is a solution of Maxwell's equation relating to absorbance and scattering, which allows calculation of extinction efficiencies of smaller metal nanoparticles [217]. A look up table can be used to calculate the size, relative to the ratio of their absorbance at the LSPR (A_{spr}) and the absorbance at 450 nm (A_{450}). With the size discovered, the extinction coefficient can be found from another look up table. GNPs of size 15 nm, for example, have $\epsilon = 2.18 \times 10^8$ $M^{-1}cm^{-1}$ while 50 nm GNPs have $\epsilon = 9.92 \times 10^9$ $M^{-1}cm^{-1}$. The concentration can be found using Equation 3.7.

$$C = \frac{A_{450}}{\epsilon_{450}} \tag{3.7}$$

Darkfield imaging and hyperspectral Imaging

The $GNP_{PEG\text{-}RGD}$ complex were imaged using darkfield microscopy and hyper spectral imaging (HSI) (CytoViva). Darkfield microscopy in combination with HSI allow for spectral information to verify the presence of GNPs. Darkfield microscopy is a useful technique for imaging non-labelled nanostructures such as GNPs in tissue, due to the microscopes high signal-to-noise performance. To view a specimen in dark field, a condenser lens ensures that only light that is scattered by objects on the slide make it to the objective. As GNPs are highly scattering, they will have a very large signal-to-noise ratio compared to tissue and can be easily visualized.

Alternatively, the use of HSI allows for a hyper-spectral cube to form from multiple wavelengths per pixel. This results in a 3D data-set (x,y,λ), where λ is the spectral information for each pixel. Using these spectra, we can verify the presence of specific materials, like GNPs, as each material has a specific spectrum, like a fingerprint. Thus, the combination of darkfield microscopy to visualize the GNPs and HSI to confirm their presence is a powerful combination.

Transmission electron imaging

Furthermore, to verify polydispersity and size distribution of the $GNP_{PEG\text{-}RGD}$ complex, transmission electron microscopy (TEM) (Hitachi HF-3300 V) images were acquired. To prepare measurement samples, GNPs were left to dry on a grid that was made of copper and carbon over night. The samples were then carefully placed in the microscope. The average diameter of the core of the GNPs was calculated using ImageJ software.

3.6.3 Cellular uptake and retention of GNP complex

Incubation with $GNP_{PEG\text{-}RGD}$ was completed at a concentration of 0.2 nM for all stated experiments. All three cell lines were plated at a density of 1×10^4 cells per well in a 6-well plate. Once the cells were adhered, they were all incubated with media containing $GNP_{PEG\text{-}RGD}$ at 37 ^{o}C with 5% O_2. After 24 hr of incubation, the cells were then rinsed with phosphate buffered saline (PBS) three times and trypsinized using 0.25% trypsin–EDTA for 5 min. The cells were counted using a Coulter Counter (Z2 Coulter; Beckman Coulter) for GNP quantification per cell. The average volume per cell was given from a distribution of the population of cells measured using the Z2 Coulter Counter. For the retention study, at 24 hr after incubation with $GNP_{PEG\text{-}RGD}$, the media was replaced and incubated for 24 hr.

To measure the gold content for each condition, the cells were treated with 65% aqua regia (3:1 ratio of HCl:HNO_3(VWR)) in a 200 ^{o}C mineral oil bath for a minimum 1 hr. Small amounts of hydrogen peroxide were added afterwards to ensure complete digestion of the cells and GNPs. These samples were then diluted down to 2.5% v/v acid content in deionized water and the gold content was quantified using inductively coupled plasma mass spectrometry (ICP-MS; Agilent 8800 Triple Quadrupole).

Calculation of the GNP concentration from the absolute number of Au atoms was done using the following equations:

$$\frac{\text{Number of Au Atoms}}{\text{GNP}}[\text{U}] = \frac{\text{Number of atoms per unit cell} \cdot \text{Volume of GNP}}{\text{Volume of unit cell}} \tag{3.8}$$
$$= 4 \cdot \frac{\frac{4}{3}\pi(\frac{D}{2})^3}{a^3}$$
$$= \frac{2}{3}\pi\Big(\frac{D}{a}\Big)^3$$

where D = core diameter of the GNP, a = length of a unit cell, 0.408 nm. GNPs that are synthesized using the citrate reduction method assemble into a face-centered cubic structure, which as a lattice containing 4 atoms per unit cell. This assumes a homogenous size of GNPs, which is verified through TEM imaging.

Using this, the number of GNPs per sample is calculated from:

$$= \text{conc. measured}[\frac{\text{g}}{\text{L}}] \cdot \text{volume[L]} \cdot \frac{1}{\text{molar weight of Au}}\Big[\frac{mol}{g}\Big] \cdot \text{N}_\text{A}\Big[\frac{\text{Au}}{\text{mol}}\Big] \cdot \frac{1}{\text{U}}\Big[\frac{\text{GNP}}{\text{Au}}\Big] \tag{3.9}$$

where N_A is Avogadro numbers. The number of GNPs per cell is then calculated by dividing the number of GNPs by the number of cells, assuming a homogenous distribution of GNPs in the cell population.

3.6.4 Preparation of cells for darkfield and confocal imaging

To prepare cells for darkfield imaging, all cell lines were plated in a six-well plate with glass coverslips placed on the bottom of each well. The cells were then treated as described previously using $\text{GNP}_{\text{PEG-RGD}}$ with a 24 hr uptake time point and a 24 hr retention time point. Upon completion of each experiment, the cells were rinsed three times with PBS and fixed using 4% PFA for 20 min at 37 ^{o}C. The cover slips were then removed from each well and mounted to a glass slide using Prolong Glass Antifade Mountant. Each sample was imaged using darkfield microscopy and HSI (CytoViva) under a 60X objective.

Live-cell imaging of the distribution and uptake of the $\text{GNP}_{\text{PEG-RGD}}$ complex was performed using confocal microscopy (Zeiss LSM 980) using a 60X oil immersion lens. $\text{GNP}_{\text{PEG-RGD}}$ complexes had PEG-Cy5 (excitation 633 nm, emission 650 nm) conjugated as previously mentioned. To see general structure of the cell, microtubules were stained with a viral transfection stain (CellLight Tubulin-GFP), which contains DNA coding for an α-tubulin/GFP construct.

To prepare cells for live-cell confocal imaging, cells were plated on 3 cm coverslip-bottom dishes in FluoroBrite media. The cells were incubated in the viral stain for $>$ 24 hr prior to treatment with fluorescent $GNP_{PEG\text{-}RGD}$. After incubation with GNPs, the cells were imaged after 24 hr of uptake and after 24 hr of retention. All conditions including acquisition settings used between experiments was maintained constant.

3.6.5 Radiation treatment

Cells were plated and incubated with GNPs 24 hr prior to any radiation treatment. The experimental setup can be seen in Figure 3.15. Treatment planning was done using Eclipse (Varian Medical Systems). The plates were then placed between two 30 cm $\times$ 30 cm $\times$ 5 cm solid water blocks at isocenter of a 6 MV medical linear accelerator (Varian TrueBeam). A single field was used for treatment, with a 180^o gantry rotation, as the air gap between the bottom of the plate and media is much less than the air gap between the media and the top of the plate. A field size of 28 cm $\times$ 28 cm field was used and the cells were placed directly at a source-axis distance (SAD) of 100 cm. The dose rate was set to 600 MU/min with a reference point at isocenter at a depth of 5.0 cm. To find the amount of monitor units (MUs), we used Equation 3.10

$$\begin{aligned} \text{MU setting} &= \text{prescribe dose (Gy)} \times \text{dose coefficient}\left(\frac{\text{MU}}{\text{Gy}}\right) \\ &= \frac{\text{prescribed dose}}{\text{RDR} \times \text{S}_\text{c} \times \text{S}_\text{p} \times \text{TMR}} \end{aligned} \tag{3.10}$$

where RDR is the reference dose rate of 1 cGy/MU, TMR is the tissue maximum ratio with a 6 MV beam, 28$\times$28cm field, and a depth of 5 cm, equal to 0.925. S_c is the collimator scattering factor in this field, of 1.038, and S_p is the phantom scatter factor in this field, of 1.032. Altogether, the dose coefficient is equal to 100.92 MU/Gy. For this work, the cells were given a 2 Gy photon dose, equivalent to 202 MU. To ensure consistency, control cells were brought to the linear accelerator but not irradiated. All set-up parameters can be seen in Table 3.1.

3.6.6 Doubling time assay

Cells were plated at a density of 2.5×10^3 to 10×10^3 cells/well in black-walled 96-well plates and covered with a breathable membrane to reduce evaporation effects.

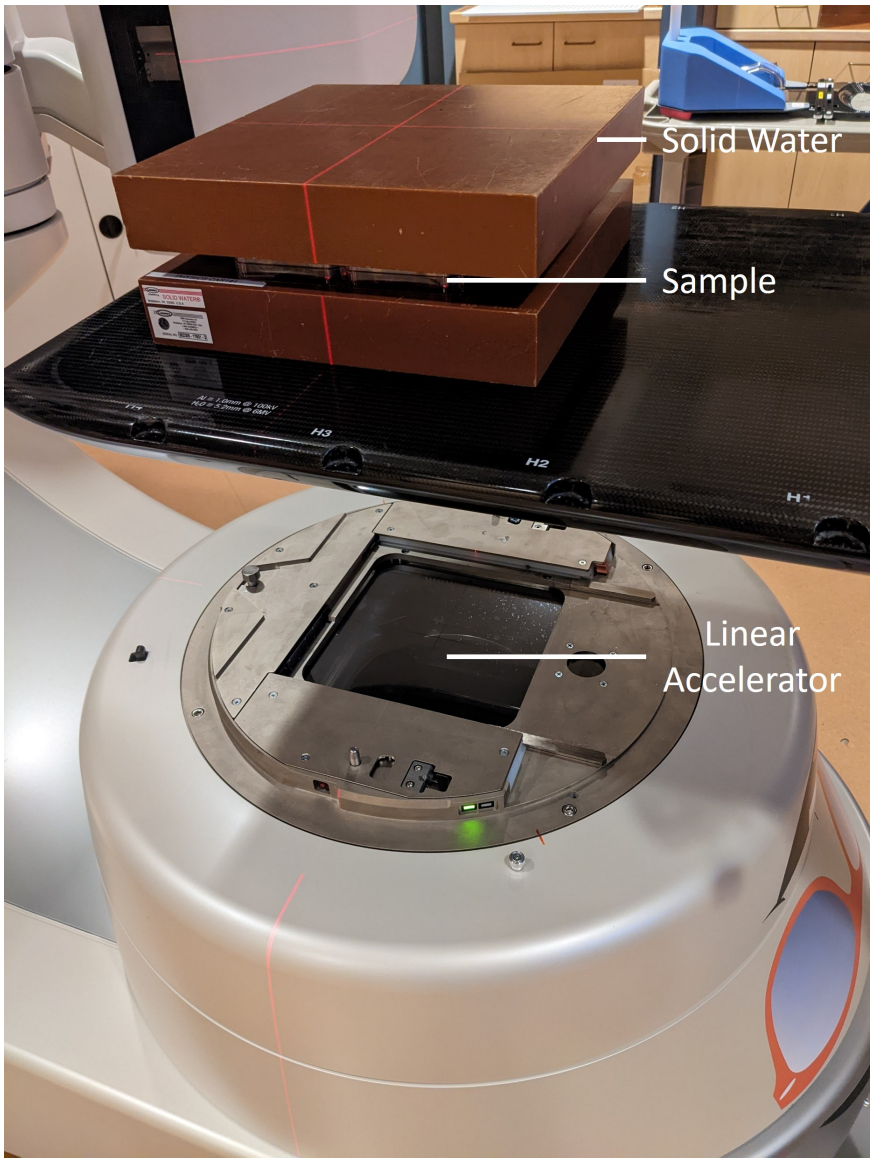


Figure 3.15: **Experimental linear accelerator clinical setup** Radiation setup with a clinically relevant linear accelerator with cells in between two 5 cm solid water blocks.

The cells were then irradiated as described above. An hour after irradiation, a row of cells had the membrane removed and rinsed with PBS, followed by incubation in 10% PrestoBlue in media, v/v, for 1 hr. PrestoBlue is a resazurin-based dye which measures viable, metabolically active cells via the reduction of resazurin to resorufin and can be detected fluorometrically [229]. Subsequent measurements were taken every day for the first three days, followed by measurements every second day until confluency was reached.

Set-Up Parameter	Value
Gantry Rotation	180.0^o
Collimator Rotation	0.0^o
X Jaw	28.0 cm
Y Jaw	28.0 cm
Source-Axis Distance	100.0 cm
Source-Skin Distance	95.0 cm
Dose Coefficient	100.92 Mu/Gy

Table 3.1: **Linear Accelerator set-up parameters**

3.6.7 Immunofluorescence assay

Cells were grown on glass coverslips in six-well plates for 24 hr prior to experimentation. After 24 hr of endocytosis of $GNP_{PEG\text{-}RGD}$ complexes, the cells were treated with radiation as described previously, and incubated for 24 hr at 37 ^{o}C. The cells were fixed with 4% PFA for 5 min at room temperature followed by two PBS washes for 5 min each. The cells were then blocked to reduce background noise using 2% BSA/0.1% Triton-X in PBS for 20 min. The two primary antibodies γH2AX and 53BP1 were diluted 1:200 in 0.5% BSA/0.1% Triton-X/PBS, while the secondary antibody was diluted 1:500 in 0.5% BSA/0.1% Triton-X/PBS. The coverslips were placed cells-down into 50 μL of a combination of the two primary antibodies on parafilm and incubated for an hour, followed by washing with PBS for five minutes. The cells were then rinsed twice with 0.5% BSA/0.175% Tween-20/PBS for 5 min. On a new parafilm, the cover slips were placed cells-down in 50 μL of both secondary antibodies and incubated in the dark for 30 min. Finally, the cells were rinsed in PBS, dried, mounted to glass coverslips with Prolong Glass, and imaged with confocal microscopy as described previously.

3.6.8 Statistical Analysis

A Welch's independent t-test with Bonferroni correction was performed using the statannot Python package. A p value <0.05 was considered statistically significant. Experiments were repeated three times and the data presented is the average, for all experiments. Welch's independent t-test works by calculating the statistic t by:

$$t = \frac{\Delta\bar{X}}{s_{\Delta\bar{x}}} = \frac{\bar{X}_1 - \bar{X}_2}{\sqrt{s^2_{\bar{X}_1} + s^2_{\bar{X}_2}}} \tag{3.11}$$

where $s_{\bar{X}_i} = s_i/\sqrt{N_i}$, $\bar{X}_i$ and $s_{\bar{X}_i}$ are the i$^{\text{th}}$ sample mean and its standar error, s_i denotes the standard deviation and N_i is the sample size.

The degrees of freedom for this test can be calculated from

$$\nu \approx \frac{\left(\frac{s_1^2}{N_1} + \frac{s_2^2}{N_2}\right)^2}{\frac{s_1^4}{N_1^2\nu_1} + \frac{s_2^4}{N_2^2\nu_2}} \tag{3.12}$$

where $\nu_i = N_i - 1$ and is the degrees of freedom for the i$^{\text{th}}$ sample. Once t and ν have been calculated, they can be inserted into the t-distribution to test the null hypothesis and get a p-value. The Bonferonni correction is a conservative method to adjust p-values that helps control for false positives but does increase the change of false negatives. However, this ensures that the data analyzed is likely statistically significant.

Chapter 4

Docetaxel to improve gold nanoparticle-based radiotherapy in multiple cell models

4.1 Preamble

Content in this section is reproduced with permission from MDPI: Cancers, and it has been published with the following citation:

> Bromma, K., Alhussan, A., Perez, M.M., Howard, P., Beckham, W., Chithrani, D.B., Three-Dimensional Tumor Spheroids as a Tool for Reliable Investigation of Combined Gold Nanoparticle and Docetaxel Treatment. *Cancers*. https://doi.org/10.3390/cancers13061465 (2021)

The candidate, KB, made substantial and direct contributions to the conception and design of the experimental plan. KB made substantial contribution to sample preparation, collection, and processing. KB made substantial contribution to the acquisition of the data.

Experimental Conception: KB, WB, DBC
Experimental Design: KB, DBC
Performed Experiments: KB, MMP, AA
Analyzed Data: KB
Made Figures: KB
Writing of Manuscript: KB

4.2 Introduction

Further improvements to the clinical response are only of value if the differential response between the tumor demise and normal tissue protection, called the therapeutic index, is increased. Towards this end, the advent of nanomaterials has allowed for the development of radiosensitizers and drug delivery systems [230, 231]. GNPs have previously been shown to act as an effective radiosensitizer in clinically relevant energy ranges [232]. Targeting of GNPs to tumors can selectively increase deposited dose, increasing the therapeutic index. Moreover, GNPs have an easily modifiable surface, allowing for production of drug delivery systems, many of which have been shown to be effective in the lab as well as in clinical trials [90]. The use of GNPs as a drug delivery system can improve the pharmacokinetics, the pharmacodynamics, and the biodistribution of various drugs, as well as allow for improved targeting to reduce widespread normal tissue toxicity due to non-specific cytotoxic drugs [233, 234]. Combination of two of these applications can lead to the use of GNPs in chemoradiotherapy, a modality shown to be superior to the use of either radiotherapy or chemotherapy alone.

Any improvements to any of the previous treatment modalities are dependent on optimization of the transport and uptake of the GNPs into the tumor cells. GNPs enter the cell largely via receptor-mediated endocytosis [198, 193]. The uptake of the GNPs on a single cell level depends on many different factors, including size, shape, and surface functionalization [200, 197]. However, in an *in vivo* environment, added complexities of the tumor microenvironment and the immune system create further obstacles to clinical translation [63]. Use of nanomaterials must also consider the interactions that occur *in vivo* and the journey of the NPs throughout the body. After administration, NPs tend to be excreted in the liver, spleen, and blood, with the clearance half-life depending on many factors, such as size, shape, and surface functionalization [235]. For example, smaller GNPs (<30 nm) would accumulate in the liver and spleen while larger (60 nm GNPs) accumulate in the blood [236]. Without functionalization, bare NPs will form a corona due to opsonin proteins in the plasma, lowering uptake efficiency while increasing removal from the circulatory system by macrophages [201]. It is important to optimize the properties present in the GNPs. However, a large portion of preclinical work involving GNPs have utilized a 2D monolayer cell model, which cannot accurately represent the complex heterogenous environment present in the tumor microenvironment. Thus, the introduction of a 3D

model that can more accurately characterize an *in vivo* environment is essential to more successful clinical translation and to better optimize GNPs in a reliable manner.

The utilization of a 3D spheroid cell model can allow for modelling of an essential aspect of the tumor microenvironment which was previously inaccessible to 2D monolayer models: the extracellular matrix (ECM). The ECM acts as a scaffold for cell growth and is comprised of a network of various macromolecules, adhesive proteins, and structural proteins [101]. The ECM is also relevant in the regulation of cellular function in the tissue, such as cell-to-cell communication, proliferation, and cell adhesion, all aspects of the tumor microenvironment that are not relevant in the simplistic monolayer model [102]. NPs have also been shown to interact with the ECM *via* hydrodynamic interactions, *via* physical interactions such as collision of the NPs with the matrix fibers, as well as electrostatic interactions when dealing with charged particles. All of these factors will as limiting forces to the diffusion of the NPs through to the cell, where we wish to cause damage with therapy [104, 103]. Thus, improvements in treatment in an environment that appropriately models these more complex interactions, such as the 3D spheroid, is critical.

An important aspect that must be taken into account is the size of the GNPs, which is a characteristic that controls the *in vivo* blood circulation, tumor accumulation and penetration, and cellular uptake [238]. The size of the NPs used is important, as the 20–40 nm spacing between collagen fibrils sets the upper limit for effective penetration, and as a result smaller nanoparticles tend to be more efficient at entering cells [105]. The use of spheroids with GNPs has been explored previously in a limited fashion [106]. Further studies on how functionalization and size of the GNPs have been explored recently, all agreeing that smaller GNPs will more effectively penetrate deeper into the cells in the more complex *in vivo* tumor microenvironment [107, 108]. However, smaller nanoparticles (<10 nm) will have a rapid elimination via renal pathways compared to larger nanoparticles [112]. Thus, optimization of the uptake such that there is a balance in circulation time as well as increased retention due to choice of GNP size is essential. This can be seen in Figure 4.1, where, in the 2D monolayer, the cells have easy access to the GNPs in serum, removing additional variables that may affect optimization of GNPs at a single cell level. With increased complexity in the 3D tumor spheroid, we can see the introduction of a concentration gradient that will alter the ability of deeper-set cells, which often are hypoxic and thus more treatment-resistant, to uptake GNPs. Optimization in a more complex environment is essential to bridge the gap between the lab and the clinic, to facilitate

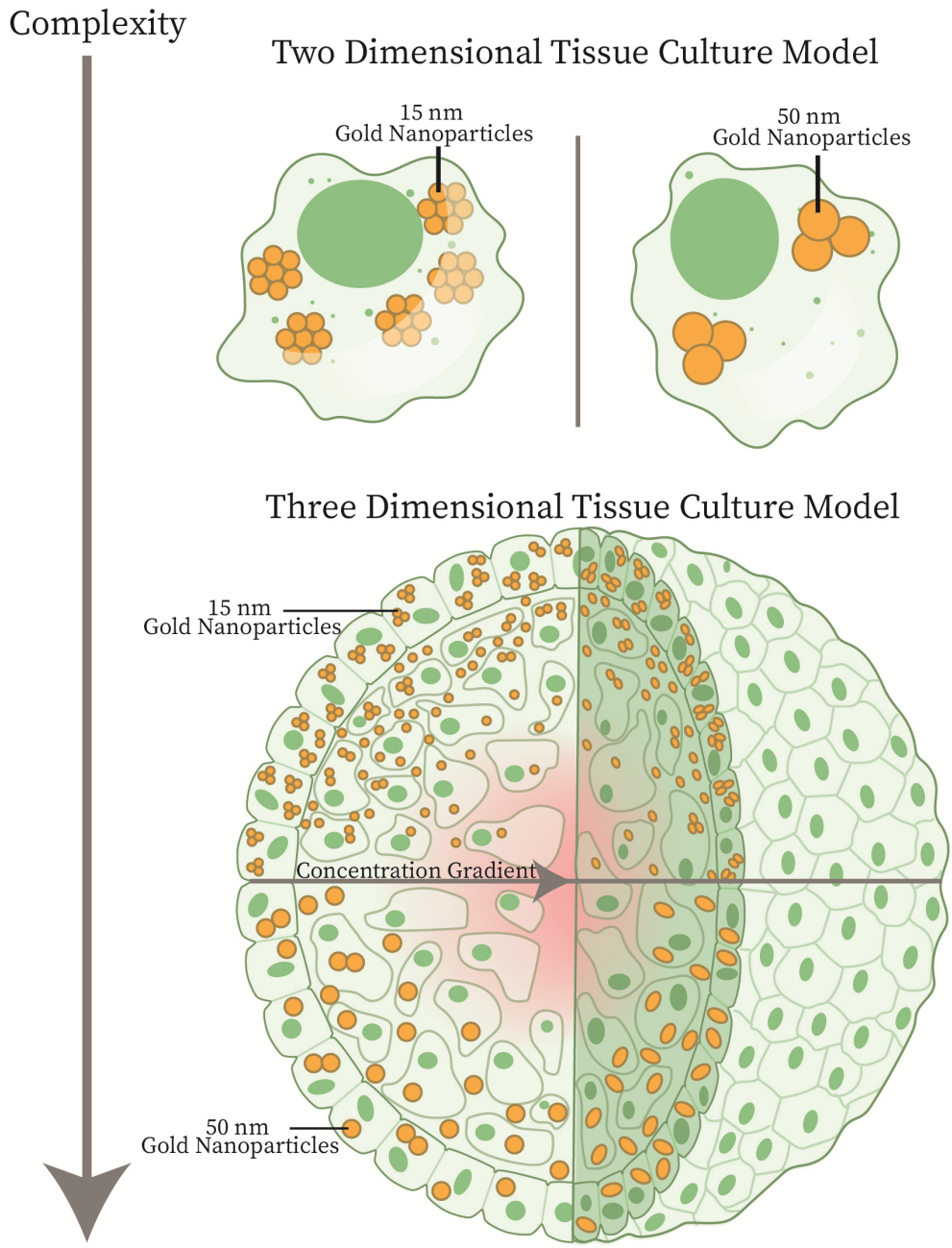


Figure 4.1: **Two-Dimensional Tissue Culture Model vs. Three-Dimensional Tissue Culture Model.** In a two-dimensional monolayer model, the gold nanoparticles have easy access to all the cells, allowing for optimization of uptake at a single cell level. However, the complexity of an *in vivo* environment is better approximated by the three-dimensional spheroid model. In a spheroid model, the uptake of smaller nanoparticles will penetrate deeper, allowing for targeting of difficult to reach cells. Further, a spheroid model allows for optimization in a tumor-like microenvironment, which can be largely affected by concurrent treatment with chemotherapy or radiotherapy. Reproduced with permission [237]. Copyright MDPI, 2021.

a quicker translation of the radiosensitizer and drug delivery system platform that GNPs provide.

In this study, we explore the differential uptake due to the alteration of size from smaller 15 nm spherical GNPs to larger 50 nm spherical GNPs in a 2D monolayer model compared to a 3D spheroid model. The GNPs used in this experiment are functionalized with PEG, for stabilization, and a peptide containing integrin binding domain RGD, for tumor targeting, to be suitable for future *in vivo* experiments. Further, the use of chemotherapeutic agents, such as DTX, in low doses has been shown to significantly alter the uptake, distribution, and retention of GNPs [239]. DTX can also act as a radiosensitizer, due to synchronizing cells in the G2/M phase of the cell cycle [40]. Thus, we will use DTX at low doses, so as not to cause increases in cytotoxicity, in both 2D and 3D models to explore optimum treatment conditions. Exploration of 3D models such as spheroids should yield increased, more accurate throughput of experimental results, hastening the use of important platforms such as GNPs into the clinic.

4.3 Results and Discussion

4.3.1 Characterization of GNPs

The size and surface characteristics of the GNP utilized is important to optimize, to improve treatment efficacy and reduce normal tissue toxicity in patients [240, 241]. Thus, smaller nanoparticles (≈16 nm) and larger nanoparticles (≈50 nm) were synthesized, functionalized, and characterized. The GNPs were functionalized with PEG and a peptide containing integrin binding domain RGD, referred to as RGD, as seen in Figure 4.2a. The use of PEG is essential for future *in-vivo* success, as it improves biostability, biodistribution, and increases the circulation half-life [242]. The optimum capping density for PEG molecules onto GNPs was previously found to be 1 PEG molecule for nm^2 of surface area, which was adhered to in these experiments [216]. While important, PEG has previously been shown to reduce the uptake of GNPs, and thus RGD, which can improve endocytosis and target tumors effectively, was used to improve uptake [201, 243]. Scanning transmission electron microscopy was employed to confirm the size of the different GNPs as seen in Figure 4.2b,c. From a minimum of 100 measured GNPs of each sample, the smaller GNPs were found to have an average diameter of 15.97 ± 1.72 nm while the larger GNPs have an average diameter of 56.12 ± 8.45 nm; these GNPs will be referred to as 15 nm and 50 nm

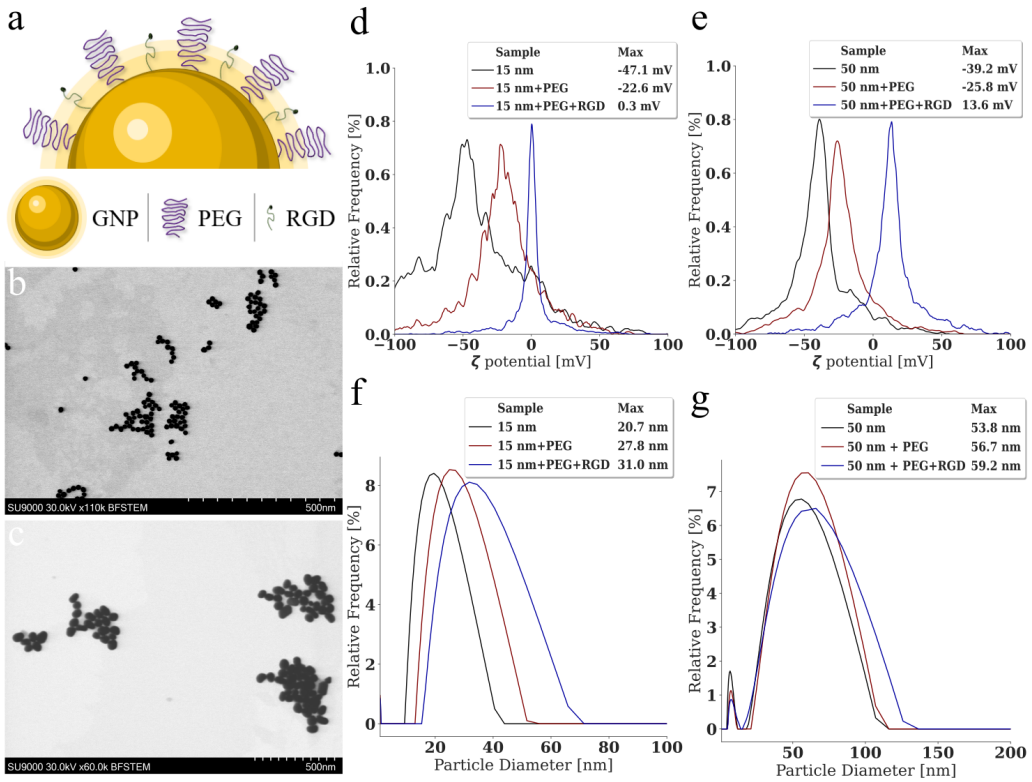


Figure 4.2: **Characterization of gold nanoparticles.** (a) A schematic diagram of the functionalization of the gold nanoparticles, which are conjugated with polyethylene glycol and a peptide containing integrin binding domain RGD. (b,c) Transmission electron microscope images of the small and large gold nanoparticles. Scale bar is 100 nm. (d,e) ζ-potential and (f,g) dynamic light scattering measurements of the gold nanoparticles prior to and following conjugation with polyethylene glycol and the RGD peptide. Reproduced with permission [237]. Copyright MDPI, 2021.

GNPs in this paper. The ζ-potential after conjugation with PEG and RGD was measured as seen in Figure 4.2d,e, along with the hydrodynamic diameter using DLS in Figure 4.2f,g.

Measuring of the ζ-potential and DLS after conjugation is a useful method of confirming functionalization and stability of the nanoparticles. The measured hydrodynamic diameter of the bare GNPs was 19.77 nm and 53.83 nm, respectively, with a polydispersity of 11.27% and 27.34% and a ζ-potential of -42.70 ± 6.16 mV and -38 ± 1.26 mV, respectively. Following conjugation with PEG and RGD, the diameter increased to 31.00 nm and 59.20 nm with a polydispersity of 19.91% and 24.33% and a ζ-potential of -1.09 ± 0.26 mV and 10.30 ± 0.51 mV, respectively. A small peak in the 50 nm GNPs DLS measurements centered around 7 nm is thought

a

Sample	Hydrodynamic Diameter [nm]	Polydispersity Index [%]	Zeta Potential [mV]
15 nm	19.77	11.27	-43.70 ± 6.16
15 nm + PEG	27.82	22.61	-20.07 ± 0.93
15 nm + PEG + RGD	31.00	19.91	-1.09 ± 0.27
50 nm	53.83	27.34	-38.12 ± 1.26
50 nm + PEG	56.66	25.59	-27.75 ± 1.38
50 nm + PEG + RGD	59.20	24.33	10.30 ± 0.51

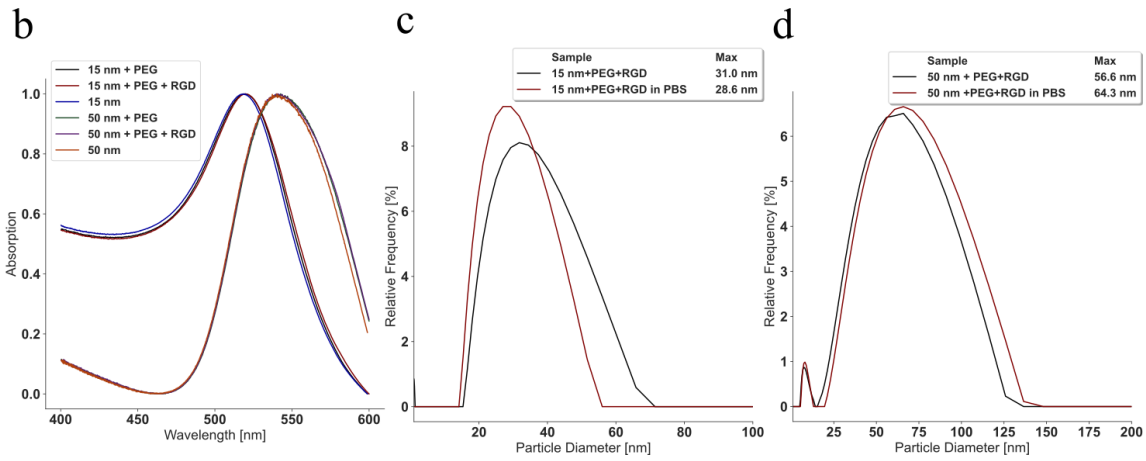


Figure 4.3: **Supplemental gold nanoparticle characterization.** (a) Measured quantities of the GNPs using dynamic light scattering and zeta potential. (b) UV-Vis measurements of the GNPs after each conjugation step, ensuring stability. (c-d) Dynamic light scattering measurements of the GNPs in the presence of phosphate buffered saline (PBS), to ensure stability in serum. Reproduced with permission [237]. Copyright MDPI, 2021.

to be excess seeds that form in the synthesis process but never congregate into the larger final product. However, these seeds do not make up a significant volume, as verified using the TEM imaging seen in Figure 4.2c. This does not occur in the 15 nm GNPs spectrum due to smaller NPs being more energetically efficient to form due to their lesser size.

All values can be seen in Figure 4.3a, where the hydrodynamic diameter of both GNPs increases with the addition of PEG and RGD as expected, while the ζ-potential grows more positive. This is due to the replacement of the negatively charged citrate molecules, used as a reducing agent to produce the GNPs, with a neutral PEG molecule and a positively charged RGD molecule. Despite the positive trend of ζ-

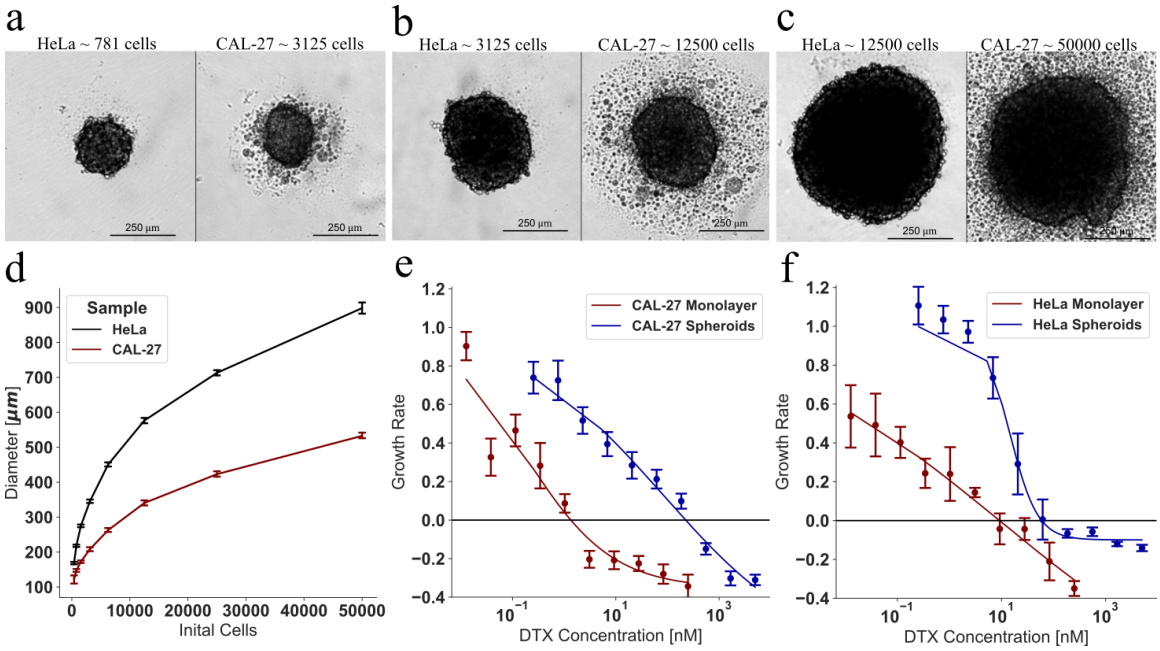


Figure 4.4: **Characterization of spheroids.** (a-c) The size of the spheroids under different initial cell counts was approximated using brightfield images taken after three days of incubation. (d) Size of spheroid for the two different cell lines under different initial cell count conditions. An approximate size range of 300 μm - 400 μm was utilized for all experiments. (e-f) Proliferation assay results after treatment of docetaxel of both (e) CAL-27 and (f) HeLa when in monolayer and spheroid. Points are average of three plates of eight samples, line is the best fit using Growth Rate Inhibition. Error bars are one standard deviation from the mean. Reproduced with permission [237]. Copyright MDPI, 2021.

potential after addition of the RGD peptide, the GNPs are still stable due to the addition of PEG molecules. The stability of the GNPs after conjugation with PEG and RGD was verified at each step as seen in Figure 4.3b using UV-Visible spectrometry measurements, which is an approximate measure of size and concentration [217]. An important aspect of the GNPs following conjugation is their ability to resist aggregation in the presence of a human body fluid-like buffer, such as PBS [244]. The stability of the GNPs in PBS was verified using dynamic light scattering as seen in Figure 4.3c,d. This is an important result when moving towards eventual *in vivo* experiments.

4.3.2 Characterization of spheroids and docetaxel

Prior to experimentation with GNPs, the cell lines used in this experiment - CAL-27, a human head and neck cancer cell line, and HeLa, a cervical cancer cell line - were characterized as spheroids as seen in Figure 4.4a–d. HeLa, a common cell line used in pre-clinical experiments, is intended as a model cell line, while CAL-27 is a tongue cancer cell line, in which the use of cytotoxic drugs like DTX can allow for improved treatment response and the use of high doses of radiation is limited due to proximity of many sensitive organs [245]. It can be seen that the different cell lines have different packing density of cells, which is known to alter the efficacy of various treatments [246, 247]. Despite this, a volume of approximately 300–400 μM was chosen as an optimum spheroid size, as larger spheroid sizes (>350 μm) introduce a larger core of necrotic cells and increased number of quiescent cells [248]. This corresponds to approximately 3,125 HeLa cells and 12,500 CAL-27 cells, with CAL-27 having a larger packing density. It is well known that the packing density of tumor cells will alter the efficacy and penetration of anticancer drugs as well as small nanoparticles, such as micelles [246, 247]. The ability to mimic this *in vivo* effect in the 3D spheroid model is a large benefit over the 2D monolayer model. The cell lines were then characterized in the presence of the anti-cancer drug DTX), as seen in Figure 4.4e. DTX can alter the uptake of the GNPs and act as a radiosensitizer causing synchronization in the highly radiosensitive G2/M phase of the cell cycle [239, 40].

For this, and future, experiments, the use of DTX is intended to not increase cell kill but rather synchronize the cells while maintaining viability. Thus, the Growth Rate Inhibition metric introduced by Hafner et al. was utilized to calculate the optimum concentration of DTX from proliferation assays such that the division time is essentially halted and cytostasis is achieved [249]. Due to the length of the assay, some cell lines would should different cell survival based on proliferation measurements due to having a more rapid doubling time. The benefit of using the Growth Rate Inhibition metric compared to a basic survival metric controls for this and gives a more accurate result. Based on this metric, a concentration in monolayer of 5 nM and 20 nM, for CAL-27 and HeLa respectively, and a concentration of 200 nM and 50 nM in spheroids, for CAL-27 and HeLa respectively, was used, for a 24 hr exposure. The increased resistance to the anticancer drug is expected, due to the more realistic tumor-like environment introduced by the 3D spheroid model. This has been observed in many different spheroid models with many different drugs,

including DTX, and is one of the many reasons that the 3D spheroid is better to test drugs than the 2D monolayer [250, 251, 252]. Due to the introduction of the ECM, penetration of the drug is reduced [253]. When comparing to clinical dosing, the area under concentration-time curve ($AUC_{0\rightarrow 24}$) for HeLa and CAL-27 are 120 nM·h and 480 nM·h for monolayer, respectively, and 480 nM·h and 4800 nM·h for spheroids, respectively. Clinically used doses see a median $AUC_{0\rightarrow 25}$ of 1284 nM·h at a dose of 20 mg/m^2 and a median of 5562 nM·h at a dose of 100 mg/m^2, showing the doses used in this experiment are comparable [254].

To verify the effects of these doses of DTX on the cell lines in both the 2D monolayer model and the 3D spheroid model, the cells were imaged using darkfield imaging as can be seen in the HeLa cells in Figure 4.5a–d. In order to image the spheroids, 10 μm sections of the spheroids were cut using a microtome and then adhered to microscope slides for microscopy, allowing for visualization of deeper internal mechanisms. The DTX can be seen to induce multinucleated cells in monolayer, which is expected due to the dose delivered. DTX at low doses will still have an observable effect on the cells, but not cause complete cell death, allowing for the exploration of dual combination treatment with GNPs. Further, the structure of spheroids appears to be disrupted, reducing the organization of the extracellular matrix produced by the cells in the spheroid, allowing for possibly easier penetration of GNPs into the core. However, the bulk of the DTX-treated spheroid appears to be morphologically similar to the non-treated samples, allowing for the overall function of the spheroids to be maintained. Improved penetration into the tumor is an important feature of all nanomedicine and is one of the main benefits of using a nanoparticle system. Increased penetration of the GNPs *in vivo* would allow for deeper set radio- and chemo-resistant cells to have an increased dose and higher probability of cell kill. Hyper spectral profiles, from HSI, of the cells and background were added to each darkfield image as an inset figure in Figure 4.5a–d, to verify the absence of measured GNPs in the image. The use of HSI to verify GNP presence in cells has been used widely in literature from monolayer to *in vivo* section analysis [219, 255]. HSI allows for the capture and spectral analysis of the reflecting and elastically scattered light. Based on the intensity, distribution, and peak of the spectral information collected within each region of interest, we can conclude that no GNPs were present in the control samples. This is completed using a spectral angle mapper classification system that classifies the spectra based on a known spectrum, which in this case is that of the GNPs. Further, it has been shown that the most radiosensitive stage of the cell

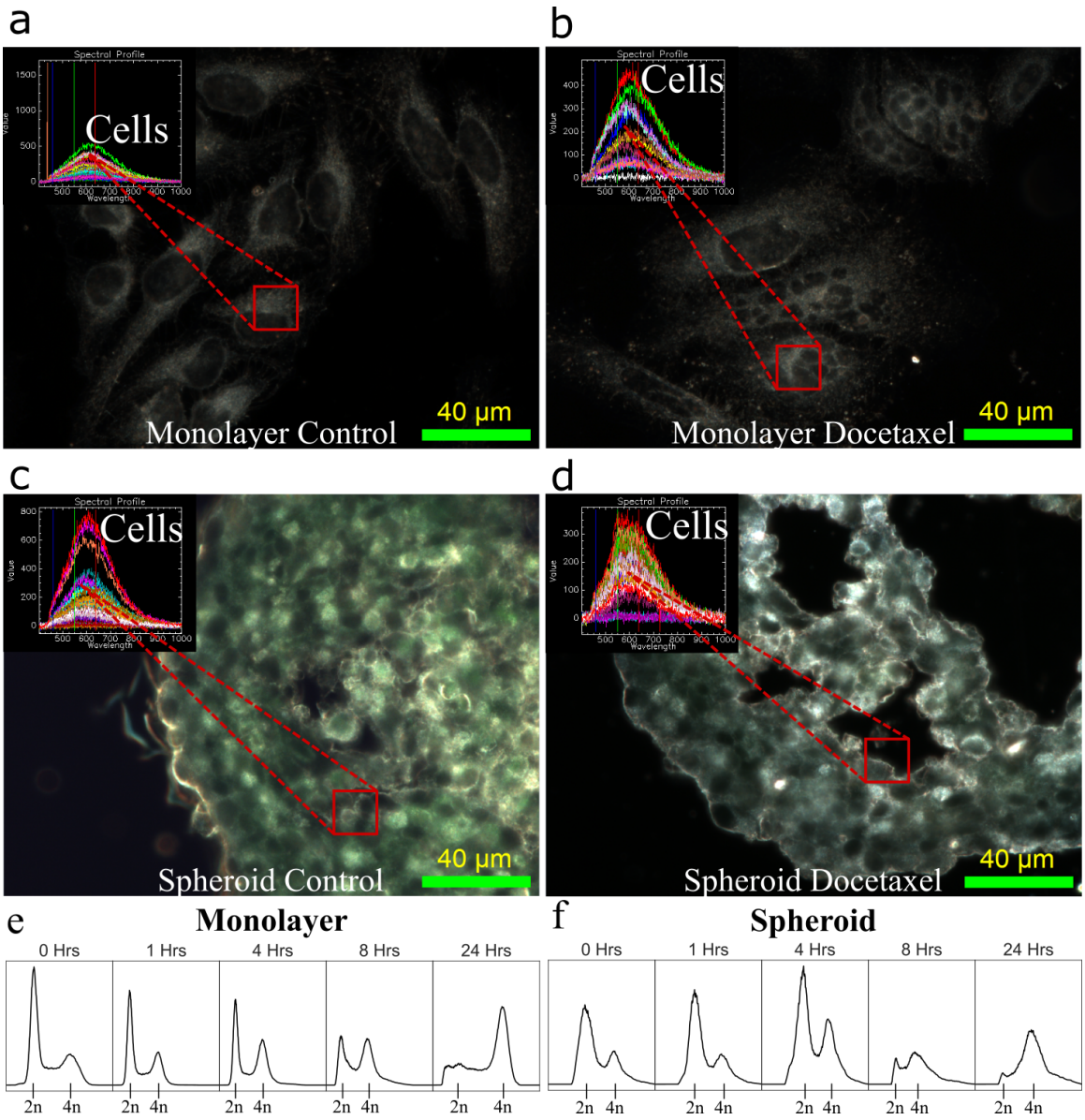


Figure 4.5: **Synchronization of tissue culture models with docetaxel.** (a,c) Darkfield images of a (a) monolayer of HeLa cells and a (c) HeLa spheroid section. (b,d) Darkfield images of a (b) monolayer of HeLa cells and a (d) HeLa spheroid section treated with docetaxel. Overlay: Hyper spectral imaging yields a spectrum that shows no gold in the images. Scale bar is 40 μm. (e,f) Cell cycle distribution after 0, 1, 4, 8, and 24 h of treatment with docetaxel in a (e) monolayer of HeLa and a (f) HeLa spheroid. Reproduced with permission [237]. Copyright MDPI, 2021.

cycle is the G2/M phase, which DTX is effective at synchronizing a cell population into [47]. To verify synchronization at the chosen dose of DTX in HeLa and CAL-27, the cells were measured following treatment as seen in Figure 4.5e,f. Over 24 h, the

cells transition from a normal cell cycle distribution to a largely synchronized population in the G2/M phase, corresponding to 4n DNA content. Thus, the dose of DTX chosen is working as intended.

4.3.3 Uptake of gold nanoparticles with docetaxel

The next step was to ascertain the difference between the 2D and 3D cell models when treated with both DTX and GNPs. Cells were dosed at a clinically relevant dose of 7.5 μg/mL for 24 hr with both sizes of GNPs. There has been a reported time-dependent effect on uptake for bare GNPs observed in monolayer, with a maximum reached after approximately 8 h, while PEG coated GNPs of size 25–40 nm can be seen to have a half-life of approximately 22 hr *in vivo* [197, 256]. Thus, a time point of 24 hr for total treatment time was chosen to ensure sufficient uptake of GNPs. Further, the dose of GNPs chosen is a clinically-achievable concentration that has shown radiosensitization *in vivo* previously, at approximately 10 μg/mL [98]. Escalation of GNP dose can be explored in the future to improve therapeutic effects, while ensuring no induced toxicity or negative side effects are introduced. In the 2D monolayer cell model, as seen in Figure 4.6a–c, we can see that following concomitant dosing of GNPs with DTX, there is a non-significant increase in the uptake of the GNPs compared to dosing with GNPs alone. The use of DTX resulted in an increased uptake of 24% and 15 for CAL-27 and HeLa with 15 nm GNPs, respectively, and an increase of 14% and 13% in uptake of 50 nm GNPs in CAL-27 and HeLa, respectively. This is a similar result found in previous experiments involving GNPs and docetaxel [239]. The difference in efficacy can be attributed to a lower DTX dose utilized in the experiments used in this work. This increase has previously been attributed to a reduced dilution of the GNPs due to inhibition of cell multiplication; however, the use of DTX has further benefits to the use of GNPs during radiotherapy such as closer localization to the nucleus and longer retention. The smaller GNPs have a larger uptake due to the addition of PEG and RGD on the surface altering the uptake efficiency. This has previously been observed and is attributed to the larger surface curvature exposing the RGD peptides more efficiently to the integrin receptors on the cell's surface. This suggests that smaller nanoparticles (<20 nm) will be a better choice with targeting agents, such as the RGD peptide, than larger particles (>20 nm), independent of the cell model used.

It is also clear that the different cell lines have different uptake patterns, which

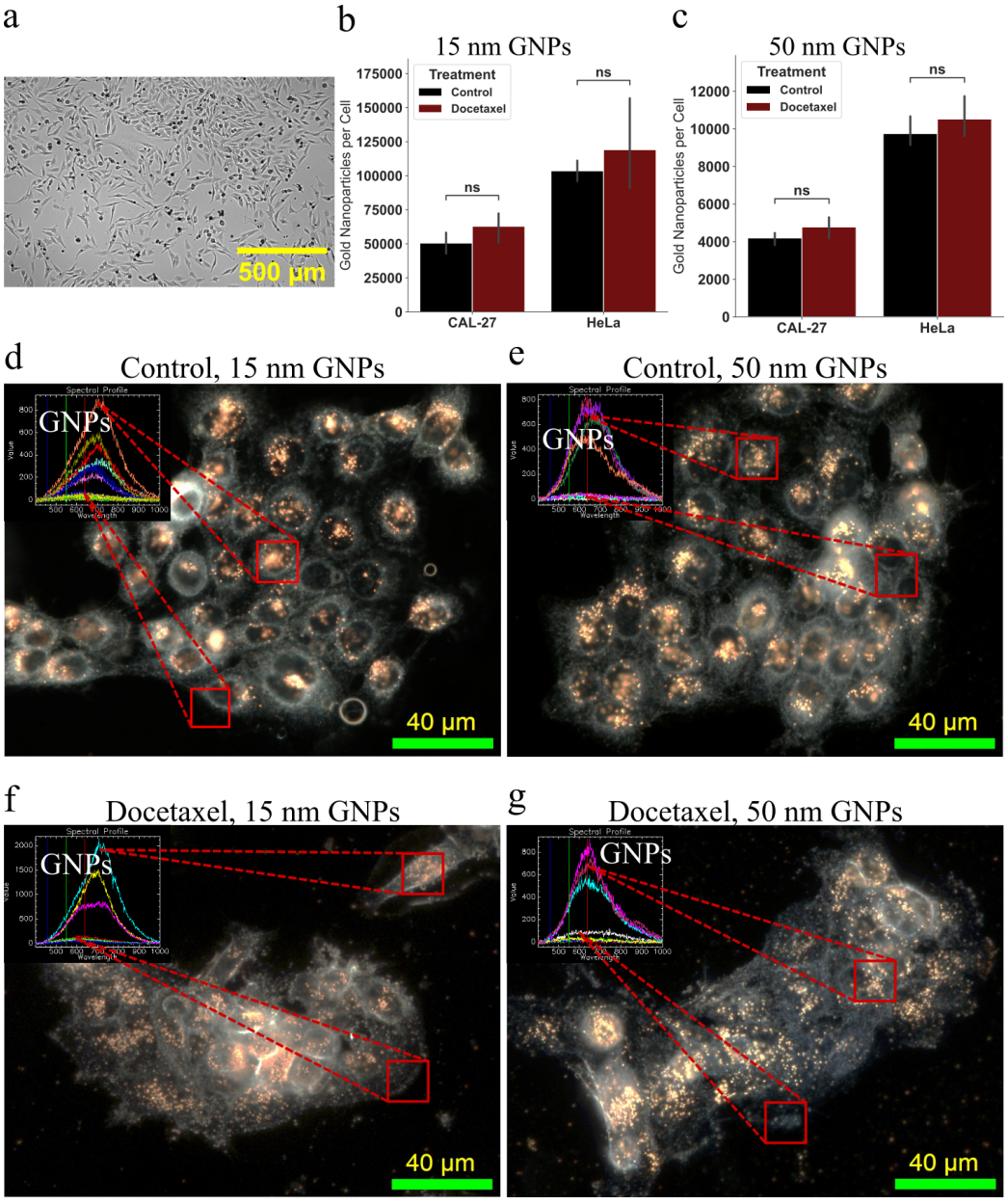


Figure 4.6: **Gold nanoparticle uptake in two-dimensional cell model.** (a) Brightfield image of a monolayer of HeLa in a 96-well microplate. Scale bar is 1000 μm. (b,c) Uptake of the 15 nm and the 50 nm functionalized gold nanoparticles, with and without docetaxel. Treatment time was 24 h. Error bars signify one standard deviation from average of three independent measurements. (d–g) Darkfield imaging of CAL-27 cells with 15 nm and 50 nm functionalized gold nanoparticles, with and without docetaxel. Overlay: Hyper spectral imaging yields a spectrum that is matched to the gold in the sample. Scale bar is 40 μm. ns indicates no significance. Reproduced with permission [237]. Copyright MDPI, 2021.

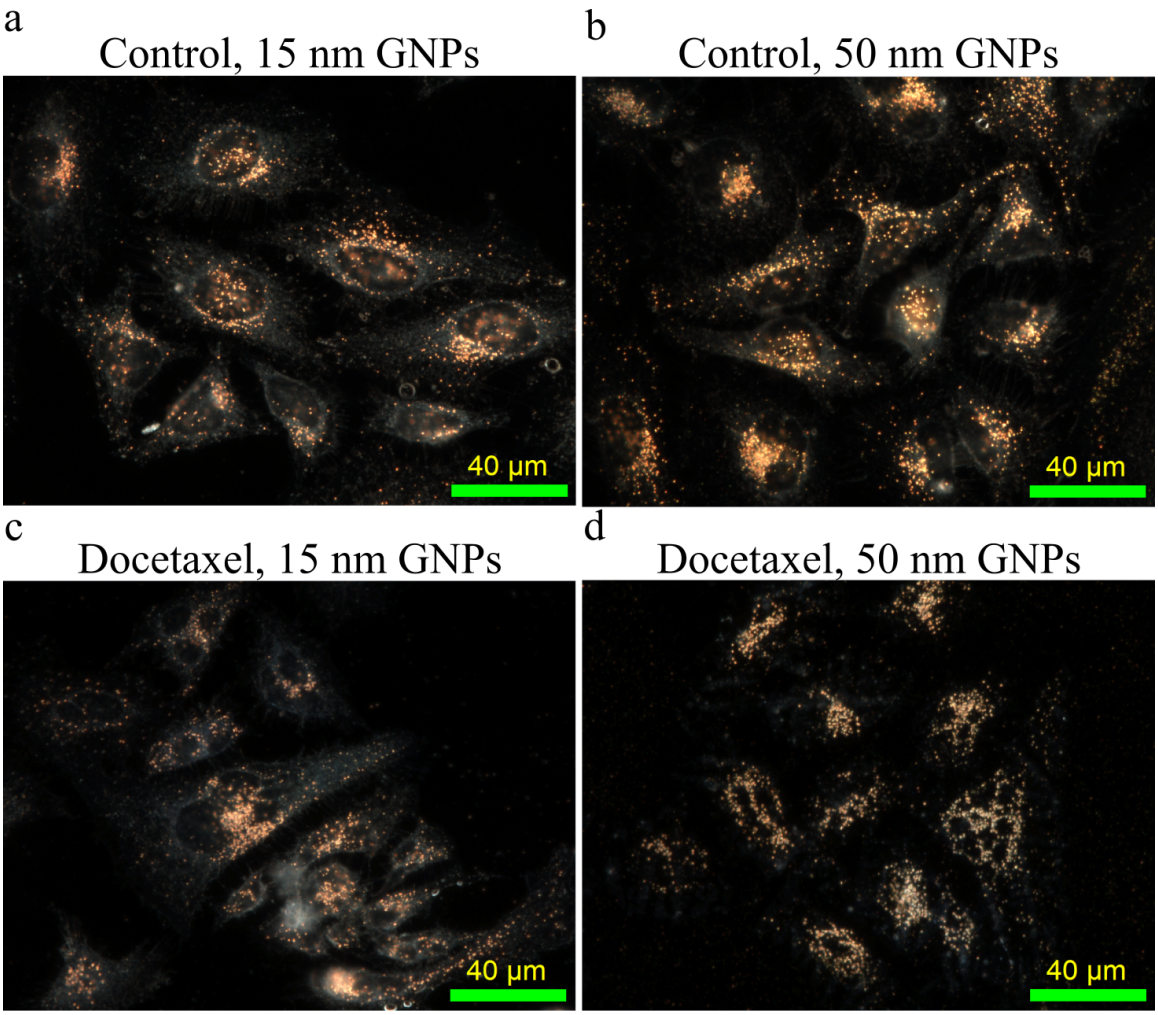


Figure 4.7: **Darkfield images of gold nanoparticle uptake in HeLa.** (a-b) Darkfield imaging of HeLa cells with 15 nm and 50 nm functionalized gold nanoparticles without docetaxel. (c-d) Darkfield imaging of HeLa cells with 15 nm and 50 nm functionalized gold nanoparticles without docetaxel. Scale bar is 40 μm. Reproduced with permission [237]. Copyright MDPI, 2021.

is consistent between different sizes of GNPs. For GNPs of size 15 nm and 50 nm, there was an increase of 100% and 130% respectively, in HeLa compared to CAL-27. Darkfield images of the monolayer of CAL-27 cells can be seen in Figure 4.6d–g, along with an inlay of the spectrum associated with GNPs and with background cells. The inset spectral profile taken from HSI images verifies the presence of GNPs in the samples as measured in the region of interest and classified using a spectral angle mapper. Comparing this spectral data to that of our UV-VIS spectrometry data in Figure 4.3, there is an observed difference in the peak wavelength measured.

This is a result of the intracellular agglomeration in endosomes and lysosomes, causing the GNPs to be in very close proximity to each other. As a result, there will be electromagnetic coupling of the plasmon spectra, leading to a peak at longer wavelengths [257]. This effect will be more exaggerated with the smaller 15 nm GNPs due to a larger number of GNPs being encapsulated in the cells compared to that of 50 nm GNPs, which is what we observe. Visually, the images agree with uptake results, with very similar number of GNPs in the cells, and is consistent with previous results. The ability to see the GNPs with darkfield is due to the aggregation of GNPs inside of endosomes within the cell [241, 243]. Similar studies have also shown that larger GNPs (>9 nm) are not likely to be localized in the nucleus unless conjugated with nuclear targeting agents, and thus are likely all within endosomes and lysosomes within the cell [258]. Images of HeLa in monolayer can be seen in Figure 4.7. Moving into 3D spheroids, we expect an altered uptake response due to the addition of an extracellular matrix.

Spheroids were grown to a size of ≈300–400 μm as previously described, as seen in Figure 4.8a, and then treated with the determined doses of DTX along with 7.5 μg/mL of GNPs for 24 h. Results can be seen in Figure 4.8b,c, along with darkfield images of 10 μM sections of the CAL-27 spheroids in Figure 4.8d,g. Similar to the monolayer model, we see larger uptake of smaller 15 nm GNPs with PEG and RGD into the spheroids when compared to the larger 50 nm GNPs, as expected. However, the magnitude of the difference changed, with HeLa only having a 23% increase in 15 nm GNP uptake relative to CAL-27, compared to 100% increase in monolayer. Interestingly, the larger 50 nm GNP uptake still had a 130% increase comparing HeLa to CAL-27. This model dependent behavior is important to note as another advantage when using a 3D spheroid over a 2D monolayer. With DTX, in the case of the 3D spheroid model, for CAL 27, there was a significant ($p=0.0016$) increase in 15 nm GNP uptake with DTX of 117% and a significant ($p=0.012$) increase in 50 nm uptake with DTX of 186%, as compared to GNP alone. Likewise, for HeLa in a 3D spheroid model, there was a significant increase ($p=0.01428$) in 15 nm GNP uptake with DTX of 47% and a significant ($p=0.0037$) increase in 50 nm GNP uptake with DTX of 56%. This is in contrast with the results seen in the 2D monolayer model; despite controlling for growth rate, there is a dramatic increase in GNP uptake with DTX, with the magnitude depending on the cell line. This may be a result of the reduced organization of the ECM due to the DTX, as can be seen in the darkfield images, allowing for deeper penetration of GNPs. However, due to the constraints of darkfield

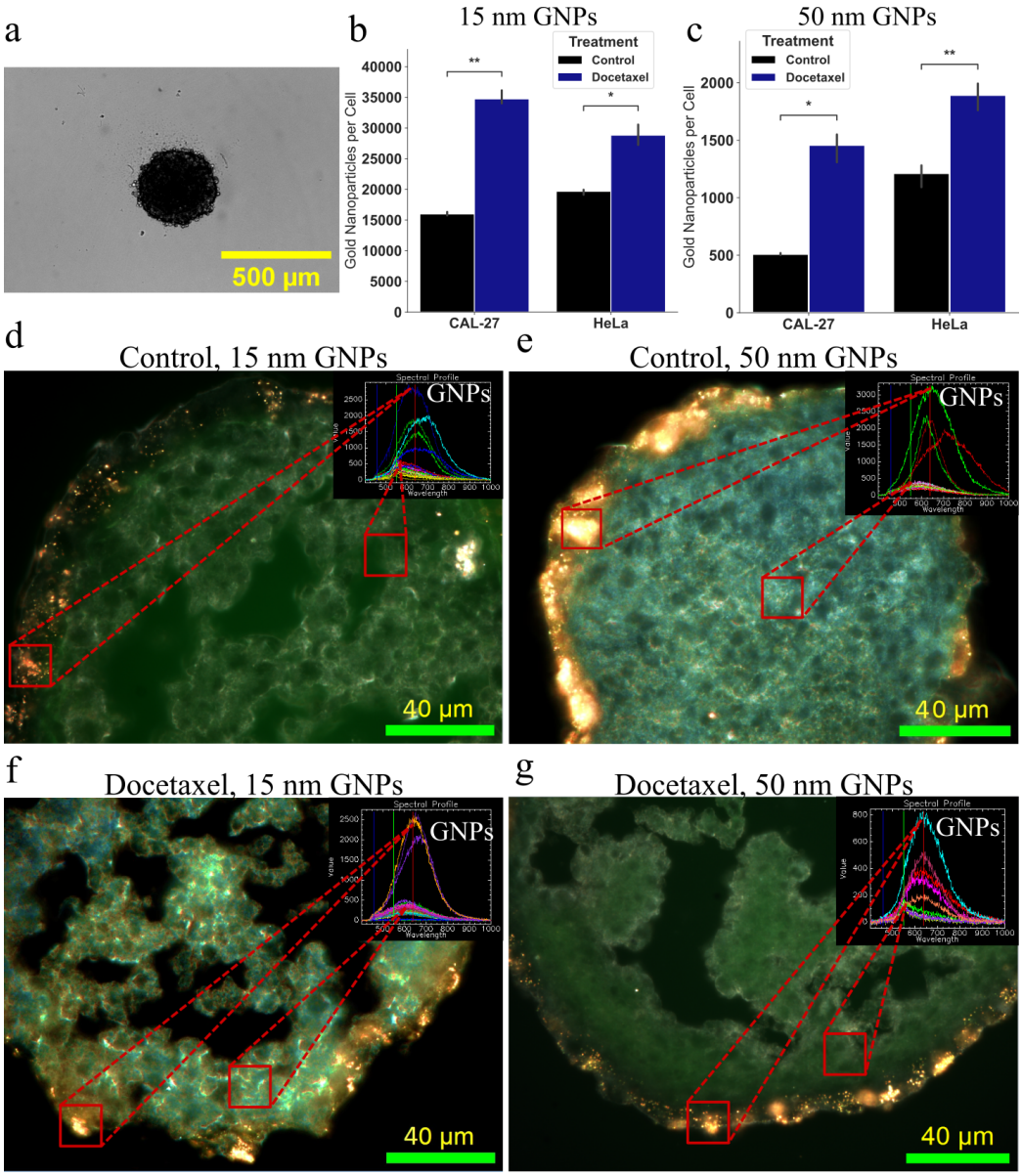


Figure 4.8: **Gold nanoparticle update in three-dimensional cell model.** (a) Brightfield image of a spheroid of HeLa in a 96-well microplate. Scale bar is 1000 μm. (b,c) Uptake of the 15 nm and the 50 nm functionalized gold nanoparticles, with and without docetaxel. Treatment time was 24 h. Error bars signify one standard deviation from average of three independent measurements. (d–g) Darkfield imaging of CAL-27 spheroid with 15 nm and 50 nm functionalized gold nanoparticles, with and without docetaxel. Overlay: Hyper spectral imaging yields a spectrum that is matched to the gold in the sample. Scale bar is 40 μm. * indicates $0.01 < p < 0.05$, ** indicates $0.001 < p < 0.01$. Reproduced with permission [237]. Copyright MDPI, 2021.

imaging, GNPs cannot be properly seen unless aggregated inside of endosomes and lysosomes within the cells. As the number of GNPs that penetrate falls off quickly with depth, the limitations of darkfield imaging hinder confirmation of this theory due to less GNPs being encapsulated in lysosomes. Improved methods of imaging may include confocal imaging and transmission electron microscopy to better analyze the mechanics of encapsulation of GNPs. Another possibility that is also likely is that, due to the higher dose of DTX given, cells on the outer radius of the spheroid see a larger effect, which are the same cells that uptake the bulk the GNPs. As a result, the effect seen in monolayer is amplified, due to the larger dose, and we see more GNPs. Images of HeLa spheroids can be seen in Figure 4.9.

As previously mentioned, the diffusion of GNPs into the spheroids is an important factor when optimizing a nanoplatform, as improved penetration allows for the GNPs to reach the hypoxic and necrotic cores that exist in highly therapeutic-resistant tumors [113]. To see if smaller GNPs had any benefit over larger 50 nm on penetration depth, darkfield images of the sections of spheroids using a 10× objective, as seen in Figure 4.10a, were analyzed for depth of visible GNPs around the surface. The results can be seen in Figure 4.10b, where there is a significant ($p=0.00057$) increase of penetration of 15 nm GNPs over 50 nm GNPs in CAL-27 from 8.83 nm depth for the larger GNPs up to 11.75 nm depth for the smaller GNPs, or a 33% increase. Likewise, there was a significant ($p=0.00029$) penetration of 15 nm GNPs over 50 nm GNPs in HeLa from 18.59 nm depth for the larger GNPs up to 21.72 nm depth for the smaller GNPs, or a 17% increase. The difference between the two cell lines in actual penetration depth is likely due to the packing density described previously, suggesting that the effectiveness of smaller GNPs over larger GNPs will be more pronounced in tightly packed tumors. The results are in agreement with literature, where smaller NPs tend to penetrate deeper into the 3D spheroid tumors, while the larger NP aggregate near the surface [259]. When moving to more personalized medicine, which is a direction that spheroids can greatly be of benefit, the utilization of patient-derived cells for producing spheroids can allow for *in vitro* simulation of individual tumor characteristics, such as emulating packing density, something that a 2D monolayer model cannot achieve [260]. Towards analyzing the root cause of the increased uptake of GNPs when using DTX in a spheroid model, the depth of the GNPs was measured similar to above, with the results in Figure 4.10c,d. There was a slight, non-significant increase in the penetration depth for most samples, except for HeLa using 15 nm GNPs. Thus, the benefits of DTX do not significantly extend

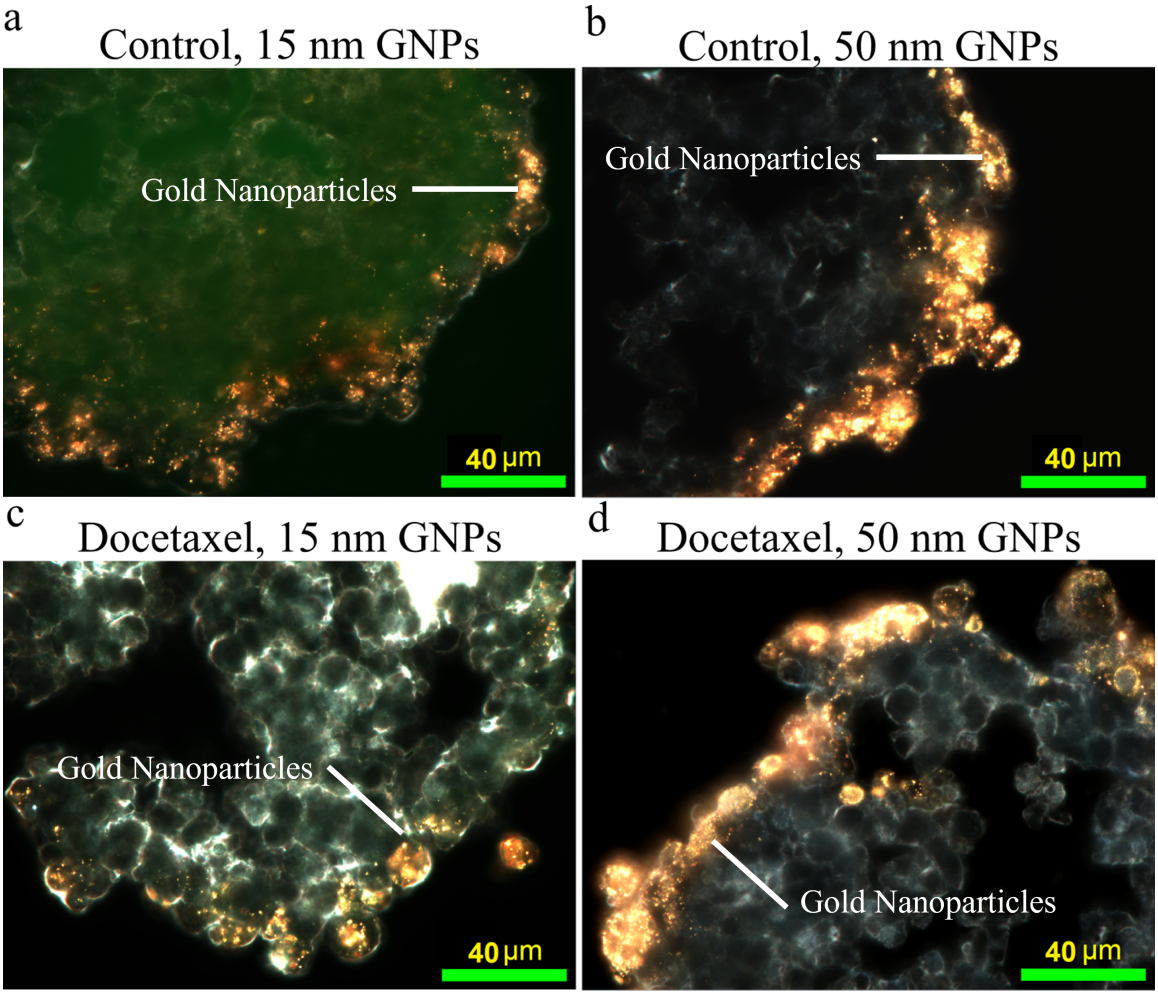


Figure 4.9: **Darkfield images of gold nanoparticles uptake in HeLa spheroid model.** (a-b) Darkfield imaging of HeLa spheroid with 15 nm and 50 nm functionalized gold nanoparticles without docetaxel. (c-d) Darkfield imaging of HeLa spheroid with 15 nm and 50 nm functionalized gold nanoparticles with docetaxel. Scale bar is 40 μm. The majority of the gold nanoparticles in the spheroids are aggregated near the periphery, similar to what will be seen *in vivo* near blood vessels. Reproduced with permission [237]. Copyright MDPI, 2021.

to the penetration depth of the GNPs.

Though the number of smaller 15 nm GNPs captured by the cells was larger than the number of larger 50 nm GNPs in both cell lines and both cell models by an order of magnitude, the total gold content, measured in picograms of Au per cell, was larger for the 50 nm GNPs, as seen in Figure 4.11, due to the larger total volume of the 50 nm GNPs. There was an average of 157%, 30%, 238%, and 106% increase in total Au content when moving from 15 nm to 50 nm GNPs, for a monolayer of

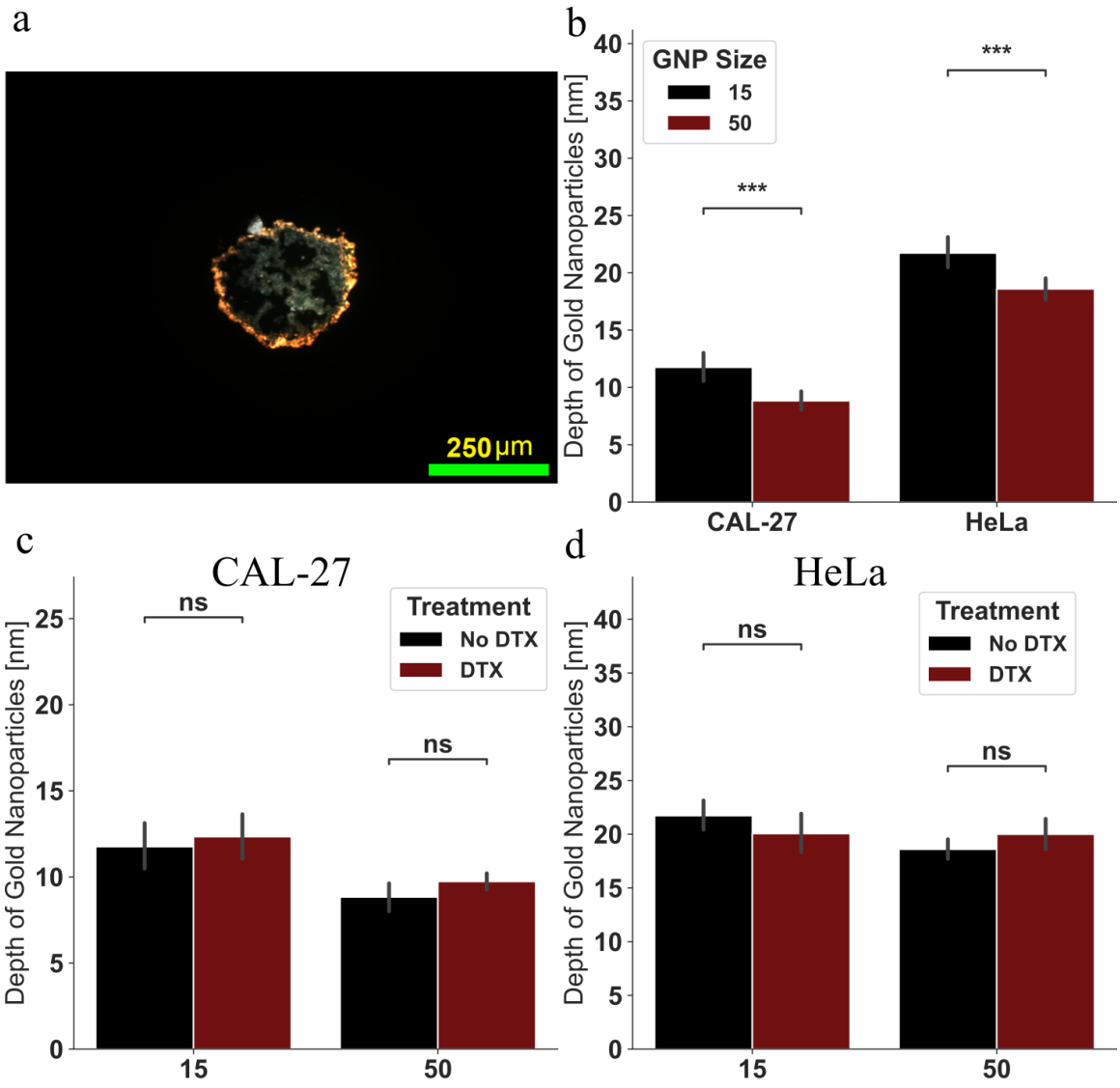


Figure 4.10: **Depth of penetration of gold nanoparticles.** (a) Darkfield image of HeLa spheroid with 50 nm functionalized gold nanoparticles without docetaxel. Scale bar is 250 μm. (b) Depth of visible penetration of gold nanoparticles as measured using darkfield images of spheroids from the 10× objective. (c,d) Depth of gold nanoparticle visible penetration with and without docetaxel for (c) CAL-27 and (d) HeLa. Error bars represent 1 standard deviation from a minimum 100 measurements. ns indicates no significance, *** indicates $0.0001 < p < 0.001$. Reproduced with permission [237]. Copyright MDPI, 2021.

CAL-27, CAL-27 spheroids, HeLa in monolayer, and HeLa spheroids, respectively. An important finding that must be elucidated in future studies is if the gold content of the larger GNPs outweighs the increase in nanoparticle content due the smaller

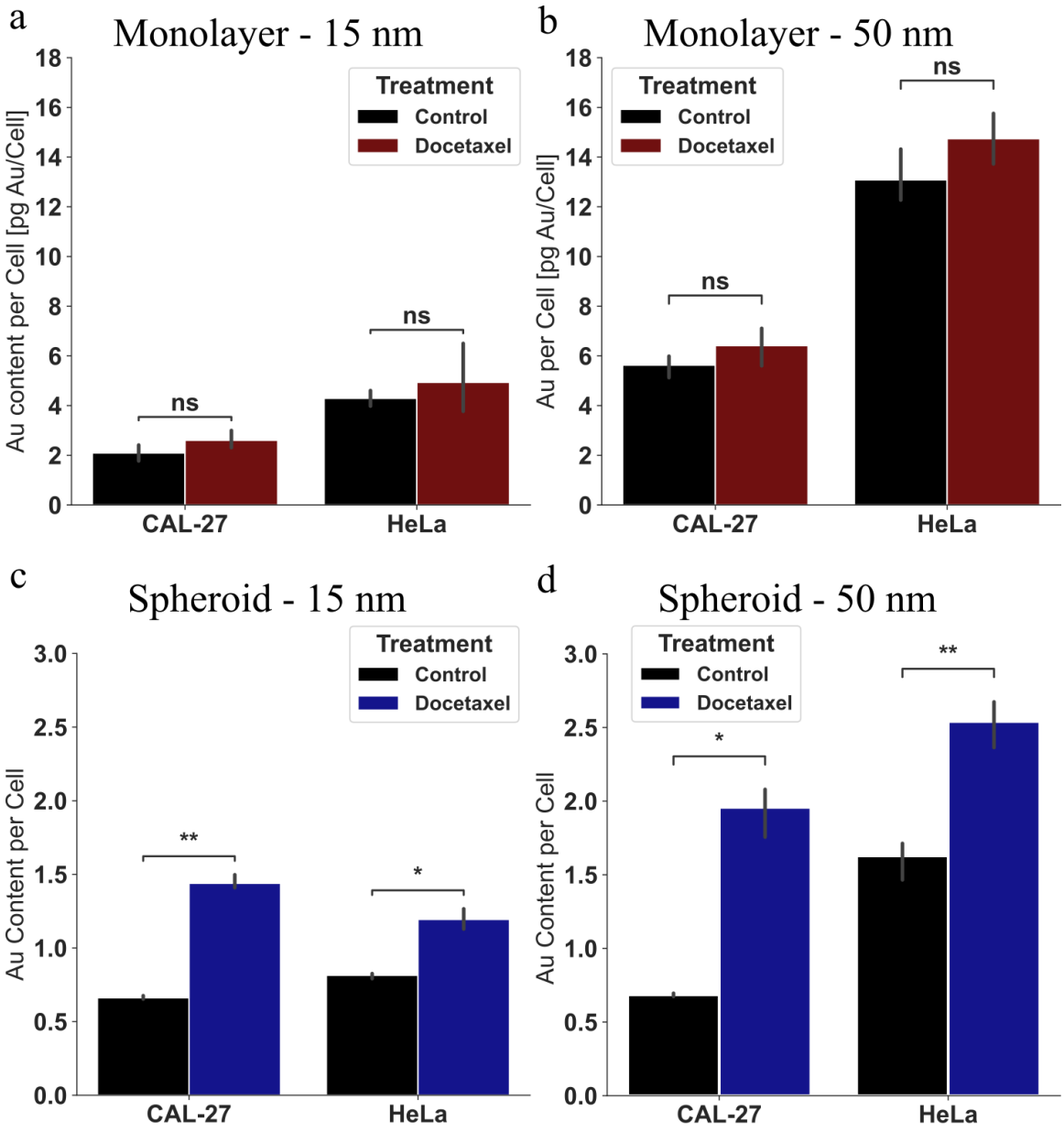


Figure 4.11: **Total gold content uptake in monolayer and spheroids.** (a-b) Total gold content due to uptake of the 15 nm and the 50 nm functionalized gold nanoparticles in monolayer, with and without docetaxel. (c-d) Total gold content due to the uptake of the 15 nm and the 50 nm functionalized gold nanoparticles in spheroids, with and without docetaxel. Error bars signify one standard deviation from average of three measurements. * indicates $0.01 < p < 0.05$, ** indicates $0.001 < p < 0.01$. Reproduced with permission [237]. Copyright MDPI, 2021.

GNPs following treatment with radiation therapy, in the 3D model *vs.* a 2D model. There are many differences when it comes to the environments present in a 2D *vs.* a 3D model. A spheroid-based 3D model introduces the ECM and enables optimizing of nano-based systems due to more realistic, tumor-like conditions. This study suggests that GNPs of different sizes will have different uptake effects based not only on the cell model - 2D *vs.* 3D - but also on the cell line, highlighting a key necessity to use 3D models to properly simulate treatments *in vitro* before transition to an *in vivo* environment. However, the benefits of the 3D spheroid model in modeling radiation combined with GNPs still must be explored in future studies. Further, biochemical analyses of the effect that DTX has on the 3D spheroids when combined with GNPs should be elucidated, beyond just the altered uptake response.

4.4 Conclusion

Gold nanoparticles present an exciting method to improve tumor response while reducing normal tissue toxicity. While shown to be very effective *in vitro* as a radiosensitizer as well as a drug delivery system, translation to the clinic has been slow [261]. Introduction of a more complex 3D tumor spheroid model that can more accurately represent the complex environment present *in vivo*, compared to a 2D monolayer, can facilitate a more rapid translation. Towards this goal, we tested small 15 nm GNPs and larger 50 nm GNPs in the two different *in vitro* models, monolayer and spheroids, and in two different cell lines, CAL-27 and HeLa. The use of DTX, an anticancer drug that can act as a cell cycle synchronizing agent at lower doses to improve uptake of NPs, was also explored in both cell models. When moving into the 3D spheroid model, there were clear benefits over the use of the 2D monolayer model, allowing for better approximation of the effects of cell density and the resulting extracellular matrix. The GNP uptake data followed a similar trend in monolayer and spheroids. However, the use of DTX had a more pronounced effect on the spheroids, increasing GNP uptake significantly. Moreover, the depth of penetration of different sizes of GNPs, an important characteristic that allows for targeting of deep-set tumor cells, found that smaller 15 nm GNPs penetrate more effectively compared to the larger 50 nm GNPs. The use of smart nanomaterials, such as the GNPs used in this study, has great potential due to their ability to act as radiosensitizers and as drug carriers. Our results demonstrate that the 2D preclinical monolayer model present an unrealistic representation of the real tumor-like environment, which could lead to in-

accurate screening of the potential of GNPs and other nanomedicines. The proposed 3D spheroid model is, we believe, an essential tool to validate the efficacy of novel therapeutics, due to the ability of these models to mimic many of the key features that are present in a real TME. Therefore, these results showcase the importance in using more accurate *in vitro* models, such as 3D tumor spheroids, to accelerate the use of nanomedicine into the clinic. The next step in this work is to explore the triple combination of GNPs, DTX, and RT in both cell models to improve cancer therapy.

4.5 Materials and methods

4.5.1 Synthesis, Surface Modification, and Characterization of Gold Nanoparticles

Gold NPs of size 17 nm and 46 nm were synthesized using the citrate reduction method. This was accomplished by adding 300 μL of 1% $HAuCl_4 \cdot 3H_2O$ (Sigma-Aldrich) to 30 mL of double–distilled water and heated on a hot plate while stirring vigorously. Once it reached the boiling point, 300 μL for the larger GNPs, and 1000 μL for the smaller GNPs, of 1% sodium citrate tribasic dihydrate (HOC(COONa) $(CH_2COONa)_2 \cdot 2H_2O$; Sigma-Aldrich) was added and mixed. Once the color of the solution changed from dark blue to red, the solution was left to boil for another ten minutes while stirring. Finally, the GNP solution was brought to room temperature while stirring. The GNPs were PEGylated using PEG of size 2000 Da, along with an RGD peptide of size 1600 Da. PEG was stirred into the GNP solutions such that the grafting density will be 1 PEG molecule per 1 nm2 of surface area. For 17 nm GNPs and 46 nm GNPs, this results in 907 PEG and 6647 PEG molecules per GNP to be added to the solution, respectively. Following PEGylation of GNPs, the peptide containing integrin binding domain RGD (CKKKKKKGGRGDMFG) was added to PEGylated GNPs at a ratio of 1 RGD molecule per 2 PEG molecules, referred through this paper as GNP-RGD. GNPs were characterized using UV-VIS spectrometry (λ Spectrophotometer, Perkin Elmer) for approximate size and concentration estimates. Further, DLS and ζ-potential (LiteSizer 500, Anton Paar) were utilized to measure the hydrodynamic diameter and the surface charge of the particles. Stability of the GNPs was measured in PBS. Imaging of the GNPs with scanning transmission electron microscopy (STEM; SU9000, Hitachi) was used to verify the diameter of the GNPs.

4.5.2 Cell Culture and Growth of Spheroids

HeLa, a human cervical cancer cell line, and CAL-27, a human head and neck cancer cell line, were purchased from the ATCC and have catalogue numbers CCL-2 and CRL-2095 respectively. Both cell lines were cultured in DMEM (Gibco) supplemented with 10% FBS (Gibco), 1% penicillin and streptomycin (Gibco), and 4 mM GlutaMax (Gibco). For cell dissociation, 0.2% trypysin-EDTA (Gibco) was used. For 2D and 3D cell models, all cells were initially split from a monolayer of cells at approximately 80% confluency. For the 2D monolayer cell model, cells were plated such that final confluency at the end point is approximately 70% in either six-well plates or 96-well plates, with initial cell count dependent on time and plate type. Once plated, cells are left in the incubator 37 ^{o}C and 5% CO_2 for 24 h to ensure adherence, after which experiments are initiated. For 3D spheroid cell models, cells are plated in ultra low attachment 96-well microplates (Corning), with 3125 cells for HeLa per well and 12,500 CAL-27 cells per well. The cells are then centrifuged at 350×g for 5 min and left in the incubator at 37 ^{o}C and 5% CO_2. Experiments are initiated once the spheroids form, after incubation for approximately 72 h.

4.5.3 Proliferation Assay of Docetaxel in Monolayer and Spheroids

For the 2D monolayer cell model, 10,000 of each cell line were plated in 96 well black clear bottom microplates (Greiner), leaving one column empty for control. Once adhered, each column (8 wells) was treated with a unique DTX dose ranging from 250 nM to 1.27×10^{-2} nM in media, ensuring that the concentration of dimethyl sulfoxide, which the DTX is stored in, is constant in all columns at approximately 0.05%. Similarly, for the 3D spheroid cell model, once formed, each column (8 wells) was treated with a unique DTX dose ranging from 5000 nM down to 0.254 nM. This was completed in triplicate, on three different plates per cell line. For monolayer, after 24 hr, the media was removed from each sample, cleaned twice with PBS (Invitrogen), and left to incubate for a further 48 hr in fresh media. For spheroids, after 24 hr, half of the media was removed carefully, ensuring the sample was not removed, and then rinsed 5 times with PBS, ensuring approximately a 162× dilution from the initial concentration. Finally, the media was replaced and left for a further 48 hr in the incubator. After 48 hr, all the media for the 2D monolayer model was removed and treated with CellTiter-Glo (Promega) Cell Viability assay, following the manufacturers protocols. Plates were gently mixed for 2 min and luminescence was

measured after a further 10 min using a Cytation 1 Cell Imaging Multi-Mode Reader (BioTek). Similarly, for the 3D spheroid model, the majority of media was removed, ensuring that the sample was not removed, and treated with CellTiter-Glo (Promega) 3D Cell Viability assay, following the manufacturer's protocols. Plates were mixed for 5 min, and luminescence was measured after a further 25 min using the Cytation 1. The proliferation was fit to the Growth Rate Inhibition metric [249]. To calculate the growth rate, we can use equation 4.1, where $GR(c)$ is the growth rate at a set concentration, $x(c)$ is the measured value compared to control, x_{ctrl}. The doubling time T_D is also necessary, along with T, the length of the assay.

$$GR(c) = 2^{\frac{\log_2(x(c)/x_{ctrl})}{T/T_D}} - 1 \tag{4.1}$$

4.5.4 Cellular Uptake of Gold Nanoparticle Complex

Incubation with GNPs was done at a concentration of 7.5 μg/mL for all the stated experiments and for all sizes of GNPs. To test the effect that DTX had on the uptake of the GNPs, the different cell models and cell lines were dosed with the desired concentration found in the cell proliferation experiments concurrently with GNP dosing. This correlated to a dose of 20 nM for a monolayer of HeLa and 50 nM for a spheroid of Hela, and a dose of 5 nM for a monolayer of CAL-27 and 200 nM for a spheroid of CAL-27. Samples were incubated at incubator 37 ^{o}C and 5% CO2 for 24 h following treatment. Cells were then rinsed with PBS at least three times, ensuring no sample is lost when cleaning spheroids, and trypsinized. For spheroid samples, the cells were left in trypsin for 30 min at 37 ^{o}C to improve dissociation and produce a single-cell homogenous solution, while the monolayer samples were left in trypsin for approximately 5 min. The cells were counted using a Coulter Counter (Z2 Coulter; Beckman Coulter) for GNP quantification per cell. To measure the gold content for each sample, 500 μL of each sample were treated with 250 μL aqua regia (3:1 ratio of HCl:HNO_3 (VWR) in a 90 ^{o}C mineral oil bath for a minimum 30 min. After, 100 μL of hydrogen peroxide (VWR) was added and the samples were returned to the oil bath for 30 min, ensuring complete cell breakdown. These samples were then diluted down to 2.5% v/v acid content in deionized water and the gold content was quantified using ICP-MS (8800 Triple Quadrupole, Agilent). Calculation of nanoparticle content based on absolute gold content can be seen in Section 3.6.3.

4.5.5 Preparation of Cells for Imaging Using Darkfield and Hyper Spectral Imaging

To prepare cells for darkfield imaging for 2D monolayer samples, all cell lines were plated in a six-well plate with glass coverslips placed on the bottom of each well. The cells were then treated as described previously using GNP-RGD and DTX at the desired doses. Following treatment, the cells were rinsed three times with PBS and fixed using 4% PFA for 20 min at 37 ^{o}C. The cover slips were then removed from each well and mounted to a glass slide using Permount Mounting Medium (Fisher Scientific). Similarly, for 3D spheroid samples, following treatment of spheroids with GNP-RGD and DTX, the cells were cleaned 5× to dilute GNPs down dramatically, fixed in PFA for 30 min at 37 ^{o}C, and then embedded in optical cutting temperature (OCT) compound (Fisher) and left in a -20 ^{o}C freezer. The spheroids were then sectioned using a MicroTome in a CryoStat (Leica) into 10 μM thick sections and adhered to a charged microscope slide. The sections are washed with acetone to remove excess OCT, then rinsed with water. The slides are then stained again with the eosin stain for 30 s and cleaned three times with 100% ethanol. Finally, the cells are rinsed three times with xylenes which acts as a clearing agent. Coverslips were mounted onto the glass slides using Permount Mounting Medium and were dried overnight for microscopy. Each sample, either monolayer or spheroid, was imaged using darkfield microscopy and HSI (CytoViva) under a 10× and 60× objective. The depth of the GNPs from the surface of each spheroid section sample was measured using ImageJ. A minimum of 100 measurements of depth were taken for each sample using the spheroids imaged with the 10× objective.

4.5.6 Cell Cycle Analysis of Docetaxel Using Flow Cytometry

DTX was administered to the cells at desired concentrations as found in proliferation assay. After set time points of 0, 1, 4, 8, and 24 h, the cells were harvested as described previously using trypsin, and a single cell suspension was formed. Cells were washed with PBS and centrifuged at 300×g for 5 min twice. Cell pellet was then re-suspended in 1% paraformaldehyde in PBS for fixation and incubated on ice for 15 min. Cells were again washed in PBS and centrifuged at 350×g for 5 min. Cells were re-suspended in 0.3 mL PBS and 0.7 mL freezer cold 100% ethanol (overall 70% ethanol). Samples were incubated in the dark at 4 ^{o}C for at least an hour, further fixing and dehydrating the cell sample. Samples were then centrifuged at 350×g for

10 min at 20 ^{o}C. The cell pellet was re-suspended in 1 mL of 0.5% BSA in PBS, denoted as PBS/BSA and centrifuged at 350×g for 5 min at 20 ^{o}C. To permeabilize the cell membrane and degrade RNA, the cell pellet was re-suspended in PBTB (PBS, 0.5% BSA, 0.1% Triton-X 100) followed by an addition of RNaseA at a concentration of 100 μg/mL. Samples were then left to shake at 37 ^{o}C for 25 min. For labelling DNA, tubes were covered in foil, propidium iodide (PI) was added at a concentration of 10 μg/mL and incubated on a shaker at 4 ^{o}C for at least 1 h. The cells were then centrifuged at 350×g for 5 min at 20 ^{o}C. Finally, we re-suspended PI-stained cells in 1 mL of PBS/BSA and passed the solution through a 50 μM cell strainer before running on a flow cytometer (FACS Calibur, BD Biosciences). PI is highly fluorescent at 488 nm with broad emission centered around 600 nm. The amount of DNA content indicates which phase the cell population is in, and thus how synchronized it is.

4.5.7 Statistical Analysis

A Welch's independent t-test with Bonferroni correction was performed using the statannot Python package, as described in Section 3.6.8. A p value <0.05 was considered statistically significant. Experiments were repeated three times and the data presented is the average, for all experiments.

Chapter 5

Combined cancer therapy and gold nanoparticles

5.1 Preamble

Partial content in this section is reproduced with permission from Nature: Scientific Reports, and parts of it have been published with the following citation:

> Bromma, K., Dos Santos, N., Bartra, I., Alexander, A., Beckham, W., Krishnan, S., Chithrani, D.B., Enhancing nanoparticle accumulation in two dimensional, three dimensional, and xenograft mouse cancer cell models in the presence of docetaxel. *Scientific Reports*. https://doi.org/10.1038/s41598-022-17752-5 (2022)

The candidate, KB, made substantial and direct contributions to the conception and design of the experimental plan. KB made substantial contribution to sample preparation, collection, and processing. K.B. made substantial contribution to the acquisition of the data, including all monolayer and spheroid data.

Experimental Conception: KB, AA, WB, SK, DBC
Experimental Design: KB, AA, WB, SK, DBC
Performed Experiments: KB, NDS, IB
Analyzed Data: KB
Made Figures: KB
Writing of Manuscript: KB

5.2 Introduction

When optimizing the treatment of a combined therapy platform, a two-dimensional (2D) monolayer of cells has been largely utilized. However, the use of a flat surface of cells has been criticized for being an inaccurate view of the complex, heterogeneous tumor microenvironment (TME) that exists within a malignancy [262]. There is a loss of tissue-specific architecture, intra-cellular contact, and cell-cell communication that is present in a tumour. Further, a monolayer of cells is grown on a flat substrate that allows the cells to stretch, forming an increased surface area that is directly exposed to culture medium, including drug treatments [263]. There is compelling evidence that the TME plays a critical role in cancer development and progression, which monolayer culture can not properly model [264]. These limitations, however, give way to the large advantage that a monolayer of cells provides, such as low cost, high throughput, and a high degree of control over environmental factors [252]. Aside from these benefits, there may be many inconsistencies when it comes to comparing monolayer culture to *in vivo* experimental results, and thus a better *in vitro* solution should be explored.

By growing a three-dimensional (3D) structure in the lab, we can bridge the gap between monolayer and *in vivo* approaches and improve the physiological relevance of *in vitro* assays. There are many various types of 3D culture models that can be implemented in the lab, such as tumour tissue explants, tumor grown on chips, and multicellular spheroids [263]. While various models have benefits, multicellular spheroids are one of the most well characterized models of *in vitro* cancer. Spheroids are aggregates of either a single or multiple cell types which have 3D cell-cell contact and proliferate in a geometry that is very similar to that observed *in vivo*. Thus, spheroids can stimulate the production of an extracellular matrix (ECM) [265]. There are many benefits that can be ascertained from the 3D structure of spheroids. This includes the establishment of a gradient of nutrients, O_2, and pH as they grow larger. Further, a cross section of a spheroid reveals concentric rings of a heterogeneous cell population that is commonly observed *in vivo*, as can be partially observed in Figure 5.1a. These populations generally comprise of an innermost necrotic zone, a middle quiescent layer where the cells are viable but not growing, and an outer proliferative layer that leads to most of the tumour growth [266]. However, while 3D multicellular spheroids have proven to be a better model to mimic an *in vivo* tumour, experimentation in furthering cancer treatments has not been widely explored.

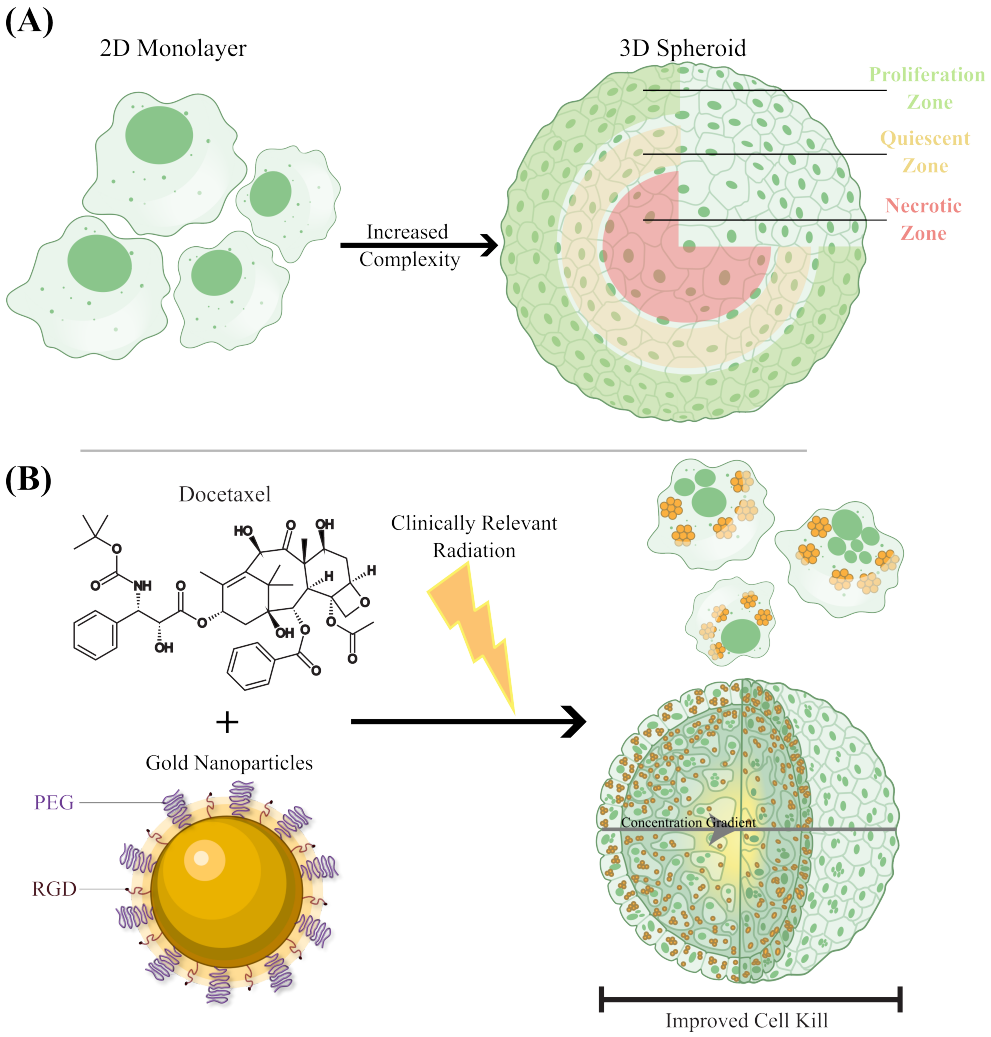


Figure 5.1: **Improved cell kill with combined cancer therapy.** (a) A multicellular spheroid is a three-dimensional *in vitro* tissue structure that can better approximate the complex heterogeneous *in vivo* tumour microenvironment. This includes modelling the extracellular matrix, which has a proliferation zone on the outer edge of the spheroid, a quiescent zone in the middle of the spheroid where the cancer does not grow effectively, and possible necrotic core, where the cells lack the nutrients to survive due to the concentration gradient and are either hypoxic or are dead. (b) With the addition of GNPs and DTX, the cancer cells become more sensitized to radiation, and we see an improved cell kill response. This occurs even in clinically relevant 6 MV radiation.

When evaluating the effect of radiotherapy (RT) on the survival of cancer cells, 3D spheroids are a more viable option compared to the 2D monolayer as they are more representative of an actual *in vivo* TME. There is an observed increase in resistance to RT when comparing 3D spheroids to 2D culture [267]. Furthermore, while the use of RT is widely used in the clinic, the benefits it provides to treating tumours have been largely optimized by modalities such as image guided RT (IGRT) for precise beam positioning and intensity modulated RT (IMRT) for dose conformity [268, 22]. Thus, to improve patient outcomes, novel techniques must be explored, such as the use of nanomaterials. One nanomaterial, gold nanoparticles (GNP), offer many potential applications in cancer therapy due to its high density (Z=79) compared to soft tissue (Z≈7.5). GNPs can be used to enhance the effectiveness of radiation treatment by increasing the absorption of radiation in cancer cells. When GNPs are exposed to ionizing radiation, such as X-rays or gamma rays, they can generate cascades of electrons that can cause damage and produce reactive oxygen species that can kill cancer cells. This process, known as the GNP-mediated radiosensitization effect, has been shown to be effective in preclinical studies using animal models [269]. We have previously optimized the uptake dynamics of GNPs in 2D monolayer and 3D spheroids, using various cell lines that approximate the TME in Chapters 3 and 4.

To further improve the combined treatment of RT and GNPs, we can also include the chemotherapeutic agent DTX. DTX is a commonly used therapeutic agent that is used to treat a number of cancers, including cervical cancer and prostate cancer [270, 271]. DTX works by causing the unregulated formation of microtubules [272]. Further, DTX can also act as a radiosensitizer due to its ability to arrest the cell cycle and synchronize a population into the radiosensitive G2/M phase. As explained in Section 2.1, a cell forms a mitotic spindle when going through cell division. However, with DTX, the microtubules are sequestered into bundles and thus hinder the formation of the mitotic spindle [273]. DTX also forms asters and bundles independent of centrosomes which can allow for multiple cleavage planes, leading to a mitotic catastrophe. This results in cells that are either stuck in mitosis, or form a multinucleated cell as the nuclear envelope surrounds the multiple asters. Thus, when combining DTX with GNPs and RT, we expect to see an additional radiosensitizing effect beyond GNPs and RT alone. The use of DTX with GNPs has also been shown to improve long term retention, a benefit when it comes fractionated therapy [239]. The benefit of using this combined therapy can be seen in Figure 5.1b, where the utilization of GNPs and DTX adds two radiosensitizers that can stimulate further

damage in the tumour periphery with radiation, leading to improved cell kill and a reduced growth response. By more effectively removing the outer cells of the spheroid, a tumour can be 'peeled' like an onion with multiple fractions, leading to eventual death of the cancer.

This study's goal was to explore the application of GNPs and DTX in a combined therapy modality with RT. This response will be compared in a 2D monolayer model and 3D spheroid model to showcase the benefit of using GNP and DTX even if the penetration depth of the combination treatment follows the concentration gradient. Further, this work can be used to compare in future work in *in vivo* animal models to observe any limitations in dose response. This is one of the the final pillars in the foundation for a better platform for testing GNPs in the lab before entering the clinic.

5.3 Results and Discussion

5.3.1 Characterization of gold nanoparticles and spheroids

For this study, small spherical GNPs of approximately 17 nm in diameter were conjugated with PEG and a peptide containing integrin binding domain RGD. The addition of PEG ensures stability in serum, such as *in vivo* circulation, while the addition of the RGD peptide improves uptake and can target integrin-overexpressing cells, commonly found in cancer [243, 216]. Further, the use of RGD is also beneficial in targeting the ECM. The RGD motif is expressed within various proteins such as fibronectin, vitronectin, fibrinogen, osteopontin, and bone sialoprotein [205].

Smaller nanoparticles have been found to enter cancer cells more effectively in complex spheroid environments, as shown in Chapter 4, as well as in an *in vivo* environment [275]. This is a result of the ECM limiting the penetration depth of larger NPs. Visualization of the GNP complexes can be done using hyper spectral imaging (HSI), as seen in Figure 5.2a, to gather their spectrum for future verification in cells. Verification of GNP presence using HSI has been widely utilized in literature, from monolayer to *in vivo* section analysis [219]. HSI is a useful technique as it allows for each pixel in an image to be associated with a complete reflectance spectral response, with a spectral resolution of 2 nm in the visible-near infrared range. GNPs have a unique reflectance spectral response, due to their surface plasmon resonance [82]. Thus, using HSI allows us to capture this response and easily identify GNPs compared to tissue or cells. The GNP complexes were also measured using scanning

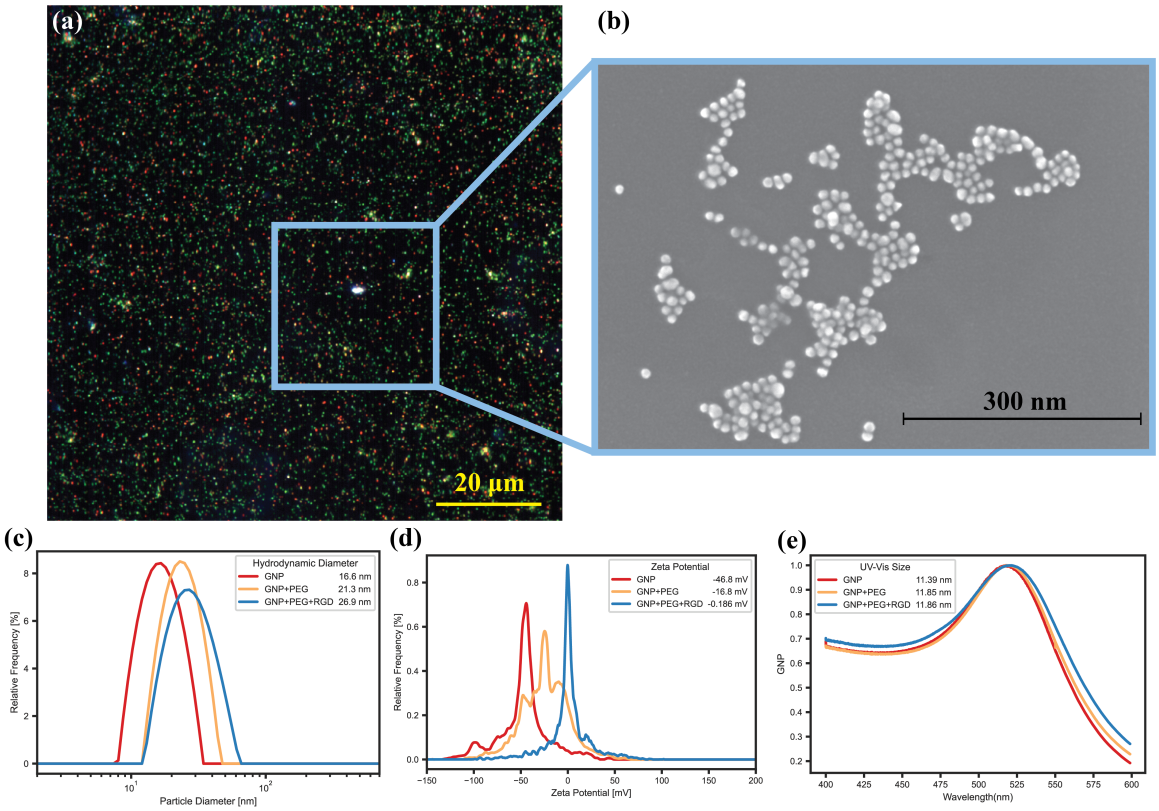


Figure 5.2: **Characterization of gold nanoparticles.** (a) Hyper spectral imaging of gold nanoparticles decorated with polyethylene glycol (PEG) and a peptide containing RGD. Scale bar is 20 μm. (b) Secondary electron image from a transmission electron microscope of gold nanoparticles. Scale bar is 300 nm. (c) Size of gold nanoparticles measured by dynamic light scattering while bare, with PEG, and with PEG and RGD. (d) Surface ζ-potential of bare and decorated GNPs. (e) Size as measured by the UV-Visible absorbance spectrum of bare and decorated GNPs. Partially reproduced with permission [274]. Copyright Nature, 2022.

transmission electron microscopy (STEM; Figure 5.2b) to verify GNP size, shape, and stability following functionalization. The measured average core size was 12.47 ± 1.21 nm after conjugation with PEG and RGD. Bare GNPs had a similar measured core size of 12.76 ± 2.8 nm, signifying no aggregation was present. Measurement of the GNPs before and after conjugation with PEG and RGD was also done using dynamic light scattering (DLS; Figure 5.2c). DLS measured the bare GNPs to have a hydrodynamic diameter of 16.6 ± 0.33 nm, 21.3 ± 0.43 nm after PEGylation, and 26.9 ± 0.54 nm after addition of RGD peptide. The combination of GNP, PEG, and RGD is referred to as a GNP complex throughout this work. The difference in the size of the measured diameter in DLS and measurement using STEM is due to the

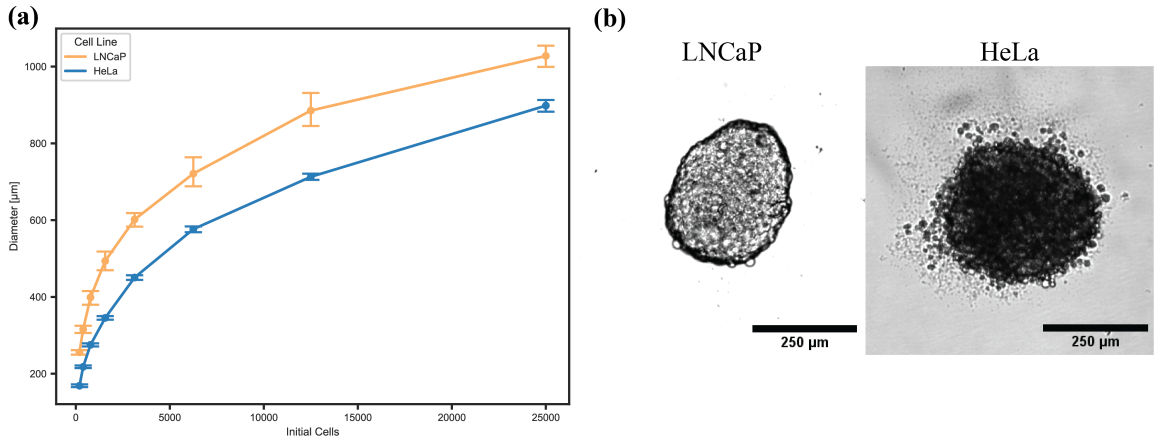


Figure 5.3: **Characterizing spheroid size.** (a) Size of the spheroids for HeLa and LNCaP under different initial cell count conditions. An approximate size of 300-400 μm was used for all experiments. (b,c) Brightfield images of the spheroids under different initial cell counts, scale bar is 250 μm.

DLS measuring the hydrodynamic diameter, which includes surface ligands. STEM images only show the dense gold in the nanoparticle core [276]. The size of the GNPs was also measured using Ultraviolet-Visible (UV–VIS) spectrometry to estimate the size and concentration whilst confirming stability of the GNP complex (Figure 5.2e) [217]. The measured size was found to increase from 11.4 ± 0.1 nm to 11.9 ± 0.1 nm following functionalization with PEG and RGD, further indicating no aggregation and a stable formulation.

The ζ-potential is a useful measure of the suspension stability and can be used to confirm surface adsorption due to different electric potentials of various moieties [277]. To verify conjugation of PEG and RGD, the ζ-potential (Figure 5.2d) was measured to be -46.80 ± 1.24 mV for bare GNPs, -16.80 ± 0.63 mV for PEGylated GNPs, and -0.19 ± 0.28 mV for GNP complexes. The increase in the ζ-potential is due to the replacement of the negatively charged citrate molecules on the surface of GNPs with neutral PEG molecules and positively charged RGD peptides. As indicated in Section 4.3, the GNP complexes are stable in highly ionic environments and are suitable for testing purposes.

To optimize the treatment with GNPs, the 3D spheroids were characterized. While a 2D model involves single cells, the 3D spheroids introduce a more complex environment, including the ECM and a drug concentration gradient, as seen in Figure 5.1. For the 3D spheroid, a diameter of approximately 300–400 μm was chosen as an optimum spheroid size. Larger spheroid sizes (>350 μm) can introduce a necrotic

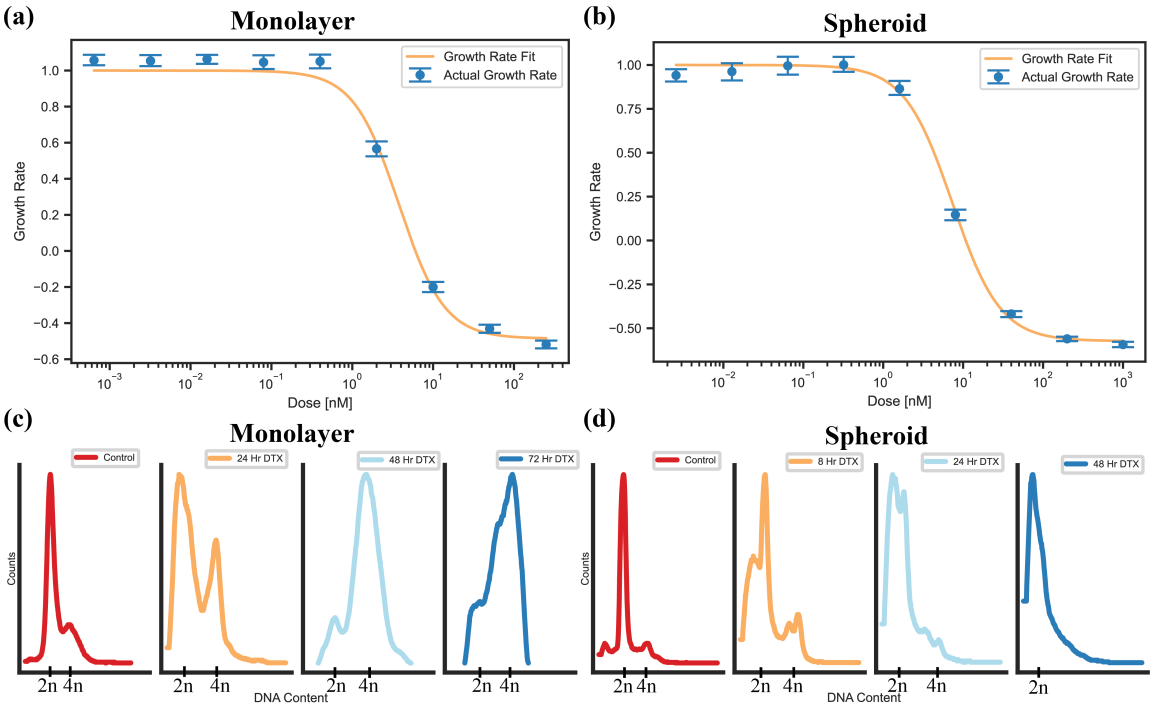


Figure 5.4: **Docetaxel characterization in HeLa.** (a,b) Proliferation assays for a (a) two-dimensional monolayer and a (b) three-dimensional spheroid, for the cervical cancer cell line HeLa, treated with docetaxel. (c,d) Cell cycle analysis of a (c) monolayer and (d) spheroids of HeLa cells treated with the GR50 dose of docetaxel, calculated per modality.

core and increased number of quiescent cells, affecting results [248]. Different cell lines will have different packing densities and thus will require a varying number of initial cells for spheroid formation. It was observed that 3125 cells for HeLa and 1000 cells for LNCaP spheroids was optimal, as seen in Figure 5.3. The packing density has been previously shown to affect the efficacy and penetration of anticancer drugs and smaller nanoparticles. Mimicking these *in vivo* effects is one of the many benefits of using a 3D spheroid model over a 2D monolayer model [246].

5.3.2 Docetaxel in spheroids and monolayer

DTX has been shown to synchronize cells in the G2/M phase of the cell cycle, thus effectively acting as a radiosensitizer. Further, DTX can alter the uptake of GNPs in monolayer as well as spheroids, as seen in Chapter 4. Due to toxicity of DTX at higher doses, the ideal dose will not increase cell death, but rather synchronize the cell population. This will effectively improve the uptake of GNPs and act synergistically

with the radiosensitizing effects of the GNP complexes. To measure the optimal dose, we used the growth rate inhibition metric to observe the dose in which division time was essentially halted and cytostasis was achieved [249]. For monolayer, this occurred at 3.779 ± 0.16 nM and 0.94 ± 0.034 nM for HeLa and LNCaP, respectively (Figure 5.4a). These doses agree with IC50 values found in literature. For spheroids, the resulting DTX dose showed the higher resistance to treatment inherent to the more complex 3D environment, with HeLa needing a dose of 7.33 ± 0.25 nM and LNCaP requiring a dose of 3.93 ± 0.50 nM (Figure 5.4b). Proliferation data for LNCaP can be seen in Figure 5.5a, b. Compared to a clinical dose, the area under concentration-time curve ($AUC_{0\rightarrow 24}$) is 90.70 ± 3.84 nM·h and 22.56 ± 0.82 nM·h for a monolayer of HeLa and LNCaP, respectively, and 175.92 ± 6.00 nM·h and 94.32 ± 12.00 nM·h for HeLa and LNCaP spheroids, respectively. A median $AUC_{0\rightarrow 24}$ of 1284 nM·h is observed clinically for a lower dose of 20 mg/m^2, showing the implemented doses are clinically comparable. Further, the doses tested will have low concerns of potential side effects when translating to a clinical environment[254].

The synchronization effects of DTX in monolayer and in spheroids were then explored using flow cytometry (Figure 5.4c,d). DTX has previously been shown to synchronize cell populations in the radiosensitive G2/M phase of the cell cycle. For a monolayer of HeLa, there was a fast shift from a normal cell population to a large population of cells in the G2 phase after 24 hr. The shift to a G2-synchronized cell population happened more gradually for spheroids. These results indicate the chosen dose is working as desired.The inability to differentiate between G1/G2 peaks in the spheroids may be indicative of mitotic catastrophe, where the cells become multinucleated and only have single pairs of DNA or less per nucleus. However, they are still synchronized. This synchronization effect was maintained for at least 72 hr for both cell models. For LNCaP (Figure 5.5c,d), we did not see a synchronization effect in the monolayer or spheroids, indicating either a resistance in the LNCaP cells to DTX or cells that were affected by DTX failed to transition through S phase to the G2 phase. This has previously been observed in literature [278].

The cell response due to the desired doses of DTX were explored using darkfield imaging. DTX causes unregulated formations of microtubules, sequestering them into bundles which hinders the formation of the mitotic spindle necessary for cell division [273]. As a result, in a monolayer of HeLa cells, compared to control (Figure 5.6a,b), we can see some multinucleated cells caused by this mechanism of action in the darkfield images. The multinucleated cell is circled in red in Figure 5.6b.

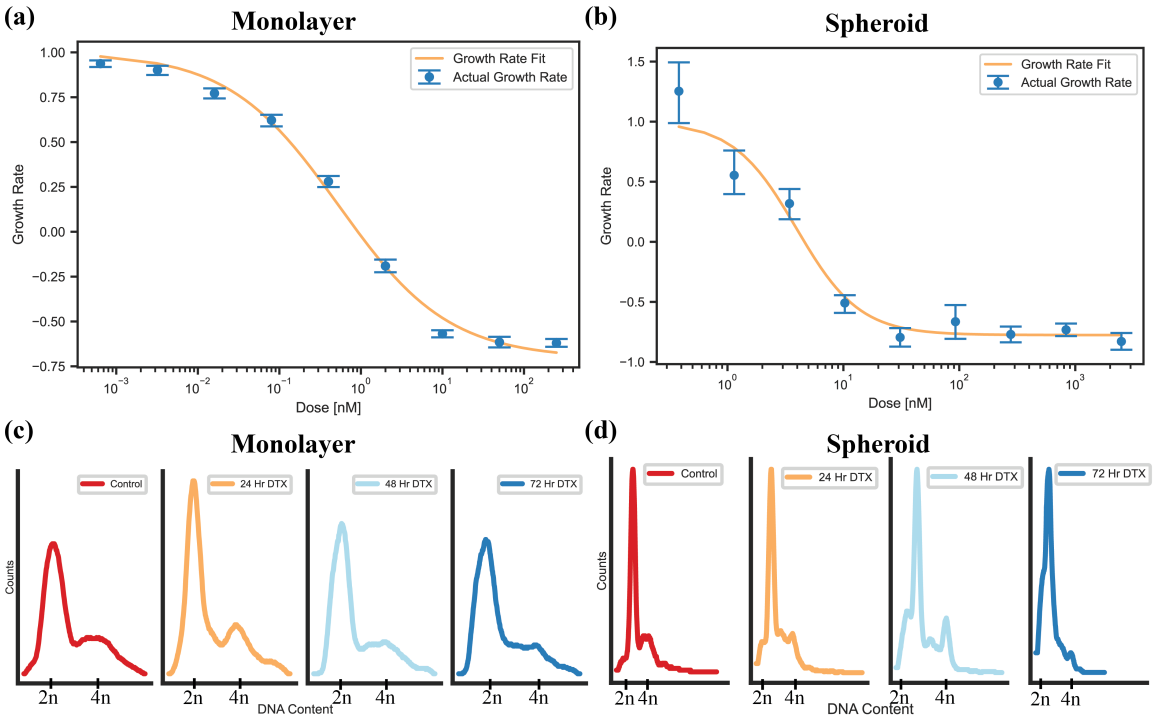


Figure 5.5: **Docetaxel characterization in LNCaP.** (a,b) Proliferation assays for a (a) two-dimensional monolayer and a (b) three-dimensional spheroid, for the prostate cancer cell line LNCaP, treated with docetaxel. (c,d) Cell cycle analysis of a (c) monolayer and (d) spheroids of LNCaP cells treated with the GR50 dose of docetaxel, calculated per modality.

Spheroids appear to have a slightly disrupted core compared to untreated spheroids (Figure 5.6c,d.). However, the extent is limited, allowing for the bulk of the spheroid to maintain a spherical structure. Hyper spectral profiles, from HSI microscopy, of the cells and background were added to each darkfield image as an inset figure to verify the presence or absence of measured GNPs in the image. The lines in the image are the mapping of what wavelength corresponds to blue, green, and red for the displayed hyper spectral image.

To compare the *in vitro* 2D and 3D models, we measured the GNP uptake in monolayer as well as in spheroids after treatment with DTX. Both models were treated with the GNP complex at a clinically relevant dose of 10 μg/mL for 24 h. This dose has shown radiosensitization effects before at megavoltage (MV) energy ranges in a prostate cancer *in vivo* model [98]. We can see in Figure 5.7a the measured uptake of the GNP complex in monolayer for both cell lines for control and DTX. There was a 15% increase for HeLa which was not significant, while in LNCaP, there was a

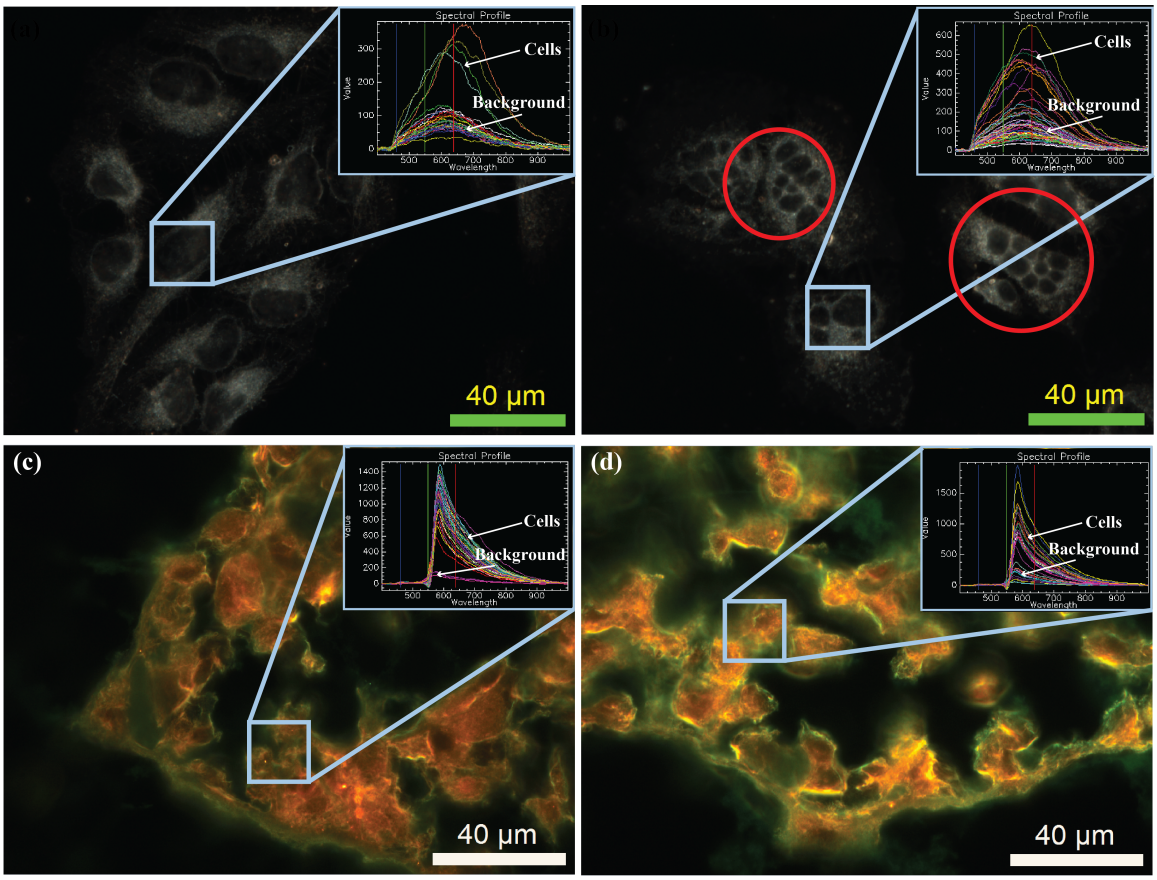


Figure 5.6: **Darkfield images of monolayer and spheroids.** (a,b) Darkfield images of a monolayer of HeLa (a) without and (b) with docetaxel. Cells with multinucleated cells due to docetaxel have been circled in red on (b). Scale bar is 30 μm. (c,d) Darkfield images of 10 μm sections of HeLa spheroids (c) without and (d) with docetaxel. Inset is hyper spectral spectrum of cells. Scale bar is 40 μm. Partially reproduced with permission [274]. Copyright Nature, 2022.

significant increase in uptake of 75.4% ($p<0.05$). While LNCaP did not have observed synchronization of the cells, there was still an effect on both cell lines that increased the GNP uptake.

In Figure 5.7b, the measure uptake of GNP complex in spheroids for both cell lines, with and without treatment of DTX, is displayed. There was a significant increase in uptake after dosing with DTX of 46.57% ($p<0.001$) and 111.9% ($p<0.001$) in both HeLa and LNCaP spheroids, respectively. Both HeLa and LNCaP saw beneficial uptake in monolayer and in spheroids with the addition of DTX, with the increase in spheroids being more drastic. This effect is observed despite the dose of DTX being normalized to the same growth rate. This may be a result of a higher dose of DTX

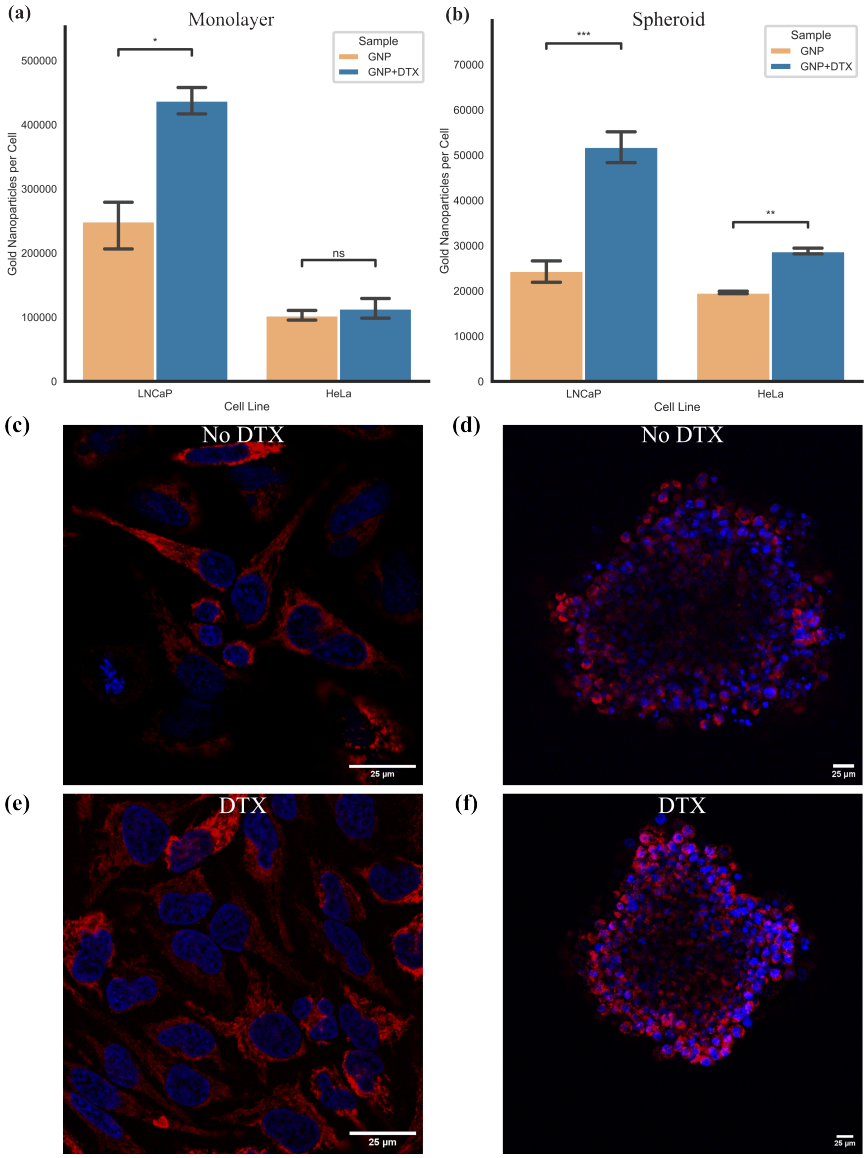


Figure 5.7: **Gold nanoparticle uptake in monolayer and spheroid.** (a,b) Uptake of gold nanoparticles in (a) monolayer and (b) spheroids of HeLa and LNCaP with and without docetaxel. Error bars are the 95% confidence interval from three independent experiments. (c,e) Confocal images of a monolayer of HeLa with gold nanoparticles, (c) without and (e) with docetaxel. (d, f) Confocal images of spheroids of HeLa with gold nanoparticles, (d) without and (f) with docetaxel. Gold nanoparticles and nuclei are marked in red and blue, respectively. Scale bars are 25 μm. ns indicates no significance, * indicates $0.01<P<0.05$, ** indicates $0.001<P<0.01$, *** indicates $0.0001<P<0.001$.

in spheroids that will disproportionately affect the outer cells. The outer cells are the same cells that will have the largest uptake of GNPs, due to the concentration

gradient. These cells will experience a larger DTX effect due to the higher dose and have an amplified uptake compared to monolayer. In monolayer, there is a lower dose of DTX and thus less effect on the cells. This increased effect agrees with previously measured values on separate cell lines from prior experiments in Chapter 3 and 4. . Due to the synchronization of the cells into the G2/M phase with DTX, it is expected for a higher quantity of GNPs to be present in the cell population relative to other phases. This is a result of having a larger time in the cell cycle to accumulate GNPs before division. The process of cell division will lead to the dilution of the per-cell GNP load, observed in cells that are distributed in the cell cycle more regularly.

For the HeLa cancer cells, after concomitant treatment of DTX and GNP complex, we can see in confocal images the accumulated GNPs in monolayer (Figure 5.7c,e) and in the spheroids (Figure 5.7d,f) *vs* control. The GNPs can be visually seen to increase in the monolayer of cells, despite the quantification not having an observable statistically significant increase in uptake. We have also previously shown that DTX-treated cells tend to gather the GNPs closer to the nucleus, which may result in an increased radiosensitization effect to the most vulnerable organelle35. Further, we can see how the distribution of GNPs is largely contained to the edge of the spheroid in the confocal images of the spheroids ((Figure 5.7d,f). In the DTX-treated sample, the spheroid is slightly smaller, possibly due to halting of the cell cycle, while also having a visual increase in the amount of gold. The increased GNP uptake in the shell of the spheroid can allow for an increased efficacy in a fractionated treatment. This can more effectively 'peel the onion' of the tumour layer by layer – or fraction by fraction - due to the increased radiosensitization caused by GNPs.

5.3.3 Radiation response in monolayer

As mentioned in Chapter 3, the gold standard for measuring cell reproductive death following treatment with radiation is the clonogenic assay. However, while the clonogenic assay is effective, it is susceptible to human error and inconsistencies. The application of a proliferation assay can measure viable cells over time effectively and with very little error due to larger cell counts. Additionally, a 2D based assay like the clonogenic assay that is applicable to a more homogeneous population is not the most optimum approach, due to the heterogeneous nature of 3D structures. Thus, for a monolayer of HeLa and LNCaP, the use of the PrestoBlue assay was applied to measure radiation efficacy. PrestoBlue is a resazurin based reagent that, in the pres-

ence of various proteins in the cell that are relevant in cellular respiration like FADH and NADPH, will reduce to resorufin [279]. Resorufin is strongly fluorescing and is an accurate measurement of total cell viability. Thus, following radiation, we can use PrestoBlue to measure the metabolically active cells under different treatments. This will be a proxy for how effective each treatment is.

Measurement of monolayer growth using PrestoBlue was limited to 6 days, as the populations reached confluence past this point. Following 24 hours of treatment with GNPs and DTX, the cells were either not radiated, or radiated with 2 Gy, 5 Gy, and 10 Gy. The metabolically active cells after 6 days can be seen Figure 5.8a,b. We can observe that for unirradiated samples for HeLa (Figure 5.8a), DTX limited the growth in monolayer effectively. DTX limited the growth in monolayer effectively. Moreover, for 0 Gy, there was no significant difference when adding GNPs to either untreated samples or samples treated with DTX. This highlights the safety of these GNP complexes. When the cells are irradiated with 2 Gy, we can see that there is a significant difference in active cells between control and GNP-treated samples. Active cell count lowers from 97.82% to 86.79%, a relative change of 11.29% ($p<0.001$). There was no significant difference in DTX treated samples. In 5 Gy and 10 Gy samples, we see a similar trend in difference in active cells between control and GNP-treated samples. After 5 Gy, there is a reduction in active cells from 85.40% to 69.62%, a relative change of 18.48% ($p<0.001$). For 10 Gy, the amount of active cells reduces from 45.45% to 27.02%, a relative change of 40.55% ($p<0.00001$). Further, in DTX-treated and combined GNP+DTX-treated samples, we see a significant decrease in active cells after radiation with 5 Gy and 10 Gy. For 5 Gy, DTX samples reduced active cells to 15.84% and DTX+GNP reduced active cells to 13.27%, a relative change of 16.22% ($p<0.05$). For 10 Gy, DTX lowered active cells to 8.04% and DTX+GNP lowered active cells to 6.09%, a relative change of 24.25% ($p<0.05$). LNCaP (Figure 5.8b) had a similar result.

There is an observed trend of a larger relative decrease in active cells in GNP-treated samples when the dose of radiation increases. This observation makes sense when recalling the mechanism of action of GNPs. As more high energy X-rays interact with the GNPs, there will be a larger amount of energy absorbed in the gold relative to soft tissue. This will lead to increased cascades of Auger electrons as well as an increase in ROS production. As a result, there will be an increase in damage to DNA and cellular structures. With larger doses, this effect will be amplified as the repair abilities in the cell will be overloaded due to the increase in damage. When adding

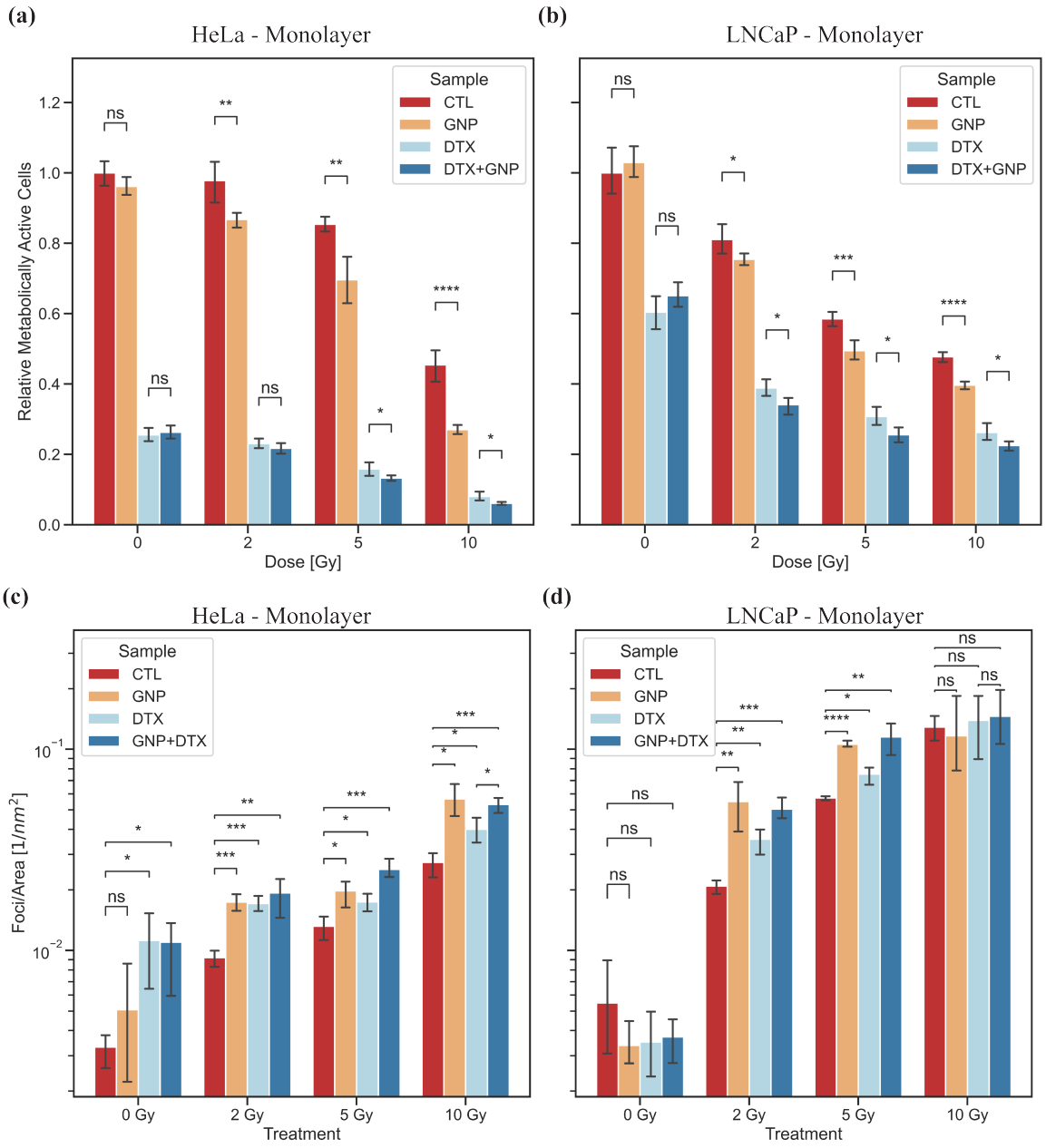


Figure 5.8: **Radiation response in monolayer.** (a,b) Normalized PrestoBlue proliferation assay after 6 days following radiation for (a) HeLa and (b) LNCaP. Error bars are the 95% confidence interval from three independent experiments. (c,d) Normalized 53BP1 foci per nuclear area 24 hours following radiation in (c) HeLa and (b) LNCaP. Error bars are the 95% confidence interval from at least 50 nuclei from three experiments. ns indicates no significance, * indicates 0.01<P<0.05, ** indicates 0.001<P<0.01, *** indicates 0.0001<P<0.001, **** indicates P<0.0001.

DTX, there is a further increase in radiosensitizing effect. DTX's radiosensitizing ability is accomplished through cell cycle synchronization in the G2/M phase. As there is no increase in secondary electrons or ROS production, the effect of DTX should be relatively consistent as the radiation dose increases. When adding GNPs to DTX-treated samples, we observe a similar decrease in active cells with increasing radiation dose. Overall, in monolayer, there appears to be a benefit in using GNPs with higher doses. This may be especially useful in prostate cancer, as many protocols that treat these malignancies require hypo-fractioned dose regimes [280].

We performed an immunofluorescent assay to further validate the data generated from cell proliferation curves. This was done by probing DNA damage using antibodies against the repair protein 53BP1. This protein is present in the event of a DNA DSB. The 53BP1 foci were measured 24 hrs after treatment which allows us to gather information of residual damage. The remaining DNA damage is likely to go unrepaired and is more likely to lead to loss of clonogenic potential [225]. As explained in Section 3.4, 53BP1 foci signal a repair that is facilitated by NHEJ and is largely a DNA DSB sensor, while other repair proteins such as γH2AX can be related to defective DNA repair or genomic instability, and thus are less reliable. Confocal images of HeLa and LNCaP showcasing 53BP1 foci (green) in the nuclei (blue) can be seen in Figure 5.9 and Figure 5.10, respectively.

Further, the number of foci were quantified as described in Section 5.5. HeLa, after no radiation, we observe that DTX had a significant increase in foci/area (DTX: $p<0.05$, GNP+DTX: $p<0.05$) relative to control. DTX is not known to increase production of DNA DSBs by itself, so this result could simply be due to radiosensitization caused by DTX. This increase in radiosensitivity can then allow the background radiation to cause more damage in the genomically unstable HeLa cells41. This same effect was not observed in LNCaP. This is likely due to LNCAP having a lower response to DTX as well as being more genetically stable [281].

When looking at irradiated HeLa and LNCaP, there is a significant increase in 53BP1 foci when treated with GNPs, DTX, and combined GNP/DTX. For LNCaP, after being radiated with 10 Gy, the number of 53BP1 foci was saturated and counting the increase of individual foci was rendered difficult. As a result, at 10 Gy, LNCaP had no significant result. As expected, the base level - without GNPs and DTX - of 53BP1 foci per area increased with increasing radiation dose. Following radiation for both HeLa and LNCaP, the increase of 53BP1 foci can be observed in both GNP and GNP+DTX treated samples, compared to control and just DTX. For HeLa,

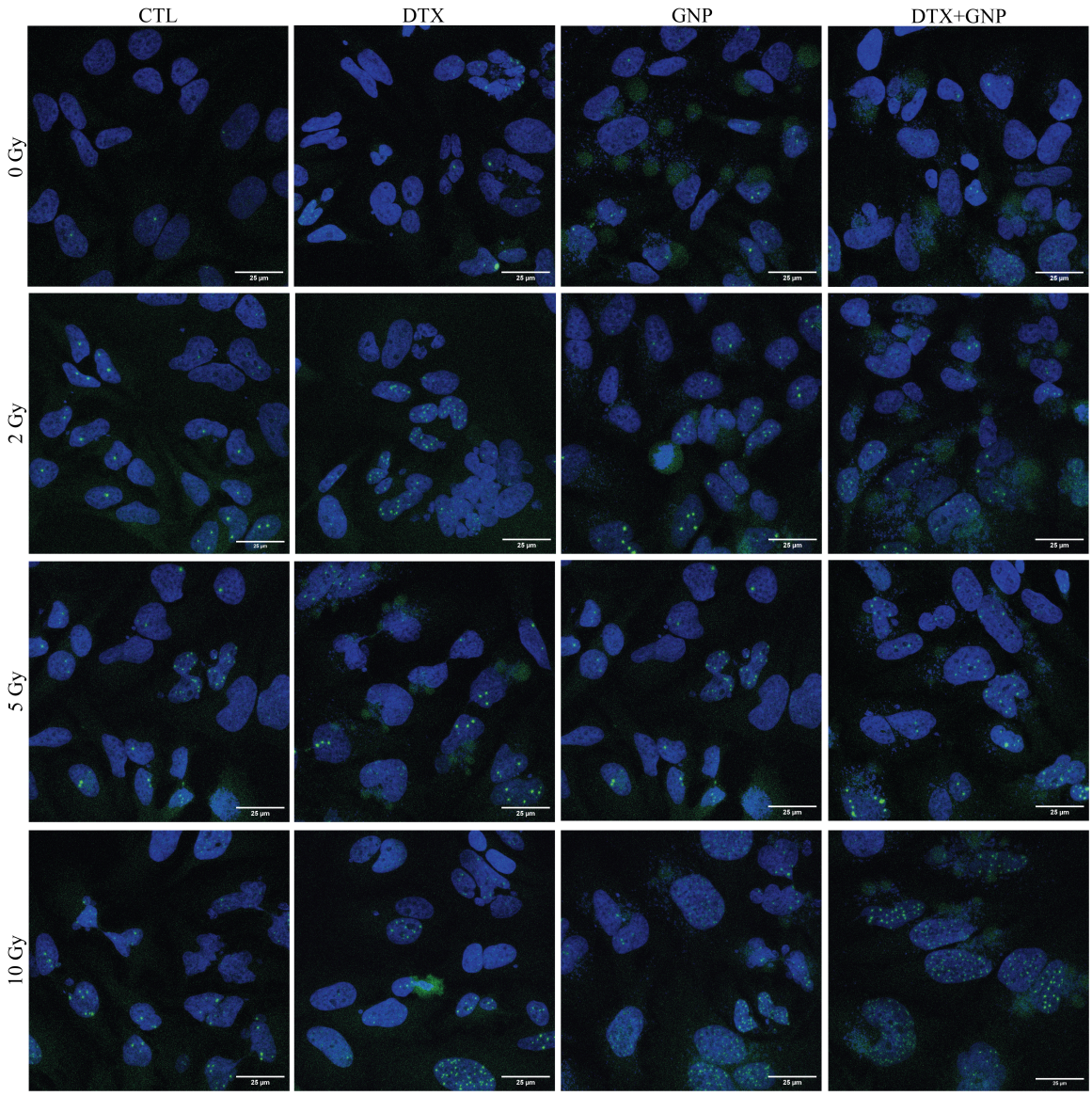


Figure 5.9: **Confocal images of 53BP1 foci in monolayer of HeLa.** Images of HeLa nuclei 24 hours after being irradiated with 2 Gy, 5 Gy, and 10 Gy. Samples include untreated, docetaxel treated, gold nanoparticle treated, and combined docetaxel and gold nanoparticle treatment. Nuclei and 53BP1 foci are marked in blue and green, respectively. Scale bar is 25 μm.

compared to control after irradiation with 2 Gy, we see an increase in DNA DSB foci per nuclear area of 87.9% ($p<0.001$), 85.7% ($p<0.001$), and 109.9% ($p<0.01$) for GNP, DTX, and GNP+DTX treated samples, respectively. Likewise, for 5 Gy, we see an increase of 49.6% ($p<0.05$), 31.9% ($p<0.05$), and 91.6% ($p<0.001$) for GNP, DTX, and GNP+DTX treated samples, respectively. Finally, for a 10 Gy dose, we see an

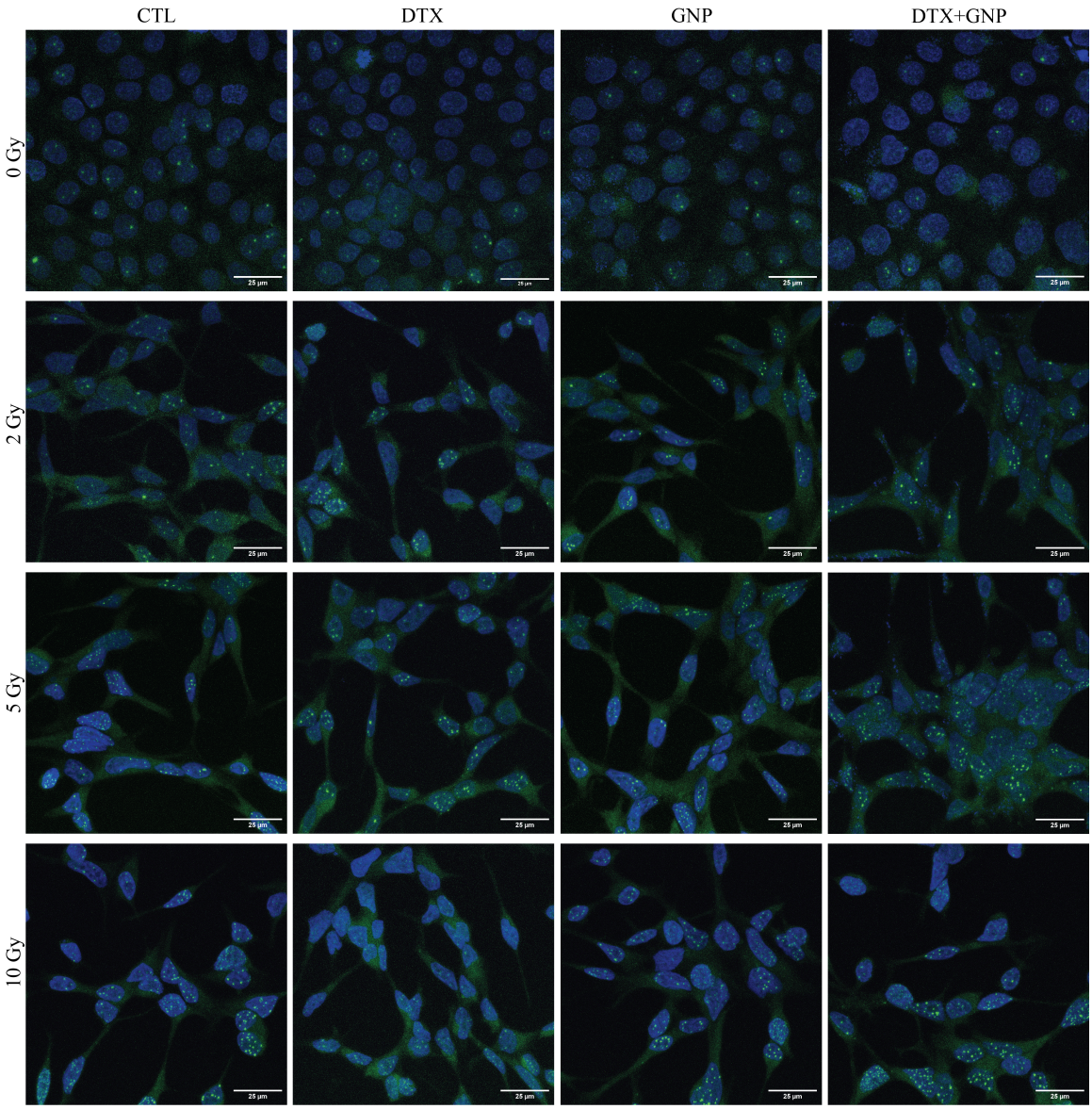


Figure 5.10: **Confocal images of 53BP1 foci in monolayer of LNCaP.** Images of LNCaP nuclei 24 hours after being irradiated with 2 Gy, 5 Gy, and 10 Gy. Samples include untreated, docetaxel treated, gold nanoparticle treated, and combined docetaxel and gold nanoparticle treatment. Nuclei and 53BP1 foci are marked in blue and green, respectively. Scale bar is 25 μm.

increase in foci of 107.0% ($p<0.05$), 46.1% ($p<0.05$), and 94.3% ($p<0.001$) in GNP, DTX, and GNP+DTX treated samples, respectively. Similar results were observed for LNCaP, except when signal was saturated at 10 Gy.

We have previously shown that GNPs can increase the number of foci present in a sample following 2 Gy of radiation. This is consistent with this result, while

also showing that higher doses of radiation lead to an increase in DSBs compared to DTX and control. Further, LNCaP has a larger relative increase in DNA DSBs when irradiated with any dose, indicating that LNCaP in monolayer has a larger DNA damage response than HeLa.

5.3.4 Radiation response in spheroids

Exploration of the trends observed in a 2D monolayer and if they will stay consistent in a 3D spheroid will help elucidate the benefits of both models. As seen in Chapter 4 and Figure 5.7, there will be a differential amount of uptake of GNPs in spheroids when treated with DTX, compared to monolayer. However, to ensure the spheroids we are testing have normoxic conditions, we qualitatively measured the hypoxia present in the core of the cells. It is important to ascertain the approximate oxygen levels, as hypoxia is one of the most important factors reducing RT effectiveness [282]. To accomplish this, we used Image-iT Hypoxia Reagent, that fluoresces in states of low oxygen. In spheroids, this would occur naturally within the core when they grow too large, due to the concentration gradient. In Figure 5.11, we measured spheroids of diameter ranging from 200 μm up to 1000 μm. For the spheroids used in our experiments, which have a diameter of approximately 300-400 μm, there was no visible fluorescence and thus no measured hypoxia. However, once spheroids were sizes larger than about 600 μm, fluorescence started being observed, signifying a lack of O_2 and formation of a hypoxic core.

As the spheroids we are using are all normoxic, there should be no reduction in effect from radiation due to lack of ROS production. To measure the effect radiation had on the spheroids, we measured the remaining metabolically active cells in the spheroids after 14 days using a luminescent 3D-based cell viability assay. Like monolayer, following 24 hrs of treatment with GNPs and DTX, the HeLa and LNCaP spheroids were either unirradiated, or radiated with 2 Gy, 5 Gy, and 10 Gy. As seen in Figure 5.12a,b, there was no a significant difference in active cells in non-irradiated samples when treated with GNPs. This further demonstrates the safety of the current GNP complexes after a longer time span of 14 days. Moreover, when HeLa spheroids are treated with GNPs and 2 Gy of radiation, there is a significant decrease in active cells from 86.18% to 70.12%, a relative change of 18.6% ($p<0.05$). With DTX treated HeLa spheroids, this does not translate to a significantly different result after 2 Gy. For all 2 Gy treated LNCaP spheroids, there is no statistically significant change in

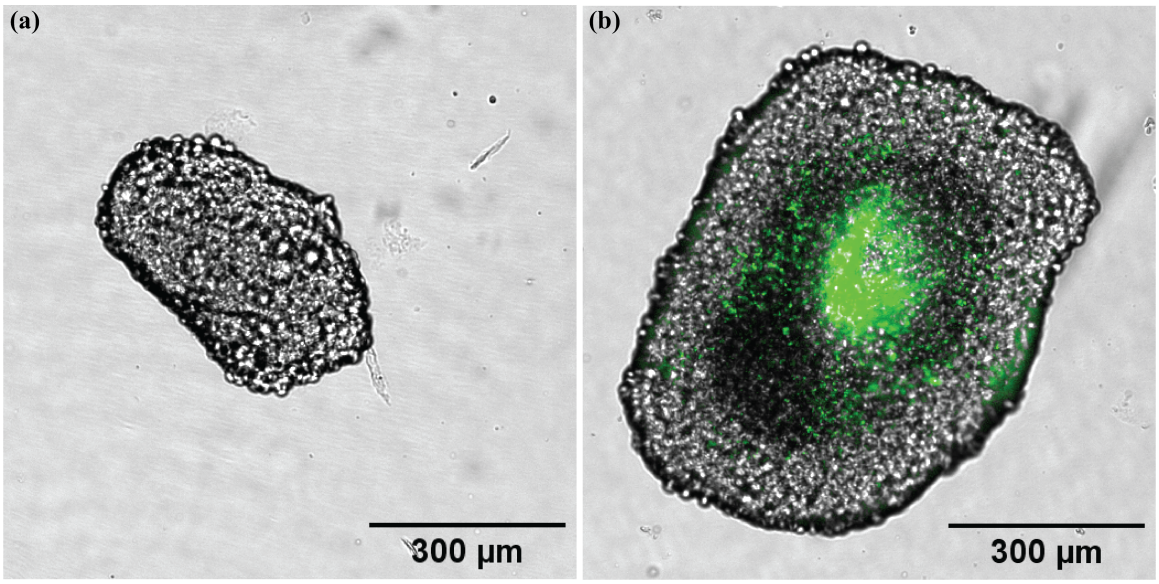


Figure 5.11: **Hypoxia analysis in spheroids.** (a,b) Analysis of hypoxic core in spheroids of (a) experimental size (diameter ≈ 300-400 μm) and (b) spheroids of diameter > 600μm. Due to radiations ability to create reactive oxygen species, a core that is normoxic is desirable to do more damage to all the cells.

active cells, though there is a trend of more damage with GNPs in both control and DTX treated samples.

When we move up to higher radiation doses of 5 Gy and 10 Gy, a trend of increased damage due to the addition of GNPs can be seen. After irradiating HeLa spheroids with 5 Gy (Figure 5.12a)), there is a relative decrease in active cells of 27.74% between control and GNP samples, from 41.14% to 29.7% ($p<0.01$). Between DTX and DTX+GNPs treated samples, there is a relative decrease in active cells of 16.55%, from 24.87% to 18.07% ($p<0.01$). Likewise, for HeLa treated with 10 Gy, there is a relative change of 32.33%, from 6.01% active cells to 4.06% for control and GNP($p<0.001$). Finally, for DTX and DTX+GNPs samples irradiated with 10 Gy, there was a 27.85% relative reduction from 2.65% to 1.92% ($p<0.05$) active cells.

We see a similar trend in LNCaP irradiated with 5 Gy and 10 Gy. For LNCaP and 5 Gy (Figure 5.12b)), we see a reduction in active cells from 44.82% for control to 40.08% for GNPs, a relative change of 10.54% ($p<0.001$). Further, there is reduction in active cells from 17.01% to 13.45% for DTX vs DTX+GNP samples, a relative change of 20.90% ($p<0.001$). For 10 Gy, there is a similar effect, with a relative change of 15.61% when comparing control (24.22%) and GNP-treated (20.44%) samples ($p<0.001$). Lastly, when comparing DTX and DTX+GNPs for LNCaP with 10

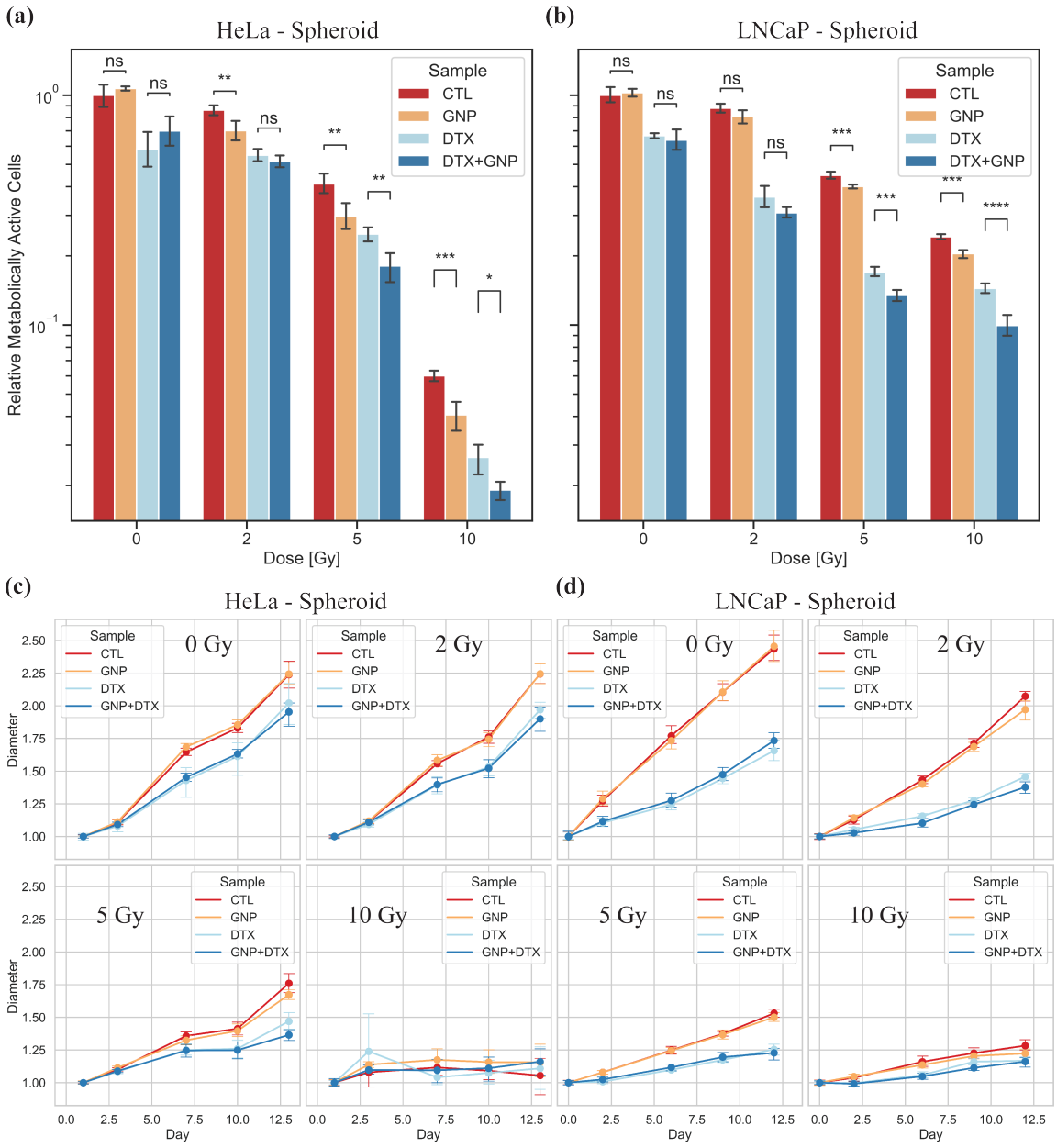


Figure 5.12: **Radiation response in spheroids.** (a,b) Normalized CellTiter-Glo 3D cell viability assay after 13 days following radiation for spheroids of (a) HeLa and (b) LNCaP. (c,d) Normalized increase of diameter relative to starting size of (c) HeLa spheroids and (d) LNCaP spheroids over 13 days following radiation. Error bars are the 95% confidence interval from three independent experiments with at least 5 repeats per condition per experiment. ns indicates no significance, * indicates 0.01<P<0.05, ** indicates 0.001<P<0.01, *** indicates 0.0001<P<0.001, **** indicates P<0.0001.

Gy, there is a relative change of 31.04%, with DTX having 14.43% active cells, and DTX+GNP having 9.95% active cells ($p<0.0001$).

Unlike the DSB measurements in monolayer, we can see that HeLa is more radiosensitive compared to LNCaP and will naturally have lower count of active cells as radiation doses increase. For both cell lines in both monolayer and spheroids, it appears that a dose of 2 Gy is not enough to elicit a large radiosensitization effect. However, there is a trend pointing towards more damage overall with GNPs added to treatment. When moving into higher doses, such as 5 Gy and 10 Gy, there is a significant decrease in active cells of the cancer cells due to the addition of GNPs, both in spheroid and in monolayer. For LNCaP spheroids, this effect seems to be consistently around $\approx$ 10-15% when not treated with DTX, and $\approx$ 20-30% when treated with DTX. This suggests that for LNCaP, the addition of DTX and GNPs as a combined therapy works synergistically to improve the radiosensitization effect. Interestingly for HeLa spheroids, when treating at higher doses, this does not seem to be the case. While there is an increase in damage when adding GNPs with DTX, it does not lead to a larger relative change than in control with GNPs without DTX. There is a general change of $\approx$ 16-32% when GNPs are added overall in HeLa for higher doses.

One limitation of using the CellTiter-Glo 3D assay for spheroids as well as the PrestoBlue resazurin-based assay for monolayer is the measurement of quiescent cells in the cancer population. This will be more pronounced for spheroids, as they tend to form a quiescent mid-layer, as described in 5.1a, as they grow. Moreover, with the addition of cytotoxic drugs like DTX and radiation, there will be an increase of senescent cells. These cells are seriously damaged but not dead. Therefore, they will still add to the signal due to metabolic activity. However, highly utilized alternatives such as a clonogenic assay are not really viable for a spheroid, due to the many layers that include necrotic and senescent cells that will lead to a heterogeneous population. Further, clonogenic assay does not account for how spheroids will be structurally altered as growth occurs following treatment. Thus, despite the limitations of viability-based assays like CellTiter-Glo 3D, it allows for the spheroids to maintain their structure until measurement. This leads to a more accurate representation of the state of the cancer.

We can use the growth curves (Figure 5.12c,d) to visualize the relative change in diameter of the spheroids over approximately two weeks following treatment. As expected, with more radiation, there was a decrease in visual spheroid growth with

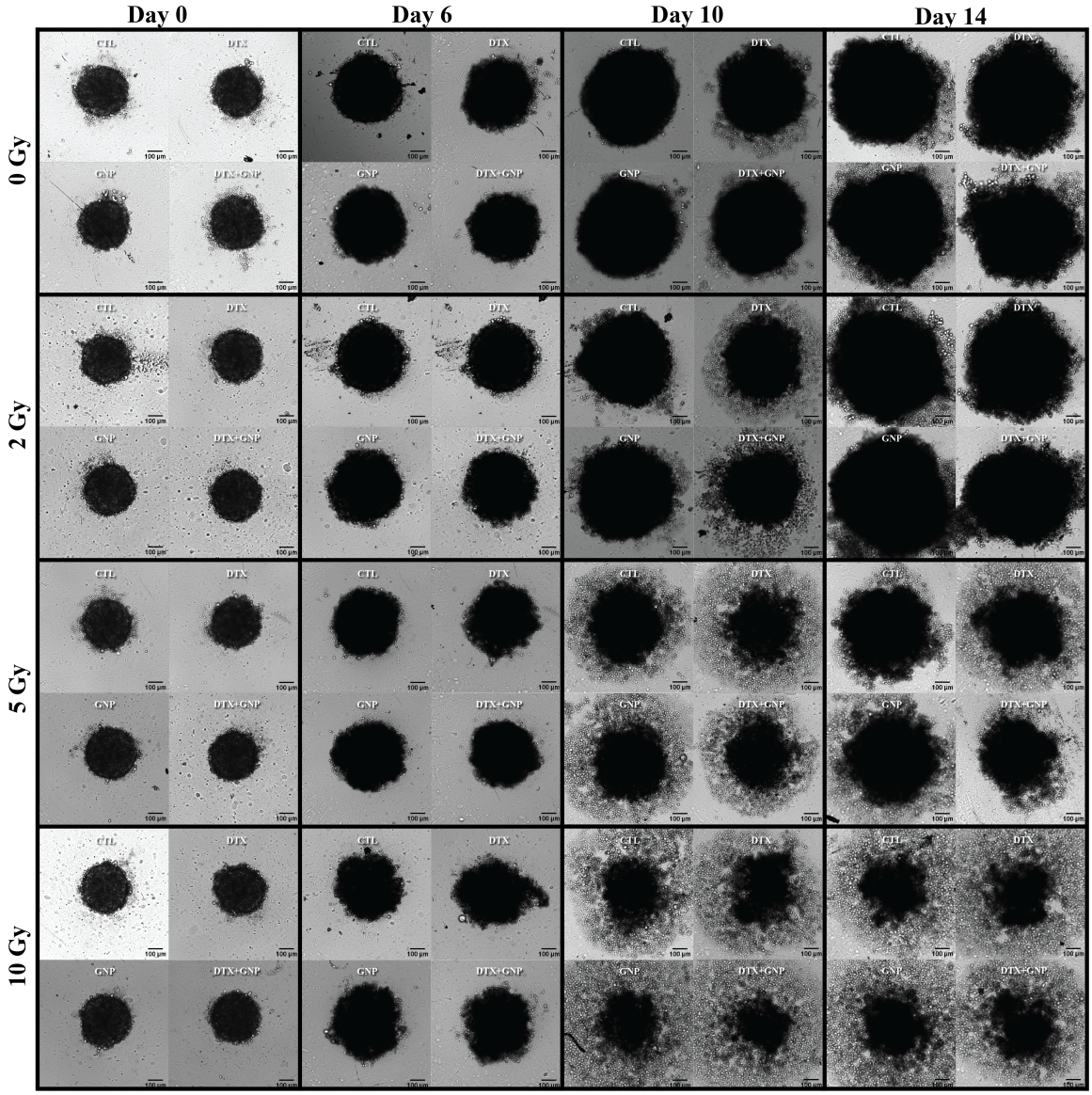


Figure 5.13: **Growth of HeLa spheroids following radiation.** Brightfield images of HeLa spheroids that have been untreated, treated with docetaxel, treated with gold nanoparticles, and treated with docetaxel and gold nanoparticles, and then radiated with 2 Gy, 5 Gy, and 10 Gy. Scale bar is 100 μm.

an increase in radiation and with treatment of DTX. DTX will naturally slow the growth, due to blockade of the cells into G2/M phase of the cell cycle [283]. In general, when measuring the spheroids diameters, there was no statistically significant change in the diameter following radiation and treatment with GNPs and DTX. However, there were trends which are useful to observe. After radiation, the GNP treated samples, whether with or without DTX, always had a slightly smaller diameter than

observed in no GNPs samples. Further, DTX had a large effect on the diameter of the spheroids, even in unirradiated control. Visualizing a statistically large difference in diameter is difficult, as more damage will lead to a loss in contractile forces in the cells contained within the spheroid. This leads to an initial expansion of the spheroids following damage. This is then followed by atrophy, which shrinks the tumour [284]. Meanwhile, healthy spheroids will maintain these contractile forces and may seem smaller despite the larger number of viable cells. The 3D viability assays done previously accounts for metabolically active cells only, and thus is more reliable of an indicator.

We can see the growth of HeLa in Figure 5.13 with pictures from treatment day (Day 0) to two weeks following treatment. As there is more damage accumulation, a lot of cell debris starts forming around the core of the spheroid. The core of the spheroid is also decimated, losing its structure, and spreading out because of loss of contractile forces in the cytoskeletons of the dead cells. For 10 Gy, the spheroids see a loss of compact structure, which leads to a larger measured diameter after Day 6. The structure appears to completely fail following Day 10 and Day 14. These results agree with the measured proliferation results (Figure 5.12a), where there are just a slim percentage of cells alive. Further, we can see the effect DTX has on long term spheroid growth. The DTX-treated spheroids gather a halo of cell debris compared to control samples, which is exacerbated by radiation.

LNCaP spheroid growth can be observed in Figure 5.14, where we can see very tightly packed spheroids for control samples all through the 2 weeks. However, when treated with DTX, we see a loss of this tighter structure, and the growth of LNCaP is drastically delayed. As the radiation dose is increased, the spheroids do not grow very much but still maintain a structure that is indicative of a spheroid, unlike what was seen with HeLa. This also agrees to what is measured using the viability assay above (Figure 5.12b). Further, we see that after 14 days, the spheroids generally only have a larger amount of cell debris if treated with DTX, showing that despite the drug not appearing to largely effect the cell cycle of LNCaP, it is still able to slow growth dramatically and cause increased damage. Like HeLa, we see that the addition of GNPs did not lead to a statistically significant reduction in growth. The trend remains, however, that the samples with GNPs were smaller than their control and DTX-treated counterparts.

These results highlight the effectiveness of spheroids as a model for testing cancer treatments, including nanomaterials like GNPs. While the trends are similar in

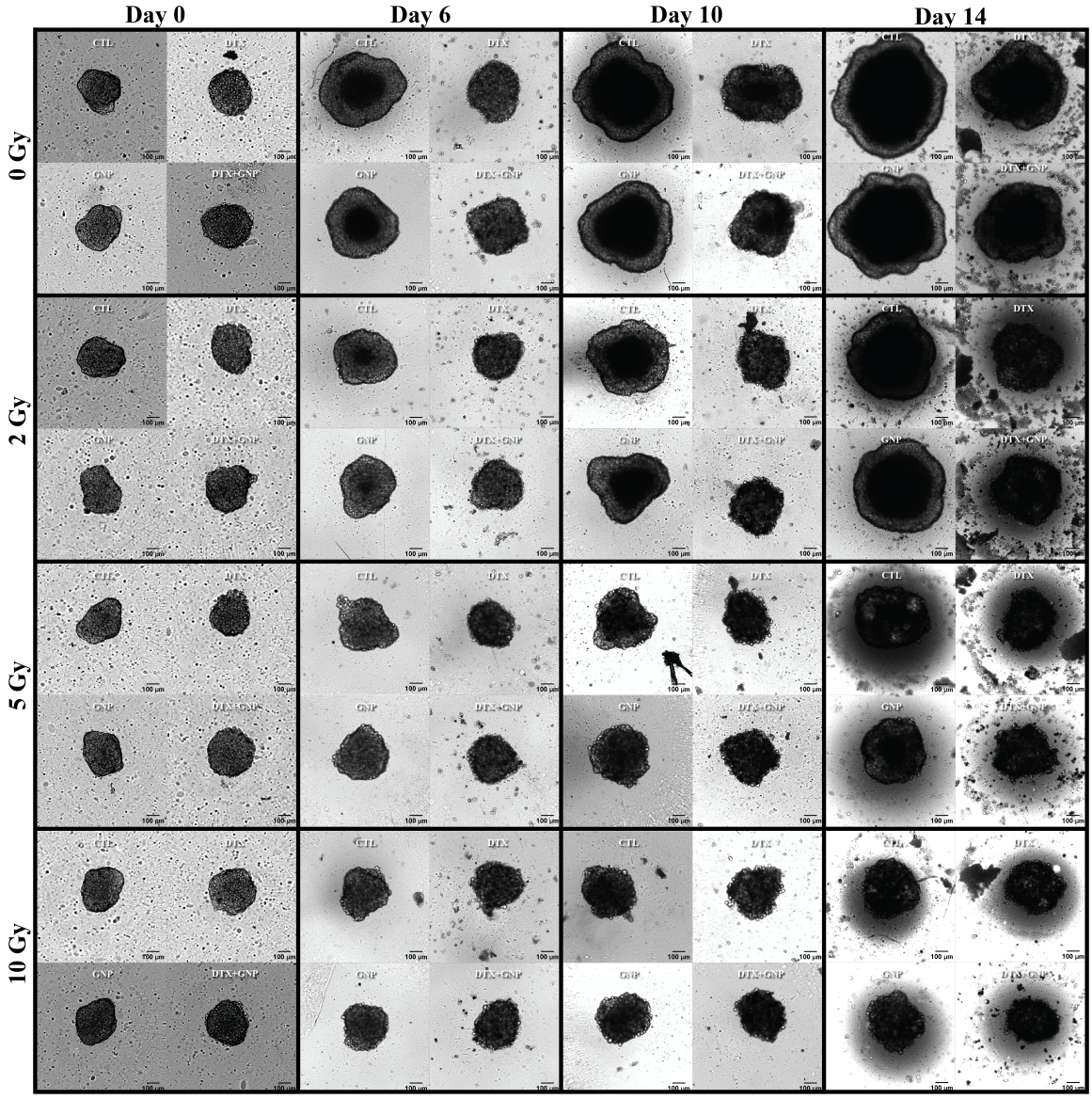


Figure 5.14: **Growth of LNCaP spheroids following radiation.** Brightfield images of LNCaP spheroids that have been untreated, treated with docetaxel, treated with gold nanoparticles, and treated with docetaxel and gold nanoparticles, and then radiated with 2 Gy, 5 Gy, and 10 Gy. Scale bar is 100 μm.

monolayer to spheroids, the spheroids tell a much larger and complete story. Further, the spheroids have many of the tendencies that are observed in tumours, which is important when considering moving to a more personalized treatment option. We can see that LNCaP and HeLa both respond differently to both radiation as well as the addition of the combined treatment of GNPs and DTX. Using a patient's own cells could have many benefits, by forming organoids in the lab. Organoid models

have many advantages if implemented into a personalized medicine protocol. The use of a patient's own cells allows for the maintenance of the heterogeneity present *in vivo* [260]. In the future, the use of spheroids and organoids to screen chemoradiotherapy protocols with GNPs may enable an accurate assessment of response and allow for tailored, personalized medical care.

5.4 Conclusions

By combining multiple effective treatment regimes into one, we can optimize a platform for improving patient outcome and reduce normal tissue toxicity. The use of radiosensitizers like GNPs and cytotoxic drugs like DTX is appealing due to their ability to synergistically work together [239]. GNPs will increase the damage due to radiation by causing increased cascades of secondary electrons and production of ROS. Meanwhile, DTX will synchronize cells into the radiosensitive G2/M cell cycle phase, allowing the damage to more effectively build up. However, testing in a monolayer is not an effective measure of how a tumour might respond given this treatment, as it is very simplified and does not have the many complex elements present in cancer, such as a TME. Thus, using 3D structures *in vitro* such as a multicellular spheroid can allow for an improved platform for optimizing a treatment regime. The combined treatment of DTX and GNPs with radiation showed a statistically significant increase in damage to the monolayer as well as the spheroids. Further, combining DTX with GNPs and radiation drastically changed how the spheroids grow, especially at higher doses of 5 Gy and 10 Gy. These results highlight the benefit of using spheroids for mimicking the *in vivo* TME. Spheroids are a far more flexible platform compared to monolayer which allow a deeper understanding of the mechanisms at hand, whether through visualization techniques or through simple viability measurements. By optimizing at a 3D level, and in the future comparing to an *in vivo* model, we can enable a swifter translation of GNPs to the clinic and implementation into modern RT regimes.

5.5 Materials and methods

5.5.1 Cells and culture conditions

HeLa, a cervical cancer cell line, and LNCaP, a prostate cancer cell lines, were purchased from the ATCC and have catalogue numbers CCL-2 and CRL-1740 re-

spectively. HeLa was cultured in DMEM (Gibco) supplemented with 10% FBS (Gibco), 1% Penicillin and Streptomycin (Gibco), and 4 mM GlutaMax (Gibco). LNCaP was cultured with RPMI-1640 Medium (Gibco), supplemented with 10% Fetal Bovine Serum (Gibco), 1% Penicillin and Streptomycin (Gibco), and 2 mM GlutaMax (Gibco). For cell dissociation, TrpyLE (Gibco) was used.

5.5.2 Synthesis, surface modification, and characterization of gold nanoparticles

Gold NPs of size ≈17 nm were synthesized using the citrate reduction method. This was accomplished by adding 1.18 mL of 1% $HAuCl_4 \cdot 3H_2O$ (Sigma Aldrich) to 28.82 mL of double–distilled water and heated on a hot plate while stirring vigorously. Once it reached the boiling point, 1.2 mL of 5% sodium citrate tribasic dihydrate ($HOC(COONa)(CH_2COONa)_2 \cdot 2H_2O$; Sigma Aldrich) was added and mixed. Once the color of the solution changed from dark blue to red, the solution was left to boil for another five minutes while stirring. Finally, the GNP solution was brought to room temperature while stirring.

The GNPs were PEGylated using PEG of size 2000 Da, along with an RGD peptide of size 1600 Da. PEG was stirred into the GNP solutions such that the grafting density will be 1 PEG molecule per 1 nm^2 of surface area. For 17 nm GNPs, this results in 907 PEG per GNP to be added to the solution. Following PEGylation of GNPs, the peptide containing integrin binding domain RGD (CKKKKKKG-GRGDMFG) was added to PEGylated GNPs at a ratio of 1 RGD molecule per 2 PEG molecules.

GNPs were characterized using UV–VIS spectrometry (Perkin Elmer λ Spectrophotometer) for approximate size and concentration estimates. Further, DLS and ζ-potential (Anton Paar LiteSizer 500) were utilized to measure the hydrodynamic diameter and the surface charge of the particles. Stability of the GNPs was measured in PBS. Imaging of the GNPs with scanning transmission electron microscopy (STEM; Hitachi SU9000) was used to verify the diameter of the GNPs. Brightfield, secondary electron, and high-angle annular dark-field images of each location were taken using 14 keV STEM. Brightfield images were used for GNP diameter measurement purposes.

5.5.3 Cell culture and growth of spheroids

For 2D and 3D cell models, all cells were initially split from a monolayer of cells at approximately 80% confluence. For the 2D monolayer cell model, cells were plated such that final confluence at the end point is approximately 70% in either six-well plates or 96-well plates, with initial cell count dependent on the experiment. Once plated, cells are left in the incubator at 37 ^{o}C and 5% CO_2 for 24 h to ensure adherence, after which experiments are initiated.

For 3D spheroid cell models, cells are plated in ultra-low attachment 96-well microplates (Corning). Diameter of spheroids were optimized before experiments by serial dilution from 50,000 cells for HeLa and 25,000 cells for LNCaP. 3,125 cells for HeLa per well and 1,000 LNCaP cells per well were found to form spheroids of approximately 300-400 μm. The cells are then centrifuged at 350$\times$g for 5 min, at 4 ^{o}C and left in the incubator at 37 ^{o}C and 5% CO_2. Experiments are initiated once the spheroids form, after incubation for approximately 72 hr.

5.5.4 Proliferation assay of docetaxel in monolayer and spheroids

For the 2D monolayer cell model, cells were plated such that there was 40,000 cells after 4 days, based off their doubling times. For LNCaP, this resulted in 6,000 cells from LNCaP and 2,500 cells from HeLa to be plated in 96 well black clear bottom microplates (Greiner), leaving one column empty for control. Once adhered, each column (8 wells) was treated with a unique docetaxel dose ranging from 250 nM to 6.4×10^{-4} nM in media, ensuring that the concentration of dimethyl sulfoxide (DMSO) in which the DTX is stored, is constant in all columns. Similarly, for the 3D spheroid cell model, once formed to sizes of approximately 300-400 μm, each column (8 wells) was treated with a unique DTX dose ranging from 250 nM down to 6.4×10^{-4} nM. This was completed in triplicate, on three different plates per cell line. At the same time, a control column without treatment of DMSO or DTX was measured using PrestoBlue Cell Viability Reagent (Invitrogen). A 10% solution of PrestoBlue in DMEM or RPMI, depending on the cell line, was added to the cells and left in the incubator for 1 hour. The resulting fluorescence was measured using a Cytation 1 Cell Imaging Multi-Mode Reader (BioTek) for the single column.

For monolayers, the media was removed from each sample after 24 hr, rinsed twice with PBS, and left to incubate for a further 48 hr in fresh media. For spheroids, half of the media was removed carefully after 24 hr, and then rinsed 5 times with PBS,

ensuring approximately a 162× dilution from the initial concentration. Finally, the media was replaced and left for a further 48 hr in the incubator.

After 48 hr, all the media for the 2D monolayer model was removed and treated with 10% PrestoBlue in media assay, following the manufacturers protocols. Plates were left in the incubator, and fluorescence was measured after 1 hour using the Cytation 1. Similarly, for the 3D spheroid model, the media was removed until 100 μL remained, ensuring that the sample was not aspirated, and then 30 μL of CellTiter-Glo 3D was added to make a final concentration of 23% CellTiter-Glo 3D. The plates were then shaken for 5 minutes at room temperature then left for 25 minutes shielded from light before measuring using the Cytation 1.

5.5.5 Cellular uptake of gold nanoparticle complexes

Incubation with GNP complex was done at a concentration of 10 μg/mL for all the stated experiments in monolayer and in spheroids. To test the effect that DTX had on the uptake of the GNPs, the different cell models and cell lines were dosed with the desired concentration found in the cell proliferation experiments concurrently with GNP dosing. This correlated to a dose of 1 nM for a monolayer of LNCaP, a 4 nM for a spheroid of LNCaP, a dose of 4 nM for a monolayer of HeLa and a dose of 7 nM for a spheroid of HeLa. Samples were incubated at 37 ^{o}C and 5% CO_2 for 24 hr following treatment. Cells were then rinsed with PBS at least three times, ensuring no sample is lost while aspirating. For spheroid samples, the cells were left in Accumax (STEMCELL Technologies) for 30 min at 37 ^{o}C to improve dissociation and produce a single-cell homogenous solution, while the monolayer samples were left in TrypLE for approximately 5 min. The cells were counted using a Coulter Counter (Z2 Coulter; Beckman Coulter) for GNP quantification per cell.

To measure the gold content for each sample, 500 μL of each sample were treated with 250 μL aqua regia (3:1 ratio of HCl:HNO_3 (VWR)) in a 90 ^{o}C mineral oil bath for a minimum of 30 min. After, 100 μL of hydrogen peroxide (VWR) was added and the samples were returned to the oil bath for 30 min, ensuring complete cell breakdown. These samples were then diluted down to 2.5% v/v acid content in deionized water and the gold content was quantified using inductively coupled plasma mass spectrometry (ICP-MS; Agilent 8800 Triple Quadrupole). Spheroid samples were filtered first in a 0.2-micron filter (Fisher). Calculation of nanoparticle content based on absolute gold content can be seen in Section 3.6.3.

5.5.6 Preparation of cells for imaging using darkfield and hyper spectral imaging

To prepare cells for darkfield imaging for 2D monolayer samples, all cell lines were plated in a six-well plate with glass coverslips placed on the bottom of each well. The cells were then treated as described previously using GNP complex and DTX at the desired doses. Following treatment, the cells were rinsed three times with PBS and fixed using 4% PFA for 20 min at 37 ^{o}C. The cover slips were then removed from each well and mounted to a glass slide using Permount Mounting Medium (Fisher).

Similarly, for 3D spheroid samples, following treatment of spheroids with GNP complex and DTX, the cells were cleaned 5× to dilute GNPs down dramatically, fixed in paraformaldehyde for 30 min at 37 ^{o}C, and then embedded in OCT compound (Fisher) and left in a -20 ^{o}C freezer. The spheroids were then sectioned at 10 μm using a cryostat (Leica) and adhered to a charged microscope slide. The sections are washed with acetone to remove excess OCT, then rinsed with water. The slides are then stained with Eosin (SelecTech; Leica) stain for 30 s and washed three times with 100% ethanol. Finally, the cells were rinsed three times with xylenes, coverslipped, were mounted onto the glass slides using Permount, and dried overnight for microscopy. Each sample, either monolayer or spheroid, was imaged using darkfield microscopy and HSI (CytoViva) under a 10× and 60× objective.

5.5.7 Preparation for live cell confocal imaging

For gold nanoparticle imaging, 50% of the PEG on the GNP surface was replaced with a PEG-Cy5 complex (excitation 633 nm, emission filter 650 nm LP). The GNPs were prepared otherwise the same as described previously. Glass bottom coverslip dishes (MatTek) were used to facilitate live cell imaging. Cells were first incubated with the Cy5-labelled GNPs for 24 h with the dose of DTX elucidated before. Approximately 1 hour before imaging, spheroids with incubated with NucBlue Live ReadyProbe Reagent (Invitrogen) which uses Hoechst 33342 to stain the nuclei. For monolayer, this was also completed 30 minutes prior to imaging. Image processing was performed using ImageJ [285].

5.5.8 Cell cycle analysis of Docetaxel using flow cytometry

DTX was administered to the monolayer and spheroid cells at desired concentrations as found in proliferation assay. After set time points of 0, 24, 48, and 72 h, the cells

were harvested as described previously using TrypLE and Accumax, and a single cell suspension was formed. Cells were washed with PBS and centrifuged at 300×g for 5 min twice. The cell pellet was then re-suspended in 1% PFA in PBS for fixation and incubated on ice for 15 min. Cells were again washed in PBS and centrifuged at 350×g for 5 min. Cells were re-suspended in 0.3 mL PBS and 0.7 mL freezer cold 100% ethanol (overall 70% ethanol). Samples were incubated in the dark at 4 ^{o}C for at least an hour, further fixing and dehydrating the cell sample. For tumour samples, the tumours were treated in Collagenase/Dispase (Roche) according to manufacturer's instructions for two hours. Following this, the solutions were filtered through a 100-micron cell strainer and treated with the monolayer and spheroid samples.

Samples were then centrifuged at 350×g for 10 min at 20 ^{o}C. The cell pellet was re-suspended in 1 mL of 0.5% BSA in PBS, denoted as PBS/BSA and centrifuged at 350×g for 5 min at 20 ^{o}C. To permeabilize the cell membrane and degrade RNA, the cell pellet was re-suspended in PBTB (PBS, 0.5% BSA, 0.1% Triton-X 100) followed by an addition of RNaseA at a concentration of 100 μg/mL. Samples were then left to shake at 37 ^{o}C for 25 min. For labelling DNA, tubes were covered in foil, PI was added at a concentration of 10 μg/mL and incubated on a shaker at 4 ^{o}C for at least 1 hr. The cells were then centrifuged at 350×g for 5 min at 20 ^{o}C. Finally, we re-suspended PI-stained cells in 1 ml of PBS/BSA and passed the solution through a 50 μm cell strainer before running on Flow Cytometer (BD FACS Calibur).

5.5.9 Radiation of monolayer and spheroids

Radiation was completed as described in Section 3.6.5. For 2 Gy, 5 Gy, and 10 Gy, 202, 505, and 1010 MUs were delivered, respectively.

5.5.10 Radiation proliferation assays

For monolayer, cells were plated such that there are 40,000 cells after 6 days. This corresponded to 1,250 cells for HeLa and 3,750 cells for LNCaP. The cells were plated such that were was at least 7 samples per condition (Control, DTX, GNP, and DTX + GNP), and measurements could be taken three separate times per plate, with each measurement having a blank well, as seen in Figure 5.15a. Three 96 well plates per radiation dose were plated.

Following radiation as described above with 2 Gy, 5 Gy, and 10 Gy, samples in the first four columns were measured on the first day, then measurements were taken

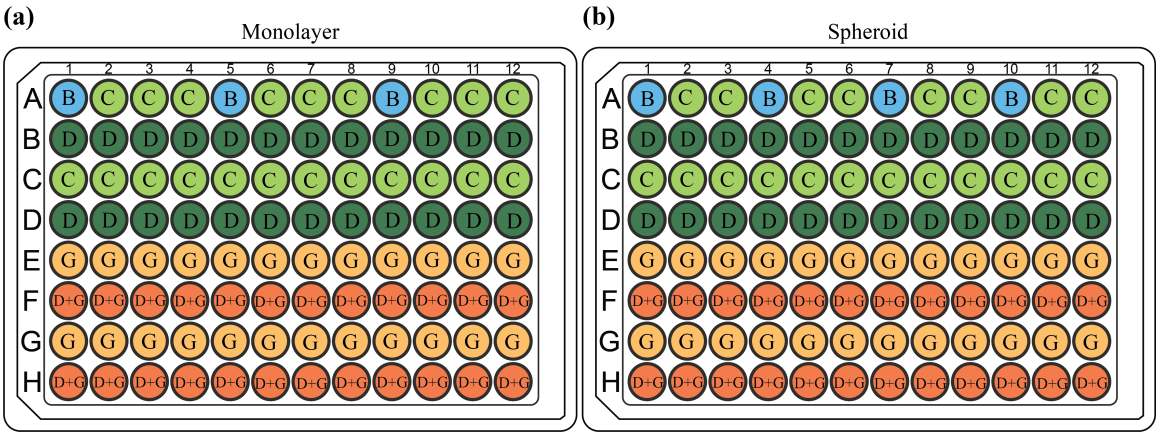


Figure 5.15: **Plate set up for radiation.** (a) Plate setup for monolayer radiation. Each measurement comprises of four columns and one blank. (b) Plate setup for spheroid radiation. Each measurement comprises of three columns and one blank.

again on the third day and sixth day. To measure the cell proliferation, PrestoBlue Cell Viability Reagent (Invitrogen) was employed. A 10% solution of PrestoBlue in DMEM or RPMI, depending on the cell line, was added to the cells and left in the incubator for 1 hour. The resulting fluorescence was measured using a Cytation 1.

For spheroids, cells were plated such that spheroids of 300-400 μm were formed. The cells were plated such that were was at least 5 samples per condition (Control, DTX, GNP, and DTX + GNP), and measurements could be taken four separate times per plate, with each measurement having a blank well, as seen in Figure 5.15b. Three 96 well plates per radiation dose were plated.

Following radiation as described above with 2 Gy, 5 Gy, and 10 Gy, samples in the first three columns were measured on the first day, then measurements were taken again on the 6th day, 10th day, and 14 day. To measure the cell proliferation, CellTiter-Glo 3D (Promega) was employed. The media was removed until 100 μL remained, ensuring that the sample was not aspirated, and then 30 μL of CellTiter-Glo 3D was added to make a final concentration of 23% CellTiter-Glo 3D. The plates were then shaken for 5 minutes at room temperature then left for 25 minutes shielded from light before measuring using the Cytation 1.

For monolayers, the media was removed from each sample prior to radiation, rinsed twice with PBS, and media replaced. For spheroids, half of the media was removed carefully prior to radiation, and then rinsed 5 times with PBS, ensuring approximately a 162$\times$ dilution from the initial concentration. Finally, the media was replaced.

5.5.11 Immunofluorescence assay

Cells were grown on glass coverslips in six-well plates for 24 h prior to experimentation. Following 24 h of treatment with GNP complexes and DTX, the cells were treated with radiation as described previously at 2 Gy, 5 Gy, and 10 Gy, and incubated for 24 hr at 37 ^{o}C. The cells were fixed with 4% PFA for 5 min at room temperature followed by two PBS washes for 5 min each. The cells were then blocked to reduce background noise using 2% BSA/0.1% Triton-X in PBS for 20 min. The two primary antibodies γH2AX and 53BP1 were diluted 1:200 in 0.5% BSA/0.1% Triton-X/PBS, while the secondary antibody was diluted 1:500 in 0.5% BSA/0.1% Triton-X/PBS. The coverslips were placed cells-down into 50 μL of a combination of the two primary antibodies on parafilm and incubated for 1 hr, followed by washing with PBS for 5 mins. The cells were then rinsed twice with 0.5% BSA/0.175% Tween-20/PBS for 5 min. On a new parafilm, the cover slips were placed cells-down in 50 μL of both secondary antibodies and incubated in the dark for 30 min. Finally, the cells were rinsed in PBS, dried, mounted to glass coverslips with Prolong Glass combined with NucBlue nuclear stain (Invitrogen).

Imaging of the 53BP1 foci was performed using confocal microscopy (Zeiss LSM 980) using a 60$\times$ oil immersion lens. The secondary antibody that attached to 53BP1 primary antibody was tagged with Alex Fluor 488 (Excitation 490 nm, Emission 525 nm), and NucBlue (Excitation 360 nm, Emission 460 nm) stained the nucleus. All conditions including acquisition settings used between experiments was maintained constant.

5.5.12 Growth analysis of spheroids

Spheroids were plated for radiation as described above. Brightfield images of the spheroids were taken every two days following radiation using the Cytation 1 using a 4$\times$ objective. To calculate the average diameter of a spheroid, ImageJ was used. An outline of the spheroid was drawn and then the area was calculated. From this area, the diameter was calculated using $d = 2\sqrt{A/\pi}$. Outlines of the spheroids were drawn manually and did not include cell debris that appeared due to damage from either DTX or radiation. A minimum of 5 and a maximum of 20 spheroids were used per time point to calculate the average diameter of each condition.

5.5.13 Hypoxic analysis of spheroids

A wide range of spheroid sizes were grown. For HeLa, 200 μm to 1000 μm were grown and for LNCaP, 280 μm to 1100 μm spheroids were grown. The spheroids were then incubated with 10 μM of Image-iT Hypoxia Reagent (Invitrogen) and then were incubated for 1 hour at 37 ^{o}C. The media was then exchanged with fresh medium, DMEM or RPMI depending on cell line. Brightfield images of the spheroids were then taken using the Cytation 1 using a 4$\times$ objective. Further, a GFP filter set (Excitation 469/35 nm, Emission 525/39 nm) was used to image the hypoxia reagent (Excitation 488 nm, Emission 520 nm).

5.5.14 Statistical analysis

A Welch's independent t-test with Bonferroni correction was preformed using the statannot python package, as described in Section 3.6.8. A p value < 0.05 was considered statistically significant. Experiments were repeated three times and the data presented is the average, for all experiments.

Chapter 6

Conclusion

6.1 Conclusions

The work done in this dissertation presents key steps towards the implementation of GNPs into a clinical application of RT. Various elements of the TME that directly affect the growth and proliferation of the cancer were explored. The TME is made up of many different cell types, including cancer associated fibroblasts (CAFs). Evidence of larger uptake in cancer and cancer-associated cells, such as CAFs and tumor cells, compared to normal, healthy fibroblasts, suggests an important avenue of exploration into specifically targeting the TME. We tested the uptake of GNPs into multiple tumor cell lines, including HeLa (cervical cancer), LNCaP (prostate cancer), CAL-27 (head and neck cancer), and PC-3 (prostate cancer) to set up future work. Another important element in the TME is the ECM, made up of various proteins to form a lattice that hinders nanomaterial movement. By modelling this behaviour in an *in vitro* 3D spheroid, the ability for GNPs to impact treatment with chemotherapy and RT was elucidated. Overall, the applicability of 3D spheroids to testing the efficacy of treatments such as GNPs combined with chemotherapy and RT was shown to be highly successful.

In monolayer, the translation of an *in vitro* response to an *in vivo* response is minimal, due to the many factors that are present in the TME. However, by isolating some aspects such as specific cell types, an overall strategy of attack can be formed in a far simpler environment. So far, much focus has been on cancer cells, but FBs and CAFs also play a critical role: FBs suppress the tumor growth while CAFs promote it. By observing the differential uptake that occurs in CAFs compared to FBs and HeLa cells, we can ascertain how effective a treatment involving GNPs may be. The cancer cells and CAFs had over 25- and 10-fold higher NP uptake per unit

cell volume compared to FBs, respectively. As a result, there was a direct correlation to an increase in 53BP1-related DNA damage foci 24 hrs after 2 Gy of radiation with a clinically relevant 6 MV linac. The selective targeting of CAFs and cancer cells like HeLa with GNPs over normal cells, that we want to survive following treatment, may allow GNPs to be an effective tool in future RT regimes.

To further explore other aspects of the TME, the use of a 3D spheroid introduces the ECM. The ECM is a conglomeration of molecules such as collagen that provides structural and biochemical support to the cells within. In tumours, the ECM will help form a concentration gradient as the cancer grows uncontrollably, leading to hypoxic and necrotic cores, while making it difficult for nanomaterials to penetrate deep. We tested the uptake of smaller 15 nm GNPs and larger 50 nm GNPs on spheroids to evaluate the differences in uptake between a 2D and 3D model. Further, we introduced the use of a chemotherapy agent, DTX, which also can act as a radiosensitizer. Compared to monolayer, the addition of DTX improved the uptake of smaller 15 nm GNPs dramatically, by up to 186% relative to no DTX. Further, it was observed the 15 nm GNPs were able to better penetrate the spheroids compared to the larger 50 nm GNPs, as a result of the lattice size in the ECM.

With these observations in mind, the spheroids were then treated in a combined treatment modality with smaller $\approx$ 15 nm GNPs, RT, and DTX. Following radiation with 5 Gy and 10 Gy with a 6 MV clinically relevant linac, spheroids that were treated with GNPs had a significant increase in damage that lead to a lower survival fraction after two weeks. DTX further exacerbated this response, depending on cell line response to the drug. In the case of the head and neck cancer cell line LNCaP, there was a synergistic advantage when GNPs were combined with DTX and RT. However, not all cell lines reacted the same to GNP radiosensitization when combined with DTX. HeLa had a similar change in survival when GNP were added in DTX treated and untreated samples, with no synergistic response. Compared to monolayer, the information provided by 3D spheroids in a combined treatment modality was vaster and more valuable as it is more similar to an actual *in vivo* TME.

These results highlight the necessity to optimize GNP treatment conditions in a 3D spheroid model that can capture important details, such as different packing densities from different cancer cell lines and differential GNP uptake patterns when treated in a combined therapy regime. The various ways cancer structurally forms will differ between different tissue types, which will directly affect the ability for GNPs to penetrate deep into the tumour. By optimizing in a simpler 3D spheroid model

compared to animal models, the application of GNPs into the clinic can be more rapidly facilitated. This is an important step towards optimizing the treatment of cancer with GNPs, as it forms a platform for the routine experimentation of multiple different treatment options in an environment that can more accurately mimic the complex *in vivo* TME.

6.2 Preliminary Future Work

To compare the more complex *in vitro* spheroid model to an actual *in vivo* environment, we optimized the uptake conditions within a mouse model. The work performed in this study involves the use of GNPs functionalized with polyethylene glycol (PEG) and a peptide containing the integrin binding domain RGD. These GNPs were then combined with low doses of DTX to compare the different gold nanoparticle uptake kinetics in a 2D monolayer model, 3D spheroid model, and *in vivo* mouse xenograft model, all with prostate cancer cell lines. While a 2D monolayer model is a good basis for further experimentation, it does not properly simulate the complex heterogenous environment present in a tumor microenvironment. The introduction of a 3D spheroid model can allow for a more accurate approximation of the *in vivo* environment and accelerate the use of radiosensitizers like GNPs to the clinic. For the 2D model and 3D model, we use two prostate cancer cell lines, PC-3 and LNCaP, and for the mouse xenograft model, we used a subcutaneous tumour model with PC-3. By determining and comparing GNP uptake in all three models when combined with DTX, we can lay the foundation for future experiments that facilitate a quicker translation to the clinic.

6.2.1 Materials and Methods

Cells and Culture Conditions

PC-3 and LNCaP, both human prostate cancer cell lines, were purchased from the American Type Culture Centre (ATCC) and have catalogue numbers CRL-1435 and CRL-1740 respectively. PC3 was cultured in Dulbecco's Modified Eagle Medium (DMEM; Gibco) supplemented with 10% Fetal Bovine Serum (Gibco), 1% Penicillin and Streptomycin (Gibco), and 4 mM GlutaMax (Gibco). LNCaP was cultured with RPMI-1640 Medium (Gibco), supplemented with 10% Fetal Bovine Serum (Gibco), 1% Penicillin and Streptomycin (Gibco), and 2 mM GlutaMax (Gibco). For cell

dissociation, TrpyLE (Gibco) was used.

Synthesis and surface modification of gold nanoparticles

Gold nanoparticles were synthesized and their surface was modified as described in Chapter 5. Gold nanoparticles that were sent to animal facilities were characterized after multiple months to ensure stability, while stored at 4 ^{o}C.

Cell culture and growth of spheroids

For 3D cell models, all cells were initially split from a monolayer of cells at approximately 80% confluence. For 3D spheroid cell models, cells are plated in ultra-low attachment 96-well microplates (Corning), with 1500 cells for PC-3 per well and 1000 LNCaP cells per well. For PC-3, the media was supplemented with 3% Geltrex matrix (Gibco) on ice, ensuring the temperature did not rise above 15 ^{o}C. The cells are then centrifuged at 350xg for 5 min, at 4 ^{o}C and left in the incubator at 37 ^{o}C and 5% CO_2. Experiments are initiated once the spheroids form, after incubation for approximately 72 h.

Animal xenograft model

Male NRC mice (ages six to ten weeks old) were purchased from the BC Cancer Research Institute for the in vivo experiments (GNP uptake with and without DTX). The methodology has been used, in general, falls within a service-oriented Animal Care Protocol that has been reviewed and approved by the Institutional Animal Care Committee (IACC) at the University of British Columbia. During the study the care, housing and use of animals will be performed in accordance with the Canadian Council on Animal Care Guidelines. Reporting of animal data in this study followed the recommendations set out in the ARRIVE guidelines.

Cell preparation and implantation into mice

Cells are started from a frozen vial of lab stock which were frozen down from the ATCC original vial, tested for mycoplasma negative and kept in lab liquid nitrogen tanks. Cell cultures with passage #3 to #10 and a confluence of 80-90% were harvested for in vivo studies. Cells were grown in Ham's F12 (Gibco) medium supplemented with 2 mM L-glutamine (Gibco) and 10% FBS (Gibco) at 37 ^{o}C in 5% CO_2 environment.

Cells are sub-cultured once a week with split ratio 1:3 to 1:6 and expanded. The medium needed to be renewed once a week.

Cells were rinsed briefly one time with 2 ml of fresh Trypsin/EDTA solution (0.25% trypsin with EDTA 4Na) and aspirated. Then 1.5 ml of Trypsin/EDTA was added and the cells were allowed to dissociate with the flask at 37 ^{o}C for a few minutes. Fresh medium was added to the cells, and 50 μl of cell suspension was mixed with Trypan Blue (1:1) and the cell count and cell viability on a cellometer Auto4 was measured. The cells were then centrifuged at 200×g for 7 min and the supernatant aspirated. Re-suspend the cells in cold growth medium to 2 times of desired concentration (50×10^6/ml), and the mix on ice with Matrigel (1:1). The cell number for inoculation is 5×10^6 cells in an injection volume of 100 μl per animal. All equipment coming into contact with Matrigel (needles, syringes, pipette tips) were chilled prior to injection.

On study day 0, 5×10^6 tumour cells in a volume of 100 μL were implanted subcutaneously into each animal's flank using a 28-gauge needle. Tumour growth was monitored by measuring tumour dimensions with calipers beginning on first day of treatment. Tumour length and width measurements were obtained every Monday, Wednesday and Friday. Tumour volumes were calculated according to the equation $\mathrm{L} \times \mathrm{W}^2 \times 0.5$ with the length (mm) being the longer axis of the tumour. Animals were also be weighed at the time of tumour measurement. Tumours were allowed to grow to a maximum of 800mm^3 before euthanasia All animals were observed daily for general health. In particular, signs of ill health were based on body weight loss, change in appetite, behavioural changes such as altered gait, lethargy and gross manifestations of stress. If signs tumour-related illness were seen, the animals would have been euthanized (isoflurane anesthesia then CO_2 asphyxiation).

Gold nanoparticle and docetaxel treatment of mouse xenograft model

Treatment of mice began once the tumours were measured to be about $250-300$mm^3. For this study, Docetaxel (Sandoz) was provided in 10 mg/mL solution, containing 96% Citric Acid, ethanol, PEG 300, and polysorbate 80. Unopened vials were kept at 20-25 ^{o}C and protected from light. The GNP complex solution was prepared as described and stored at 4 ^{o}C while protected from light. The dose for DTX was 6 mg/kg of mouse, administered intravenously, while the dose for GNP complex was 1.5 mg/kg of mouse. GNPs were also administered intravenously.

The mice were broken up into 3 study groups: a) untreated, b) GNP complex only, and c) DTX+GNP complex, administered concurrently. For group a), 6 mice were allocated to measure PC-3 tumour growth kinetics. For groups b) and c), 16 mice were allocated for each group, with 4 mice per four different time points: 8, 24, 48, and 72 h after dosing.

Pharmacokinetic tissue sampling

After mice are injected with the test articles (GNPs or GNP+DTX complex) and an appropriate amount of time has passed based on time points, cardiac puncture and tissue harvest was performed. For each time point, 3 out of 4 mice were used for histopathology, where 50% of the tumour was placed in 10% neutral buffered formalin, and the other 50% will be frozen for use in the biodistribution study. Further, 3 out of 4 of the mice had the spleen, both kidneys, the liver, and blood plasma frozen for use in the biodistribution study. The entire tumour of each remaining mouse from each time point was placed in 70% ethanol for further cell cycle analysis, kept at -20 ^{o}C, and their blood taken for Complete Blood Count with Differential and blood chemistry (performed at IDEXX), while their organs were also placed in 10% neutral buffered formalin for histopathology.

For the harvested *in vivo* samples, the tissue had to be disassociated first to measure GNP uptake. To accomplish this, each sample was weighed and then placed in 2 mL of TrypLE and blended using a handheld homogenizer (Fisher). These samples were then diluted to 5 mL in Millipore water and treated with aqua regia along with the monolayer and spheroids. The digestion of the cells is as described in Chapter 5.

Histopathology

10% neutral buffered formalin-fixed tissues were placed in labeled tissue processing cassettes and processed overnight into paraffin using an automated tissue processor (Leica ASP6025S). Processed tissues were then embedded into paraffin blocks and sectioned at a thickness of 4 μm. Sections from three levels spaced 50 μm apart were collected and mounted onto microscope slides (two slides per level; one for Haemtoxylin and Eosin (H&E) staining and another for coverslipping only).

After air drying overnight, the slides were loaded into a robotic stainer and coverslipper (Autostainer XL and CV5030 coverslipper; Leica), baked at 65 ^{o}C for 15

min and then de-waxed in xylene. Half of the slides were then coverslipped with a resinous mounting medium for darkfield imaging and the other half were stained with H&E according to standard procedures for brightfield images.

Cell cycle analysis of Docetaxel using flow cytometry

Tissues gathered from the tumour were gathered after set time points of 0, 8, 24, 48, 72 hrs. The tumours were treated in Collagenase/Dispase (Roche) according to manufacturer's instructions for two hours. Following this, the solutions were filtered through a 100-micron cell strainer. Samples were then treated as described in previous Chapters (i.e. Chapter 5).

Ethics approval

The methodology described here has been described, in general, within a service oriented Animal Care Protocol that has been reviewed and approved by the Institutional Animal Care Committee (IACC) at UBC - protocol #A18-0276. This study protocol will be made available to the IACC on requested and under a confidentiality agreement. All data collected and reported on this study protocol will be made available to the IACC on requested and under a confidentiality agreement. During the study the care, housing and use of animals will be performed in accordance with the Canadian Council on Animal Care Guidelines.

6.2.2 Results and Discussion

Gold nanoparticle uptake in monolayer and spheroid models

We can see in Figure 6.1a the measured uptake of the GNP complex in monolayer for both cell lines for control and DTX. There was a 13.2% increase for PC-3 which was not significant, while in LNCaP, there was a significant increase in uptake of 75.4% ($p=0.02392$). While LNCaP did not have observed synchronization of the cells, there was still an effect on both cell lines that increased the GNP uptake, although more drastically in LNCaP. In 6.1b, the measure uptake of GNP complex in spheroids for both cell lines with and without treatment of DTX is displayed. There was a significant increase in uptake after dosing with DTX of 134% ($p=0.0029$) and 109% ($p=0.0010$) in both PC-3 and LNCaP spheroids, respectively. Both PC-3 and LNCaP saw beneficial uptake in monolayer and in spheroids with the addition of DTX, with

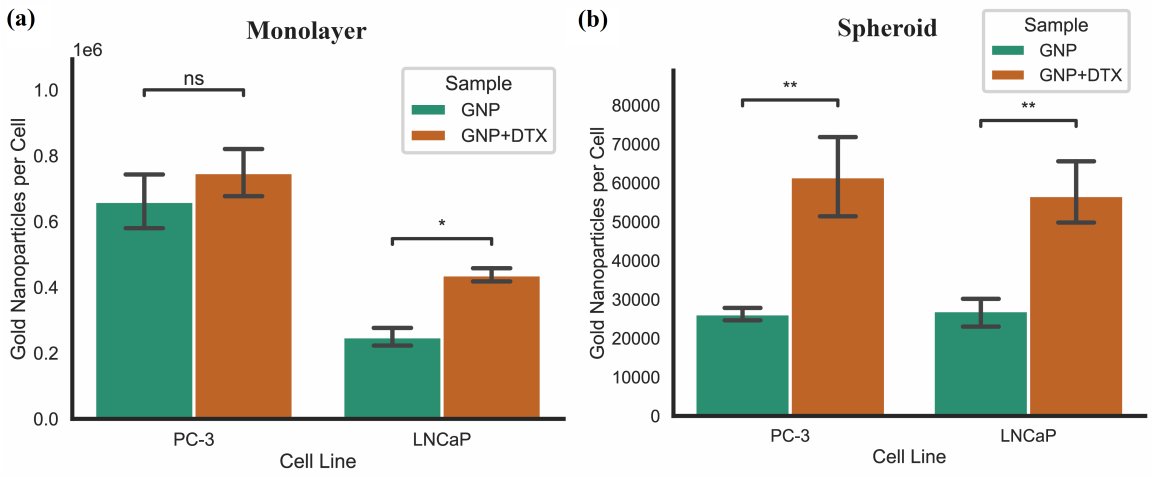


Figure 6.1: **Gold nanoparticle uptake in two-dimensional and three-dimensional models.**(a,b) Uptake of gold nanoparticles in (a) monolayer and (b) spheroids of PC-3 and LNCaP with and without docetaxel. Error bars are the 95% confidence interval from three independent experiments. ns indicates no significance, * indicates $0.01<P<0.05$, ** indicates $0.001<P<0.01$. Reproduced with permission [274]. Copyright Nature, 2022.

the change in spheroids being more drastic, despite the dose of DTX being normalized to the same growth rate. This may be a result of a higher dose of DTX in spheroids that will disproportionately affect the outer cells, which are the same cells that will have the largest uptake of GNPs. Thus, these cells will experience a larger DTX effect and have an amplified uptake compared to monolayer, where there is a lower dose of DTX and thus less effect. This increased effect is in agreement with previously measured values on separate cell lines from Chapter 4 and Chapter 5. Due to the synchronization of the cells into the G2/M phase with DTX, it is expected for a higher quantity of GNPs to be present relative to other phases, due to having a larger time to accumulate GNPs before division. The process of cell division will lead to the dilution of the per-cell GNP load, which explains the increase in GNPs per cell in samples treated with DTX.

In vivo effects of Docetaxel

Compared to a monolayer and spheroid, the mouse xenograft model introduces a more complex environment including immune infiltrate, circulating blood, and many other cell types in the tumour microenvironment such as fibroblasts and cancer associated fibroblasts. Clinically, doses of DTX of 20 mg/m^2 have been indicated to have ra-

diosensitizing levels in plasma for up to 1 week and are better tolerated with less side effects compared to higher doses [254, 286]. As the goal of this work is to optimize the use of DTX with GNPs in a mouse xenograft for subsequent radiation experimentation, this dosage was also employed in this research. The animal equivalent dose for a mouse xenograft is 6.65 mg/kg; for simplicity, this was rounded to 6 mg/kg [287]. NRG mice were chosen for this study, as they are well suited for cell line derived xenografts and can tolerate higher doses of radiation and chemotherapy treatment. PC-3 was implanted subcutaneously, and treatment to assess biodistribution began once tumours reached a measured volume of 250–300 mm^3.

To observe the effects of DTX on the tumour microenvironment, tumours were collected after 8, 24, 48, and 72 hr of DTX treatment, stained with hematoxylin and eosin (H&E) and imaged as seen in Figure 6.2a–e. As time progresses, there appears to be an increase of cellular and nuclear pleomorphism, indicative of altered morphology induced by DTX over time. Further, the mitoses that are occurring appear to be irregular in nature, with increasing condensed chromatin occurring following dosing (Figure 6.2f). This is expected due to the nature of DTX and how it acts on cells, as the cells will be synchronized into G2/M and should more regularly exhibit mitotic morphology. As a lower dosage was used, a significant increase in cell death via apoptotic pathways was not observed in the H&E images.

To further verify the increase of G2/M synchronization via DTX dosing, a single cell suspension of the tumour was produced, and the DNA content was measured *via* flow cytometry. As can be seen in Figure 6.2g, after 24 hr, most of the cells are in the G2/M phase of the cell cycle in the tumour. After 48 hr, this is still the case, though the number of cells in the G1 phase is returning to normal. After 72 hr, the cell population is continuing to trend back to G1 phase, with many cells still in G2/M. In the clinic, DTX treatments can be administered weekly in the clinic, and our results suggest the cells will be partially synchronized in the G2/M phase for at least 72 hr. This synergizes well with a fractionated radiotherapy treatment regime that generally has one dose of radiation a day over 5 consecutive weekdays, minimizing the amount of DTX patients can be treated with.

In vivo accumulation of gold nanoparticles with Docetaxel

To facilitate the optimum time points for treatment of prostate tumours, the mice were treated intravenously with DTX and GNP complexes with a dose of 1.5 mg/kg.

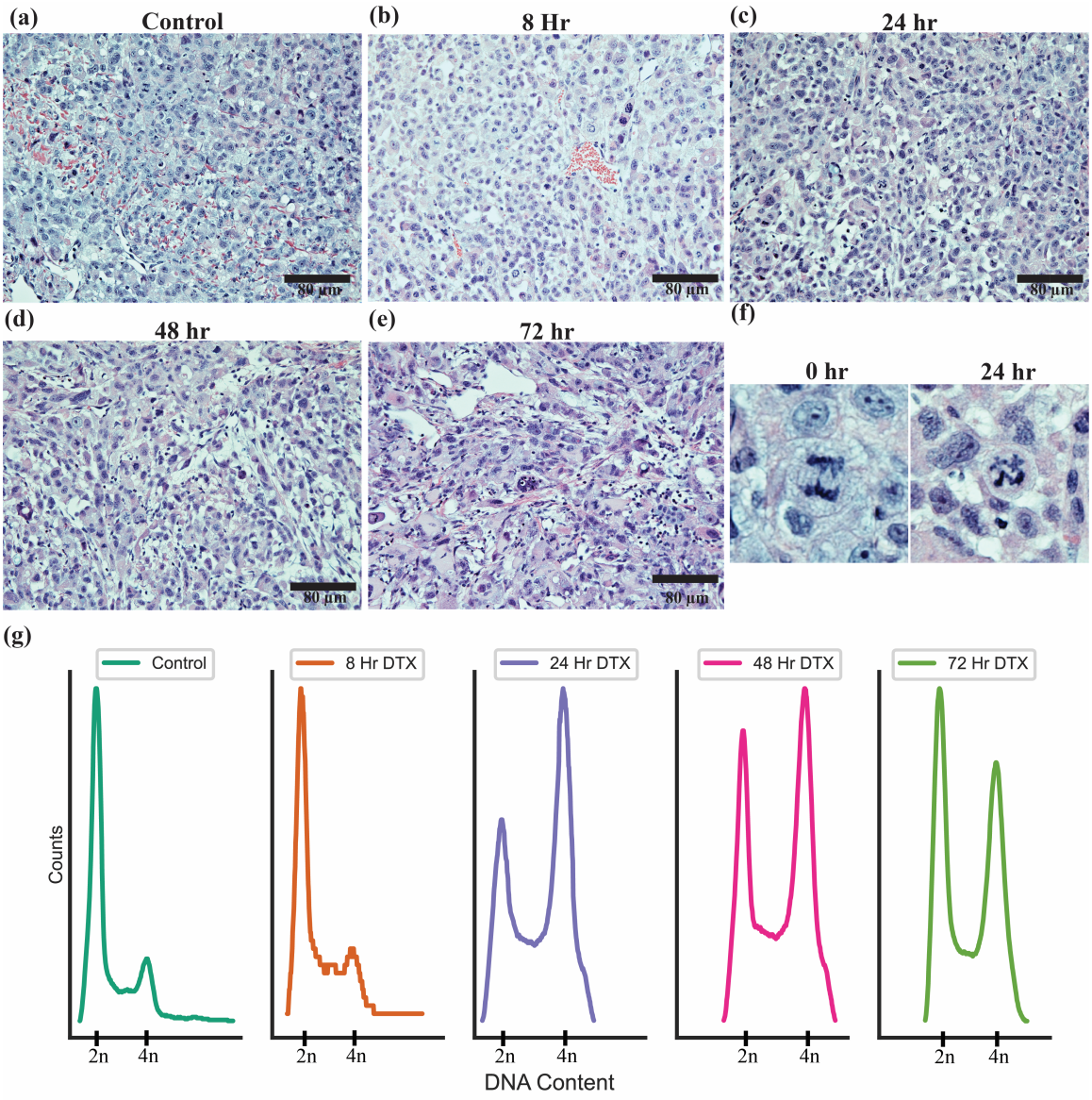


Figure 6.2: **Treatment of PC-3 subcutaneous tumour with docetaxel.** (a–e) Hematoxylin and eosin-stained sections of PC-3 tumour 0, 8, 24, 48, and 72 h after dosing with docetaxel. Scale bar is 80 μm. (f) Mitoses in present in the sections of the PC-3 tumour for control and after 24 h of dosing with docetaxel (g) Cell cycle analysis of PC-3 tumours after dosing with docetaxel and the subsequent shift in cell cycle synchronization over 0, 8, 24, 48, and 72 h. Reproduced with permission [274]. Copyright Nature, 2022.

While this is slightly lower than the 10 μg/mL given *in vivo* (eqv. 10 mg/kg), doses can be scaled in future studies to allow higher radiosensitization effects when radiation is introduced, as GNPs are non-toxic at low doses [288]. Accumulation of GNPs

into the tumour is facilitated by a couple mechanisms. First, structural features of solid tumours such as hypervascularization causing a defective vasculature architecture with little supportive tissues, leading to the formation of so-called 'leaky vessels', which are pores in the endothelial gaps ranging in diameter from 2 to 100 nm [289]. Combined with impaired lymphatic drainage, the tumours have an enhanced permeability and retention (EPR) effect present which increases the uptake of GNPs and better retains them compared to normal, healthy tissue. Further, due to the functionalization of the GNPs with RGD, we expect even further targeting of tumours, due to the increased expression of integrin dimers - i.e. $\alpha_v\beta_3$, $\alpha_v\beta_5$, and $\alpha_5\beta_1$, which can recognize the RGD motif - in various cancers including PC-3 and LNCaP [290].

Comparing the tumour when treated with GNP complex alone to GNP complex and DTX (Figure 6.3a), we found that there was a significant increase in uptake of GNP complex after 8 hr and 24 hr of dosing with DTX of 125% (p=0.045) and 126% (p=0.013). However, there was no significant increase after 48 hr and 72 hr, which corresponds with the reduction of cells synchronized in the G2/M phase of the cell cycle. The increase in uptake of GNPs is due to the same mechanism that caused an increase in monolayer and spheroids, mainly the synchronization of cells into the G2/M phase. This facilitates a higher per-cell uptake compared to other phases in the cell cycle, allowing for more GNPs in each cell to be utilized in future radiotherapy studies. When looking at the control organs (Figure 6.3b) and organs treated with DTX (Figure 6.3c), when normalized to GNPs per gram of tissue, we can see that there is a relative increase in GNP uptake in the tumour compared to the rest of the organs. For control, we found that after 8, 24, 48, and 72 hr, 0.52%, 0.46%, 0.79%, and 0.58% of the deposited dose is accumulated within the tumour, respectively, while with DTX, after 8, 24, 48, and 72 hr, 1.13%, 1.02%, 0.68%, and 0.70% respectively accumulated in the tumour. Further, the DTX does not significantly increase the deposited dose of GNPs into the normal organs. This indicates that there is a short-term increase in the GNP uptake due to the DTX that maintains a higher total accumulation in the tumour relative to control over 72 hr. When moving to radiation, this is an ideal result, indicating that both the DTX and the GNPs will stay inside the tumour, allowing for a synergistic radiosensitization effect up to 72 hr after initial dosing, and indicating the best time for the first dose of radiation is 24 hr after initial treatment.

To visualize the GNP uptake into the tumour, darkfield images were taken for all time points. For control tissue samples (Figure 6.3d), there is not an observed large

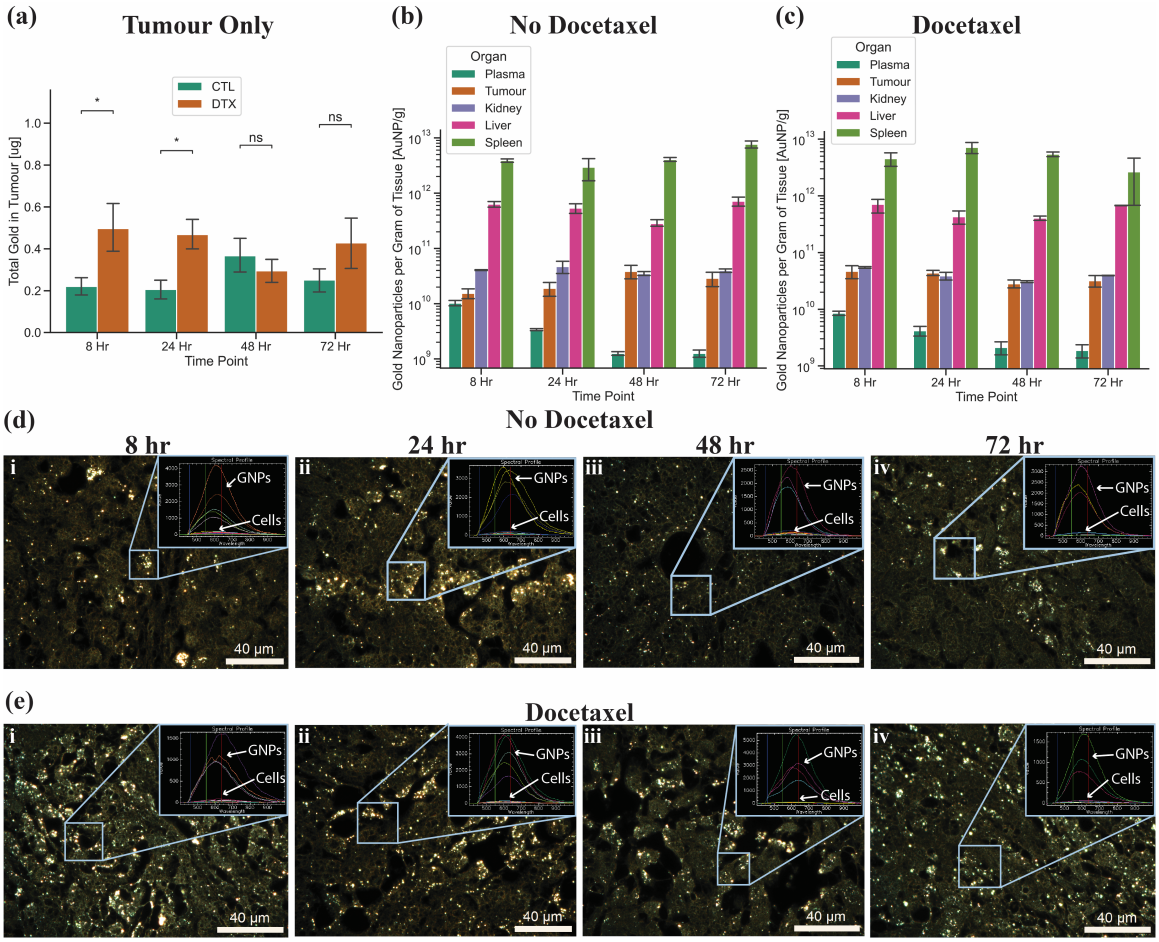


Figure 6.3: **Gold nanoparticle uptake in *in vivo* mouse xenograft model.** (a) Total gold uptake in the tumour after 8, 24, 48, and 72 h for tumours treated with gold or treated with gold and docetaxel. DTX refers to docetaxel treated samples and CTL refers to control samples with no docetaxel. (b,c) Total gold nanoparticles per gram of tissue for plasma, tumour, kidney, liver, and spleen after treatment (b) without docetaxel and (c) with docetaxel, after 8, 24, 38, and 72 h. Error bars are the 95% confidence interval from four independent mice. ns indicates no significance, * indicates $0.01<p<0.05$. (d,e) Darkfield images of 5 μm sections of tumour tissue 8, 24, 48, and 72 h after (d) gold nanoparticle treatment and after (e) concurrent gold nanoparticle and docetaxel treatment. Inset is hyper spectral spectrum of gold nanoparticles and cells. Scale bar is 40 μm. Reproduced with permission [274]. Copyright Nature, 2022.

difference between all four time points, although the amount of gold appears higher in the 8 hr and 24 hr time point. However, when compared to samples treated with DTX (Figure 6.3e), we can immediately see a visual increase in the amount of gold. This agrees with the quantified increase in uptake of GNPs found previously. A result

that was observed consistently in the tumour sections was a large quantity of GNPs around the blood vessels. When comparing the darkfield images of the tumours to that of the spheroids (where the media acts as a blood vessel), we see a similar effect, where there is a concentration gradient acting on the GNPs, reducing the penetration depth. Further, compared to the PC-3 spheroid model, which had a 130% increase in GNP uptake, there was a very similar 126% increase in the tumour after 24 h. These results highlight the benefits of using a spheroid model over a monolayer model to facilitate a quick translation of GNPs to the clinic.

6.2.3 Conclusion

Improving activity against cancerous tumour tissue while preserving normal tissue and reducing toxicity is achievable with the use of radiosensitizers like GNPs. To further synergize this effect, the addition of docetaxel can allow for an improved therapeutic effect within the tumour. By escalating the dose of radiation within a tumour while minimizing the dose to normal tissue, with targeting of tumours with radiosensitizers, we can improve patient outcomes and quality of life. Before radiation can be introduced, however, the combination of GNPs and DTX must be optimized. Thus, in this work, we measured the alteration in uptake of GNPs following treatment with DTX in a *in vivo* mouse xenograft, using prostate cancer cell lines PC3 and LNCaP. In spheroids and the mouse xenograft, it was found that with the addition of DTX, there was a significant increase in the gold uptake relative to no DTX, and that the two different cell models mimicked each other in both the relative increase of gold as well as the distribution of gold, while the monolayer of cells did not show similar effects. These results are the building blocks for the use of radiation with DTX and GNPs in an *in vivo* mouse xenograft and highlight the benefits of using an *in vitro* model such as the 3D spheroids that can better mimic the tumor microenvironment. By optimizing at a 3D level and comparing to an *in vivo* model, we can enable swifter RT experiments with higher prospects of future treatment success.

6.3 Future Directions

Application of the 3D spheroid technology in a framework that involves radiotherapy and GNPs is intended to further reduce normal tissue toxicity in cancer patients while also increasing deposited dose into the tumour. This can be achieved through a general treatment model where several populations of different tumour types are

measured and an average treatment plan is produced. However, a better approach may be the introduction of spheroids into a patient-centric model where personalized responses to the specific treatment options can be elucidated in the lab prior to actual patient treatment. To move towards personalized medical care with GNPs - using spheroids as an assessment tool - certain strategies will have to be employed and obstacles overcome [291].

The work done within this dissertation lays the groundwork the for application of *in vitro* spheroids to improve radiation treatment with DTX as a synergistic agent. However, spheroids, and the analogous patient derived organoids, should be seen as avascular tumors, with limitations. While spheroids give a simple way to achieve an ECM in the lab, along with many other advantages, they do not supply a complete *in vivo* environment. The TME involves a multitude of cell types that the 3D spheroids used within this work do not have. This includes tumor cells, tumour stromal cells like CAFs, and immune infiltrate [292]. Having a total picture with all of these elements would lead to a more complete picture of how cancer would respond to a specific treatment. To accomplish this, future work using spheroids should involve the combination of CAFs, FBs, cancer cells, and immune infiltrate to further mimic the *in vivo* environment. This will have to be accomplished in such a way that the combination of all cell types resembles similar ratios seen in tumours, and would be best completed with all patient derived cells. This will ensure the highest accuracy.

For work exploring the benefit of GNPs in a non-personalized regime, the introduction of 3D bio-printing can also be explored. By printing full organs, and simulating cancers in these organs, an actual TME can be created with high precision [293]. This can also allow for the addition of fluid pressures *via* 3D printed vasculature, allowing for modelling of the shear forces that can lead to metastasis. The downside of this approach is the scalability, which is limited due to the printing process, and reproducibility will have to be ascertained. For testing new treatment regimes in a vastly superior model compared to anything else, including spheroids, 3D printed tumours may be the best option. For fast throughput however, spheroids are likely the best option, especially in personalized medicine that has to move quicker in a clinical setting.

Alongside improving the spheroid model in the lab, experimentation must be done on animal models to ensure the *in vitro* response corresponds to that observed *in vivo*. With GNPs and DTX, the uptake profile in a mouse model was partially completed above, in Section 6.2. However, the effect radiation has with GNPs and DTX over a

long period in various cancer types, including prostate cancer, has to be elucidated. This is an important step before entering clinical trials. We have seen that the uptake response in spheroids is very similar to what is observed *in vivo*, proving the efficacy of spheroids. Final comparisons between spheroids and *in vivo* can be completed once the radiation response is found in the more complex mouse model.

On the other hand, previous *in vitro* work has shown the applicability of GNPs to a combined chemotherapy and radiotherapy treatment regime. Pivoting to a novel combined immunotherapy and radiotherapy nano-delivery platform may allow for drastically improved treatment outcomes with far fewer side effects relative to current treatment options. Immunotherapy by itself, such as the use of PD-L1 blockades, has been explored as a potential treatment option. Tumours often over-express the PD-L1 pathway, which is rarely expressed on normal tissue [294]. PD-L1 has been shown to be an effective treatment option in patients who are both PD-L1 positive and negative, leading to blockade therapy as a new standard second line of treatment over chemotherapy [295]. However, the use of immunotherapy can lead to the emergence of novel toxic features and reactions in multiple organ systems [296]. Towards a more effective treatment, the combination of radiotherapy and immunotherapy has been suggested and clinical trials show a positive result [297]. To take advantage of this, I propose the combination of nanotechnology in the form of the radiosensitizing GNPs and the targeting of PD-L1 into a lipid nanoparticle system for combined targeted treatment. The use of small interfering RNA can achieve suppression of PD-L1 production, and when encapsulated in a liposomal complex allows for targeted delivery to tumours *via* the enhanced permeability and retention effect [298]. This complex can have the possibility of improving treatment efficacy, as well as expanding our understanding of how the immune system interacts with the tumour following radiotherapy.

Translation to the clinic will require more work at the bio–nano interface. The payoff would be tremendous, allowing for treatment options such as chemoradiotherapy to be testing on patient cells *in vitro* prior to treatment to elucidate cellular response and improve efficacy. Finally, it must be accepted the spheroids are a simplistic model when compared to an *in vivo* environment and will not be able to predict everything. However, despite this, the use of GNPs with organoid models for personalized medicine may be able to help save lives and improve the quality of lives in the future.

Bibliography

[1] Bert Vogelstein and Kenneth W. Kinzler. The multistep nature of cancer. *Trends in Genetics*, 9(4):138–141, 4 1993.

[2] Hyuna Sung, Jacques Ferlay, Rebecca L. Siegel, Mathieu Laversanne, Isabelle Soerjomataram, Ahmedin Jemal, and Freddie Bray. Global Cancer Statistics 2020: GLOBOCAN Estimates of Incidence and Mortality Worldwide for 36 Cancers in 185 Countries. *CA: A Cancer Journal for Clinicians*, 71(3):209–249, 5 2021.

[3] Michael C. Joiner and Albert J. van der Kogel. *Basic Clinical Radiobiology*. CRC Press, 5 edition, 2018.

[4] Ervin B Podgorsak. *Review of Radiation Oncology Physics: A Handbook for Teachers and Students*. International Atomic Energy Agency, Vienna, 1 edition, 2005.

[5] Ervin B Podgorsak. *Radiation Physics for Medical Physicists*. Springer, Berlin, Heidelberg, 2 edition, 2016.

[6] I F Tannock, Richard P. Hill, Robert G. Bristow, and Lea Harrington. *Basic science of oncology*. McGraw-Hill Education, 5 edition, 2005.

[7] Douglas Hanahan and Robert A. Weinberg. Hallmarks of cancer: The next generation. *Cell*, 144(5):646–674, 2011.

[8] Sarah Crawford. Is it time for a new paradigm for systemic cancer treatment? Lessons from a century of cancer chemotherapy. *Frontiers in pharmacology*, 4, 2013.

[9] Rajamanickam Baskar, Kuo Ann Lee, Richard Yeo, and Kheng Wei Yeoh. Cancer and Radiation Therapy: Current Advances and Future Directions. *International Journal of Medical Sciences*, 9(3):193, 2 2012.

[10] Geoff Delaney, Susannah Jacob, Carolyn Featherstone, and Michael Barton. The role of radiotherapy in cancer treatment. *Cancer*, 104(6):1129–1137, 9 2005.

[11] G. P. Delaney and M. B. Barton. Evidence-based estimates of the demand for radiotherapy. *Clinical oncology*, 27(2):70–76, 2 2015.

[12] W. K. Rontgen. On A New Kind of Rays. *CA: A Cancer Journal for Clinicians*, 22(3), 1972.

[13] Pierre Radvanyi and Jacques Villain. The discovery of radioactivity. *Comptes Rendus Physique*, 18(9-10):544–550, 11 2017.

[14] F. Baclesse. Comparative study of results obtained with conventional radiotherapy (200 KV) and cobalt therapy in the treatment of cancer of the larynx. *Clinical Radiology*, 18(3):292–300, 1 1967.

[15] H. E. Johns, L. M. Bates, and T. A. Watson. The Saskatchewan Cobalt 60 Unit. *British Journal of Radiology*, 25(294):296–302, 1 2014.

[16] Godfrey N. Hounsfield. Computed medical imaging. *Medical Physics*, 7(4):283–290, 7 1980.

[17] C Nutting, D P Dearnaley, and S Webb. Intensity modulated radiation therapy: a clinical review. *British Journal of Radiology*, 73(869):459–469, 5 2000.

[18] Byungchul Cho. Intensity-modulated radiation therapy: a review with a physics perspective. *Radiation Oncology Journal*, 36(1):1, 3 2018.

[19] Gustavo Nader Marta, Valter Silva, Heloisa De Andrade Carvalho, Fernando Freire De Arruda, Samir Abdallah Hanna, Rafael Gadia, João Luis Fernandes Da Silva, Sebastião Francisco Miranda Correa, Carlos Eduardo Cintra Vita Abreu, and Rachel Riera. Intensity-modulated radiation therapy for head and neck cancer: Systematic review and meta-analysis. *Radiotherapy and Oncology*, 110(1):9–15, 1 2014.

[20] G. Bauman, R. B. Rumble, J. Chen, A. Loblaw, and P. Warde. Intensity-modulated Radiotherapy in the Treatment of Prostate Cancer. *Clinical Oncology*, 24(7):461–473, 9 2012.

[21] Marcia Bockbrader and Edward Kim. Role of intensity-modulated radiation therapy in gastrointestinal cancer. *Expert Review of Anticancer Therapy*, 9(5):637–647, 2014.

[22] Karl Otto. Volumetric modulated arc therapy: IMRT in a single gantry arc. *Medical Physics*, 35(1):310–317, 1 2008.

[23] Anders Brahme. Recent advances in light ion radiation therapy. *International Journal of Radiation Oncology Biology Physics*, 58(2):603–616, 2 2004.

[24] M. Durante. New challenges in high-energy particle radiobiology. *The British Journal of Radiology*, 87(1035), 3 2014.

[25] Bin Qiu, Abudureyimujiang Aili, Lixiang Xue, Ping Jiang, and Junjie Wang. Advances in Radiobiology of Stereotactic Ablative Radiotherapy. *Frontiers in Oncology*, 10:1165, 8 2020.

[26] William C. Jackson, Jessica Silva, Holly E. Hartman, Robert T. Dess, Amar U. Kishan, Whitney H. Beeler, Laila A. Gharzai, Elizabeth M. Jaworski, Rohit Mehra, Jason W.D. Hearn, Todd M. Morgan, Simpa S. Salami, Matthew R. Cooperberg, Brandon A. Mahal, Payal D. Soni, Samuel Kaffenberger, Paul L. Nguyen, Neil Desai, Felix Y. Feng, Zachary S. Zumsteg, and Daniel E. Spratt. Stereotactic Body Radiation Therapy for Localized Prostate Cancer: A Systematic Review and Meta-Analysis of Over 6,000 Patients Treated On Prospective Studies. *International Journal of Radiation Oncology, Biology, Physics*, 104(4):778–789, 7 2019.

[27] Leila T. Tchelebi, Eric J. Lehrer, Daniel M. Trifiletti, Navesh K. Sharma, Niraj J. Gusani, Christopher H. Crane, and Nicholas G. Zaorsky. Conventionally fractionated radiation therapy versus stereotactic body radiation therapy for locally advanced pancreatic cancer (CRiSP): An international systematic review and meta-analysis. *Cancer*, 126(10):2120–2131, 5 2020.

[28] Kavitha M Prezzano, Sung Jun Ma, Gregory M Hermann, Charlotte I Rivers, Jorge A Gomez-Suescun, and Anurag K Singh. Stereotactic body radiation therapy for non-small cell lung cancer: A review. *World Journal of Clinical Oncology*, 10(1):14, 1 2019.

[29] James Rijken, Scott Crowe, Jamie Trapp, and Tanya Kairn. A review of stereotactic body radiotherapy for the spine. *Physical and Engineering Sciences in Medicine*, 43(3):799–824, 9 2020.

[30] Michael Baumann, Mechthild Krause, Jens Overgaard, Jürgen Debus, Søren M. Bentzen, Juliane Daartz, Christian Richter, Daniel Zips, and Thomas Bortfeld. Radiation oncology in the era of precision medicine. *Nature Reviews Cancer*, 16(4):234–249, 3 2016.

[31] Kathrine S. Rallis, Thomas Ho Lai Yau, and Michail Sideris. Chemoradiotherapy in Cancer Treatment: Rationale and Clinical Applications. *Anticancer Research*, 41(1):1–7, 1 2021.

[32] Jennifer Couzin-Frankel. Cancer immunotherapy. *Science*, 342(6165):1432–1433, 12 2013.

[33] Allison N. DuRoss, Megan J. Neufeld, Shushan Rana, Charles R. Thomas, and Conroy Sun. Integrating Nanomedicine into Clinical Radiotherapy Regimens. *Advanced drug delivery reviews*, 144:35, 4 2019.

[34] Emil Frei III. Curative Cancer Chemotherapy. *Cancer Research*, 45(12):6523–6537, 12 1985.

[35] Alecsandru Ioan Baba and Cornel Câtoi. Principles of Anticancer Therapy. In *Comparative Oncology*, chapter 19. The Publishing House of the Romanian Academy, Bucharest, 2007.

[36] Philip Rubin and Stephen K. Carter. Combination radiation therapy and chemotherapy: A logical basis for their clinical use. *CA: A Cancer Journal for Clinicians*, 26(5):274–292, 9 1976.

[37] Laurie L. Herscher, John A. Cook, Roberto Pacelli, Harvey I. Pass, Angelo Russo, and James B. Mitchell. Principles of chemoradiation: Theoretical and practical considerations. *Oncology*, 13(10 SUPPL. 5):11–22, 10 1999.

[38] Tamer A. Elbayoumi. Nano drug-delivery systems in cancer therapy: Gains, pitfalls and considerations in DMPK and PD. *Therapeutic Delivery*, 1(2), 2010.

[39] Katherine A. Lyseng-Williamson and Caroline Fenton. Docetaxel: A review of its use in metastatic breast cancer. *Drugs*, 65(17):2513–31, 2005.

[40] Parvesh Kumar. A new paradigm for the treatment of high-risk prostate cancer: radiosensitization with docetaxel. *Reviews in urology*, 5 Suppl 3(Suppl 3):71–7, 2003.

[41] Giorgio V. Scagliotti and Andrew T. Turrisi. Docetaxel-Based Combined-Modality Chemoradiotherapy for Locally Advanced Non-Small Cell Lung Cancer. *The Oncologist*, 8(4):361–374, 8 2003.

[42] A. Dimitrios Colevas and Marshall R. Posner. Docetaxel in head and neck cancer: A review. *American Journal of Clinical Oncology: Cancer Clinical Trials*, 21(5):482–6, 1998.

[43] Bret Fulton and Caroline M. Spencer. Docetaxel: A Review of its Pharmacodynamic and Pharmacokinetic Properties and Therapeutic Efficacy in the Management of Metastatic Breast Cancer. *Drugs*, 1996.

[44] Roy S. Herbst and Fadlo R. Khuri. Mode of action of docetaxel - A basis for combination with novel anticancer agents. *Cancer Treatment Reviews*, 2003.

[45] Vijay Maruti Patil, Vanita Noronha, Nandini Sharrel Menon, Sarbani Laskar, Ashwini Budrukkar, Monali Swain, Atanu Bhattacharjee, Arun Balaji, Pankaj Chaturvedi, Devendra A Chaukar, P. S. Pai, Sudhir Vasudevan Nair, Nilendu Purandare, Archi Agrawal, Ameya Puranik, Kavita Prakash Nawale, Vijayalakshmi Mathrudev, and Kumar Prabhash. Results of phase 3 randomized trial for use of docetaxel as a radiosensitizer in patients with head and neck cancer unsuitable for cisplatin-based chemoradiation. *Journal of Clinical Oncology*, 40(17), 6 2022.

[46] Wei Shi, Yin Yuan, Min Chu, Shuang Zhao, Qingle Song, Xiaoqian Mu, Shuangbing Xu, Zhiping Zhang, and Kunyu Yang. Radiosensitization of TPGS-emulsified docetaxel-loaded poly(lactic-co-glycolic acid) nanoparticles in CNE-1 and A549 cells. *Journal of biomaterials applications*, 30(8):1127–1141, 3 2016.

[47] Timothy M. Pawlik and Khandan Keyomarsi. Role of cell cycle in mediating sensitivity to radiotherapy. *International Journal of Radiation Oncology, Biology, Physics*, 59(4):928–942, 7 2004.

[48] Jane T. Hickok, Joseph A. Roscoe, Gary R. Morrow, Karen Mustian, Paul Okunieff, and Christopher W. Bole. Frequency, severity, clinical course, and

correlates of fatigue in 372 patients during 5 weeks of radiotherapy for cancer. *Cancer*, 104(8):1772–1778, 10 2005.

[49] Chien Liang Lin, Shang Yin Wu, Wen Tsung Huang, Yin Hsun Feng, Ching Yi Yiu, Wei Fan Chiang, Sheng Yow Ho, and Sheng Hsiang Lin. Subsequent thyroid disorders associated with treatment strategy in head and neck cancer patients: A nationwide cohort study. *BMC Cancer*, 19(1):1–11, 5 2019.

[50] M. Baharvand, N. Shoalehsaadi, R. Barakian, and E. Jalali Moghaddam. Taste alteration and impact on quality of life after head and neck radiotherapy. *Journal of Oral Pathology & Medicine*, 42(1):106–112, 1 2013.

[51] Nam P. Nguyen, Cheryl Frank, Candace C. Moltz, Paul Vos, Herbert J. Smith, Ulf Karlsson, Suresh Dutta, Allan Midyett, Jessica Barloon, and Sabah Sallah. Impact of dysphagia on quality of life after treatment of head-and-neck cancer. *International Journal of Radiation Oncology, Biology, Physics*, 61(3):772–778, 3 2005.

[52] Avraham Eisbruch, Marco Schwartz, Coen Rasch, Karen Vineberg, Eugene Damen, Corina J. Van As, Robin Marsh, Frank A. Pameijer, and Alfons J.M. Balm. Dysphagia and aspiration after chemoradiotherapy for head-and-neck cancer: Which anatomic structures are affected and can they be spared by IMRT? *International Journal of Radiation Oncology, Biology, Physics*, 60(5):1425–1439, 12 2004.

[53] Primož Strojan, Katherine A. Hutcheson, Avraham Eisbruch, Jonathan J. Beitler, Johannes A. Langendijk, Anne W.M. Lee, June Corry, William M. Mendenhall, Robert Smee, Alessandra Rinaldo, and Alfio Ferlito. Treatment of late sequelae after radiotherapy for head and neck cancer. *Cancer Treatment Reviews*, 59:79–92, 9 2017.

[54] Padmanidhi Agarwal, H. R. Shiva Kumar, and Kirthi Kumar Rai. Trismus in oral cancer patients undergoing surgery and radiotherapy. *Journal of Oral Biology and Craniofacial Research*, 6:S9–S13, 11 2016.

[55] Annu Singh, Joseph M. Huryn, Kenneth L. Kronstadt, SaeHee K. Yom, Joseph R. Randazzo, and Cherry L. Estilo. Osteoradionecrosis of the jaw: A mini review. *Frontiers in Oral Health*, 0:78, 7 2022.

[56] Andrew J. Evans. Treatment effects in prostate cancer. *Modern Pathology*, 31(1):110–121, 1 2018.

[57] Mary Weinstein Dunn and Meredith Wallace Kazer. Prostate Cancer Overview. *Seminars in Oncology Nursing*, 27(4):241–250, 11 2011.

[58] Paul A. Cohen, Anjua Jhingran, Ana Oaknin, and Lynette Denny. Cervical cancer. *The Lancet*, 393(10167):169–182, 1 2019.

[59] Ammoren Dohm, Julian Sanchez, Eden Stotsky-Himelfarb, Field F Willingham, and Sarah Hoffe. Strategies to Minimize Late Effects From Pelvic Radiotherapy. *American Society of Clinical Oncology*, 41(41):158–168, 3 2021.

[60] Mark E. Davis, Zhuo Chen, and Dong M. Shin. Nanoparticle therapeutics: an emerging treatment modality for cancer. *Nature Reviews Drug Discovery*, 7(9):771–782, 2008.

[61] Abigail K.R. Lytton-Jean, Kevin J. Kauffman, James C. Kaczmarek, and Robert Langer. Cancer nanotherapeutics in clinical trials. *Cancer Treatment and Research*, 166:293–322, 2015.

[62] Aaron C. Anselmo and Samir Mitragotri. Nanoparticles in the clinic: An update. *Bioengineering & Translational Medicine*, 4(3), 9 2019.

[63] Jan Schuemann, Alexander F. Bagley, Ross Berbeco, Kyle Bromma, Karl T. Butterworth, Hilary L. Byrne, B. Devika Chithrani, Sang Hyun Cho, Jason R. Cook, Vincent Favaudon, Yaser H. Gholami, Elisabetta Gargioni, James F. Hainfeld, Félicien Hespeels, Anne Catherine Heuskin, Udoka M. Ibeh, Zdenka Kuncic, Sijumon Kunjachan, Sandrine Lacombe, Stéphane Lucas, François Lux, Stephen McMahon, Dmitry Nevozhay, Wilfred Ngwa, J. Donald Payne, Sébastien Penninckx, Erika Porcel, Kevin M. Prise, Hans Rabus, Sharif M. Ridwan, Benedikt Rudek, Léon Sanche, Bijay Singh, Henry M. Smilowitz, Konstantin V. Sokolov, Srinivas Sridhar, Yaroslav Stanishevskiy, Wonmo Sung, Olivier Tillement, Needa Virani, Wassana Yantasee, and Sunil Krishnan. Roadmap for metal nanoparticles in radiation therapy: current status, translational challenges, and future directions. *Physics in Medicine & Biology*, 65(21):21RM02, 10 2020.

[64] Zhenyuan Zhang, Alexander Berg, Haim Levanon, Richard W. Fessenden, and Dan Meisel. On the interactions of free radicals with gold nanoparticles. *Journal of the American Chemical Society*, 125(26):7959–7963, 7 2003.

[65] Yi Zheng and Léon Sanche. Low Energy Electrons in Nanoscale Radiation Physics: Relationship to Radiosensitization and Chemoradiation Therapy. *Reviews in Nanoscience and Nanotechnology*, 2(1):1–28, 3 2013.

[66] Helen E. Townley, Jeewon Kim, and Peter J. Dobson. In vivo demonstration of enhanced radiotherapy using rare earth doped titania nanoparticles. *Nanoscale*, 4(16):5043–5050, 7 2012.

[67] C. Mirjolet, A. L. Papa, G. Crehange, O. Raguin, C. Seignez, C. Paul, G. Truc, P. Maingon, and N. Millot. The radiosensitization effect of titanate nanotubes as a new tool in radiation therapy for glioblastoma: A proof-of-concept. *Radiotherapy and Oncology*, 108(1):136–142, 7 2013.

[68] Junko Takahashi and Masaki Misawa. Analysis of potential radiosensitizing materials for x-ray-induced photodynamic therapy. *Nanobiotechnology*, 3(2):116–126, 5 2007.

[69] Wensha Yang, Paul W. Read, Jun Mi, Joseph M. Baisden, Kelli A. Reardon, James M. Larner, Brian P. Helmke, and Ke Sheng. Semiconductor Nanoparticles as Energy Mediators for Photosensitizer-Enhanced Radiotherapy. *International Journal of Radiation Oncology, Biology, Physics*, 72(3):633–635, 11 2008.

[70] Devika B. Chithrani, Salomeh Jelveh, Farid Jalali, Monique Van Prooijen, Christine Allen, Robert G. Bristow, Richard P. Hill, and David A. Jaffray. Gold Nanoparticles as Radiation Sensitizers in Cancer Therapy. *Radiation Research*, 173(6):719–728, 6 2010.

[71] Géraldine Le Duc, Imen Miladi, Christophe Alric, Pierre Mowat, Elke Bräuer-Krisch, Audrey Bouchet, Enam Khalil, Claire Billotey, Marc Janier, François Lux, Thierry Epicier, Pascal Perriat, Stéphane Roux, and Olivier Tillement. Toward an image-guided microbeam radiation therapy using gadolinium-based nanoparticles. *ACS Nano*, 5(12):9566–9574, 12 2011.

[72] Peidang Liu, Zhihai Huang, Zhongwen Chen, Ruizhi Xu, Hao Wu, Fengchao Zang, Cailian Wang, and Ning Gu. Silver nanoparticles: a novel radiation sensitizer for glioma? *Nanoscale*, 5(23):11829–11836, 11 2013.

[73] James F. Hainfeld, Daniel N. Slatkin, and Henry M. Smilowitz. The use of gold nanoparticles to enhance radiotherapy in mice. *Physics in Medicine & Biology*, 49(18):N309, 9 2004.

[74] James F. Hainfeld, F. Avraham Dilmanian, Daniel N. Slatkin, and Henry M. Smilowitz. Radiotherapy enhancement with gold nanoparticles. *Journal of Pharmacy and Pharmacology*, 60(8):977–985, 8 2008.

[75] Yi Zheng and Lon Sanche. Gold Nanoparticles Enhance DNA Damage Induced by Anti-cancer Drugs and Radiation. *Radiation Research*, 172(1):114–119, 7 2009.

[76] Xiaopei Hu, Yuting Zhang, Tingting Ding, Jiang Liu, and Hang Zhao. Multifunctional Gold Nanoparticles: A Novel Nanomaterial for Various Medical Applications and Biological Activities. *Frontiers in Bioengineering and Biotechnology*, 8:990, 8 2020.

[77] Susie Eustis and Mostafa A. El-Sayed. Why gold nanoparticles are more precious than pretty gold: Noble metal surface plasmon resonance and its enhancement of the radiative and nonradiative properties of nanocrystals of different shapes. *Chemical Society Reviews*, 35(3):209–217, 2 2006.

[78] K. Lance Kelly, Eduardo Coronado, Lin Lin Zhao, and George C. Schatz. The optical properties of metal nanoparticles: The influence of size, shape, and dielectric environment. *Journal of Physical Chemistry B*, 107(3):668–677, 1 2003.

[79] Yi Cheun Yeh, Brian Creran, and Vincent M. Rotello. Gold nanoparticles: preparation, properties, and applications in bionanotechnology. *Nanoscale*, 4(6):1871–1880, 3 2012.

[80] Rares Stiufiuc, Cristian Iacovita, Raul Nicoara, Gabriela Stiufiuc, Adrian Florea, Marcela Achim, and Constantin M. Lucaciu. One-Step Synthesis of PEGylated Gold Nanoparticles with Tunable Surface Charge. *Journal of Nanomaterials*, 2013:1–7, 2013.

[81] Nikolai Khlebtsov and Lev Dykmana. Biodistribution and toxicity of engineered gold nanoparticles: a review of in vitro and in vivo studies. *Chemical Society Reviews*, 40(3):1647–1671, 2 2011.

[82] Vincenzo Amendola and Moreno Meneghetti. Size evaluation of gold nanoparticles by UV-vis spectroscopy. *Journal of Physical Chemistry C*, 113(11):4277–4285, 3 2009.

[83] Mir Hadi Jazayeri, Hamed Amani, Ali Akbar Pourfatollah, Hamidreza Pazoki-Toroudi, and Bijan Sedighimoghaddam. Various methods of gold nanoparticles (GNPs) conjugation to antibodies. *Sensing and Bio-Sensing Research*, 9:17–22, 7 2016.

[84] Hannu Häkkinen. The gold–sulfur interface at the nanoscale. *Nature Chemistry*, 4(6):443–455, 5 2012.

[85] Daniel V. Leff, Lutz Brandt, and James R. Heath. Synthesis and characterization of hydrophobic, organically-soluble gold nanocrystals functionalized with primary amines. *Langmuir*, 12(20):4723–4730, 10 1996.

[86] Ravi Shukla, Vipul Bansal, Minakshi Chaudhary, Atanu Basu, Ramesh R. Bhonde, and Murali Sastry. Biocompatibility of gold nanoparticles and their endocytotic fate inside the cellular compartment: A microscopic overview. *Langmuir*, 21(23):10644–10654, 11 2005.

[87] Małgorzata Kus-liśkiewicz, Patrick Fickers, and Imen Ben Tahar. Biocompatibility and Cytotoxicity of Gold Nanoparticles: Recent Advances in Methodologies and Regulations. *International Journal of Molecular Sciences*, 22(20):10952, 10 2021.

[88] A. Reznickova, N. Slavikova, Z. Kolska, K. Kolarova, T. Belinova, M. Hubalek Kalbacova, M. Cieslar, and V. Svorcik. PEGylated gold nanoparticles: Stability, cytotoxicity and antibacterial activity. *Colloids and Surfaces A: Physicochemical and Engineering Aspects*, 560:26–34, 1 2019.

[89] Rakesh K. Jain. Transport of molecules, particles, and cells in solid tumors. *Annual Review of Biomedical Engineering*, 1(1):241–263, 1999.

[90] Steven K. Libutti, Giulio F. Paciotti, Adriana A. Byrnes, H. Richard Alexander, William E. Gannon, Melissa Walker, Geoffrey D. Seidel, Nargiza Yuldasheva, and Lawrence Tamarkin. Phase I and pharmacokinetic studies of CYT-6091, a novel PEGylated colloidal gold-rhTNF nanomedicine. *Clinical Cancer Research*, 16(24):6139–6149, 12 2010.

[91] Inc Nanospectra Biosciences. Efficacy Study of AuroLase Therapy in Subjects With Primary and/or Metastatic Lung Tumors. Technical report, Cancer Treatment Centers of America Eastern Regional Medical Center, Philadelphia, Pennsylvania, United States, 2016.

[92] Inc. Nanospectra Biosciences. MRI/US Fusion Imaging and Biopsy in Combination With Nanoparticle Directed Focal Therapy for Ablation of Prostate Tissue. Technical report, Johns Hopkins Hospital, Baltimore, Maryland, United States, 2016.

[93] Clinicaltrials. Pilot study of AuroLase(tm) therapy in refractory and/or recurrent tumors of the head and neck. Technical report, Cancer Treatment Centers of American Western Regional Medical Center, Goodyear, Arizona, United States, 2010.

[94] Northwesten Universty. NU-0129 in Treating Patients With Recurrent Glioblastoma or Gliosarcoma Undergoing Surgery. Technical report, Northwestern University, Chicago, Illinois, United States, 2022.

[95] Celina Yang, Kyle Bromma, Wonmo Sung, Jan Schuemann, and Devika Chithrani. Determining the radiation enhancement effects of gold nanoparticles in cells in a combined treatment with cisplatin and radiation at therapeutic megavoltage energies. *Cancers*, 10(5), 2018.

[96] Celina Yang, Kyle Bromma, Caterina Di Ciano-Oliveira, Gaetano Zafarana, Monique van Prooijen, and D.B. Devika B. Chithrani. Gold nanoparticle mediated combined cancer therapy. *Cancer Nanotechnology*, 9(1), 2018.

[97] Allison M. Khoo, Sang Hyun Cho, Francisco J. Reynoso, Maureen Aliru, Kathryn Aziz, Monica Bodd, Xi Yang, Md F. Ahmed, Selcuk Yasar, Nivedh Manohar, Jongmin Cho, Ramesh Tailor, Howard D. Thames, and Sunil Krishnan. Radiosensitization of Prostate Cancers in Vitro and in Vivo to Erbium-

filtered Orthovoltage X-rays Using Actively Targeted Gold Nanoparticles. *Scientific Reports*, 2017.

[98] Tatiana Wolfe, Dev Chatterjee, Jihyoun Lee, Jonathan D. Grant, Shanta Bhattarai, Ramesh Tailor, Glenn Goodrich, Patricia Nicolucci, and Sunil Krishnan. Targeted gold nanoparticles enhance sensitization of prostate tumors to megavoltage radiation therapy in vivo. *Nanomedicine: Nanotechnology, Biology, and Medicine*, 2015.

[99] Stefan Wilhelm, Anthony J. Tavares, Qin Dai, Seiichi Ohta, Julie Audet, Harold F. Dvorak, and Warren C.W. Chan. Analysis of nanoparticle delivery to tumours. *Nature Reviews Materials*, 1, 2016.

[100] Han Fan, Utkan Demirci, and Pu Chen. Emerging organoid models: Leaping forward in cancer research. *Journal of Hematology and Oncology*, 12, 2019.

[101] Michael W Pickup, Janna K Mouw, and Valerie M Weaver. The extracellular matrix modulates the hallmarks of cancer. *EMBO reports*, 15(12):1243–1253, 12 2014.

[102] A Teti. Regulation of cellular functions by extracellular matrix. *Journal of the American Society of Nephrology*, 2(10), 1992.

[103] Triantafyllos Stylianopoulos, Ming Zher Poh, Numpon Insin, Moungi G. Bawendi, Dai Fukumura, Lance L. Munn, and Rakesh K. Jain. Diffusion of particles in the extracellular matrix: The effect of repulsive electrostatic interactions. *Biophysical Journal*, 99(5):1342–1349, 9 2010.

[104] Ayse Basak Engin, Dragana Nikitovic, Monica Neagu, Petra Henrich-Noack, Anca Oana Docea, Mikhail I. Shtilman, Kirill Golokhvast, and Aristidis M. Tsatsakis. Mechanistic understanding of nanoparticles' interactions with extracellular matrix: The cell and immune system, 6 2017.

[105] Alain Pluen, Yves Boucher, Saroja Ramanujan, Trevor D. McKee, Takeshi Gohongi, Emmanuelle Di Tomaso, Edward B. Brown, Yotaro Izumi, Robert B. Campbell, David A. Berk, and Rakesh K. Jain. Role of tumor-host interactions in interstitial diffusion of macromolecules: Cranial vs. subcutaneous tumors. *Proceedings of the National Academy of Sciences of the United States of America*, 98(8):4628–4633, 4 2001.

[106] Tushar D. Rane and Andrea M. Armani. Two-Photon Microscopy Analysis of Gold Nanoparticle Uptake in 3D Cell Spheroids. *PLOS ONE*, 11(12):e0167548, 12 2016.

[107] Boris Chelobanov, Julia Poletaeva, Anna Epanchintseva, Anastasiya Tupitsyna, Inna Pyshnaya, and Elena Ryabchikova. Ultrastructural Features of Gold Nanoparticles Interaction with HepG2 and HEK293 Cells in Monolayer and Spheroids. *Nanomaterials*, 10(10):2040, 10 2020.

[108] Hongxu Lu, Jiaying Su, Russul Mamdooh, Yimeng Li, and Martina H. Stenzel. Cellular Uptake of Gold Nanoparticles and Their Movement in 3D Multicellular Tumor Spheroids: Effect of Molecular Weight and Grafting Density of Poly(2-hydroxyl ethyl acrylate). *Macromolecular Bioscience*, 20(1):1900221, 1 2020.

[109] Viktoriya Sokolova, Gehad Mekky, Selina Beatrice van der Meer, Michael C. Seeds, Anthony J. Atala, and Matthias Epple. Transport of ultrasmall gold nanoparticles (2 nm) across the blood–brain barrier in a six-cell brain spheroid model. *Scientific Reports*, 10(1):18033, 12 2020.

[110] Keyang Huang, Huili Ma, Juan Liu, Shuaidong Huo, Anil Kumar, Tuo Wei, Xu Zhang, Shubin Jin, Yaling Gan, Paul C. Wang, Shengtai He, Xiaoning Zhang, and Xing Jie Liang. Size-dependent localization and penetration of ultrasmall gold nanoparticles in cancer cells, multicellular spheroids, and tumors in vivo. *ACS Nano*, 6(5):4483–4493, 5 2012.

[111] Shuaidong Huo, Shubin Jin, Xiaowei Ma, Xiangdong Xue, Keni Yang, Anil Kumar, Paul C. Wang, Jinchao Zhang, Zhongbo Hu, and Xing Jie Liang. Ultrasmall gold nanoparticles as carriers for nucleus-based gene therapy due to size-dependent nuclear entry. *ACS Nano*, 8(6):5852–5862, 6 2014.

[112] Miao Fan, Yu Han, Shutao Gao, Hongyu Yan, Lingzhi Cao, Zhenhua Li, Xing Jie Liang, and Jinchao Zhang. Ultrasmall gold nanoparticles in cancer diagnosis and therapy, 2020.

[113] Stephen Riffle, Ram Naresh Pandey, Morgan Albert, and Rashmi S. Hegde. Linking hypoxia, DNA damage and proliferation in multicellular tumor spheroids. *BMC Cancer*, 17(1):338, 5 2017.

[114] Se Jik Han, Sangwoo Kwon, and Kyung Sook Kim. Challenges of applying multicellular tumor spheroids in preclinical phase. *Cancer Cell International*, 21(1):1–19, 3 2021.

[115] Tristan Courau, Julie Bonnereau, Justine Chicoteau, Hugo Bottois, Romain Remark, Laura Assante Miranda, Antoine Toubert, Mathieu Blery, Thomas Aparicio, Matthieu Allez, and Lionel Le Bourhis. Cocultures of human colorectal tumor spheroids with immune cells reveal the therapeutic potential of MICA/B and NKG2A targeting for cancer treatment. *Journal for ImmunoTherapy of Cancer*, 7(1):74, 12 2019.

[116] Yousef Ahmed Fouad and Carmen Aanei. Revisiting the hallmarks of cancer. *American Journal of Cancer Research*, 7(5):1016, 2017.

[117] Esther Witsch, Michael Sela, and Yosef Yarden. Roles for Growth Factors in Cancer Progression. *Physiology*, 25(2):85, 2010.

[118] K. Rieck, K. Bromma, W. Sung, A. Bannister, J. Schuemann, and D.B. Chithrani. Modulation of gold nanoparticle mediated radiation dose enhancement through synchronization of breast tumor cell population. *British Journal of Radiology*, 92(1100), 2019.

[119] Helen K. Matthews, Cosetta Bertoli, and Robertus A.M. de Bruin. Cell cycle control in cancer. *Nature Reviews Molecular Cell Biology*, 23(1):74–88, 9 2021.

[120] Marcos Malumbres and Mariano Barbacid. Cell cycle, CDKs and cancer: a changing paradigm. *Nature Reviews Cancer*, 9(3):153–166, 3 2009.

[121] Kaleigh Fernald and Manabu Kurokawa. Evading apoptosis in cancer. *Trends in cell biology*, 23(12):620, 12 2013.

[122] Claire M. Pfeffer and Amareshwar T.K. Singh. Apoptosis: A Target for Anticancer Therapy. *International Journal of Molecular Sciences*, 19(2), 2 2018.

[123] J. Lopez and S. W.G. Tait. Mitochondrial apoptosis: killing cancer using the enemy within. *British Journal of Cancer*, 112(6):957–962, 3 2015.

[124] Rana Elkholi, Thibaud T Renault, Madhavika N Serasinghe, and Jerry E Chipuk. Putting the pieces together: How is the mitochondrial pathway of apop-

tosis regulated in cancer and chemotherapy? *Cancer & Metabolism*, 2(1):1–15, 10 2014.

[125] V. Labi and M. Erlacher. How cell death shapes cancer. *Cell Death & Disease*, 6(3):e1675, 3 2015.

[126] Domenico Ribatti, Beatrice Nico, and Enrico Crivellato. The development of the vascular system: A historical overview. *Methods in Molecular Biology*, 1214:1–14, 2015.

[127] Peter Carmeliet and Rakesh K. Jain. Angiogenesis in cancer and other diseases. *Nature*, 407(6801):249–257, 9 2000.

[128] Rajendra S. Apte, Daniel S. Chen, and Napoleone Ferrara. VEGF in Signaling and Disease: Beyond Discovery and Development. *Cell*, 176(6):1248–1264, 3 2019.

[129] Roberta Lugano, Mohanraj Ramachandran, and Anna Dimberg. Tumor angiogenesis: causes, consequences, challenges and opportunities. *Cellular and Molecular Life Sciences*, 77(9):1745–1770, 5 2020.

[130] Hiroya Hashizume, Peter Baluk, Shunichi Morikawa, John W. McLean, Gavin Thurston, Sylvie Roberge, Rakesh K. Jain, and Donald M. McDonald. Openings between defective endothelial cells explain tumor vessel leakiness. *The American journal of pathology*, 156(4):1363–1380, 2000.

[131] Jun Wu. The Enhanced Permeability and Retention (EPR) Effect: The Significance of the Concept and Methods to Enhance Its Application. *Journal of Personalized Medicine*, 11(8), 8 2021.

[132] Yuko Nakamura, Ai Mochida, Peter L. Choyke, and Hisataka Kobayashi. Nanodrug delivery: Is the enhanced permeability and retention (EPR) effect sufficient for curing cancer? *Bioconjugate chemistry*, 27(10):2225, 10 2016.

[133] Patricia S. Steeg. Tumor metastasis: mechanistic insights and clinical challenges. *Nature Medicine*, 12(8):895–904, 8 2006.

[134] Joan Massagué and Anna C. Obenauf. Metastatic colonization by circulating tumour cells. *Nature*, 529(7586):298–306, 1 2016.

[135] Xin Ye and Robert A. Weinberg. Epithelial-Mesenchymal Plasticity: A Central Regulator of Cancer Progression. *Trends in cell biology*, 25(11):675–686, 11 2015.

[136] Raghu Kalluri and Robert A. Weinberg. The basics of epithelial-mesenchymal transition. *The Journal of Clinical Investigation*, 119(6):1420, 6 2009.

[137] S. Curran and G. I. Murray. Matrix metalloproteinases: molecular aspects of their roles in tumour invasion and metastasis. *European journal of cancer*, 36(13):1621–1630, 2000.

[138] Mikala Egeblad and Zena Werb. New functions for the matrix metalloproteinases in cancer progression. *Nature Reviews Cancer*, 2(3):161–174, 2002.

[139] Alexandra Naba, Karl R. Clauser, Huiming Ding, Charles A. Whittaker, Steven A. Carr, and Richard O. Hynes. The extracellular matrix: Tools and insights for the "omics" era. *Matrix Biology*, 49:10–24, 1 2016.

[140] Juliane Winkler, Abisola Abisoye-Ogunniyan, Kevin J. Metcalf, and Zena Werb. Concepts of extracellular matrix remodelling in tumour progression and metastasis. *Nature Communications*, 11(1):1–19, 10 2020.

[141] Otto Warburg, Franz Wind, and Erwin Negelein. The metabolism of tumors in the body. *The Journal of General Physiology*, 8(6):519, 3 1927.

[142] Christian Plathow and Wolfgang A Weber. Tumor Cell Metabolism Imaging. *J Nucl Med*, 49:43–63, 2008.

[143] Rob A. Cairns, Isaac S. Harris, and Tak W. Mak. Regulation of cancer cell metabolism. *Nature Reviews Cancer*, 11(2):85–95, 1 2011.

[144] Inmaculada Martínez-Reyes and Navdeep S. Chandel. Cancer metabolism: looking forward. *Nature Reviews Cancer*, 21(10):669–680, 7 2021.

[145] Andrew R. Mullen, William W. Wheaton, Eunsook S. Jin, Pei Hsuan Chen, Lucas B. Sullivan, Tzuling Cheng, Youfeng Yang, W. Marston Linehan, Navdeep S. Chandel, and Ralph J. Deberardinis. Reductive carboxylation supports growth in tumour cells with defective mitochondria. *Nature*, 481(7381):385–388, 11 2011.

[146] Isaac S. Harris and Gina M. DeNicola. The Complex Interplay between Antioxidants and ROS in Cancer. *Trends in Cell Biology*, 30(6):440–451, 6 2020.

[147] Natalya N. Pavlova and Craig B. Thompson. The Emerging Hallmarks of Cancer Metabolism. *Cell Metabolism*, 23(1):27–47, 1 2016.

[148] Ralph J. De Berardinis and Navdeep S. Chandel. Fundamentals of cancer metabolism. *Science advances*, 2(5), 5 2016.

[149] Pearl Lee, Karen H Vousden, and Eric C Cheung. TIGAR, TIGAR, burning bright. *Cancer & Metabolism*, 2(1):1–9, 1 2014.

[150] Jeremy B. Swann and Mark J. Smyth. Immune surveillance of tumors. *The Journal of Clinical Investigation*, 117(5):1137–1146, 5 2007.

[151] Brian F. Zamarron and Wanjun Chen. Dual Roles of Immune Cells and Their Factors in Cancer Development and Progression. *International Journal of Biological Sciences*, 7(5):651, 2011.

[152] Gavin P. Dunn, Allen T. Bruce, Hiroaki Ikeda, Lloyd J. Old, and Robert D. Schreiber. Cancer immunoediting: from immunosurveillance to tumor escape. *Nature immunology*, 3(11):991–998, 2002.

[153] Brian T. Fife and Jeffrey A. Bluestone. Control of peripheral T-cell tolerance and autoimmunity via the CTLA-4 and PD-1 pathways. *Immunological Reviews*, 224(1):166–182, 8 2008.

[154] Dorothy K. Sojka, Angela Hughson, and Deborah J. Fowell. CTLA-4 is required by CD4+CD25+ Treg to control CD4+ T-cell lymphopenia-induced proliferation. *European Journal of Immunology*, 39(6):1544–1551, 6 2009.

[155] Mary E. Keir, Manish J. Butte, Gordon J. Freeman, and Arlene H. Sharpe. PD-1 and its ligands in tolerance and immunity. *Annual review of immunology*, 26:677–704, 2008.

[156] E. John Wherry and Makoto Kurachi. Molecular and cellular insights into T cell exhaustion. *Nature Reviews Immunology*, 15(8):486–499, 7 2015.

[157] Ian A. Darby, Betty Laverdet, Frédéric Bonté, and Alexis Desmoulière. Fibroblasts and myofibroblasts in wound healing. *Clinical, Cosmetic and Investigational Dermatology*, 7:301, 11 2014.

[158] Nicole M. Anderson and M. Celeste Simon. The tumor microenvironment. *Current Biology*, 30(16):R921–R925, 8 2020.

[159] Erik Sahai, Igor Astsaturov, Edna Cukierman, David G. DeNardo, Mikala Egeblad, Ronald M. Evans, Douglas Fearon, Florian R. Greten, Sunil R. Hingorani, Tony Hunter, Richard O. Hynes, Rakesh K. Jain, Tobias Janowitz, Claus Jorgensen, Alec C. Kimmelman, Mikhail G. Kolonin, Robert G. Maki, R. Scott Powers, Ellen Puré, Daniel C. Ramirez, Ruth Scherz-Shouval, Mara H. Sherman, Sheila Stewart, Thea D. Tlsty, David A. Tuveson, Fiona M. Watt, Valerie Weaver, Ashani T. Weeraratna, and Zena Werb. A framework for advancing our understanding of cancer-associated fibroblasts. *Nature Reviews Cancer*, 20(3):174–186, 1 2020.

[160] G. Gabbiani, G. B. Ryan, and G. Majno. Presence of modified fibroblasts in granulation tissue and their possible role in wound contraction. *Experientia*, 27(5):549–550, 5 1971.

[161] Dorothy A. Beacham and Edna Cukierman. Stromagenesis: The changing face of fibroblastic microenvironments during tumor progression. *Seminars in Cancer Biology*, 15(5):329–341, 10 2005.

[162] Twana Alkasalias, Lidia Moyano-Galceran, Marie Arsenian-Henriksson, and Kaisa Lehti. Fibroblasts in the tumor microenvironment: Shield or spear?, 2018.

[163] William G Stetler-Stevenson, Sadie Aznavoorian, and Lance A Liotta. Tumor Cell Interactions with the Extracellular Matrix During Invasion and Metastasis. *Annu. Rev. Cell Bioi*, 9:541–73, 1993.

[164] George S. Karagiannis, Theofilos Poutahidis, Susan E. Erdman, Richard Kirsch, Robert H. Riddell, and Eleftherios P. Diamandis. Cancer-associated fibroblasts drive the progression of metastasis through both paracrine and mechanical pressure on cancer tissue. *Molecular cancer research*, 10(11):1403–1418, 11 2012.

[165] Shicheng Su, Jianing Chen, Herui Yao, Jiang Liu, Shubin Yu, Liyan Lao, Minghui Wang, Manli Luo, Yue Xing, Fei Chen, Di Huang, Jinghua Zhao, Linbin Yang, Dan Liao, Fengxi Su, Mengfeng Li, Qiang Liu, and Erwei Song. CD10+GPR77+ Cancer-Associated Fibroblasts Promote Cancer Formation

and Chemoresistance by Sustaining Cancer Stemness. *Cell*, 172(4):841–856, 2 2018.

[166] Harold F. Dvorak. Tumors: Wounds That Do Not Heal—Redux. *Cancer Immunology Research*, 3(1):1–11, 1 2015.

[167] Zhanhuai Wang, Yang Tang, Yinuo Tan, Qichun Wei, and Wei Yu. Cancer-associated fibroblasts in radiotherapy: Challenges and new opportunities. *Cell Communication and Signaling*, 17(1):1–12, 5 2019.

[168] Kaspar Haume, Soraia Rosa, Sophie Grellet, Małgorzata A. Śmiałek, Karl T. Butterworth, Andrey V. Solov'yov, Kevin M. Prise, Jon Golding, and Nigel J. Mason. Gold nanoparticles for cancer radiotherapy: a review. *Cancer Nanotechnology*, 7(1), 12 2016.

[169] Shane Harding, Robert Hill, and Robert Bristow. Molecular and Cellular Basis of Radiotherapy. In *The Basic Science of Oncology*. McGraw-Hill Education Medical, New York, NY, 5 edition, 2016.

[170] Andrew Travers and Georgi Muskhelishvili. DNA structure and function. *The FEBS Journal*, 282(12):2279–2295, 6 2015.

[171] Marikki Laiho and Leena Latonen. Cell cycle control, DNA damage checkpoints and cancer. *Annals of Medicine*, 35(6):391–397, 2013.

[172] Emmy P. Rogakou, Chye Boon, Christophe Redon, and William M. Bonner. Megabase chromatin domains involved in DNA double-strand breaks in vivo. *The Journal of cell biology*, 146(5):905–915, 1999.

[173] Stephanie Panier and Simon J. Boulton. Double-strand break repair: 53BP1 comes into focus. *Nature Reviews Molecular Cell Biology*, 15(1):7–18, 12 2013.

[174] Carsten Doil, Niels Mailand, Simon Bekker-Jensen, Patrice Menard, Dorthe Helena Larsen, Rainer Pepperkok, Jan Ellenberg, Stephanie Panier, Daniel Durocher, Jiri Bartek, Jiri Lukas, and Claudia Lukas. RNF168 Binds and Amplifies Ubiquitin Conjugates on Damaged Chromosomes to Allow Accumulation of Repair Proteins. *Cell*, 136(3):435–446, 2 2009.

[175] Kevin J. Barnum and Matthew J. O'Connell. Cell Cycle Regulation by Checkpoints. *Methods in molecular biology*, 1170:29, 2014.

[176] Indra A. Shaltiel, Lenno Krenning, Wytse Bruinsma, and René H. Medema. The same, only different - DNA damage checkpoints and their reversal throughout the cell cycle. *Journal of Cell Science*, 128(4):607–620, 2 2015.

[177] Nimrat Chatterjee and Graham C. Walker. Mechanisms of DNA damage, repair and mutagenesis. *Environmental and molecular mutagenesis*, 58(5):235, 6 2017.

[178] Carol Featherstone and Stephen P. Jackson. DNA double-strand break repair. *Current Biology*, 9(20):R759–R761, 10 1999.

[179] Nicolaas A.P. Franken, Hans M. Rodermond, Jan Stap, Jaap Haveman, and Chris van Bree. Clonogenic assay of cells in vitro. *Nature protocols*, 1(5):2315–2319, 12 2006.

[180] David J. Brenner. The linear-quadratic model is an appropriate methodology for determining isoeffective doses at large doses per fraction. *Seminars in radiation oncology*, 18(4):234–239, 10 2008.

[181] Stephen Joseph McMahon. The linear quadratic model: usage, interpretation and challenges. *Physics in medicine and biology*, 64(1), 1 2018.

[182] Juan Tamargo, Jean Yves Le Heuzey, and Phillipe Mabo. Narrow therapeutic index drugs: a clinical pharmacological consideration to flecainide. *European journal of clinical pharmacology*, 71(5):549–567, 5 2015.

[183] Eric J. Hall. Intensity-modulated radiation therapy, protons, and the risk of second cancers. *International journal of radiation oncology, biology, physics*, 65(1):1–7, 5 2006.

[184] Turid Hellevik and Iñigo Martinez-Zubiaurre. Radiotherapy and the Tumor Stroma: The Importance of Dose and Fractionation. *Frontiers in Oncology*, 4, 2014.

[185] Elisabeth Daguenet, Jonathan Khalifa, Alain Tolédano, Delphine Borchiellini, Yoann Pointreau, Claire Rodriguez-Lafrasse, Cyrus Chargari, and Nicolas Magné. To exploit the 5 'R' of radiobiology and unleash the 3 'E' of immunoediting: 'RE'-inventing the radiotherapy-immunotherapy combination. *Therapeutic Advances in Medical Oncology*, 12, 2020.

[186] Brita Singers Sørensen and Michael R. Horsman. Tumor Hypoxia: Impact on Radiation Therapy and Molecular Pathways. *Frontiers in Oncology*, 10:562, 4 2020.

[187] E Segre, H Goldstein, F W Spiers, G E Hine, R C Murty, and H Tellez-Plasencia. Effective Atomic Numbers of Heterogeneous Materials. *Nature*, 207(4995):398–399, 1965.

[188] John Cunningham and Harold Johns. *Physics of Radiology*. Charles C Thomas, Springfield, 4 edition, 1983.

[189] J H. Hubbell and Stephen M. Seltzer. Tables of X-Ray Mass Attenuation Coefficients and Mass Energy-Absorption Coefficients 1 keV to 20 MeV for Elements Z = 1 to 92 and 48 Additional Substances of Dosimetric Interest, 1995.

[190] Yuji Yazaki. How the Klein–Nishina formula was derived: Based on the Sangokan Nishina Source Materials. *Proceedings of the Japan Academy*, 93(6):399, 6 2017.

[191] Parisa Foroozandeh and Azlan Abdul Aziz. Insight into Cellular Uptake and Intracellular Trafficking of Nanoparticles. *Nanoscale Research Letters*, 13(1):1–12, 10 2018.

[192] Devika B Chithrani. Optimization of Bio-Nano Interface Using Gold Nanostructures as a Model Nanoparticle System. *Insciences*, 1(3):115–135, 7 2011.

[193] Devika B. Chithrani. Intracellular uptake, transport, and processing of gold nanostructures. *Molecular membrane biology*, 27(7):299–311, 10 2010.

[194] Hong Jin, Daniel A. Heller, and Michael S. Strano. Single-particle tracking of endocytosis and exocytosis of single-walled carbon nanotubes in NIH-3T3 cells. *Nano Letters*, 8(6):1577–1585, 6 2008.

[195] Xiaowei Ma, Yanyang Wu, Shubin Jin, Yuan Tian, Xiaoning Zhang, Yuliang Zhao, Li Yu, and Xing Jie Liang. Gold nanoparticles induce autophagosome accumulation through size-dependent nanoparticle uptake and lysosome impairment. *ACS Nano*, 5(11):8629–8639, 11 2011.

[196] Mengmeng Liu, Qian Li, Le Liang, Jiang Li, Kun Wang, Jiajun Li, Min Lv, Nan Chen, Haiyun Song, Joon Lee, Jiye Shi, Lihua Wang, Ratnesh Lal, and

Chunhai Fan. Real-time visualization of clustering and intracellular transport of gold nanoparticles by correlative imaging. *Nature Communications*, 8(1):1–10, 5 2017.

[197] B. Devika Chithrani, Arezou A. Ghazani, and Warren C.W. Chan. Determining the size and shape dependence of gold nanoparticle uptake into mammalian cells. *Nano Letters*, 6(4):662–668, 4 2006.

[198] Huajian Gao, Wendong Shi, and Lambert B. Freund. Mechanics of receptor-mediated endocytosis. *Proceedings of the National Academy of Sciences of the United States of America*, 102(27):9469–9474, 7 2005.

[199] Hong Jin, Daniel A. Heller, Richa Sharma, and Michael S. Strano. Size-dependent cellular uptake and expulsion of single-walled carbon nanotubes: Single particle tracking and a generic uptake model for nanoparticles. *ACS Nano*, 3(1):149–158, 1 2009.

[200] B. Devika Chithrani and Warren C.W. Chan. Elucidating the mechanism of cellular uptake and removal of protein-coated gold nanoparticles of different sizes and shapes. *Nano Letters*, 7(6):1542–1550, 6 2007.

[201] Charmainne Cruje and Devika B. Chithrani. Polyethylene Glycol Functionalized Nanoparticles for Improved Cancer Treatment. *Reviews in Nanoscience and Nanotechnology*, 3(1):20–30, 6 2014.

[202] Catherine Carnovale, Gary Bryant, Ravi Shukla, and Vipul Bansal. Gold nanoparticle biodistribution and toxicity: Role of biological corona in relation with nanoparticle characteristics. *Metal Nanoparticles in Pharma*, pages 419–436, 1 2017.

[203] Celina Yang, Kyle Bromma, and Devika Chithrani. Peptide Mediated In Vivo Tumor Targeting of Nanoparticles through Optimization in Single and Multi-layer In Vitro Cell Models. *Cancers*, 10(3), 3 2018.

[204] Hua Qin Yin, Feng Li Bi, and Feng Gan. Rapid synthesis of cyclic RGD conjugated gold nanoclusters for targeting and fluorescence imaging of melanoma A375 cells. *Bioconjugate Chemistry*, 26(2):243–249, 2 2015.

[205] Susan L. Bellis. Advantages of RGD peptides for directing cell association with biomaterials. *Biomaterials*, 32(18):4205, 6 2011.

[206] E. Lechtman, N. Chattopadhyay, Z. Cai, S. Mashouf, R. Reilly, and J. P. Pignol. Implications on clinical scenario of gold nanoparticle radiosensitization in regards to photon energy, nanoparticle size, concentration and location. *Physics in medicine and biology*, 56(15):4631–4647, 8 2011.

[207] Michael K.K. Leung, James C.L. Chow, B. Devika Chithrani, Martin J.G. Lee, Barbara Oms, and David A. Jaffray. Irradiation of gold nanoparticles by x-rays: Monte Carlo simulation of dose enhancements and the spatial properties of the secondary electrons production. *Medical physics*, 38(2):624–631, 2011.

[208] Cuihong Wang, Yuhua Jiang, Xiaohong Li, and Likuan Hu. Thioglucose-bound gold nanoparticles increase the radiosensitivity of a triple-negative breast cancer cell line (MDA-MB-231). *Breast Cancer*, 22(4):413–420, 7 2015.

[209] Suneil Jain, Jonathan A. Coulter, Alan R. Hounsell, Karl T. Butterworth, Stephen J. McMahon, Wendy B. Hyland, Mark F. Muir, Glenn R. Dickson, Kevin M. Prise, Fred J. Currell, Joe M. O'Sullivan, and David G. Hirst. Cell-Specific Radiosensitization by gold nanoparticles at megavoltage radiation energies. *International Journal of Radiation Oncology Biology Physics*, 79(2):531–539, 2 2011.

[210] Karl T. Butterworth, Stephen J. McMahon, Fred J. Currell, and Kevin M. Prise. Physical basis and biological mechanisms of gold nanoparticle radiosensitization. *Nanoscale*, 4(16):4830–4838, 7 2012.

[211] Kyle Bromma, Leah Cicon, Wayne Beckham, and Devika B. Chithrani. Gold nanoparticle mediated radiation response among key cell components of the tumour microenvironment for the advancement of cancer nanotechnology. *Scientific Reports*, 10(1):1–14, 7 2020.

[212] Roy M. Bremnes, Tom Dønnem, Samer Al-Saad, Khalid Al-Shibli, Sigve Andersen, Rafael Sirera, Carlos Camps, Inigo Marinez, and Lill Tove Busund. The role of tumor stroma in cancer progression and prognosis: emphasis on carcinoma-associated fibroblasts and non-small cell lung cancer. *Journal of thoracic oncology*, 6(1):209–217, 2011.

[213] Maonan Wang, Jingzhou Zhao, Lishen Zhang, Fang Wei, Yu Lian, Yingfeng Wu, Zhaojian Gong, Shanshan Zhang, Jianda Zhou, Ke Cao, Xiayu Li, Wei Xiong,

Guiyuan Li, Zhaoyang Zeng, and Can Guo. Role of tumor microenvironment in tumorigenesis. *Journal of Cancer*, 8(5):761, 2017.

[214] Daniel Öhlund, Ela Elyada, and David Tuveson. Fibroblast heterogeneity in the cancer wound. *The Journal of Experimental Medicine*, 211(8):1503, 7 2014.

[215] Jean Albrengues, Thomas Bertero, Eloise Grasset, Stephanie Bonan, Majdi Maiel, Isabelle Bourget, Claude Philippe, Cecilia Herraiz Serrano, Samia Benamar, Olivier Croce, Victoria Sanz-Moreno, Guerrino Meneguzzi, Chloe C. Feral, Gael Cristofari, and Cedric Gaggioli. Epigenetic switch drives the conversion of fibroblasts into proinvasive cancer-associated fibroblasts. *Nature Communications*, 6(1):1–15, 12 2015.

[216] Joanne Manson, Dhiraj Kumar, Brian J. Meenan, and Dorian Dixon. Polyethylene glycol functionalized gold nanoparticles: The influence of capping density on stability in various media. *Gold Bulletin*, 44(2):99–105, 4 2011.

[217] Wolfgang Haiss, Nguyen T.K. Thanh, Jenny Aveyard, and David G. Fernig. Determination of size and concentration of gold nanoparticles from UV-Vis spectra. *Analytical Chemistry*, 79(11):4215–4221, 6 2007.

[218] Aaron Bannister, Dushanthi Dissanayake, Antonia Kowalewski, Leah Cicon, Kyle Bromma, and Devika B. Chithrani. Modulation of the Microtubule Network for Optimization of Nanoparticle Dynamics for the Advancement of Cancer Nanomedicine. *Bioengineering*, 7(2):56, 6 2020.

[219] Paula Zamora-Perez, Dionysia Tsoutsi, Ruixue Xu, and Pilar Rivera-Gil. Hyperspectral-Enhanced Dark Field Microscopy for Single and Collective Nanoparticle Characterization in Biological Environments. *Materials*, 11(2):243, 2 2018.

[220] M. H. Zwietering, I. Jongenburger, F. M. Rombouts, and K. Van't Riet. Modeling of the Bacterial Growth Curve. *Applied and Environmental Microbiology*, 56(6):1875, 1990.

[221] Thomas T Goodman, Peggy L Olive, and Suzie H Pun. Increased nanoparticle penetration in collagenase-treated multicellular spheroids. *International Journal of Nanomedicine*, 2(2):265, 2007.

[222] Jun Fang, Hideaki Nakamura, and Hiroshi Maeda. The EPR effect: Unique features of tumor blood vessels for drug delivery, factors involved, and limitations and augmentation of the effect. *Advanced Drug Delivery Reviews*, 63(3):136–151, 3 2011.

[223] Norbert Orgovan, Beatrix Peter, Szilvia Bosze, Jeremy J. Ramsden, Bálint Szabó, and Robert Horvath. Dependence of cancer cell adhesion kinetics on integrin ligand surface density measured by a high-throughput label-free resonant waveguide grating biosensor. *Scientific Reports*, 4(1):1–8, 2 2014.

[224] M. Chernyavska, M. Schmid, P. C. Freitag, V. Palacio-Castañeda, A. Piruska, W. T.S. Huck, A. Plückthun, and W. P.R. Verdurmen. Unravelling Receptor and RGD Motif Dependence of Retargeted Adenoviral Vectors using Advanced Tumor Model Systems. *Scientific Reports*, 9(1):1–13, 12 2019.

[225] Judit P. Banáth, Dmitry Klokov, Susan H. MacPhail, C. Adriana Banuelos, and Peggy L. Olive. Residual γH2AX foci as an indication of lethal DNA lesions. *BMC Cancer*, 10(1):1–12, 1 2010.

[226] Henning D. Popp, Susanne Brendel, Wolf Karsten Hofmann, and Alice Fabarius. Immunofluorescence Microscopy of γH2AX and 53BP1 for Analyzing the Formation and Repair of DNA Double-strand Breaks. *JoVE*, 2017(129):e56617, 11 2017.

[227] Jingsong Yuan, Rachel Adamski, and Junjie Chen. Focus on histone variant H2AX: To be or not to be. *FEBS Letters*, 584(17):3717–3724, 9 2010.

[228] J. Kimling, M. Maier, B. Okenve, V. Kotaidis, H. Ballot, and A. Plech. Turkevich Method for Gold Nanoparticle Synthesis Revisited. *Journal of Physical Chemistry B*, 110(32):15700–15707, 8 2006.

[229] Magdalena Boncler, Marek Rózalski, Urszula Krajewska, Anna Podswdek, and Cezary Watala. Comparison of PrestoBlue and MTT assays of cellular viability in the assessment of anti-proliferative effects of plant extracts on human endothelial cells. *Journal of Pharmacological and Toxicological Methods*, 69(1):9–16, 1 2014.

[230] Jayanta Kumar Patra, Gitishree Das, Leonardo Fernandes Fraceto, Estefania Vangelie Ramos Campos, Maria del Pilar Rodriguez-Torres, Laura Susana

Acosta-Torres, Luis Armando Diaz-Torres, Renato Grillo, Mallappa Kumara Swamy, Shivesh Sharma, Solomon Habtemariam, and Han-Seung Shin. Nano based drug delivery systems: recent developments and future prospects. *Journal of Nanobiotechnology*, 2018.

[231] Yue Pan, Peijun Xue, Shaopeng Liu, Lechuan Zhang, Qingbao Guan, Jianliang Zhu, and Xin Tian. Metal-Based Hybrid Nanoparticles as Radiosensitizers in Cancer Therapy, 3 2018.

[232] R. Ab Rashid, K. Abdul Razak, M. Geso, R. Abdullah, N. Dollah, and W. N. Rahman. Radiobiological Characterization of the Radiosensitization Effects by Gold Nanoparticles for Megavoltage Clinical Radiotherapy Beams. *Bio-NanoScience*, 8(3):713–722, 9 2018.

[233] Partha Ghosh, Gang Han, Mrinmoy De, Chae Kyu Kim, and Vincent M. Rotello. Gold nanoparticles in delivery applications. *Advanced Drug Delivery Reviews*, 60(11):1307–1315, 8 2008.

[234] Giulio F. Paciotti, David G.I. Kingston, and Lawrence Tamarkin. Colloidal gold nanoparticles: A novel nanoparticle platform for developing multifunctional tumor-targeted drug delivery vectors. *Drug Development Research*, 67(1):47–54, 1 2006.

[235] Tanveer A. Tabish, Priyanka Dey, Sara Mosca, Marzieh Salimi, Francesca Palombo, Pavel Matousek, and Nicholas Stone. Smart Gold Nanostructures for Light Mediated Cancer Theranostics: Combining Optical Diagnostics with Photothermal Therapy. *Advanced Science*, 7(15):1903441, 8 2020.

[236] Xiao-Dong Zhang, Wu, Shen, Liu, Sun, Zhang, and Fan. Size-dependent in vivo toxicity of PEG-coated gold nanoparticles. *International Journal of Nanomedicine*, 6:2071, 9 2011.

[237] Kyle Bromma, Abdulaziz Alhussan, Monica Mesa Perez, Perry Howard, Wayne Beckham, and Devika B. Chithrani. Three-Dimensional Tumor Spheroids as a Tool for Reliable Investigation of Combined Gold Nanoparticle and Docetaxel Treatment. *Cancers*, 13(6):1465, 3 2021.

[238] Ya-Ru Zhang, Run Lin, Hong-Jun Li, Wei-ling He, Jin-Zhi Du, and Jun Wang. Strategies to improve tumor penetration of nanomedicines through nanoparticle

design. *Wiley Interdisciplinary Reviews: Nanomedicine and Nanobiotechnology*, 11(1):1519, 1 2019.

[239] Aaron Henry Bannister, Kyle Bromma, Wonmo Sung, Mesa Monica, Leah Cicon, Perry Howard, Robert L. Chow, Jan Schuemann, and Devika Basnagge Chithrani. Modulation of nanoparticle uptake, intracellular distribution, and retention with docetaxel to enhance radiotherapy. *British Journal of Radiology*, 93(1106), 12 2020.

[240] Sukru Gokhan Elci, Ying Jiang, Bo Yan, Sung Tae Kim, Krishnendu Saha, Daniel F. Moyano, Gulen Yesilbag Tonga, Liam C. Jackson, Vincent M. Rotello, and Richard W. Vachet. Surface Charge Controls the Suborgan Biodistributions of Gold Nanoparticles. *ACS Nano*, 10(5):5536–5542, 5 2016.

[241] Paola Nativo, Ian A. Prior, and Mathias Brust. Uptake and intracellular fate of surface-modified gold nanoparticles. *ACS Nano*, 2(8):1639–1644, 8 2008.

[242] Kyle Bromma and Devika B. Chithrani. Advances in Gold Nanoparticle-Based Combined Cancer Therapy. *Nanomaterials*, 10(9):1671, 8 2020.

[243] Ping-Hsiu Hsiu Wu, Yasuhito Onodera, Yuki Ichikawa, Erinn B. Rankin, Amato J. Giaccia, Yuko Watanabe, Wei Qian, Takayuki Hashimoto, Hiroki Shirato, and Jin-Min Min Nam. Targeting integrins with RGD-conjugated gold nanoparticles in radiotherapy decreases the invasive activity of breast cancer cells. *International Journal of Nanomedicine*, pages 5069–5085, 7 2017.

[244] Shangfeng Du, Kevin Kendall, Panteha Toloueinia, Yasamin Mehrabadi, Gaurav Gupta, and Jill Newton. Aggregation and adhesion of gold nanoparticles in phosphate buffered saline. *Journal of Nanoparticle Research*, 14(3):1–14, 3 2012.

[245] Tien En Chiang, Ching Liang Ho, Chun Shu Lin, and Yuan Wu Chen. Complete remission in very advanced oral cancer by docetaxel, cisplatin, 5-fluorouracil based induction chemotherapy followed by concurrent chemoradiation, 3 2018.

[246] Rama Grantab, Shankar Sivananthan, and Ian F. Tannock. The penetration of anticancer drugs through tumor tissue as a function of cellular adhesion and packing density of tumor cells. *Cancer Research*, 66(2):1033–1039, 1 2006.

[247] Andrew S. Mikhail, Sina Eetezadi, and Christine Allen. Multicellular Tumor Spheroids for Evaluation of Cytotoxicity and Tumor Growth Inhibitory Effects of Nanomedicines In Vitro: A Comparison of Docetaxel-Loaded Block Copolymer Micelles and Taxotere. *PLoS ONE*, 8(4):e62630, 4 2013.

[248] Suraj Kumar Singh, Sabiya Abbas, Ajit Kumar Saxena, Swasti Tiwari, Lokendra Kumar Sharma, and Meenakshi Tiwari. Critical role of three-dimensional tumorsphere size on experimental outcome. *BioTechniques*, 69(5):333–338, 11 2020.

[249] Marc Hafner, Mario Niepel, Mirra Chung, and Peter K. Sorger. Growth rate inhibition metrics correct for confounders in measuring sensitivity to cancer drugs. *Nature Methods*, 13(6):521–527, 6 2016.

[250] Angelika Riedl, Michaela Schlederer, Karoline Pudelko, Mira Stadler, Stefanie Walter, Daniela Unterleuthner, Christine Unger, Nina Kramer, Markus Hengstschläger, Lukas Kenner, Dagmar Pfeiffer, Georg Krupitza, and Helmut Dolznig. Comparison of cancer cells in 2D vs 3D culture reveals differences in AKT-mTOR-S6K signaling and drug responses. *Journal of Cell Science*, 130(1):203–218, 2017.

[251] Chun Li Li, Tao Tian, Ke Jun Nan, Na Zhao, Ya Huan Guo, Jie Cui, Jin Wang, and Wang Gang Zhang. Survival advantages of multicellular spheroids vs. monolayers of HepG2 cells in vitro. *Oncology Reports*, 20(6):1465–1471, 12 2008.

[252] Rasheena Edmondson, Audrey F. Adcock, and Liju Yang. Influence of Matrices on 3D-Cultured Prostate Cancer Cells' Drug Response and Expression of Drug-Action Associated Proteins. *PLOS ONE*, 11(6):e0158116, 6 2016.

[253] Hoda Soleymani Abyaneh, Maximilian Regenold, Trevor D. McKee, Christine Allen, and Marc A. Gauthier. Towards extracellular matrix normalization for improved treatment of solid tumors, 2020.

[254] Paal Fr Brunsvig, Anders Andersen, Steinar Aamdal, Vessela Kristensen, and Harald Olsen. Pharmacokinetic analysis of two different docetaxel dose levels in patients with non-small cell lung cancer treated with docetaxel as monotherapy or with concurrent radiotherapy. *BMC Cancer*, 7(1):197, 10 2007.

[255] Christopher G. England, Justin S. Huang, Kurtis T. James, Guandong Zhang, AndréM Gobin, and Hermann B. Frieboes. Detection of phosphatidylcholine-coated gold nanoparticles in orthotopic pancreatic adenocarcinoma using hyperspectral imaging. *PLoS ONE*, 10(6), 6 2015.

[256] Kalishwaralal Kalimuthu, Bat Chen Lubin, Andrii Bazylevich, Gary Gellerman, Ofer Shpilberg, Galia Luboshits, and Michael A. Firer. Gold nanoparticles stabilize peptide-drug-conjugates for sustained targeted drug delivery to cancer cells. *Journal of Nanobiotechnology*, 16(1):34, 3 2018.

[257] Allen L. Chen, Ying S. Hu, Meredith A. Jackson, Adam Y. Lin, Joseph K. Young, Robert J. Langsner, and Rebekah A. Drezek. Quantifying spectral changes experienced by plasmonic nanoparticles in a cellular environment to inform biomedical nanoparticle design. *Nanoscale Research Letters*, 9(1):454, 2014.

[258] C. Yang, J. Uertz, D. Yohan, and B. D. Chithrani. Peptide modified gold nanoparticles for improved cellular uptake, nuclear transport, and intracellular retention. *Nanoscale*, 6(20):12026–12033, 10 2014.

[259] Inês Mó, Ivo J. Sabino, Duarte De Melo-Diogo, Rita Lima-Sousa, Cátia G. Alves, and Ilídio J. Correia. The importance of spheroids in analyzing nanomedicine efficacy, 6 2020.

[260] Aliya Fatehullah, Si Hui Tan, and Nick Barker. Organoids as an in vitro model of human development and disease. *Nature Cell Biology*, 18(3):246–54, 2016.

[261] Sébastien Penninckx, Anne Catherine Heuskin, Carine Michiels, and Stéphane Lucas. Gold nanoparticles as a potent radiosensitizer: A transdisciplinary approach from physics to patient, 8 2020.

[262] Francesco Pampaloni, Emmanuel G. Reynaud, and Ernst H.K. Stelzer. The third dimension bridges the gap between cell culture and live tissue. *Nature Reviews Molecular Cell Biology*, 8(10):839–845, 10 2007.

[263] Sritama Nath and Gayathri R. Devi. Three-dimensional culture systems in cancer research: Focus on tumor spheroid model. *Pharmacology & Therapeutics*, 163:94–108, 7 2016.

[264] Daniela F. Quail and Johanna A. Joyce. Microenvironmental regulation of tumor progression and metastasis. *Nature Medicine*, 19(11):1423–1437, 11 2013.

[265] Christophe Dubessy, Jean Louis Merlin, Christian Marchal, and François Guillemin. Spheroids in radiobiology and photodynamic therapy. *Critical Reviews in Oncology/Hematology*, 36(2-3):179–192, 11 2000.

[266] Franziska Hirschhaeuser, Heike Menne, Claudia Dittfeld, Jonathan West, Wolfgang Mueller-Klieser, and Leoni A. Kunz-Schughart. Multicellular tumor spheroids: An underestimated tool is catching up again. *Journal of Biotechnology*, 148(1):3–15, 7 2010.

[267] Sarah C. Brüningk, Ian Rivens, Carol Box, Uwe Oelfke, and Gail ter Haar. 3D tumour spheroids for the prediction of the effects of radiation and hyperthermia treatments. *Scientific Reports*, 2020.

[268] Lei Xing, Brian Thorndyke, Eduard Schreibmann, Yong Yang, Tian Fang Li, Gwe Ya Kim, Gary Luxton, and Albert Koong. Overview of image-guided radiation therapy. *Medical Dosimetry*, 31(2):91–112, 6 2006.

[269] By Jihye Choi, Kyung Oh Jung, Edward E. Graves, and Guillem Pratx. A gold nanoparticle system for enhancement of radiotherapy and simultaneous monitoring of reactive-oxygen-species formation. *Nanotechnology*, 29(50):504001, 12 2018.

[270] Michael L. Pearl, Carolyn M. Johnston, and D. Scott McMeekin. A phase II study of weekly docetaxel for patients with advanced or recurrent cancer of the cervix. *Gynecologic and obstetric investigation*, 64(4):193–198, 11 2007.

[271] Javier Puente, Enrique Grande, Ana Medina, Pablo Maroto, Nuria Lainez, and Jose Angel Arranz. Docetaxel in prostate cancer: a familiar face as the new standard in a hormone-sensitive setting. *Therapeutic Advances in Medical Oncology*, 9(5):307, 5 2017.

[272] KJ Pienta. Preclinical mechanisms of action of docetaxel and docetaxel combinations in prostate cancer. *Seminars in oncology*, 28(4 Suppl 15):3–7, 8 2001.

[273] Anne Paoletti, Nicole Giocanti, Vincent Favaudon, and Michel Bornens. Pulse treatment of interphasic HeLa cells with nanomolar doses of docetaxel affects

centrosome organization and leads to catastrophic exit of mitosis. *Journal of Cell Science*, 110(19):2403–2415, 10 1997.

[274] Kyle Bromma, Nancy Dos Santos, Ingrid Barta, Abraham Alexander, Wayne Beckham, Sunil Krishnan, and Devika B. Chithrani. Enhancing nanoparticle accumulation in two dimensional, three dimensional, and xenograft mouse cancer cell models in the presence of docetaxel. *Scientific Reports*, 12(1):1–14, 8 2022.

[275] Wan Seob Cho, Minjung Cho, Jinyoung Jeong, Mina Choi, Beom Seok Han, Hyung Seon Shin, Jin Hong, Bong Hyun Chung, Jayoung Jeong, and Myung Haing Cho. Size-dependent tissue kinetics of PEG-coated gold nanoparticles. *Toxicology and Applied Pharmacology*, 245(1):116–123, 5 2010.

[276] Gongke Wang, Changling Yan, Shuyan Gao, and Yufang Liu. Surface chemistry of gold nanoparticles determines interactions with bovine serum albumin. *Materials Science and Engineering: C*, 103:109856, 10 2019.

[277] Renliang Xu. Progress in nanoparticles characterization: Sizing and zeta potential measurement. *Particuology*, 6(2):112–115, 4 2008.

[278] Sang Han Lee and Yoon Jin Lee. Synergistic anticancer activity of resveratrol in combination with docetaxel in prostate carcinoma cells. *Nutrition Research and Practice*, 15(1):12, 2 2021.

[279] Manlong Xu, David J. McCanna, and Jacob G. Sivak. Use of the viability reagent PrestoBlue in comparison with alamarBlue and MTT to assess the viability of human corneal epithelial cells. *Journal of pharmacological and toxicological methods*, 71:1–7, 1 2015.

[280] Brigid E. Hickey, Melissa L. James, Tiffany Daly, Feng Yi Soh, and Mark Jeffery. Hypofractionation for clinically localized prostate cancer. *The Cochrane Database of Systematic Reviews*, 2019(9), 9 2019.

[281] Stephanie B. Greene, Angel E. Dago, Laura J. Leitz, Yipeng Wang, Jerry Lee, Shannon L. Werner, Steven Gendreau, Premal Patel, Shidong Jia, Liangxuan Zhang, Eric K. Tucker, Michael Malchiodi, Ryon P. Graf, Ryan Dittamore, Dena Marrinucci, and Mark Landers. Chromosomal Instability Estimation Based

on Next Generation Sequencing and Single Cell Genome Wide Copy Number Variation Analysis. *PLoS ONE*, 11(11):165089, 11 2016.

[282] Michael R. Horsman, Lise Sakso Mortensen, Jorgen B. Petersen, Morten Busk, and Jens Overgaard. Imaging hypoxia to improve radiotherapy outcome. *Nature Reviews Clinical Oncology*, 9(12):674–687, 11 2012.

[283] H. Hernández-Vargas, J. Palacios, and G. Moreno-Bueno. Molecular profiling of docetaxel cytotoxicity in breast cancer cells: uncoupling of aberrant mitosis and apoptosis. *Oncogene 2007 26:20*, 26(20):2902–2913, 11 2006.

[284] Ana Carrasco-Mantis, Héctor Castro-Abril, Teodora Randelovic, Ignacio Ochoa, Manuel Doblaré, and José A. Sanz-Herrera. A mechanobiological model for tumor spheroids evolution: application to glioblastoma. *bioRxiv*, page 2021.10.08.463617, 10 2021.

[285] Johannes Schindelin, Ignacio Arganda-Carreras, Erwin Frise, Verena Kaynig, Mark Longair, Tobias Pietzsch, Stephan Preibisch, Curtis Rueden, Stephan Saalfeld, Benjamin Schmid, Jean Yves Tinevez, Daniel James White, Volker Hartenstein, Kevin Eliceiri, Pavel Tomancak, and Albert Cardona. Fiji: an open-source platform for biological-image analysis. *Nature Methods 2012 9:7*, 9(7):676–682, 6 2012.

[286] Michael Perrotti, Todd Doyle, Parvesh Kumar, Daryl McLeod, William Badger, Susan Prater, Michael Moran, Stuart Rosenberg, Cora Bonatsos, Carrie Kreitner, Ralf Kiehl, Theodore Chang, and Michael Kolodziej. Phase I/II trial of docetaxel and concurrent radiation therapy in localized high risk prostate cancer (AGUSG 03-10). *Urologic Oncology: Seminars and Original Investigations*, 26(3):276–280, 5 2008.

[287] Anroop B. Nair and Shery Jacob. A simple practice guide for dose conversion between animals and human. *Journal of Basic and Clinical Pharmacy*, 7(2):27, 2016.

[288] Hisato Konoeda, Hiromitsu Takizawa, Annette Gower, Michael Zhao, Oyedele A. Adeyi, and Mingyao Liu. Pharmacokinetics, tissue distribution and safety of gold nanoparticle/PKC Delta inhibitor peptide hybrid in rats. *Nanotoxicology*, 14(3):341–354, 3 2019.

[289] Dnyaneshwar Kalyane, Nidhi Raval, Rahul Maheshwari, Vishakha Tambe, Kiran Kalia, and Rakesh K. Tekade. Employment of enhanced permeability and retention effect (EPR): Nanoparticle-based precision tools for targeting of therapeutic and diagnostic agent in cancer. *Materials Science and Engineering: C*, 98:1252–1276, 5 2019.

[290] Mark Sutherland, Andrew Gordon, Steven D. Shnyder, Laurence H. Patterson, and Helen M. Sheldrake. RGD-Binding Integrins in Prostate Cancer: Expression Patterns and Therapeutic Prospects against Bone Metastasis. *Cancers*, 4(4):1106–1145, 10 2012.

[291] Joaquim Vives and Laura Batlle-Morera. The challenge of developing human 3D organoids into medicines, 2020.

[292] Roghayyeh Baghban, Leila Roshangar, Rana Jahanban-Esfahlan, Khaled Seidi, Abbas Ebrahimi-Kalan, Mehdi Jaymand, Saeed Kolahian, Tahereh Javaheri, and Peyman Zare. Tumor microenvironment complexity and therapeutic implications at a glance. *Cell Communication and Signaling*, 18(1):1–19, 4 2020.

[293] Pallab Datta, Madhuri Dey, Zaman Ataie, Derya Unutmaz, and Ibrahim T. Ozbolat. 3D bioprinting for reconstituting the cancer microenvironment. *npj Precision Oncology*, 4(1):1–13, 7 2020.

[294] Xin Wang, Feifei Teng, Li Kong, and Jinming Yu. PD-L1 expression in human cancers and its association with clinical outcomes. *OncoTargets and Therapy*, 9:5023–5039, 8 2016.

[295] Xian Shen and Bin Zhao. Efficacy of PD-1 or PD-L1 inhibitors and PD-L1 expression status in cancer: meta-analysis. *BMJ*, 362:3529, 9 2018.

[296] Chaoyue Su, Hui Wang, Yunru Liu, Qiaoru Guo, Lingling Zhang, Jiajun Li, Wenmin Zhou, Yanyan Yan, Xinke Zhou, and Jianye Zhang. Adverse Effects of Anti-PD-1/PD-L1 Therapy in Non-small Cell Lung Cancer. *Frontiers in Oncology*, 10:1821, 9 2020.

[297] Hiro Sato, Noriyuki Okonogi, and Takashi Nakano. Rationale of combination of anti-PD-1/PD-L1 antibody therapy and radiotherapy for cancer treatment. *International Journal of Clinical Oncology*, 25(5):801–809, 5 2020.

[298] Xiang Li, Xiong Zhou, Jun Liu, Jing Zhang, Yulin Feng, Fang Wang, Yao He, Anping Wan, Nina Filipczak, Satya Siva Kishan Yalamarty, Yi Jin, and Vladimir P. Torchilin. Liposomal Co-delivery of PD-L1 siRNA/Anemoside B4 for Enhanced Combinational Immunotherapeutic Effect. *ACS Applied Materials and Interfaces*, 14(25):28439–28454, 6 2022.